Research Topics

Source-grid-load-storage collaborative and interactive optimization control technology of new types of active distribution network

Edited by
Fei Wang, Zhijian Liu, Tianguang Lu, Pierluigi Siano and Jin Lin

Published in
Frontiers in Energy Research

ISSN 1664-8714
ISBN 978-2-83252-032-1
DOI 10.3389/978-2-83252-032-1

About Frontiers

Frontiers is more than just an open access publisher of scholarly articles: it is a pioneering approach to the world of academia, radically improving the way scholarly research is managed. The grand vision of Frontiers is a world where all people have an equal opportunity to seek, share and generate knowledge. Frontiers provides immediate and permanent online open access to all its publications, but this alone is not enough to realize our grand goals.

Frontiers journal series

The Frontiers journal series is a multi-tier and interdisciplinary set of open-access, online journals, promising a paradigm shift from the current review, selection and dissemination processes in academic publishing. All Frontiers journals are driven by researchers for researchers; therefore, they constitute a service to the scholarly community. At the same time, the *Frontiers journal series* operates on a revolutionary invention, the tiered publishing system, initially addressing specific communities of scholars, and gradually climbing up to broader public understanding, thus serving the interests of the lay society, too.

Dedication to quality

Each Frontiers article is a landmark of the highest quality, thanks to genuinely collaborative interactions between authors and review editors, who include some of the world's best academicians. Research must be certified by peers before entering a stream of knowledge that may eventually reach the public - and shape society; therefore, Frontiers only applies the most rigorous and unbiased reviews. Frontiers revolutionizes research publishing by freely delivering the most outstanding research, evaluated with no bias from both the academic and social point of view. By applying the most advanced information technologies, Frontiers is catapulting scholarly publishing into a new generation.

What are Frontiers Research Topics?

Frontiers Research Topics are very popular trademarks of the *Frontiers journals series*: they are collections of at least ten articles, all centered on a particular subject. With their unique mix of varied contributions from Original Research to Review Articles, Frontiers Research Topics unify the most influential researchers, the latest key findings and historical advances in a hot research area.

Find out more on how to host your own Frontiers Research Topic or contribute to one as an author by contacting the Frontiers editorial office: frontiersin.org/about/contact

Source-grid-load-storage collaborative and interactive optimization control technology of new types of active distribution network

Topic editors
Fei Wang — North China Electric Power University, China
Zhijian Liu — North China Electric Power University, China
Tianguang Lu — Shandong University, China
Pierluigi Siano — University of Salerno, Italy
Jin Lin — Tsinghua University, China

Citation
Wang, F., Liu, Z., Lu, T., Siano, P., Lin, J., eds. (2023). *Source-grid-load-storage collaborative and interactive optimization control technology of new types of active distribution network*. Lausanne: Frontiers Media SA.
doi: 10.3389/978-2-83252-032-1

Table of contents

frontiers | Frontiers in Energy Research

BRIEF RESEARCH REPORT
published: 01 June 2022
doi: 10.3389/fenrg.2022.906406

A Game Optimization Scheduling Strategy of Active Distribution Network With Multi-Microgrid Sharing Energy Storage

Fei Li[1,2]*, *Xianshan Li*[1,2], *Zijian Fang*[2] *and Lei Zhang*[2]

[1]Hubei Provincial Key Laboratory for Operation and Control of Cascaded Hydropower Station, China Three Gorges University, Yichang, China, [2]College of Electrical Engineering and New Energy, China Three Gorges University, Yichang, China

In a multi-microgrid grid-connected system, a MGCO is formed to participate in the optimization scheduling of the ADN by sharing ES, which can promote the efficient utilization of resources and obtain win–win interests for all participants. According to the complementary characteristics of ES behaviors and energy production–consumption of MGs, a game scheduling model of the ADN with the MGCO for sharing ES is established to obtain energy reciprocity and balance the interest of both parties. The ADN formulates the ToU price policy to maximize the operational benefits, and the MGCO responds to the price to obtain each member's energy-dispatching strategy for minimizing the total operating costs. Furthermore, all members in the MGCO distribute the cooperation surplus based on the Shapley value method. The example results show that the proposed game model can balance the benefits between the ADN and multi-microgrid with sharing ES and maximize the mutual benefits of the MGCO through energy reciprocity.

Keywords: sharing energy storage, microgrid coalition, active distribution network, game scheduling, Shapley value method, energy reciprocity

Edited by:
Fei Wang,
North China Electric Power University, China

Reviewed by:
Tianle Sun,
Huazhong University of Science and Technology, China
Yang Yu,
North China Electric Power University, China

Correspondence:
Fei Li
lifei_ctgu@163.com

Specialty section:
This article was submitted to Smart Grids,
a section of the journal
Frontiers in Energy Research

Received: *28 March 2022*
Accepted: *22 April 2022*
Published: *01 June 2022*

Citation:
Li F, Li X, Fang Z and Zhang L (2022) A Game Optimization Scheduling Strategy of Active Distribution Network With Multi-Microgrid Sharing Energy Storage.
Front. Energy Res. 10:906406.
doi: 10.3389/fenrg.2022.906406

1 INTRODUCTION

The ADN (active distribution network) can actively carry out flexible management of distributed generation, load, and ES, which makes it more open and interactive for new energy access and consumption. Distributed generations with new energy are usually connected to the ADN in the form of all kinds of MGs. ES can be used to improve the flexibility, economy, and security of power systems (Ruiz-Cortes et al., 2019; Dai et al., 2021; Li and Wang, 2021). However, the chaotic charge–discharge behaviors without coordination may cause considerable waste of resources from the overall perspective. According to the complementary characteristics of the ES behaviors and energy production–consumption of MGs, a multi-microgrid joint system with shared ES can be formed as an MGCO obtain energy reciprocity (Feng et al., 2018; Shi et al., 2022). Sharing ES and coalition mechanism in multi-microgrids may change the scheduling strategies and the benefits of the ADN. Consequently, this study is devoted to research on the optimal scheduling strategies of the ADN with the MGCO-sharing ES to promote efficient operation and energy reciprocity.

At present, there are abundant research results on the optimal scheduling of the ADN with MGs, but the scheduling with sharing ES has not been addressed much in literatures. In a study by Fu et al. (2020), an energy management framework of a hybrid AC/DC distribution system with MGs is established, and the benefit equilibrium of various entities is obtained by a master–slave game model. Marzband et al. (2018a) proposed an advanced retail electricity market model for the optimal operation of home MGs and the interaction with the ADN to encourage market participation and improve profits for all participants. In a study by Zhang et al. (2019), a novel data-adaptive robust optimization method for the ADN with renewables is proposed to enhance the economics of the system. Huang et al. (2021) constructed a double-layer distributed optimization model for multi-stakeholders with the ADN as the leader and MGs as the follower. In a study by Sheng et al. (2021), a novel scheduling method with demand response and user satisfaction is proposed to promote the power fluctuation damping and the renewable energy consumption. In a study by Liu et al. (2020), a novel distributed P2P trading method based on the Stackelberg game in the ADN is proposed to improve the economic and technical benefits. Gu (2019) proposed a general model of interactive games to gain more revenue with the cooperation between the MG and ADN. Wei et al. (2014) proposed a game-theoretic coalition formulation strategy for the MGs for minimizing power loss.

Moreover, the research on shared ES is also extensive. In studies by Liu et al. (2019a) and Yang et al. (2021), the energy sharing strategy is supported by a transactive energy mechanism in a regional integrated energy system to achieve distributed optimization of energy sharing. In a study by Cui et al. (2021), a novel bargaining-based benefit-sharing model is proposed for prosumers to share the benefits of energy cooperation based on their contributions. Xiao et al. (2022) proposed a novel ES sharing framework considering ES allocation for prosumers, which can reduce the electricity costs of prosumers and improve the practical feasibility. In a study by Liu et al. (2018a), a decision-making model of cloud ES operators and consumers is established to improve the economic benefits by using their complementary characteristics. In a study by He and Zhang (2021), an adaptive double-side auction mechanism is introduced to obtain the optimal market price for the game equilibrium to save energy-sharing costs and increase agent benefits. In a study by Marzband et al. (2018b), multiple home MGs are integrated into coalitions for gaining competitiveness in the market and obtaining the maximum profits by sharing ES. Tan et al. (2021) proposed a cooperative trading model that is based on a cooperative game, which can improve both the total gains and individual gains of MGs. In a study by Jeon and Hong (2019), an energy-sharing framework between the prosumer and consumer is proposed to handle double-energy spending problems. In a study by Liu et al. (2017), a P2P trading structure is proposed to integrate the PV prosumers into an energy-sharing zone for maximizing the economic benefits. However, the abovementioned studies are mainly focused on market trading in integrated energy systems or community MGs and are rarely related to ADN scheduling.

Based on the abovementioned research, this study proposed an energy optimization scheduling strategy for the ADN with multi-microgrid sharing ES. The main contributions are as follows:

1) An optimal dispatching strategy of the MGCO with shared ES is proposed to obtain energy reciprocity and maximize the mutual benefits of MGs by using their complementary characteristics of ES utilization.
2) A master–slave game model of the ADN with the MGCO is constructed. The price strategy of the ADN and the energy-dispatching strategy of the MGCO are optimized to promote the overall energy utilization and win–win interests for all participants.

2 ENERGY RECIPROCITY STRATEGY OF THE MGCO SHARING ES

The complementary characteristics of the ES behaviors and energy production–consumption are used to obtain energy reciprocity among MGs and improve the utilization rate of ES. **Eq. 1** denotes the amount of residual electricity power before the MG i joins the energy mutual compensation:

$$\begin{cases} \Delta P_{i,B}^{t} = P_{i,\mathrm{B}}^{t} - P_{i,\mathrm{C}}^{t} \\ \Delta P_{i,G}^{t} = P_{i,\mathrm{G}}^{t} - P_{i,\mathrm{D}}^{t} \end{cases}, \tag{1}$$

Energy reciprocity among MGs needs to satisfy the following principles: MGs can transfer or receive the residual electricity power with other members, but the total power exchange shall not exceed their electric power surplus or the shortage power. **Eq. 2** represents the constraint conditions of energy reciprocity.

$$\begin{cases} \sum\limits_{j=1,j\neq i}^{n} D_{ij}P_{ij}^{t} \leq \Delta P_{i,B}^{t} \\ \sum\limits_{j=1,j\neq i}^{n} D_{ji}P_{ji}^{t} \leq \Delta P_{i,G}^{t} \end{cases} i = 1,\ldots,n, \tag{2}$$

where n is the number of MGCO members; $\sum\limits_{j=1,j\neq i}^{n} (D_{ji}P_{ji}^{t} - D_{ij}P_{ij}^{t})$ represents the reciprocal power in the coalition; D_{ji} is a binary state variable of [0,1], represents whether transmit the power among MGs.

In the view of MGs, they may sell their energy surplus to the ADN for increasing the revenue. When the MGs are integrated into a coalition, the members obtain energy reciprocity by sharing ES. It seems that energy sharing is free for all members on the surface; however, according to the difference in the ADN's purchase and sale price in each time sequence, energy reciprocity may greatly reduce the cost of power interaction between MGs and the ADN, and the cooperation surplus obtained by energy reciprocity will bring additional benefits for the coalition. If each member's revenue is distributed by marginal contributions, the MGs may obtain higher revenues than their independent operation.

3 OPTIMAL SCHEDULING STRATEGY OF THE ADN WITH MULTI-MICROGRID SHARING ES

When the MGCO joins in the scheduling of the ADN, the coalition mechanism may change the scheduling strategies and

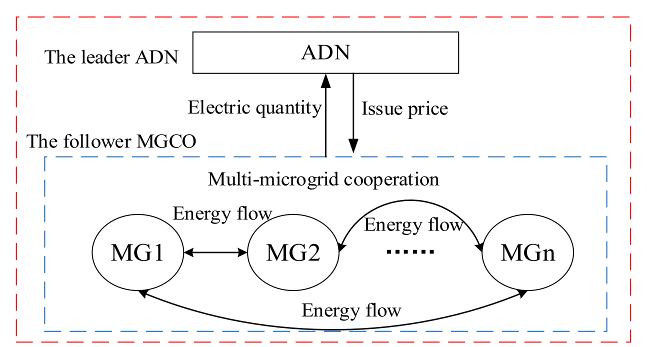

FIGURE 1 | Game scheduling framework of the ADN with the MGCO.

the benefits of the ADN. Since the two participants belong to different entities and have their own operating objectives, based on the game theory (Lee et al., 2015), a master–slave game scheduling relationship is formed with the ADN as the leader and the MGCO as the follower. The ADN implements price incentives with the objective of maximizing operation benefits, and the MGCO responds to the price and optimizes the energy-dispatching strategy to obtain the minimum cost. The cooperation benefits of the coalition can be distributed by the Shapley value method. The game scheduling framework of the ADN and MGCO is built as shown in **Figure 1**.

4 GAME OPTIMIZATION SCHEDULING MODEL OF THE ADN WITH THE MGCO SHARING ES

4.1 Optimization Model of the ADN

4.1.1 Objective

The objective is to minimize the total operation costs, including generation costs $C_{\mathrm{G}}^{\mathrm{ADN}}$, operation and maintenance costs of the units $C_{\mathrm{OM}}^{\mathrm{ADN}}$, power interaction costs with the upper grid C_{g}, and power interaction costs with the MGCO $C_{\mathrm{PCC,MGCO}}$, as shown in **Eq. 3**.

$$J_{\mathrm{ADN}} = \min C_{\mathrm{ADN}} = C_{\mathrm{PCC,MGCO}} + C_{\mathrm{G}}^{\mathrm{ADN}} + C_{\mathrm{OM}}^{\mathrm{ADN}} + C_{\mathrm{g}}, \tag{3}$$

$$\begin{cases} C_{\mathrm{g}} = \sum_{t=1}^{24}\left(\lambda_s^t \cdot P_{\mathrm{ADN},b}^t - \lambda_b^t \cdot P_{\mathrm{ADN},s}^t\right) \\ C_{\mathrm{PCC,MGCO}} = \sum_{t=1}^{24}\left(\rho_b^t P_{\mathrm{PCC,MGCO},s}^t - \rho_s^t P_{\mathrm{PCC,MGCO},b}^t\right) \\ C_{\mathrm{G}}^{\mathrm{ADN}} = \sum_{j=1}^{k}\sum_{t=1}^{24}\left(a_{mj}\left(P_{Gj}^t\right)^2 + b_{mj}P_{Gj}^t + c_{mj}\right) \\ C_{\mathrm{OM}}^{\mathrm{ADN}} = \sum_{j=1}^{k}\sum_{t=1}^{24} k_{mj}P_{Gj}^t \end{cases}, \tag{4}$$

where k represents the number of units in the ADN.

4.1.2 Constraints

The constraint conditions of the ADN optimization model mainly include power flow constraints, output constraints of units, and electricity price constraints. The details are as follows:

$$\begin{cases} P_{i_1} - U_{i_1} \sum\limits_{j_1=1, j1 \neq i_1}^{n_1} U_{j_1}\left(G_{i_1 j_1}\cos\delta_{i_1 j_1} + B_{i_1 j_1}\sin\delta_{i_1 j_1}\right) = 0 \\ Q_{i_1} - U_{i_1} \sum\limits_{j_1=1, j_1 \neq i_1}^{n1} U_{j_1}\left(G_{i_1 j_1}\sin\delta_{i_1 j_1} - B_{i_1 j_1}\cos\delta_{i_1 j_1}\right) = 0 \end{cases} \quad i_1 = 1, 2, \ldots, n_1, \tag{5}$$

$$\begin{cases} 0 \le Pl_{i_1,j_1}^t \le Pl_{i_1,j_1}^{\max} & i_1, j_1 = 1, 2, \ldots, n_1 \\ U_{i_1}^{\min} \le U_{i_1} \le U_{i_1}^{\max} & i_1 \neq j_1 \\ P_{Gj}^{\min} \le P_{Gj}^t \le P_{Gj}^{\max} & j = 1, \ldots, k \end{cases}, \tag{6}$$

$$\begin{cases} \rho_s^t = \begin{cases} \rho_{sg}, t \in T_g \\ \rho_{sp}, t \in T_p \\ \rho_{sf}, t \in T_f \end{cases} \\ \rho_{sf} \ge \rho_{sp} \ge \rho_{sg} \end{cases}, \tag{7}$$

$$\begin{cases} \rho_b^t = \begin{cases} \rho_{bg}, t \in T_g \\ \rho_{bp}, t \in T_p \\ \rho_{bf}, t \in T_f \end{cases} \\ \rho_{bf} \ge \rho_{bp} \ge \rho_{bg} \end{cases}, \tag{8}$$

where n_1 is the number of the nodes in the ADN.

4.2 Optimization Model of the MGCO

4.2.1 Objective

The objective function of the MGCO includes the total costs of gas turbine generation costs $C_{\mathrm{MT\Sigma}}$, power interaction costs $C_{\mathrm{PCC,MGCO}}$, and the total costs of unit operation and maintenance $C_{\mathrm{OM\Sigma}}$, as shown in **Eq. 9**.

$$J_{\mathrm{MGCO}} = \min C_{\mathrm{MGCO}} = \min\left(C_{\mathrm{MT\Sigma}} + C_{\mathrm{PCC,MGCO}} + C_{\mathrm{OM\Sigma}}\right), \tag{9}$$

$$\begin{cases} C_{\mathrm{MT\Sigma}} = \sum_{i=1}^{n}\sum_{t=1}^{24} a_{Mi}\left(P_{\mathrm{MT},i}^t\right)^2 + b_{Mi}P_{\mathrm{MT},i}^t + c_{Mi} \\ C_{\mathrm{PCC,MGCO}} = \sum_{i=1}^{n}\sum_{t=1}^{24}\left(\rho_s^t P_{\mathrm{PCC}i,\mathrm{buy}}^t - \rho_b^t P_{\mathrm{PCC}i,\mathrm{sell}}^t\right) \\ C_{\mathrm{OM\Sigma}}\sum = \sum_{i=1}^{n}\sum_{j=1}^{m}\sum_{t=1}^{24} c_{\mathrm{OM},j}^{\mathrm{j}} P_{i,j}^t \end{cases}, \tag{10}$$

where m represents the number of units in the MG.

4.2.2 Constraints

The constraint conditions of the MGCO optimization model mainly include power balance constraints, energy reciprocity constraints, tie-line power constraints, and SOC constraints of ES. The detailed constraints of each member in the MGCO are as follows:

$$P_{\mathrm{load},i}^t = P_{\mathrm{new},i}^t + \left(P_{\mathrm{PCC}i,\mathrm{buy}}^t - P_{\mathrm{PCC}i,\mathrm{sell}}^t\right) + P_{\mathrm{MT},i}^t + \sum_{j=1, j \neq i}^{n}\left(D_{ji}P_{ji}^t - D_{ij}P_{ij}^t\right) + \left(P_{i,\mathrm{D}}^t - P_{i,\mathrm{C}}^t\right) i = 1, 2, \ldots, n \tag{11}$$

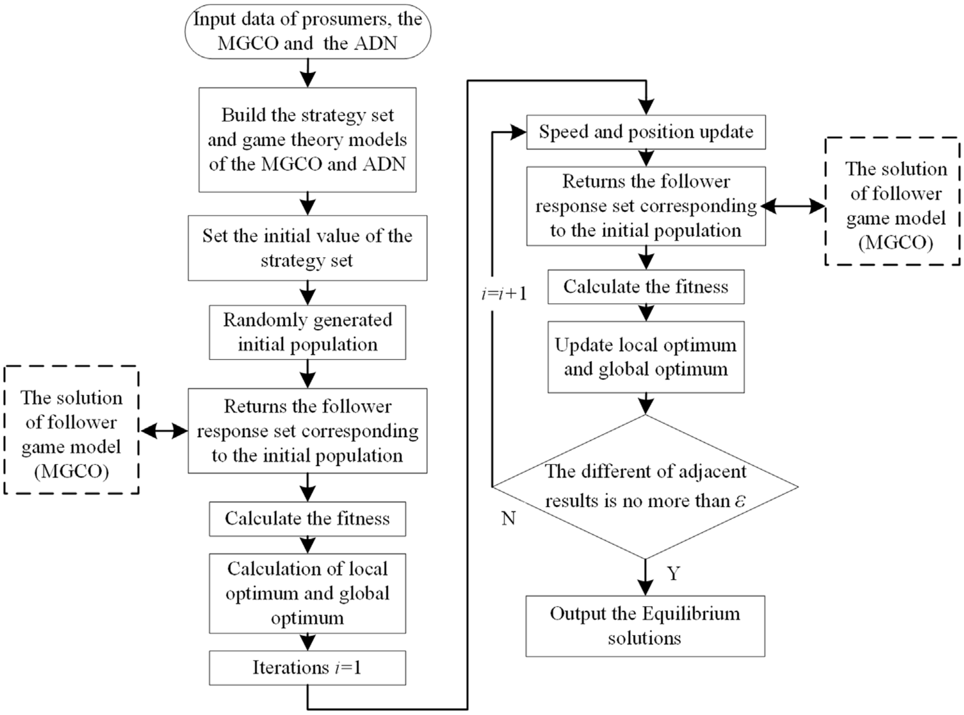

FIGURE 2 | Solving process of the proposed game model.

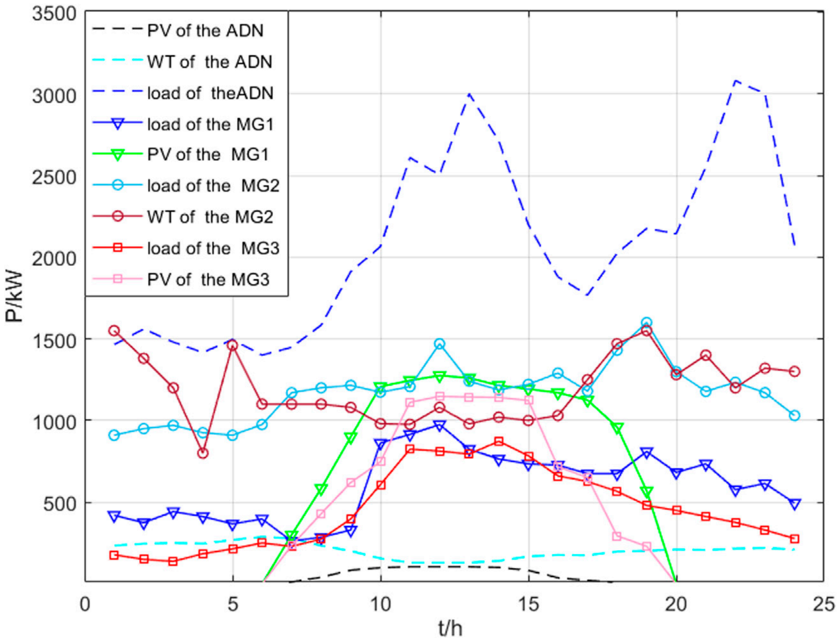

FIGURE 3 | Load and new energy output of the ADN with MGs.

TABLE 1 | Relevant parameters of micro sources in MGs.

	Parameters	MG1	MG2	MG3
Gas turbines	$P_{\mathrm{MT,i}}^{\max}$ (kW)	375	275	300
	$P_{\mathrm{MT,i}}^{\min}$ (kW)	80	70	100
	$c_{OM,i}$ (CNY/kWh)	0.081	0.073	0.068
	a_{Mi} (CNY/kWh^2)	0.0015	0.0035	0.0025
	b_{Mi} (CNY/kWh)	0.3312	0.2084	0.2538
	c_{Mi} (CNY/h)	5.25	3.075	3.04
ES	Power capacity (kW)	230	180	145
	Energy capacity (kWh)	1,490	845	775
	Initial SOC	0.2	0.4	0.2
Tie-line power	Maximum power (kW)	750	1,100	750

$$\begin{cases} P_{\mathrm{PCC},i}^{\min} \le P_{\mathrm{PCC}i,\mathrm{buy}}^{t}, P_{\mathrm{PCC}i,\mathrm{sell}}^{t} \le P_{\mathrm{PCC},i}^{\max} \\ P_{\mathrm{MT},i}^{\min} \le P_{\mathrm{MT},i}^{t} \le P_{\mathrm{MT},i}^{\max} \\ 0 \le P_{i,\mathrm{C}}^{t}, P_{i,\mathrm{D}}^{t} \le P_{i}^{\mathrm{Cap}} \\ \mathrm{SOC}_{i}^{\min} E_{i}^{\mathrm{Cap}} \le E_{i}^{t} \le E_{i}^{\mathrm{Cap}} \\ E_{i}^{t} = E_{i}^{t-1} + \Delta t\left(\eta_{i}^{\mathrm{C}} P_{i,\mathrm{C}}^{t} - \dfrac{P_{i,\mathrm{D}}^{t}}{\eta_{i}^{\mathrm{D}}}\right) \end{cases} \quad i = 1, 2, \ldots, n. \tag{12}$$

4.3 Distribution for the Cooperation Surplus Based on the Shapley Value Method

The Shapley value method is introduced for a fair distribution of cooperation surplus obtained by forming a coalition, which can be interpreted as the average value of marginal contribution related to all possible coalition types (Liu et al., 2018b). The income of member i distributed by the method is shown in **Eq. 13**.

$$\begin{cases} v(i) = \sum\limits_{s(i \in s_i)} \omega(|s|) \cdot \left[v(s) - v\left(s/_{i}\right)\right] \\ \omega(|s|) = \dfrac{(n-|s|)!\,(|s|-1)!}{n!} \\ MC_i = v(s) - v\left(s/_{i}\right) \end{cases} \quad i = 1, 2, \ldots, n, \tag{13}$$

where s represents the coalition set comprising all members; $v(i)$ is the revenue distributed for member i; $|s|$ is the subset number; $\omega(|s|)$ is the weight factor; $v(s)$ is the residual cooperation of coalition s; $v(s/_{i})$ is the residual cooperation of sub-alliance excluding member i; and MC_i is the marginal contributions of member i in the coalition s.

Cooperation surplus is defined as the difference in the total revenue between all member cooperation and their independent operation. According to the optimization model of the MGCO, the difference of benefits between coalition and independent operation is mainly caused by the model whether considering the energy reciprocity.

5 THE SOLUTION OF THE PROPOSED GAME MODEL

First, the leader sets the initial price$\{\rho_s^0, \rho_b^0\}$; the follower responds to the price to minimize the total operation cost (**Eq. 9**) with the constraints (**Eqs 2**, **11**, **12**) to obtain the optimal dispatching strategies $(P_{\mathrm{PCC,MGCO},b}^{0}, P_{\mathrm{PCC,MGCO},s}^{0})$; the leader receives the strategies of the follower and re-optimizes the electricity price for minimizing the objective function (**Eq. 3**) with the constraints (**Eqs 5–8**), to obtain the new price $\{\rho_b^1, \rho_s^1\}$; the follower continues to respond to the price and obtains the new optimal dispatching strategies $\{P_{\mathrm{PCC,MGCO},b}^{1}, P_{\mathrm{PCC,MGCO},s}^{1}\}$. In this way, the optimal strategies of the participants in each round are solved by repeated alternating iterations. When the strategies of both sides in the game model are no longer changed, the Nash equilibrium state is achieved.

$$\begin{cases} \gamma_1^* = \{\rho_s^*, \rho_b^*\} = \arg\min J_{\mathrm{ADN}}\left(\rho_s, \rho_b, P_{\mathrm{PCC,MGCO},b}^{*}, P_{\mathrm{PCC,MGCO},s}^{*}\right) \\ \gamma_2^* = \left\{P_{\mathrm{PCC,MGCO},b}^{*}, P_{\mathrm{PCC,MGCO},s}^{*}\right\} = \arg\min J_{\mathrm{MGCO}}\left(\rho_s^*, \rho_b^*, P_{\mathrm{PCC,MGCO},b}, P_{\mathrm{PCC,MGCO},s}\right) \end{cases}. \tag{14}$$

The proposed optimization scheduling model belongs to the category of bi-level optimization game. Based on the bi-level optimization theory (Liu et al., 2017), the solving process of the lower optimization model can be inserted into the upper model: the PSO algorithm is used to solve the upper optimization model within the lower optimization strategy solved using the Yalmip/Cplex toolbox. The optimal solutions are continuously updated with the iteration increase until Nash equilibrium solutions are obtained, as shown in **Figure 2**, and the main steps are as follows:

Step 1: The PSO algorithm randomly generates the ADN's initial price strategies with a certain number of populations, the initial iterations $i = 1$;

Step 2: The fitness is calculated considering the influence of the MGCO's strategy solved using the Cplex toolbox;

Step 3: Local optimum and global optimum are updated, and iterations are updated ($i = i + 1$);

Step 4: The speed and position of the populations are updated, and steps 2–4 are repeated until the difference of the price solutions in adjacent rounds is no more than ε ($\varepsilon = 0.0001$) to obtain the Nash equilibrium and then enter Step 5.

Step 5: The optimal price of the ADN's strategy corresponding to the Nash equilibrium solution is output. The MGCO's optimal strategy can be obtained by responding to the ADN's optimal price.

TABLE 2 | ToU price of the ADN after game equilibrium (CNY/kWh).

	Periods	Selling Price	Buying Price
Valley section	0:00-8:00	0.3371	0.2697
Flat section	8:00-10:00 ; 14:00-20:00 ; 23:00-24:00	0.6743	0.5394
Peak section	10:00-14:00 ; 20:00-23:00	1.0114	0.8091

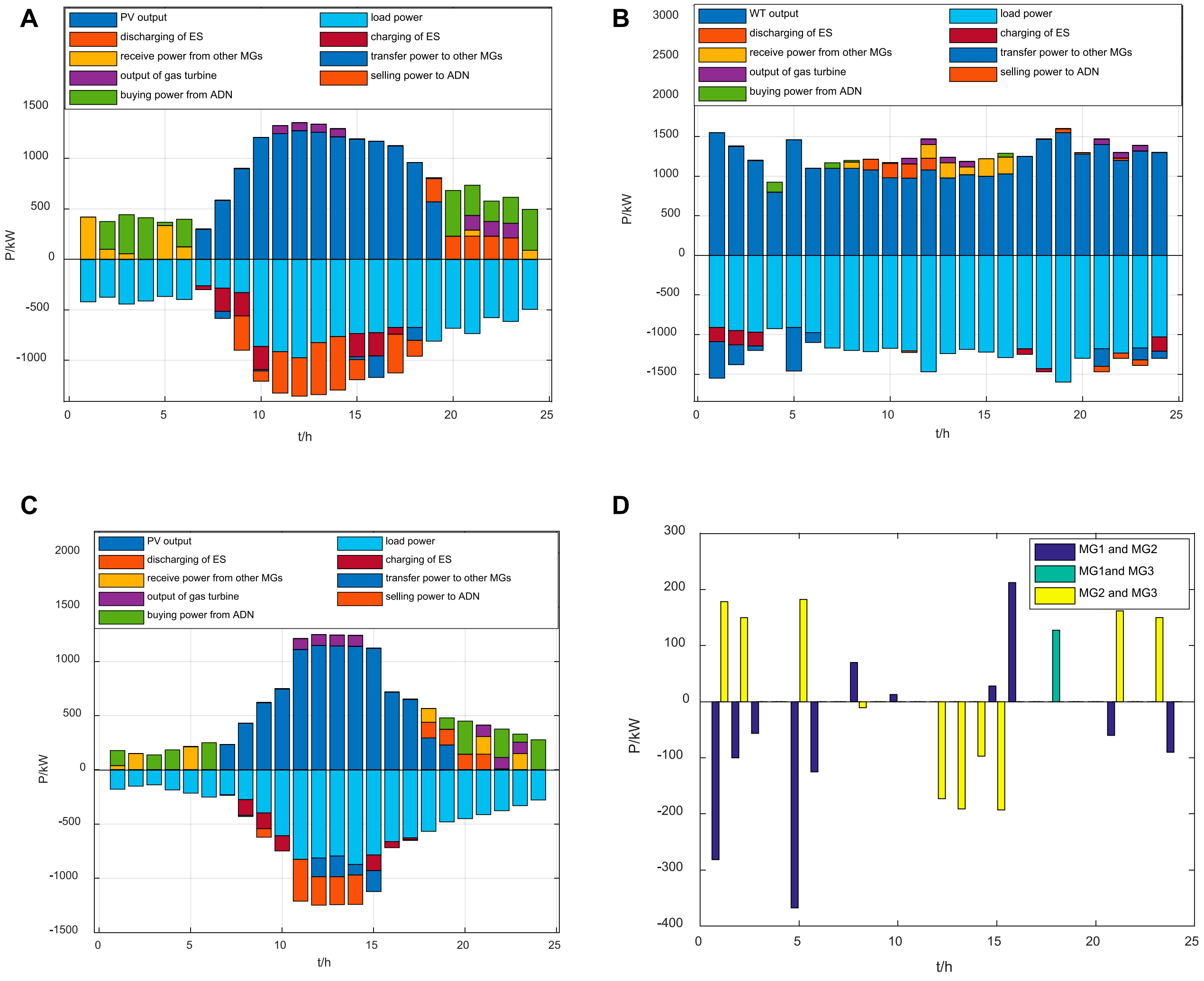

FIGURE 4 | Simulation results of MGs. **(A)** Energy dispatching of MG1. **(B)** Energy dispatching of MG2. **(C)** Energy dispatching of MG3. **(D)** Energy reciprocity among MGs.

TABLE 3 | Economic benefits comparison of the ADN and the MGCO.

Optimization index	After optimization	Before optimization
Cost of the ADN (CNY)	23,206	27,641
Cost of the MGCO (CNY)	4,802.21	4,965
ADN peak-valley difference rate (%)	61.62%	69.95%
Load square deviation of the ADN (kW)	553.61	689.35

6 SIMULATION RESULTS AND ANALYSIS

6.1 Case Parameters

The ADN example is based on the IEEE14-bus system with the parameters shown in the study by Liu et al. (2019b). MG1, MG2, and MG3 are installed on nodes 6,11, and 13, respectively, and the three MGs are integrated into an MGCO. Node 1 is the common connection point between the ADN and the upper grid. PV units, wind turbines, and controllable units are installed on nodes 2, 3, and 8, respectively. The new energy output and load curves of MGs and the ADN on a typical day are shown in **Figure 3**. The operation and maintenance coefficients of new energies are 0.0096 and 0.0296, respectively. The electricity selling price of the upper grid is 0.55 CNY/kW. The parameters of the gas turbine and ES in MGs are shown in **Table 1**. The charging–discharging efficiency of ES is 0.95.

The parameters of the PSO algorithm are as follows: population number is 500, maximum iterations are 2000,

TABLE 4 | Comparison of cost in various forms of cooperation (CNY).

Coalition type	Cost saving amount	MC_1	MC_2	MC_3	MG1 Cost	MG2 Cost	MG3 Cost	Total Cost
{MG1}, {MG2}, {MG3}	0	0	0	0	1837.00	1928.59	1,396.01	5,161.60
{MG1, MG2}, {MG3}	326.42	326.42	326.42	0	1,673.79	1765.38	1,396.01	4,835.18
{MG1, MG3}, {MG2}	17.21	17.21	0	17.21	1828.4	1928.59	1,387.41	5,144.39
{MG2, MG3}, {MG1}	243.78	0	243.78	243.78	1837.00	1806.7	1,274.12	4,917.82
{MG1, MG2, MG3}	359.33	115.55	342.12	32.91	1741.19	1719.50	1,341.52	4,802.21

range in particle velocity is from −1 to 1, learning factor is 1.5, initial inertia weight is 0.9, and final inertia weight is 0.4. The computer is configured as an intel Core i7 processor with a 1.8 GHz main frequency and 16 GB memory capacity.

6.2 Optimization Result Analysis

6.2.1 Analysis of Results Obtained by the Proposed Game Model

The optimized ToU price is shown in **Table 2**, and the simulation results of MGs are shown in **Figure 4**.

Taking MG1 as an example from **Figure 4A**, the dispatching strategy is as follows: MG1 is mainly supplied by its PV power. In 0:00–7:00 of valley periods, MG1 received the mutual power from other MGs, and the residual power shortage was balanced by the interaction with the ADN. In 19:00–24:00 of flat periods, MG1 is supplied by the gas turbine and purchasing electricity from the ADN after using the ES discharging. In 23:00–24:00 of flat periods, MG1 receives the reciprocal power from other MGs and then compensated by the gas turbine and ADN. In the periods of 7:00–19:00, PV power is enough. MG1 provides mutual assistance to other MGs and then sells residual electricity to the ADN.

The economic benefits and the peak-valley difference of both parties are shown in **Table 3**. The ADN implements the ToU price policy to stimulate the MGCO to adjust the energy-dispatching strategy for peak load clipping and valley filling, further reducing the peak-valley difference and obtaining win–win interests for both parties.

6.2.2 Mutual Benefits Analysis of the MGCO

Table 4 shows the comparison of the cost with all kinds of coalitions. The coalition type of MG1, MG2, and MG3 obtains the maximum cost saving amount, and the total operation cost is reduced to 4,802.21CNY. Furthermore, each MG's cost is less than the cost of their independent operation. In addition, MG1 and MG3 are the PV-type MGs, but MG2 is a WT type. Power reciprocity is mainly found between MG2 and MG1 or between MG2 and MG3, as shown in **Figure 4D**. Therefore, when the benefits are distributed according to the Shapley value method, the cost saving amount shared for MG1 and MG3 is relatively small, while the value of MG2 is relatively more, and the marginal contribution of MG2 is higher than that of other MGs, as shown in **Table 4**.

7 CONCLUSION

A game optimization scheduling strategy of the ADN with multi-microgrid sharing ES is proposed in this study. The conclusions can be obtained by the following theoretical analysis and simulations:

1) For the complementary characteristics of the charging–discharging behaviors and energy production–consumption of MGs, the MGCO is formed to obtain energy reciprocity for maximizing the mutual benefit.
2) A master–slave game competition between the ADN and MGCO is proposed to promote overall energy utilization and obtain win–win interests for all participants.

The future study mainly focuses on considering the uncertainty of the new energy output for the proposed model.

DATA AVAILABILITY STATEMENT

The original contributions presented in the study are included in the article/supplementary material; further inquiries can be directed to the corresponding author.

AUTHOR CONTRIBUTIONS

FL: conceptualization, methodology, validation, formal analysis, writing—review and editing, and project administration. XL: writing—review and editing, supervision, and project administration. ZF: methodology, software, validation, investigation, and data curation. LZ: validation, investigation, and funding acquisition.

FUNDING

This work was supported in part by the National Natural Science Foundation of China under Grant 52007103, and in part by the Research Fund for Excellent Dissertation of China Three Gorges University under Grant 2021BSPY008.

REFERENCES

Cui, S., Wang, Y.-W., Liu, X.-K., Wang, Z., and Xiao, J.-W. (2021). Economic Storage Sharing Framework: Asymmetric Bargaining-Based Energy Cooperation. *IEEE Trans. Ind. Inf.* 17 (11), 7489–7500. doi:10.1109/TII.2021.3053296

Dai, R., Esmaeilbeigi, R., and Charkhgard, H. (2021). The Utilization of Shared Energy Storage in Energy Systems: a Comprehensive Review. *IEEE Trans. Smart Grid* 12 (4), 3163–3174. doi:10.1109/TSG.2021.3061619

Feng, X., Gu, J., and Guan, X. (2018). Optimal Allocation of Hybrid Energy Storage for Microgrids Based on Multi-Attribute Utility Theory. *J. Mod. Power Syst. Clean. Energy* 6 (1), 107–117. doi:10.1007/s40565-017-0310-3

Fu, Y., Zhang, Z., Li, Z., and Mi, Y. (2020). Energy Management for Hybrid AC/DC Distribution System with Microgrid Clusters Using Non-cooperative Game Theory and Robust Optimization. *IEEE Trans. Smart Grid* 11 (2), 1510–1525. doi:10.1109/TSG.2019.2939586

Gu, K. (2019). Research on the Cooperation-Competition Mechanism of Microgrid and Active Power Distribution Network Based on Game Theory. *IOP Conf. Ser. Earth Environ. Sci.* 267 (4), 042052–42052. doi:10.1088/1755-1315/267/4/042052

He, L., and Zhang, J. (2021). A Community Sharing Market with PV and Energy Storage: an Adaptive Bidding-Based Double-Side Auction Mechanism. *IEEE Trans. Smart Grid* 12 (3), 2450–2461. doi:10.1109/TSG.2020.3042190

Huang, Z., Zhang, Y., Zheng, F., Lin, J., An, X., and Shi, H. (2021). Day-ahead and Real-Time Energy Management for Active Distribution Network Based on Coordinated Optimization of Different Stakeholders. *Power Syst. Technol.* 45 (6), 2299–2308. doi:10.13335/j.1000-3673.pst.2020.0410

Jeon, J. M., and Hong, C. S. (2019). "A Study on Utilization of Hybrid Blockchain for Energy Sharing in Micro-grid," in 2019 20th Asia-Pacific Network Operations and Management Symposium (APNOMS), Matsue, Japan.

Lee, J., Guo, J., Choi, J. K., and Zukerman, M. (2015). Distributed Energy Trading in Microgrids: a Game-Theoretic Model and its Equilibrium Analysis. *IEEE Trans. Ind. Electron.* 62 (6), 3524–3533. doi:10.1109/TIE.2014.2387340

Li, X., and Wang, S. (2021). Energy Management and Operational Control Methods for Grid Battery Energy Storage Systems. *CSEE J. Power Energy Syst.* 7 (5), 1026–1040. doi:10.17775/CSEEJPES.2019.00160

Liu, B., Liu, F., Zhai, B., and Lan, H. (2019). Investigating Continuous Power Flow Solutions of IEEE 14-bus System. *IEEJ Trans. Elec Electron Eng.* 14 (1), 157–159. doi:10.1002/tee.22773

Liu, H., Li, J., Ge, S., He, X., Li, F., and Gu, C. (2020). Distributed Day-Ahead Peer-To-Peer Trading for Multi-Microgrid Systems in Active Distribution Networks[J]. *IEEE Access* 8 (99), 66961–66976. doi:10.1109/ACCESS.2020.2983645

Liu, J., Zhang, N., Kang, C., Kirschen, D. S., and Xia, Q. (2018). Decision-making Models for the Participants in Cloud Energy Storage. *IEEE Trans. Smart Grid* 9 (6), 5512–5521. doi:10.1109/TSG.2017.2689239

Liu, N., Wang, J., and Wang, L. (2019). Hybrid Energy Sharing for Multiple Microgrids in an Integrated Heat-Electricity Energy System. *IEEE Trans. Sustain. Energy* 10 (3), 1139–1151. doi:10.1109/TSTE.2018.2861986

Liu, N., Yu, X., Wang, C., Li, C., Ma, L., and Lei, J. (2017). Energy-sharing Model with Price-Based Demand Response for Microgrids of Peer-To-Peer Prosumers. *IEEE Trans. Power Syst.* 32 (5), 3569–3583. doi:10.1109/TPWRS.2017.2649558

Liu, T., Tan, X., Sun, B., Wu, Y., and Tsang, D. H. K. (2018). Energy Management of Cooperative Microgrids: a Distributed Optimization Approach. *Int. J. Electr. Power & Energy Syst.* 96, 335–346. doi:10.1016/j.ijepes.2017.10.021

Marzband, M., Azarinejadian, F., Savaghebi, M., Pouresmaeil, E., Guerrero, J. M., and Lightbody, G. (2018). Smart Transactive Energy Framework in Grid-Connected Multiple Home Microgrids under Independent and Coalition Operations. *Renew. Energy* 126, 95–106. doi:10.1016/j.renene.2018.03.021

Marzband, M., Javadi, M., Pourmousavi, S. A., and Lightbody, G. (2018). An Advanced Retail Electricity Market for Active Distribution Systems and Home Microgrid Interoperability Based on Game Theory. *Electr. Power Syst. Res.* 157, 187–199. doi:10.1016/j.epsr.2017.12.024

Ruiz-Cortes, M., Gonzalez-Romera, E., Amaral-Lopes, R., Romero-Cadaval, E., Martins, J., Milanes-Montero, M. I., et al. (2019). Optimal Charge/discharge Scheduling of Batteries in Microgrids of Prosumers. *IEEE Trans. Energy Convers.* 34 (1), 468–477. doi:10.1109/TEC.2018.2878351

Sheng, H., Wang, C., Li, B., Liang, J., Yang, M., and Dong, Y. (2021). Multi-timescale Active Distribution Network Scheduling Considering Demand Response and User Comprehensive Satisfaction. *IEEE Trans. Ind. Appl.* 57 (3), 1995–2005. doi:10.1109/TIA.2021.3057302

Shi, Z., Wang, W., Huang, Y., Li, P., and Dong, L. (2022). Simultaneous Optimization of Renewable Energy and Energy Storage Capacity with Hierarchical Control. *Csee Jpes* 8 (1), 95–104. doi:10.17775/CSEEJPES.2019.01470

Tan, M., Zhou, Y., Wang, L., Su, Y., Duan, B., and Wang, R. (2021). Fair-efficient Energy Trading for Microgrid Cluster in an Active Distri-Bution Network. *Sustain. Energy, Grids Netw.* 26, 100453. doi:10.1016/j.segan.2021.100453

Wei, C., Fadlullah, Z. M., Kato, N., and Takeuchi, A. (2014). GT-CFS: A Game Theoretic Coalition Formulation Strategy for Reducing Power Loss in Micro Grids. *IEEE Trans. Parallel Distrib. Syst.* 25 (9), 2307–2317. doi:10.1109/TPDS.2013.178

Xiao, J.-W., Yang, Y.-B., Cui, S., and Liu, X.-K. (2022). A New Energy Storage Sharing Framework with Regard to Both Storage Capacity and Power Capacity. *Appl. Energy* 307, 118171. doi:10.1016/j.apenergy.2021.118171

Yang, Z., Hu, J., Ai, X., Wu, J., and Yang, G. (2021). Transactive Energy Supported Economic Operation for Multi-Energy Complementary Microgrids. *IEEE Trans. Smart Grid* 12 (1), 4–17. doi:10.1109/TSG.2020.3009670

Zhang, Y., Ai, X., Wen, J., Fang, J., and He, H. (2019). Data-adaptive Robust Optimization Method for the Economic Dispatch of Active Distribution Networks. *IEEE Trans. Smart Grid* 10 (4), 3791–3800. doi:10.1109/TSG.2018.2834952

Conflict of Interest: The authors declare that the research was conducted in the absence of any commercial or financial relationships that could be construed as a potential conflict of interest.

GLOSSARY

PV Photovoltaic

SOC state-of-charge

WT wind power

MG microgrid

MGCO microgrid coalition

ES energy storage

ADN active distribution network

ToU time-of-use

$\Delta P_{i,B}^{t}$, $\Delta P_{i,G}^{t}$ power surplus and power shortage of MG *i* at *t* time after using its ES

$P_{i,\mathrm{C}}^{t}$, $P_{i,\mathrm{D}}^{t}$ charging and discharging power of MG *i* at *t* time

$P_{i,\mathrm{B}}^{t}$, $P_{i,\mathrm{G}}^{t}$ power surplus and power shortage of MG *i* at *t* time

P_{ji}^{t} active power transmitted from MG *j* to MG *i* at *t* time

λ_{s}^{t}, λ_{b}^{t} the selling price and purchasing price from the upper power grid in *t* time

$P_{\mathrm{ADN},s}^{t}$, $P_{\mathrm{ADN},b}^{t}$ selling and purchasing quantity with the upper power grid in *t* time

$P_{\mathrm{PCC,MGCO},s}^{t}$, $P_{\mathrm{PCC,MGCO},b}^{t}$ total sale power and purchase power of MGCO at *t* period

$\rho_{s}^{t}, \rho_{b}^{t}$ selling and purchasing price of ADN at *t* time

a_{mj}, b_{mj}, c_{mj} generation cost coefficients of unit *j*

P_{Gj}^{t} output of the unit *j* in *t* period

P_{Gj}^{min}, P_{Gj}^{max} lower and upper limits of output of the unit *j*

$P_i \lim\limits_{x\to\infty}$, Q_i injected active power and active power of node *i*

$U_i \lim\limits_{x\to\infty}$, U_i^{min}, U_i^{max} voltage amplitude and lower and upper limits of voltage for node *i*

$G_{ij} \lim\limits_{x\to\infty}$, B_{ij}, δ_{ij} conductance, admittance, and voltage phase angle difference between node *i* and node *j*

$Pl_{i,j}^{t}$ active power of branch between *i* and *j* at t time in ADN

$Pl_{i,j}^{max}$ maximum transmission power of branch between *i* and *j* in ADN

T_g, T_p, T_f valley, flat, and peak periods of TOU price

$\rho_{sg}, \rho_{sp}, \rho_{sf}$ selling price in valley, flat, and peak periods of ADN, respectively

$\rho_{bg}, \rho_{bp}, \rho_{bf}$ buying price in valley, flat, and peak periods of ADN, respectively

a_{Mi}, b_{Mi}, c_{Mi} gas turbine generation cost coefficients of MG *i*

$P_{\mathrm{MT},i}^{t}$ output of gas turbine at *t* time in MG *i*

$P_{\mathrm{MT},i}^{min}, P_{\mathrm{MT},i}^{max}$ lower and upper limits of gas turbine output in MG *i*

$P_{\mathrm{PCC}i,\mathrm{buy}}^{t}$, $P_{\mathrm{PCC}i,\mathrm{sell}}^{t}$ electricity purchasing quantity and selling quantity of MG *i*

$c_{\mathrm{OM},i}^{j}$ operation and maintenance cost of unit *j* in MG *i*

$P_{i,j}^{t}$ output of unit *j* in MG *i*

$P_{\mathrm{load},i}^{t}$ load power of MG *i* at *t* time

$P_{\mathrm{new},i}^{t}$ new energy output of MG *i* at *t* time

$P_{\mathrm{PCC},i}^{min}$, $P_{\mathrm{PCC},i}^{max}$ lower and upper limits of tie-line power between MG *i* and ADN

P_{i}^{Cap}, E_{i}^{Cap} power capacity and energy capacity of ES in MG *i*

SOC_{i}^{min} minimum SOC of ES in MG *i*

E_{i}^{t} residual capacity of ES in MG *i* at *t* time

$\eta_{i}^{\mathrm{C}}, \eta_{i}^{\mathrm{D}}$ charging and discharging efficiency of ES in MG *i*

γ_{1}^{*}, γ_{2}^{*} the equilibrium solutions of the leader and follower, respectively

$\rho_{s}^{*}, \rho_{b}^{*}$ electricity selling price and electricity purchasing price of the equilibrium solutions

$P_{\mathrm{PCC,MGCO},b}^{*}, P_{\mathrm{PCC,MGCO},s}^{*}$ electricity purchasing quantity and electricity selling quantity of the equilibrium solutions

$\mathbf{argmin}\ (\cdot)$ set of variables when the objective is minimized

frontiers | Frontiers in Energy Research

ORIGINAL RESEARCH
published: 07 July 2022
doi: 10.3389/fenrg.2022.919197

Optimal Dispatch of Multiple Photovoltaic Integrated 5G Base Stations for Active Distribution Network Demand Response

Xiang Zhang[1], Zhao Wang[1], Zhenyu Zhou[1]*, Haijun Liao[1], Xiufan Ma[1], Xiyang Yin[2], Guoyuan Lv[2], Zhongyu Wang[2], Zhixin Lu[2] and Yizhao Liu[2]

[1]State Key Laboratory of Alternate Electrical Power System with Renewable Energy Source, North China Electric Power University, Beijing, China, [2]Information and Communication Company, State Grid Tianjin Electric Power Company, Tianjin, China

Multiple 5G base stations (BSs) equipped with distributed photovoltaic (PV) generation devices and energy storage (ES) units participate in active distribution network (ADN) demand response (DR), which is expected to be the best way to reduce the energy cost of 5G BSs and provide flexibility resources for the ADN. However, the standalone PV-integrated 5G BS has the characteristics of wide distribution, small volume, and large load fluctuations, which will bring strong uncertainty to the ADN by directly participating in the DR. Therefore, a system architecture for multiple PV-integrated 5G BSs to participate in the DR is proposed, where an energy aggregator is introduced to effectively aggregate the PV energy and ES resources of 5G BSs. Then, a two-stage optimal dispatch method is proposed. Specifically, in the large-timescale DR planning stage, an incentive mechanism for multiple PV-integrated 5G BSs to participate in the DR is constructed based on the contract theory, which ensures that multiple 5G BSs respond to and satisfy the peak-shaving demand of the ADN. In the small-timescale online energy optimization stage, based on the energy sharing mode among 5G BSs, a Lyapunov-based online energy optimization algorithm is proposed to optimize the shared energy flow between the internal layer and the interactive layer of 5G BSs, which further improves PV absorption and ensures operation stability of ES in the 5G BS. Simulation results show that the proposed two-stage optimal dispatch method can effectively encourage multiple 5G BSs to participate in DR and achieve the win–win effect of assisting the ADN peak-shaving and low-carbon economic operation of 5G BSs.

Keywords: multiple PV-integrated 5G BSs, active distribution network, demand response, Lyapunov optimization, energy sharing

Edited by:
Tianguang Lu,
Shandong University, China

Reviewed by:
Bingchen Wang,
ASML (United States), United States
Kazi Mohammed Saidul Huq,
University of South Wales,
United Kingdom
Fangqing Wen,
Yangtze University, China

****Correspondence:***
Zhenyu Zhou
zhenyu_zhou@ncepu.edu.cn

Specialty section:
This article was submitted to
Smart Grids,
a section of the journal
Frontiers in Energy Research

Received: *13 April 2022*
Accepted: *11 May 2022*
Published: *07 July 2022*

Citation:
Zhang X, Wang Z, Zhou Z, Liao H, Ma X, Yin X, Lv G, Wang Z, Lu Z and Liu Y (2022) Optimal Dispatch of Multiple Photovoltaic Integrated 5G Base Stations for Active Distribution Network Demand Response. Front. Energy Res. 10:919197. doi: 10.3389/fenrg.2022.919197

1 INTRODUCTION

The explosive growth of mobile data and the popularization of smart devices have accelerated the deployment of fifth-generation (5G) communication systems (Singh et al., 2020). However, while ensuring wide network coverage and high communication service quality, the high-power consumption characteristic of 5G base stations (BSs) not only imposes high electricity bills for communication operators but also exacerbates the non-negligible carbon emission problem (Piovesan et al., 2019). On the one hand, 5G BSs are equipped with 64/32-channel massive multiple-input multiple-output (MIMO) to realize high bandwidth and high communication traffic (Fu et al., 2019; Chih -Lin et al., 2020; Zhou et al., 2021), which causes the power consumption of a 5G BS to be 2–3 times higher than that of an ordinary 4G BS. On the other hand, the deployment density of 5G BSs is much higher than that of 4G BSs as 5G uses higher-frequency bands for communication (Han et al., 2021). Moreover, the standard 5G BS demands a power of more than 11.5kW (Israr et al., 2021), and the number of 5G BSs in China is expected to reach 13.1 million by 2025, with a total power consumption of 200 billion kWh. Therefore, the high-power consumption characteristic of 5G BSs has become the primary constraint to the ultra-dense network deployment in the 5G era, and it also impacts the stable operation of an active distribution network (ADN) (Pedram and Wang, 2019).

At present, powering BSs through distributed energy resources (DERs), such as photovoltaic (PV) generation and energy storage (ES), has become a common solution to reduce on-grid power consumption and build low-carbon wireless networks (Zhou et al., 2017; Hu et al., 2020). Although the introduction of DER devices increases the investment cost of communication operators, the cheapness and cleanliness of PV energy will greatly reduce the energy cost of BSs, and the spatio-temporal shifting characteristic of ES can further improve the absorption capacity of renewable energy. Moreover, 5G BSs are already equipped with battery backups during construction to ensure stable operation in case of power supply interruptions, which can be considered the inherent ES (Yong et al., 2021a; Tang et al., 2021). However, under the normal power supply status, large-scale distributed ESs in 5G BSs are always idle (Liao et al., 2020a; Ci et al., 2020). Therefore, on the basis of ensuring the uninterrupted power supply of the 5G BSs, if the energy source of the ES can be dispatched, the energy consumption flexibility of 5G BSs will be stimulated, and the high asset utilization of ES resources can be realized.

With the continuous transition from the traditional grid to smart grid (SG) and the widespread deployment of user-side smart meters (Khan and Jayaweera, 2019), PV-integrated 5G BSs participating in ADN demand response (DR) has become an irreplaceable way to reduce energy cost (Li et al., 2021). On the premise of ensuring the reliability of the 5G BS power supply, if the ES and PV resources in 5G BSs can be coordinated, more flexible dispatchable resources can be tapped to provide a powerful guarantee for the real-time balance of the source and load in the ADN. Moreover, communication operators can reduce electricity bills or obtain DR subsidy based on the time-of-use (TOU) tariff mechanism by fully exploiting the power utilization flexibility of PV-integrated 5G BSs and fully dispatching idle ES resources, thus reducing the energy cost of a 5G communication network (Yong et al., 2021b). Despite the advantages mentioned previously, the multiple PV-integrated 5G BSs participating in DR still confront several critical challenges, which are summarized as follows.

1) Because of the different spatio-temporal distributions of communication services (Huq et al., 2020) and light intensity, different degrees of power imbalance will occur in different PV-integrated 5G BSs, which increases the difficulty of 5G BS energy dispatch in the ADN. In addition, as 5G BSs belong to communication operators, the direct energy dispatch of 5G BSs by the ADN is difficult to guarantee the communication service quality of telecom users and involves user security and privacy leakage issues.

2) The participation of multiple 5G BSs in the DR increases the operation and maintenance cost of ESs and impairs the participation enthusiasm of communication operators. Meanwhile, the power supply demands of 5G BSs with different spatio-temporal distributions vary greatly, and the randomness of PV energy and BS load further exacerbates the uncertainty of ES dispatchable capacity. How to effectively encourage and quantify the participation of 5G BSs in DR is an important problem to be solved.

3) During the participation of multiple 5G BSs in the DR, the imbalance between PV generation and load demand will lead to an over-discharge of ESs or the curtailment of PV energy. In addition, the accurate prediction of PV generation and load demand increases the difficulty of ensuring the real-time energy balance and puts higher requirements on real-time energy scheduling decisions (Wang et al., 2020). How to manage the energy of 5G BSs participating in DR is another challenge.

Multiple 5G BSs can be incentivized to participate in the DR through energy aggregators. It was pointed out that energy aggregators can aggregate BSs into a limited number of groups and act as third parties to dispatch BSs to participate in the DR (Xu et al., 2015). By introducing energy aggregators, encouraging and quantifying the participation of 5G BSs in the DR can be modeled as a social welfare maximization problem based on the contract theory, that is, maximizing the total utility of energy aggregators and BSs. A contract theory–based direct trading framework was proposed by Zhang et al. (2016) to address the lack of enthusiasm for direct trading between small-scale electricity suppliers and electricity consumers. Given the low enthusiasm of electric vehicles to participate in the DR, a contract theory–based charging rate allocation criterion and access control scheme were proposed by Zhang et al. (2018). However, the application of the contract theory can only ensure that multiple 5G BSs participate in the DR regularly and quantitatively in a large timescale but cannot guarantee the low-carbon and stable operation of 5G BSs in a small timescale.

The energy optimization of 5G BSs aims to alleviate the imbalance between PV generation and load demand by fully utilizing renewable energy, thereby reducing the energy cost and maintaining the stability of ES. An energy sharing model with energy aggregators as physical carriers was proposed by Guo et al. (2014), which allowed BSs to coordinate with each other for addressing energy imbalance by simultaneously transmitting and receiving energy to and from energy aggregators. Considering the unpredictability characteristics of the shared energy of 5G BSs, the Lyapunov optimization algorithm can be used to optimize the energy sharing among BSs online and in real-time. Under the energy sharing mode, Liu et al. (2017) proposed an online energy management method based on Lyapunov optimization, aiming to fully absorb renewable energy and control the energy flow of the nano-grid group in real-time. Zhong et al. (2019) proposed an

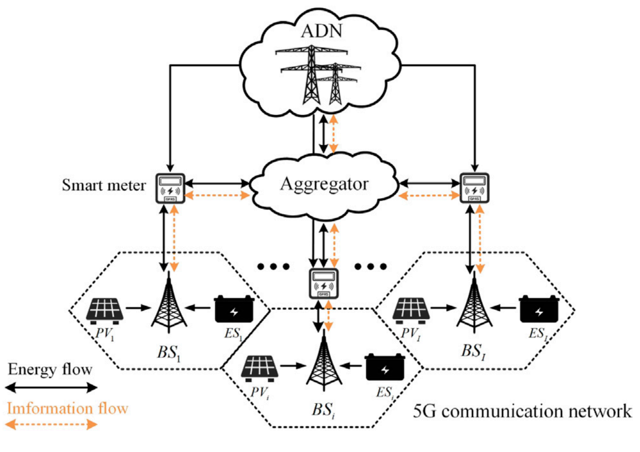

FIGURE 1 | System architecture of multiple PV-integrated 5G BSs participating in the DR.

online Lyapunov optimization–based control algorithm to optimize the shared energy in real-time in the multi-user–shared centralized ES system.

As the construction of 5G BSs is still in its infancy, research on the optimal energy dispatch of multiple PV-integrated 5G BSs participating in the DR is still relatively lacking. Motivated by the aforementioned challenges, we propose a two-stage optimal dispatch method for multiple PV-integrated 5G BSs participating in the ADN DR to fully dispatch PV and ES resources by combining Lyapunov optimization and contract theory. The main contributions of this study are summarized as follows.

1) The system architecture of multiple PV-integrated 5G BSs participating in the ADN DR is proposed, where the energy aggregator is introduced as the third party to motivate and assist the PV-integrated 5G BSs to participate in the DR.
2) A contract theory–based DR incentive mechanism is proposed to guide the discharge behavior of 5G BSs with different discharge capacities in the large-timescale DR planning stage. The peak-shaving demand of the ADN and the profit of BSs can be satisfied by optimizing the contract items.
3) A Lyapunov-based online energy optimization algorithm is proposed to make real-time decisions on the shared energy of multiple 5G BSs in the small timescale. The complex energy sharing problem is transformed into a linear programing problem, and only real-time information is required to make online decisions.

The remainder of this study is organized as follows. **Section 2** introduces the proposed system architecture and methodology of multiple PV-integrated 5G BSs participating in the ADN DR. **Section 3** elaborates the proposed contract theory–based large-timescale DR planning mechanism. In **Section 4**, the small-timescale online energy optimization algorithm for multiple PV-integrated 5G BSs based on Lyapunov optimization is proposed. **Section 5** analyzes the numerical results, followed by the conclusion in **Section 6**.

2 SYSTEM ARCHITECTURE AND METHODOLOGY

2.1 System Architecture

The system architecture of multiple PV-integrated 5G BSs participating in the ADN DR is shown in **Figure 1**, which consists of a 5G communication network, an ADN, and an energy aggregator. The 5G communication network comprises I PV-integrated 5G BSs, which is denoted as $\mathcal{I} = \{BS_1, ..., BS_i, ..., BS_I\}$. Each 5G BS is equipped with an ES unit and a distributed PV generation device, denoted as $ES_i, \forall BS_i \in \mathcal{I}$ and $PV_i, \forall BS_i \in \mathcal{I}$, respectively. Because of the intermittent and volatile nature of PV energy, its high penetration in the ADN will lead to risk of overvoltage and continuous fluctuations in electricity prices. Therefore, we assume that the PV output from multiple PV-integrated 5G BSs can only interact with the energy aggregator to indirectly participate in the ADN DR. The ADN can provide a conventional power supply for the BSs and encourage the aggregator to provide auxiliary services such as frequency modulation and peak-shaving during peak and valley load periods, but is unable to directly dispatch and control the energy resources of 5G BSs. Fortunately, the aggregator plays an intermediary role between the 5G communication network and the ADN and acts as a DR agent to encourage 5G BSs to participate in the DR and assist in energy sharing among 5G BSs. Under the coordination of the aggregator, the ADN and the 5G communication network are connected through power lines and communication links to support the interaction of energy flow and information flow (Lu et al., 2020).

1) Information flow interaction: in the DR planning stage, the incentive price signal of the aggregator and DR results of 5G BSs can be shared through two-way communication links. In the online energy optimization stage, the energy sharing requirements and results of 5G BSs also can be shared through two-way communication links.
2) Energy flow interaction: with the assistance of the aggregator, 5G BSs can be used as response loads or sources. Specifically, 5G BSs can serve as typical prosumers of the ADN, which can both generate and consume electricity.

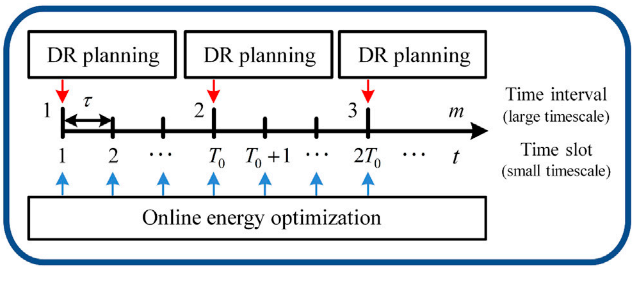

FIGURE 2 | Timescale for multiple 5G BSs participating in the DR.

In this study, we explore how the aggregator encourages and assists multiple 5G BSs to participate in the ADN DR during peak load periods. Since the DR during peak load periods and the real-time energy management of 5G BSs are optimization problems on different timescales, the participation of 5G BSs in the DR includes two stages, that is, DR planning and online energy optimization. As shown in **Figure 2**, we utilize a multi-timescale model (Yu et al., 2021) to divide the peak load period into T time slots, that is, small timescale, with length τ, the set of which is defined as $\mathcal{T} = \{1, \ldots, t, \ldots, T\}$. Consecutive T_0 time slots are combined into a time interval, that is, large timescale, the set of which is defined as $M = \{1, \ldots, m, \ldots, M\}$. Therefore, the set of time slots contained in the $m-$th time interval can be denoted as $T(m) = \{(m-1)T_0 + 1,\ (m-1)T_0 + 2, \ldots, mT_0\}$. At the beginning of each interval, the aggregator designs a contract as an incentive mechanism to encourage the BSs to participate in the DR according to the discharge capacity of the 5G BSs. In each time slot, the aggregator performs the online energy optimization of 5G BSs based on the optimal contract determined in the large timescale.

2.2 Large-Timescale Demand Response Planning

In the DR planning stage, a contract theory–based large-timescale DR planning method is proposed, which takes the peak-shaving demand of the ADN as the constraint and maximizes social welfare to obtain the optimal discharge power of 5G BSs participating in the DR. Specifically, as the DR agent, the aggregator needs to coordinate multiple 5G BSs with discharge capacity to provide peak-shaving services during the peak load period. Because of the differences in power consumption, PV energy, and the state of charge (SoC) of ES, 5G BSs show different discharge capacities. Therefore, the aggregator will design different contract items for BSs with different discharge capacities to encourage them to respond to the peak-shaving demand of the ADN. Each contract item stipulates the relationship between the discharge power and reward. Each BS will select a contract item matching its type to provide stable power to obtain the best utility. The details of the contract design and optimization will be introduced in **Section 3**.

2.3 Small-Timescale Online Energy Optimization

In the online energy optimization stage, we focus on the impact of the real-time imbalance between the PV energy and load demand of BSs participating in the DR on the stable operation of ES. In the small timescale, the PV energy is first used to supply the load demand of the BS. When the PV energy is balanced with the load demand, the ES only needs to stably participate in the DR according to the contract item. When the PV energy is more than the load demand, surplus PV energy will be generated, which will affect the stable output of the ES and may cause PV energy abandonment. When the PV energy is less than the load demand, a load gap will be generated. To satisfy the communication reliability requirements, the ES needs to respond to the demands of the ADN while balancing the BS load gap, leading to over-discharge of ES. In addition, since the PV energy and load demand of BSs are usually independent, some BSs may lack sufficient PV energy to satisfy the load demand, while other BSs may abandon surplus PV energy because of the inability of complete absorption. Therefore, the aggregator is introduced as a shared energy carrier to support energy sharing among multiple 5G BSs, and a small-timescale online energy optimization algorithm is proposed to optimize the imbalance energy between the PV energy and load demand of multiple 5G BSs. The specific procedures will be introduced in **Section 4**.

3 CONTRACT THEORY–BASED DEMAND RESPONSE PLANNING

3.1 Base Station Type Modeling

In this study, we assume that the BS with more remaining ES energy and lower load demand has a larger discharge capacity and is more willing to participate in the DR to obtain higher rewards. For the aggregator, BSs can be classified into different types based on the discharge capacity. Assuming that in the $m-$th time interval, I 5G BSs can be classified into I BS types by arranging their discharge capacity in ascending order. The set of BS types can be denoted as $\Theta(m) = \{\theta_1(m), \ldots, \theta_i(m), \ldots, \theta_I(m)\}$, where $\theta_i(m)$ is the discharge capacity of BS_i and $\theta_1(m) \le \cdots \le \theta_i(m) \le \cdots \le \theta_I(m)$.

The discharge capacity of a BS is determined by historical statistics of the source-load imbalance energy and ES energy in the first time slot of the $m-$th time interval (Wang et al., 2018). After the DR, the remaining ES energy should be greater than the minimum requirements of the ES discharge depth, which can be expressed as

$$E_i(t_0^m) + c_i - p_i(m) \cdot T_0\tau \ge E_{\min}, t_0^m = (m-1)T_0 + 1, \tag{1}$$

where t_0^m is the first time slot of the $m-$th time interval. $E_i(t_0^m)$ is the initial ES energy in time slot t_0. $T_0\tau$ is the duration of the time interval. $p_i(m)$ is the discharge power of BS_i in the $m-$th time interval. $p_i(m) \cdot T_0\tau$ is the total discharge electricity. c_i is the source-load imbalance margin, which is determined by the difference between the historical average PV energy and the load demand. When the historical average PV energy is greater than the load demand, c_i is a positive value. Otherwise, c_i is a negative value. $E_{\min}$ is the lower bound of the remaining ES energy. According to (1), the discharge power of BS_i satisfies

$$p_i(m) \le \frac{E_i(t_0^m) - E_{\min} + c_i}{T_0\tau}, t_0^m = (m-1)T_0 + 1. \tag{2}$$

Therefore, the BS type of BS_i can be quantified as

$$\theta_i(m) = \frac{E_i(t_0^m) - E_{\min} + c_i}{T_0\tau}, t_0^m = (m-1)T_0 + 1. \tag{3}$$

Considering the information security and privacy, the BS type of a specific BS is unknown to the aggregator, which means that the information is asymmetric (Zhou et al., 2019a). We assume that the aggregator can learn that there are a total of I types of BSs, and a BS belongs to type $\theta_i(m), \forall\theta_i(m) \in \Theta$ with probability P_i, that is, $\sum_{i=1}^{I} P_i = 1, \forall BS_i \in \mathcal{I}$.

3.2 Contract Formulation

The aggregator can design a contract including I different contract items for I types of BSs based on the contract theory to incentivize BSs to participate in the DR. For a type $\theta_i(m)$ BS, the aggregator pays a corresponding reward $r_i(m)$ for the discharge power $p_i(m)$ involved in the DR and specifies the performance-return correlation through the contract item $(p_i(m), r_i(m))$. The contract is denoted as $\pi = \{(p_i(m), r_i(m)), \forall BS_i \in \mathcal{I}\}$.

The principle of the aggregator contract design and BS contract signing is to maximize their own utility. Considering there are I types of 5G BSs, the utility of the aggregator is the subsidies for dispatching all response electricity minus all payment rewards, which is given by

$$U_A(\{p_i(m)\},\{r_i(m)\}) = I\sum_{i=1} P_i(T_0\tau\lambda(m)p_i(m) - r_i(m)), \quad (4)$$

where $\lambda(m)$ is the feed-in tariff of electricity in the $m-$th time interval. $T_0\tau\lambda(m)p_i(m)$ is the DR subsidy received by the aggregator. The inequality $T_0\tau\lambda(m)p_i(m) - r_i(m) \geq 0$ is always true for $\forall BS_i \in \mathcal{I}$, which means that the BSs participating in the DR are beneficial to the aggregator. Otherwise, the aggregator will lose momentum to aggregate energy of 5G BSs.

The utility of the type $\theta_i(m)$ BS which accepts the contract item $(p_i(m), r_i(m))$ is defined as the received reward minus the cost of discharging electricity, which is given by

$$U_i^{BS}(p_i(m), r_i(m)) = \theta_i(m)f(r_i(m)) - T_0\tau\xi p_i(m), \quad (5)$$

where ξ is the cost coefficient of discharging loss (Dragicevic et al., 2014). $\theta_i(m)f(r_i(m))$ is the value of $r_i(m)$ for type $\theta_i(m)$ BS, where the function $f(r_i(m))$ is a monotonically increasing concave function of $r_i(m)$ and represents the reward evaluation. Without the loss of generality, $f(r_i(m))$ is defined as a quadratic function, that is, $f(r_i(m)) = -ar_i^2(m)/2 + br_i(m)$, where a and b are positive constants which enable $f(r_i(m))$ to satisfy the constraints of $f(0) = 0$, $f'(r_i(m)) > 0$, and $f''(r_i(m)) < 0$.

According to the principle of contract design and signing, the problem of incentivizing 5G BSs to participate in the DR is transformed into the social welfare maximization problem. The expected social welfare is defined as the total utility of the aggregator and I BSs, which is given by

$$SW(\{p_i(m)\},\{r_i(m)\}) = U_A(\{p_i(m)\},\{r_i(m)\}) + I\sum_{i=1}^{I} P_i U_i^{BS}(p_i(m), r_i(m)). \quad (6)$$

3.3 Optimization Problem Modeling

The aggregator faces three constraints from the BS side when optimizing the contract design, namely, the individual rationality (IR) constraint, the incentive compatibility (IC) constraint, and the monotonicity constraint (Chen and Zhu, 2017). The IR constraint means that the BSs should receive non-negative utility after signing the contract and participating in the DR. The IC constraint means that a BS can only obtain maximum utility when signing the contract item designed for its own type. The monotonicity constraint means that the higher the BS type, the higher the reward will be. Therefore, the social welfare maximization problem is formulated as

$$\begin{aligned}
\text{P1:}\ & \max_{\{(p_i(m), r_i(m))\}} SW(\{p_i(m)\},\{r_i(m)\}) \\
s.t.\, C1:\ & \theta_i(m)f(r_i(m)) - T_0\tau\xi p_i(m) \geq 0, \\
C2:\ & \theta_i(m)f(r_i(m)) - T_0\tau\xi p_i(m) \geq \\
& \theta_i(m)f(r_{i'}(m)) - T_0\tau\xi p_{i'}(m), \\
C3:\ & 0 \leq r_1(m) < \ldots < r_i(m) < \ldots < r_I(m), \\
C4:\ & p_i(m) \leq \theta_i(m), \\
C5:\ & \sum_{i=1}^{I} p_i(m) = R(m) \qquad \forall i, i' \in \{1, \cdots, I\},
\end{aligned} \quad (7)$$

where $C1$, $C2$, and $C3$ are the IR constraint, IC constraint, and monotonicity constraint, respectively. $C4$ means that the discharge power demand stipulated in the contract should not exceed the discharge capacity of the BS. $C5$ is the peak-shaving demand constraint for power balance, where $R(m)$ is the peak-shaving demand in the $m-$th time interval.

3.4 Problem Transformation and Optimal Contract Solution

The formulated optimization problem includes I IR constraints and $I(I-1)$ IC constraints, the complexity of which is absolutely high. To facilitate the solution of the problem, the Contract Feasibility Necessary and Sufficient Condition Theorem (Zhou et al., 2019b) is used to reduce the dimensionality of IR constraints and IC constraints.

3.4.1 Individual Rationality Constraint Dimensionality Reduction

The utility of the type $\theta_i(m)(i \neq 1)$ BS should satisfy

$$\begin{aligned}
& \theta_i(m)f(r_i(m)) - T_0\tau\xi p_i(m) \geq \\
& \theta_i(m)f(r_1(m)) - T_0\tau\xi p_1(m) \geq \\
& \theta_1(m)f(r_1(m)) - T_0\tau\xi p_1(m) \geq 0,
\end{aligned} \quad (8)$$

where the first inequality satisfies the IC constraint, the second inequality satisfies the BS type definition, and the third inequality satisfies the IR constraint. Combining the first and third inequalities, we can draw that if the type $\theta_1(m)$ BS satisfies the IR constraint, the BSs with higher types will automatically satisfy the IR constraint. Therefore, only one IR constraint is retained through IR constraint dimensionality reduction, that is, $\theta_1(m)f(r_1(m)) - T_0\tau\xi p_1(m) \geq 0$.

3.4.2 Incentive Compatibility Constraint Dimensionality Reduction

We consider three adjacent BS types, that is, $\theta_{i-1}(m) < \theta_i(m) < \theta_{i+1}(m)$, the utilities of which should satisfy

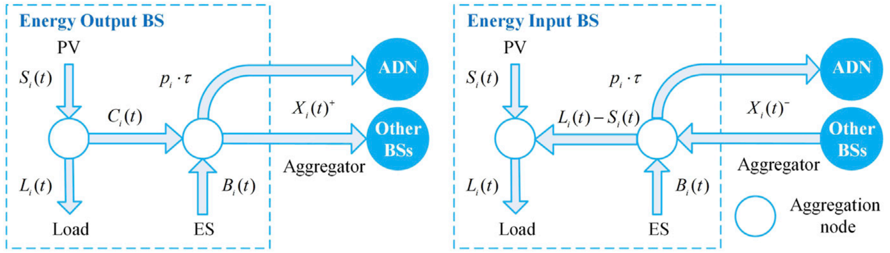

FIGURE 3 | Energy flow of 5G BSs.

$$\begin{aligned}\theta_{i+1}(m) f(r_{i+1}(m)) - T_0 \tau \xi p_{i+1}(m) \geq \\ \theta_{i+1}(m) f(r_i(m)) - T_0 \tau \xi p_i(m),\end{aligned} \tag{9}$$

$$\begin{aligned}\theta_i(m) f(r_i(m)) - T_0 \tau \xi p_i(m) \geq \\ \theta_i(m) f(r_{i-1}(m)) - T_0 \tau \xi p_{i-1}(m).\end{aligned} \tag{10}$$

Based on $r_{i-1}(m) < r_i(m) < r_{i+1}(m)$, we have

$$\begin{aligned}\theta_{i+1}(m) f(r_{i+1}(m)) - T_0 \tau \xi p_{i+1}(m) \geq \\ \theta_{i+1}(m) f(r_{i-1}(m)) - T_0 \tau \xi p_{i-1}(m).\end{aligned} \tag{11}$$

Combining (9) and (11), it can be further concluded as

$$\begin{aligned}&\theta_{i+1}(m) f(r_{i+1}(m)) - T_0 \tau \xi p_{i+1}(m) \geq \theta_{i+1}(m) f(r_{i-1}(m)) \\ &-T_0 \tau \xi p_{i-1}(m) \quad \geq \cdots \quad \geq \theta_{i+1}(m) f(r_1(m)) - T_0 \tau \xi p_1(m).\end{aligned} \tag{12}$$

Therefore, we can derive that all IC constraints hold if the IC constraint between the adjacent types holds. Through IC constraint dimensionality reduction, the number of IC constraints will be reduced from $I(I-1)$ to $I-1$.

3.4.3 Optimal Contract Solution

Based on the aforementioned analysis, $P1$ is rewritten as follows:

$$\begin{aligned}\text{P2:} \quad &\max_{\{(p_i(m), r_i(m))\}} SW(\{p_i(m)\}, \{r_i(m)\}) \\ s.t. C6: \ &\theta_1(m) f(r_1(m)) - T_0 \tau \xi p_1(m) \geq 0, \\ C7: \ &\theta_i(m) f(r_{i-1}(m)) - T_0 \tau \xi p_{i-1}(m) \leq \\ &\theta_i(m) f(r_i(m)) - T_0 \tau \xi p_i(m), \\ &C3, C4, C5 \, \forall i \in \{1, \cdots, I\}.\end{aligned} \tag{13}$$

By checking the Hessian matrix, it can be known that the objective function of $P2$ is concave. Because the difference between two concave functions is involved in $C7$, $P2$ cannot be solved directly by convex optimization. Therefore, we adopt the concave–convex process (CCP) algorithm (Wei et al., 2016) to transform $P2$ into a convex optimization problem. Denote $F_i(r_i(m)) = \theta_i(m) f(r_i(m))$, which can be differentiable with regards to $r_i(m)$. Then, $F_i(r_i(m))$ can be approximated by the first-order Taylor series expansion as

$$F_i(r_i(m)) \approx F_i(r_{i,0}[s]) + \nabla F_i(r_{i,0}[s])(r_i(m) - r_{i,0}[s]), \tag{14}$$

where $r_{i,0}[s]$ represents the initial point in the $s-$th iteration. Therefore, $C7$ is converted to the difference between a concave function and an affine function, which is expressed as

$$\begin{aligned}&\tilde{C}7\text{:} \ \theta_i(m) f(r_{i-1}(m)) - T_0 \tau \xi p_{i-1}(m) \\ &\leq \theta_i(m) [F_i(r_{i,0}[s]) + \nabla F_i(r_{i,0}[s])(r_i(m) - r_{i,0}[s])] - T_0 \tau \xi p_i(m).\end{aligned} \tag{15}$$

By replacing $C7$ with $\tilde{C}7$, $P2$ is transformed into a convex optimization problem. In the $s-$th iteration, the local optimal solutions $\hat{r}_i[s]$ and $\hat{p}_i[s]$ can be obtained by solving the transformed convex optimization problem. Then, the initial point of the Taylor series expansion in the $(s+1)-$th iteration is defined as $r_{i,0}[s+1] = \hat{r}_i[s]$, and the new local optimal solutions are derived until the iteration stop condition is met, that is, the change in the expected social welfare is less than or equal to a certain threshold, which is given by

$$SW(\{\hat{p}_i[s+1]\}, \{\hat{r}_i[s+1]\}) - SW(\{\hat{p}_i[s]\}, \{\hat{r}_i[s]\}) \leq \varepsilon. \tag{16}$$

Then, the iteration is terminated and the contract design is completed. The discharge power and corresponding reward of 5G BSs participating in the DR can be obtained based on the contract.

4 LYAPUNOV-BASED ONLINE ENERGY OPTIMIZATION

4.1 Dynamic Energy Queue Model

On the basis of obtaining the optimal discharge power of 5G BSs participating in the DR, we analyze the energy flow of BSs in the small timescale and propose the energy sharing strategy among multiple 5G BSs to further reduce the energy cost of the 5G communication network. Specifically, we classify the BSs into energy output BSs and energy input BSs, where energy output BSs share energy to absorb the surplus PV energy and energy input BSs receive the shared energy to balance the load gap. We define $\mathcal{BS}^+$ and $\mathcal{BS}^-$ as the sets of energy output BSs and energy input BSs, respectively. The load demand and the PV energy of BS_i in time slot t are denoted as $L_i(t), t \in T(m)$ and $S_i(t), t \in T(m)$, respectively. The surplus PV energy of BS_i in time slot t is denoted as $C_i(t), t \in T(m)$, which is given by

$$C_i(t) = \begin{cases} \min(S_i(t) - L_i(t), C_{\max}), & BS_i \in \mathcal{BS}^+ \\ 0, & BS_i \in \mathcal{BS}_i^- \end{cases}, \tag{17}$$

where $C_{\max}$ is the maximum surplus PV energy limited by the transmission line capacity, and the energy sharing among BSs obeys the following principles.

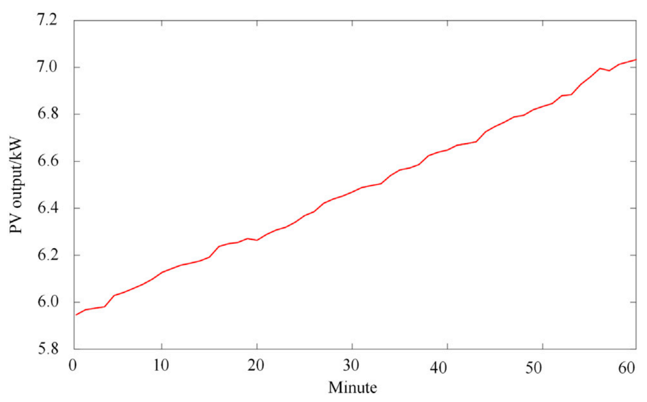

FIGURE 4 | PV output of 5G BSs.

TABLE 1 | Simulation parameters.

Project	Attribute	Value
PV generation	Capacity/kWp	10
	Power generation/kWh	64.8227
ES unit	Capacity/kWh	20.24
	Maximum discharging power/kW	10.24
	Lowest level of SoC/%	30
	Cost coefficient of discharge loss	0.14
ES initial SoC/%	BS1	38
	BS2	39
	BS3	43
	BS4	46
	BS5	48
	BS6	52
	BS7	55
	BS8	56
	BS9	59
	BS10	61

1) For $BS_i \in \mathcal{BS}^+$, the shared energy only comes from $C_i(t)$, and ES_i does not participate in energy sharing. When there is no load gap in other BSs, $C_i(t)$ and ES_i will participate in the DR together.
2) For $BS_i \in \mathcal{BS}^-$, the input energy can only be used to balance the load gap to reduce the discharge depth of ES_i and cannot participate in the DR.

Therefore, in the process of energy sharing, $BS_i \in \mathcal{BS}^+$ can share energy to other energy input BSs for absorbing surplus PV energy, and $BS_i \in \mathcal{BS}^-$ can balance the load gap by obtaining input energy to reduce the excessive utilization of ES_i energy. It is to be noted that when the input energy is insufficient to balance the load gap, the ES_i will increase the discharge energy to satisfy the load demand for $BS_i \in \mathcal{BS}^-$. The energy flows of $\mathcal{BS}^+$ and $\mathcal{BS}^-$ are shown in **Figure 3**.

The set of shared energy of BSs in time slot t can be defined as $\boldsymbol{X}(t) = [X_1(t), X_2(t), \ldots, X_I(t)]$, where $X_i(t)$ is the shared energy of BS_i. Denote $X_i(t)$ as $X_i(t)^+$ if $X_i(t) > 0$, which means the surplus PV energy $C_i(t) > 0$. Denote $X_i(t)$ as $X_i(t)^-$ if $X_i(t) < 0$, which means BS_i confronts the load gap. The power balance constraint and upper/lower bound constraint of $X_i(t)$ can be expressed as

$$\sum\nolimits_i X_i(t) = 0 \text{ and } 0 \le |X_i(t)| \le X_{\max}, \tag{18}$$

where $X_{\max}$ is the maximum transmission energy of the shared energy. In addition, based on the basic principle of energy sharing, the shared energy should satisfy

$$X_i(t) = \begin{cases} 0 \le X_i(t)^+ \le C_i(t), & BS_i \in \mathcal{BS}^+ \\ -(L_i(t) - S_i(t)) \le X_i(t)^- < 0, & BS_i \in \mathcal{BS}^- \end{cases}. \tag{19}$$

Without the energy sharing mode, the set of discharge energy of ESs in time slot t is denoted as $\boldsymbol{B}(t) = [B_1(t), B_2(t), \ldots, B_I(t)]$. The discharge energy of ES_i in time slot t is given by

$$B_i(t) = \begin{cases} p_i(m) \cdot \tau, & BS_i \in \mathcal{BS}^+ \\ \min\left([p_i(m) \cdot \tau + L_i(t) - S_i(t)], B_{\max}\right), & BS_i \in \mathcal{BS}^- \end{cases}, \tag{20}$$

where $B_{\max}$ is the maximum discharge energy, which depends on the maximum discharge power of ES.

The energy level of ES can be regarded as an ES queue, the length of which represents the remaining energy of the ES. We define the set of ES queues in time slot t as $\boldsymbol{E}(t) = [E_1(t), E_2(t), \ldots, E_I(t)]$, where $E_{\min} \le E_i(t) \le E_{\max}$. According to the energy flow of $\mathcal{BS}^+$ and $\mathcal{BS}^-$, the dynamic update equation of $E_i(t)$ can be further obtained as

$$E_i(t+1) = \begin{cases} E_i(t) - (B_i(t) + X_i(t)^+ - C_i(t)), & BS_i \in \mathcal{BS}^+ \\ E_i(t) - \left(p_i(m) \cdot \tau + L_i(t) - S_i(t) + X_i(t)^-\right), & BS_i \in \mathcal{BS}^- \end{cases}. \tag{21}$$

$\boldsymbol{E}(t)$ is called to be mean rate stable (Zhou et al., 2019c) if it satisfies

$$\lim_{t \to +\infty} \frac{\mathbb{E}\{|E_i(t)|\}}{\tau} = 0, \forall i \in \{1, \cdots, I\}. \tag{22}$$

The reason for ensuring the stability of ES queues during 5G BSs participating in the DR is that the frequent and excessive discharge of ESs will seriously shorten the life span and increase the maintenance cost of ES.

4.2 Online Energy Optimization Problem Formulation

The objective of the online energy optimization problem is to realize the full absorption of PV energy by energy sharing among 5G BSs, while ensuring the stability of ES queues. The PV absorption rate is denoted as the percentage of PV energy that can be absorbed by 5G BSs, which is given by

$$K_{pcr}(t) = \frac{\sum_i (X_i(t)^+ + N_i(t))}{\sum_i L_i(t)}, \tag{23}$$

where $N_i(t)$ is the self-produced PV energy $S_i(t)$ absorbed by the load demand of BS_i in time slot t, and $N_i(t) = \min(S_i(t), L_i(t))$.

TABLE 2 | Optimal contract parameters.

5G BS	Discharge capacity/kW	Response power/kW	BS utility	Aggregator utility	Social welfare
1	1.5	1.5	0.67	0.45	1.12
2	2.0	2.0	1.01	0.64	1.65
3	2.5	2.5	1.37	0.84	2.21
4	3.0	3.0	1.75	1.04	2.79
5	3.5	3.5	2.15	1.24	3.39
6	4.0	4.0	2.55	1.45	4.00
7	4.5	4.5	2.97	1.65	4.68
8	5.0	5.0	3.40	1.85	5.25
9	5.5	5.5	3.84	2.06	5.90
10	6.0	6.0	4.29	2.26	6.55
Summation	37.5	37.5	24	13.48	37.54

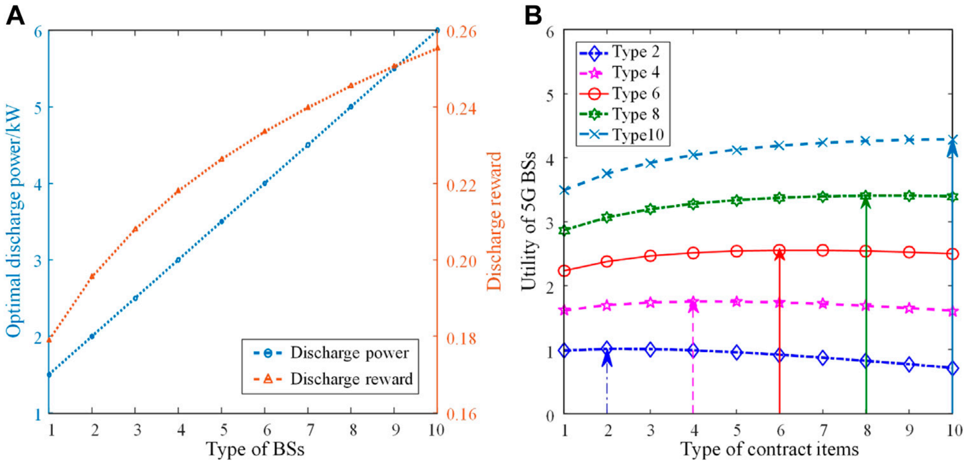

FIGURE 5 | Feasibility of the optimal contract for 5G BSs participating in DR.

Furthermore, the time-average PV absorption rate can be described as

$$\bar{K}_{pcr}(t) = \lim_{T_0\to\infty} \frac{1}{T_0} \sum\nolimits_{t=(m-1)T_0+1}^{mT_0} \frac{\sum_i \left(X_i(t)^+ + N_i(t)\right)}{\sum_i L_i(t)}. \tag{24}$$

The focus of online energy optimization is formulated to improve the PV absorption rate during the whole peak load period to minimize the energy cost of multiple 5G BSs participating in the DR by real-time decision-making on the shared energy among BSs, which can be expressed as

$$\begin{aligned} &\text{P3:}\ \max_{X_i(t)^+} \bar{K}_{pcr}(t) \\ &s.t.\ (18),\quad (19),\quad (21),\quad (22),\quad \forall i, t. \end{aligned} \tag{25}$$

As P3 is a time-coupling optimization problem due to the long-term constraints, traditional methods, such as stochastic optimization and dynamic programming, will suffer from the problem of dimensionality. Lyapunov optimization is an effective method to solve long-term optimization problems, which can transform the coupled long-term optimization problem into an independent single-slot deterministic sub-problem. Compared with traditional methods, Lyapunov optimization requires less prior information and poses lower computational complexity (Liao et al., 2020b). Therefore, we propose a Lyapunov-based online energy optimization algorithm for multiple 5G BSs participating in the DR.

4.3 Lyapunov-Based Problem Transformation and Online Energy Optimization Algorithm

The Lyapunov function is defined as $L(\boldsymbol{E}(t)) = \sum_i E_i(t)^2/2$, which represents a scalar measure of the remaining energy in ES queues. To reflect the stability of the ES queues, we define the one-slot conditional Lyapunov drift as the conditional expected change of the Lyapunov function between two adjacent time slots, which is given by

$$\Delta(\boldsymbol{E}(t)) = \mathbb{E}\{L(\boldsymbol{E}(t+1)) - L(\boldsymbol{E}(t)) | \boldsymbol{E}(t)\}. \tag{26}$$

As (25) is a maximization problem, we define the drift-minus-reward (Li et al., 2020) to maximize the PV absorption rate while ensuring the queue stability, which is given by

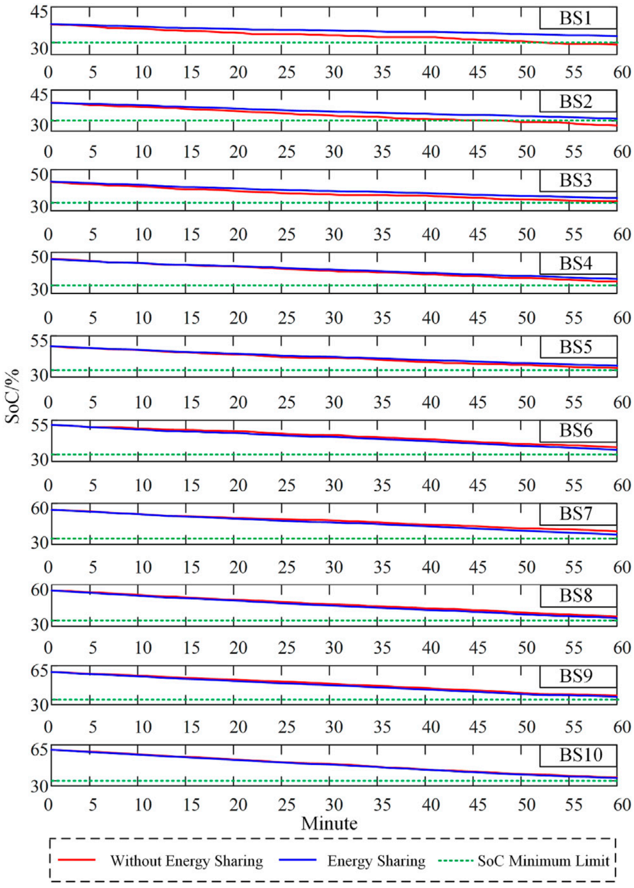

FIGURE 6 | Comparison of the ES SoC.

$$\text{P4:} \quad \min_{X_i(t)^+, X_i(t)^-} \Delta(\boldsymbol{E}(t)) - V\mathbb{E}\left\{K_{pcr}(t)\right\} \tag{27}$$
$$s.t. (18), \quad (19), \quad (21), \quad \forall i, t,$$

where V is a non-negative weight parameter used to make a tradeoff between ES queue stability and PV absorption rate maximization. In the case of all possible $\boldsymbol{E}(t)$ and $V \geq 0$, the drift-minus-reward is upper-bounded by

$$\begin{aligned}
&\Delta(\boldsymbol{E}(t)) - \mathbb{E}\left\{V \cdot \frac{\sum_i (X_i(t)^+ + N_i(t))}{\sum_i L_i(t)}\right\} \\
&\leq \sum_i \mathbb{E}\{E_i(t)[C_i(t) - X_i(t)^+ - B_i(t)] | X_i(t) \geq 0\} \\
&+ \sum_i \mathbb{E}\{E_i(t)[-p_i(m)\cdot\tau - L_i(t) + S_i(t) - X_i(t)^-] | X_i(t) < 0\} \\
&- \mathbb{E}\left\{V \cdot \frac{\sum_i (X_i(t)^+ + N_i(t))}{\sum_i L_i(t)}\right\} + Z,
\end{aligned} \tag{28}$$

where Z is a positive constant and is given by

$$Z = \sum_i (B_{\max}^2 + X_{\max}^2). \tag{29}$$

Proof: see Supplementary material.

Therefore, P4 can be further transformed into a linear programing problem by taking the iterative expectation and simplifying the upper bound of $\Delta(\boldsymbol{E}(t)) - V\mathbb{E}\{K_{pcr}(t)\}$ derived in **(28)**, which is given by

$$\text{P5:} \quad \min_{X_i(t)^+, X_i(t)^-} -\frac{V}{\sum_i L_i(t)} \sum_i X_i(t)^+ - \sum_i E_i(t) X_i(t)^+ - \sum_i E_i(t) X_i(t)^-$$
$$s.t. \quad (18), \quad (19), \quad (21), \quad \forall i, t, \tag{30}$$

Since $E_i(t)$ and $L_i(t)$ are available in time slot t, P5 is a linear programing problem with shared energy as the optimization variable, which can be solved directly using the CPLEX solver. It is observed that the Lyapunov-based online energy optimization algorithm only needs the real-time information of the remaining energy of ESs and the load demand of BSs to make the energy sharing decision, which effectively improves the efficiency of the algorithm execution. Moreover, the computational complexity of the proposed online energy optimization algorithm only increases linearly with the expansion of the number of BSs.

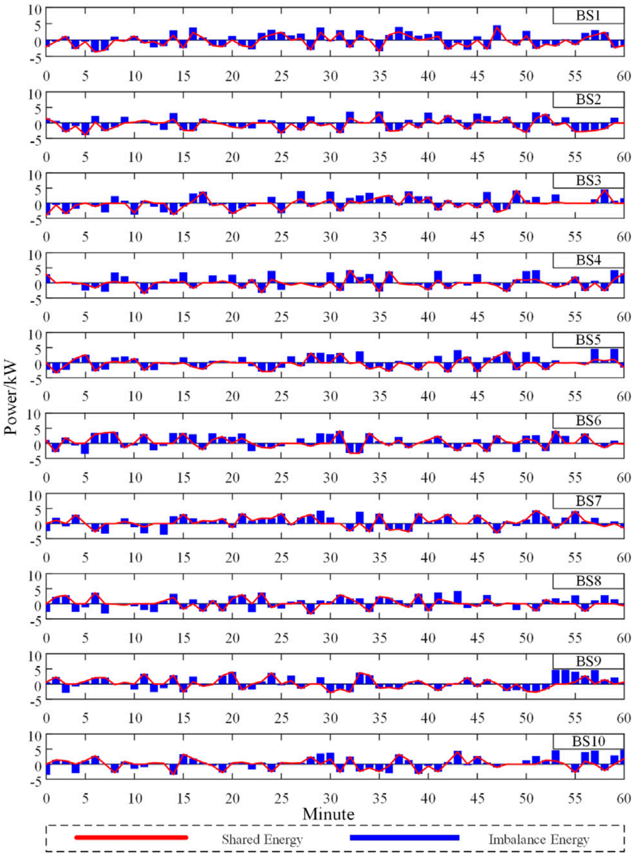

FIGURE 7 | Shared energy and imbalance energy of 5G BSs.

TABLE 3 | Comparison of the PV absorption rate of 5G BSs.

Indicator	Without DR participation	DR participation	Improvement/%
Abandoned PV/kWh	11.41	0.086	17.47
PV absorption rate/%	82.4	99.87	

5 CASE STUDY

5.1 Basic Data

In this section, we validate the performance of the proposed two-stage optimal dispatch method by simulations. We consider a scenario in which the aggregator signs the DR contract with 10 5G BSs during the peak load period. The BSs provide peak-shaving service for the ADN from 10:00 a.m. to 11:00 a.m. The feed-in tariff is CNY 0.42/ kWh, and the peak-shaving demand is 37.5 kW. The case analysis uses 1 min as the small timescale and 1 h as the large timescale. The minimum load demand is 2.193 kW when the BS is in a no-load operation state, and the maximum load demand is 10 kW when the BS is in a full-load operation state (China Mobile Research Institute, 2020). Considering that 10 5G BSs are geographically close to each other, we assume that the PV output of each BS adopts the same data. The typical PV output curve of 5G BSs from 10:00 a.m. to 11:00 a.m. is shown in **Figure 4**, and the simulation parameter settings of the DERs in 5G BSs are shown in **Table 1**. Moreover, since the daily dynamic load data of 5G BSs are still undisclosed, we assume that the load demand of 10 5G BSs obeys the random distribution within the load demand interval (2.193 kW, 10 kW).

5.2 Comparative Analysis of Optimization Results

5.2.1 Contract Theory–Based Large-Timescale Demand Response Planning

According to the initial ES capacity of the 5G BSs, the minute-level power consumption, and the PV output curve, the optimal contract can be obtained, and the corresponding parameters are shown in **Table 2**. The results show that the response power coincides with the discharge capacity, which implies that the 5G BSs with different discharge capacities choose the contract items that conform to their own types. The optimal discharge power is provided to obtain the optimal reward. The utilities of BSs and the aggregator increase with the BS type, which indicates that the aggregator prefers to sign the contract with BSs with higher discharge capacity. Moreover, we can find that the sum of the response power is equal to 37.5 kW, which accurately satisfies the peak-shaving demand of the ADN.

The optimal discharge power and discharge reward versus the BS type are shown in **Figure 5A**. It can be seen that the optimal discharge power and discharge reward increase monotonously with the BS type, indicating that the contract satisfies the monotonicity constraint, and the discharge capabilities of BSs are well-exploited. **Figure 5B** shows the utility of 5G BSs versus the type of the contract item. It can be seen that maximum utility can be achieved only when the 5G BS signs the contract item conforming to its type, indicating that the contract satisfies the IC constraint. Moreover, all 5G BSs that sign the contract can obtain non-negative utility, which is consistent with the IR constraint. In addition, the utility of the 5G BS is proportional to the BS type, which will increase the motivation of the higher type of 5G BS to sign the contract and participate in the DR.

5.2.2 Lyapunov-Based Small-Timescale Online Energy Optimization

Figure 6 shows the comparison of ES SoC with and without energy sharing. Simulation results show that 5G BSs participating in the DR without energy sharing will lead to an over-discharge or insufficient dispatching of ESs. At the end of DR, the SoCs of BS1 and BS2 are lower than the minimum capacity limit, while those of BS6 and BS7 still have enough dispatchable space. By contrast, the proposed Lyapunov-based online energy optimization algorithm with energy sharing can achieve higher discharge stability and a more balanced power level of ESs.

Figure 7 shows the shared energy and source-load imbalance energy of 10 5G BSs during the DR period. The red curve and the blue cylinder represent the shared energy optimized by the proposed online energy optimization algorithm and the imbalance energy, respectively. When the red curve is tangential to the blue cylinder, it means that the shared energy completely compensates for the imbalance energy. At this point, the ES unit is in a stable output state and only needs to output constant power based on the contract item. From 10:00 a.m. to 11:00 a.m., most BSs have surplus PV energy due to sufficient sunlight, and only a few BSs with high power consumption require shared energy. Based on the proposed online energy optimization algorithm, it can be seen that most BSs can interact with each other to compensate for the imbalance in energy through energy sharing, which further promotes PV energy consumption, reduces the curtailment of PV output, and ensures the output stability of ES units.

Table 3 shows the comparison of the PV absorption rate before and after the two-stage optimal dispatch. Compared with not participating in the DR, 5G BSs participating in the DR can improve the PV absorption rate by 17.47% and make it up to 99.87%. The reason is that the contract-based DR planning ensures rough absorption of the overall PV output during the entire peak load period, while the Lyapunov-based online energy optimization algorithm ensures the approximately complete and real-time absorption of the PV output, thus realizing the maximum absorption of PV energy during the entire peak load period.

6 CONCLUSION

In this study, we propose a two-stage optimal dispatch method based on the contract theory and Lyapunov optimization for the typical scenario of multiple PV-integrated 5G BSs participating in the ADN DR. The following conclusions are obtained:

1) The system architecture for multiple PV-integrated 5G BS participating in the ADN DR was proposed, which is composed of aggregators, a 5G communication network, and an ADN.
2) A contract theory–based large-timescale DR planning method was proposed for modeling the interaction between 5G BSs and the aggregator. Simulation results show that the proposed method can improve the motivation of 5G BSs to participate in the DR and satisfy the peak-shaving demand of the ADN.
3) A Lyapunov-based small-timescale online energy optimization algorithm was proposed for making real-time decisions on energy sharing of 5G BSs. The numerical results show that the proposed method can improve the PV absorption rate up to 99.87%, which achieves approximately complete absorption of PV energy and ensures the stability of the ES queue.

Further research will be conducted in three directions, including:

1) Implementation of energy dispatch for large-scale 5G BSs at multiple timescales including day-ahead, intra-day, and real-time and the systematical evaluation of the respond capacity of a PV-integrated 5G BS for ancillary services.
2) Energy sharing scheme and a demand response incentive mechanism that take into account power transmission losses.
3) Multi-entity benefit allocation method for participating in the DR under deregulated power markets.

DATA AVAILABILITY STATEMENT

The original contributions presented in the study are included in the article/Supplementary Material; further inquiries can be directed to the corresponding author.

AUTHOR CONTRIBUTIONS

XZ: conceptualization, methodology, software, investigation, formal analysis, and writing—original draft; ZAW: data curation and writing—original draft; ZZ: visualization and writing—original draft; HL: conceptualization, supervision, and writing—review and editing; XM: conceptualization, supervision, and writing—review and editing; XY: visualization and writing—review and editing GL: resources, supervision, and writing—review and editing; ZOW: visualization and writing—review and editing; ZL: visualization and writing—review and editing; YL: resources and supervision.

FUNDING

Authors are grateful to the financial support from Science and Technology Project of State Grid Corporation of China (KJ21-1-56).

REFERENCES

Chen, J., and Zhu, Q. (2017). Security as a Service for Cloud-Enabled Internet of Controlled Things under Advanced Persistent Threats: A Contract Design Approach. *IEEE Trans.Inform.Forensic Secur.* 12 (11), 2736–2750. doi:10.1109/tifs.2017.2718489

Chih-Lin, I., Han, S., and Bian, S. (2020). Energy-efficient 5G for a Greener Future. *Nat. Electron* 3 (4), 182–184. doi:10.1038/s41928-020-0404-1

China Mobile Research Institute (2020). 5G Telecom Power Target Network White Paper 2020. Available: https://max.book118.com/html/2020/0913/8105107075002142.shtm (updated September 14, 2020).

Ci, S., Zhou, Y., Xu, Y., Diao, X., and Wang, J. (2020). Building a Cloud-Based Energy Storage System through Digital Transformation of Distributed Backup Battery in Mobile Base Stations. *China Commun.* 17 (4), 42–50. doi:10.23919/jcc.2020.04.005

Dragicevic, T., Pandzic, H., Skrlec, D., Kuzle, I., Guerrero, J. M., and Kirschen, D. S. (2014). Capacity Optimization of Renewable Energy Sources and Battery Storage in an Autonomous Telecommunication Facility. *IEEE Trans. Sustain. Energy* 5 (4), 1367–1378. doi:10.1109/tste.2014.2316480

Fu, S., Su, Z., Jia, Y., Zhou, H., Jin, Y., Ren, J., et al. (2019). Interference Cooperation via Distributed Game in 5G Networks. *IEEE Internet Things J.* 6 (1), 311–320. doi:10.1109/jiot.2017.2743116

Guo, Y., Xu, J., Duan, L., and Zhang, R. (2014). Joint Energy and Spectrum Cooperation for Cellular Communication Systems. *IEEE Trans. Commun.* 62 (10), 3678–3691. doi:10.1109/tcomm.2014.2353632

Han, J., Liu, N., Huang, Y., and Zhou, Z. (2021). Collaborative Optimization of Distribution Network and 5G Mobile Network with Renewable Energy Sources in Smart Grid. *Int. J. Electr. Power & Energy Syst.* 130, 107027. doi:10.1016/j.ijepes.2021.107027

Hu, S., Chen, X., Ni, W., Wang, X., and Hossain, E. (2020). Modeling and Analysis of Energy Harvesting and Smart Grid-Powered Wireless Communication Networks: A Contemporary Survey. *IEEE Trans. Green Commun. Netw.* 4 (2), 461–496. doi:10.1109/tgcn.2020.2988270

Huq, K., Mumtaz, S., Zhou, Z., Chandra, K., Otung, I., and Rodriguez, J. (2020). "Energy-efficiency Maximization for D2D-Enabled UAV-Aided 5G Networks," in 2020 IEEE International Conference on Communications, Dublin, Ireland, 7-11 June 2020, 1–6. doi:10.1109/icc40277.2020.9149150

Israr, A., Yang, Q., Li, W., and Zomaya, A. Y. (2021). Renewable Energy Powered Sustainable 5G Network Infrastructure: Opportunities, Challenges and Perspectives. *J. Netw. Comput. Appl.* 175, 102910. doi:10.1016/j.jnca.2020.102910

Khan, Z. A., and Jayaweera, D. (2019). Smart Meter Data Based Load Forecasting and Demand Side Management in Distribution Networks with Embedded PV Systems. *IEEE Access* 8, 2631–2644. doi:10.1109/ACCESS.2019.2962150

Li, K., Yan, J., Hu, L., Wang, F., and Zhang, N. (2021). Two-stage Decoupled Estimation Approach of Aggregated Baseline Load under High Penetration of Behind-The-Meter PV System. *IEEE Trans. Smart Grid* 12 (6), 4876–4885. doi:10.1109/tsg.2021.3105747

Li, P., Sheng, W., Duan, Q., Li, Z., Zhu, C., and Zhang, X. (2020). A Lyapunov Optimization-Based Energy Management Strategy for Energy Hub with Energy Router. *IEEE Trans. Smart Grid* 11 (6), 4860–4870. doi:10.1109/tsg.2020.2968747

Liao, H., Zhou, Z., Ai, B., and Guizani, M. (2020). "Learning-based Energy-Efficient Channel Selection for Edge Computing-Empowered Cognitive Machine-To-Machine Communications," in 2020 IEEE 91st Vehicular Technology Conference (VTC2020-Spring),, Antwerp, Belgium, 25-28 May 2020, 1–6. doi:10.1109/vtc2020-spring48590.2020.9128780

Liao, H., Zhou, Z., Zhao, X., Zhang, L., Mumtaz, S., Jolfaei, A., et al. (2020). Learning-based Context-Aware Resource Allocation for Edge-Computing-Empowered Industrial IoT. *IEEE Internet Things J.* 7 (5), 4260–4277. doi:10.1109/jiot.2019.2963371

Liu, N., Yu, X., Fan, W., Hu, C., Rui, T., Chen, Q., et al. (2017). Online Energy Sharing for Nanogrid Clusters: A Lyapunov Optimization Approach. *IEEE Trans. Smart Grid* 9 (5), 4624–4636. doi:10.1109/TSG.2017.2665634

Lu, X., Li, K., Xu, H., Wang, F., Zhou, Z., and Zhang, Y. (2020). Fundamentals and Business Model for Resource Aggregator of Demand Response in Electricity Markets. *Energy* 204, 117885. doi:10.1016/j.energy.2020.117885

Pedram, M., and Wang, L. (2019). Energy Efficiency in 5G Cellular Network Systems. *IEEE Des. Test.* 37 (1), 64–78. doi:10.1109/MDAT.2019.2960342

Piovesan, N., Temesgene, D. A., Miozzo, M., and Dini, P. (2019). Joint Load Control and Energy Sharing for Autonomous Operation of 5G Mobile Networks in Micro-grids. *IEEE Access* 7, 31140–31150. doi:10.1109/access.2019.2903499

Singh, R., Sicker, D., and Huq, K. (2020). “MOTH- Mobility-Induced Outages in THz: A beyond 5G (B5G) Application,” in *2020 IEEE 17th Annual Consumer Communications & Networking Conference* (NV, USA: Las Vegas), 1–9. doi:10.1109/ccnc46108.2020.9045401

Tang, G., Yuan, H., Guo, D., Wu, K., and Wang, Y. (2021). “Reusing Backup Batteries as BESS for Power Demand Reshaping in 5G and beyond,” in IEEE INFOCOM 2021-IEEE Conference on Computer Communications, Vancouver, BC, Canada, 10-13 May 2021, 1–10. doi:10.1109/infocom42981.2021.9488760

Wang, F., Li, K., Liu, C., Mi, Z., Shafie-Khah, M., and Catalao, J. P. S. (2018). Synchronous Pattern Matching Principle-Based Residential Demand Response Baseline Estimation: Mechanism Analysis and Approach Description. *IEEE Trans. Smart Grid* 9 (6), 6972–6985. doi:10.1109/tsg.2018.2824842

Wang, F., Xuan, Z., Zhen, Z., Li, K., Wang, T., and Shi, M. (2020). A Day-Ahead PV Power Forecasting Method Based on LSTM-RNN Model and Time Correlation Modification under Partial Daily Pattern Prediction Framework. *Energy Convers. Manag.* 212, 112766. doi:10.1016/j.enconman.2020.112766

Wei, H., Xiao, L., Li, Y., and Zhou, S. (2016). “Queue-aware Energy-Efficient Scheduling and Power Allocation in Small-Cell Networks with Interference,” in *2016 IEEE Wireless Communications and Networking Conference* (Doha, Qatar: IEEE), 1–6. doi:10.1109/wcnc.2016.7565102

Xu, J., Duan, L., and Zhang, R. (2015). Cost-aware Green Cellular Networks with Energy and Communication Cooperation. *IEEE Commun. Mag.* 53 (5), 257–263. doi:10.1109/mcom.2015.7105673

Yong, P., Zhang, N., Liu, Y., Hou, Q., Li, Y., and Kang, C. (2021). Exploring the Cellular Base Station Dispatch Potential towards Power System Frequency Regulation. *IEEE Trans. Power Syst.* 37 (1), 820–823. doi:10.1109/TPWRS.2021.3124141

Yong, P., Zhang, N., Hou, Q., Liu, Y., Teng, F., Ci, S., et al. (2021). Evaluating the Dispatchable Capacity of Base Station Backup Batteries in Distribution Networks. *IEEE Trans. Smart Grid* 12 (5), 3966–3979. doi:10.1109/tsg.2021.3074754

Yu, H., Zhou, Z., Jia, Z., Zhao, X., Zhang, L., and Wang, X. (2021). Multi-timescale Multi-Dimension Resource Allocation for NOMA-Edge Computing-Based Power IoT with Massive Connectivity. *IEEE Trans. Green Commun. Netw.* 5 (3), 1101–1113. doi:10.1109/tgcn.2021.3076582

Zhang, B., Jiang, C., Yu, J-L., and Han, Z. (2016). A Contract Game for Direct Energy Trading in Smart Grid. *IEEE Trans. Smart Grid* 9 (4), 2873–2884. doi:10.1109/TSG.2016.2622743

Zhang, K., Mao, Y., Leng, S., He, Y., Maharjan, S., Gjessing, S., et al. (2018). Optimal Charging Schemes for Electric Vehicles in Smart Grid: A Contract Theoretic Approach. *IEEE Trans. Intell. Transp. Syst.* 19 (9), 3046–3058. doi:10.1109/tits.2018.2841965

Zhong, W., Xie, K., Liu, Y., Yang, C., Xie, S., and Zhang, Y. (2019). Online Control and Near-Optimal Algorithm for Distributed Energy Storage Sharing in Smart Grid. *IEEE Trans. Smart Grid* 11 (3), 2552–2562. doi:10.1109/TSG.2019.2957426

Zhou, C., Feng, C., and Wang, Y. (2021). Spatial-temporal Energy Management of Base Stations in Cellular Networks. *IEEE Internet Things J.* 99, 1. doi:10.1109/jiot.2021.3121325

Zhou, Z., Guo, Y., He, Y., Zhao, X., and Bazzi, W. M. (2019). Access Control and Resource Allocation for M2M Communications in Industrial Automation. *IEEE Trans. Ind. Inf.* 15 (5), 3093–3103. doi:10.1109/tii.2019.2903100

Zhou, Z., Liao, H., Zhao, X., Ai, B., and Guizani, M. (2019). Reliable Task Offloading for Vehicular Fog Computing under Information Asymmetry and Information Uncertainty. *IEEE Trans. Veh. Technol.* 68 (9), 8322–8335. doi:10.1109/tvt.2019.2926732

Zhou, Z., Sun, C., Shi, R., Chang, Z., Zhou, S., and Li, Y. (2017). Robust Energy Scheduling in Vehicle-To-Grid Networks. *IEEE Netw.* 31 (2), 30–37. doi:10.1109/mnet.2017.1600220nm

Zhou, Z., Wang, B., Guo, Y., and Zhang, Y. (2019). Blockchain and Computational Intelligence Inspired Incentive-Compatible Demand Response in Internet of Electric Vehicles. *IEEE Trans. Emerg. Top. Comput. Intell.* 3 (3), 205–216. doi:10.1109/tetci.2018.2880693

Conflict of Interest: XY, GL, ZOW, ZL, and YL were employed by Information and Communication Company, State Grid Tianjin Electric Power Company. The remaining authors declare that the research was conducted in the absence of any commercial or financial relationships that could be construed as a potential conflict of interest.

APPENDIX

Proof of **(27)**:

$$
\begin{aligned}
&\Delta(E(t)) = \mathbb{E}\{L(E(t+1)) - L(E(t))\}\\
&= \frac{1}{2}\mathbb{E}\Big\{\sum_i \left[E_i(t+1)^2 - E_i(t)^2\right]\Big\}\\
&= \frac{1}{2}\mathbb{E}\Big\{\sum_i \left[\left(E_i(t) - B_i(t) + C_i(t) - X_i(t)^+\right)^2 - E_i(t)^2\right] | X_i(t) \geq 0\Big\}\\
&+\frac{1}{2}\mathbb{E}\Big\{\sum_i \left[\left(E_i(t) - p_i(m)\cdot\tau - (L_i(t) - S_i(t)) - X_i(t)^-\right)^2\right.\\
&\left.-E_i(t)^2\right] | X_i(t) < 0\Big\}\\
&\leq \frac{1}{2}\mathbb{E}\Big\{\sum_i \left[B_i(t)^2 + C_i(t)^2 + (X_i(t)^+)^2 - 2E_i(t)\ (C_i(t) - X_i(t)^+\right.\\
&\quad\left. - B_i(t))\right] | X_i(t) \geq 0\Big\} + \frac{1}{2}\mathbb{E}\Big\{\sum_i \left[p_i(m)^2\cdot\tau^2 + (L_i(t) - S_i(t))^2\right.\\
&\quad + (X_i(t)^-)^2
\end{aligned}
$$

Thus, we can have **(28)**

$$
\begin{aligned}
&\Delta E(t) - \mathbb{E}\left\{V\cdot\frac{\sum_i (X_i(t)^+ + N_i(t))}{\sum_i L_i(t)}\right\}\\
&\leq \sum_i \mathbb{E}\{E_i(t)\left[C_i(t) - X_i(t)^+ - B_i(t)\right] | X_i(t) \geq 0\}\\
&+\sum_i \mathbb{E}\{E_i(t)\left[-p_i(m)\cdot\tau - L_i(t) + S_i(t) - X_i(t)^-\right] | X_i(t) < 0\}\\
&-\mathbb{E}\left\{V\cdot\frac{\sum_i (X_i(t)^+ + N_i(t))}{\sum_i L_i(t)}\right\} + Z
\end{aligned}
$$

The proof is completed.

frontiers | Frontiers in Energy Research

ORIGINAL RESEARCH
published: 13 July 2022
doi: 10.3389/fenrg.2022.923264

Power Coordinated Control and Parameter Analysis for Spiral Spring Energy Storage Systems Based on Backstepping Control Under Current Vector Orientation

Yang Yu[1,2]*, *Mengyun Wang*[2], *Ruifeng Zhang*[2], *Zengqiang Mi*[1,2] *and Xiaoming Zheng*[3]

[1]State Key Laboratory of Alternate Electrical Power System with Renewable Energy Sources, North China Electric Power University, Baoding, China, [2]Key Laboratory of Distributed Energy Storage and Microgrid of Hebei Province, North China Electric Power University, Baoding, China, [3]State Grid Shanxi Economic and Technological Research Institute, Taiyuan, China

OPEN ACCESS

Edited by:
Tianguang Lu,
Shandong University, China

Reviewed by:
Yubin Jia,
Southeast University, China
Roberto Quintal Palomo,
Universidad Autónoma de Yucatán, Mexico

Correspondence:
Yang Yu
ncepu_yy@163.com

Specialty section:
This article was submitted to Smart Grids,
a section of the journal
Frontiers in Energy Research

Received: *19 April 2022*
Accepted: *26 May 2022*
Published: *13 July 2022*

Citation:
Yu Y, Wang M, Zhang R, Mi Z and Zheng X (2022) Power Coordinated Control and Parameter Analysis for Spiral Spring Energy Storage Systems Based on Backstepping Control Under Current Vector Orientation.
Front. Energy Res. 10:923264.
doi: 10.3389/fenrg.2022.923264

As a new and great source of potential energy storage technology, the spiral spring energy storage (SSES) technology uses a permanent magnet synchronous machine (PMSM) to tighten or release the spiral spring for energy conversion. In allusion to the feature of simultaneous variations in torque and inertia for spiral springs in operation, it is difficult for the SSES system to show good control performance in regulating the power from/to the grid under a conventional vector control method. A power coordinated control scheme of the SSES system with the grid is proposed to integrate the grid-side converter (GSC) with the machine-side converter (MSC) based on backstepping control under the current vector orientation. First, the mathematical models of GSC and PMSM under the current vector orientation coordinate frame are established. Second, the coordinated control scheme is designed by the backstepping control principle, and its stability is proved in theory. Then, the optimal control parameters in the control scheme are determined by investigating the desired control performance. Ultimately, the simulation and experimental results show that the proposed control scheme with the chosen control parameters coordinates the GSC and the MSC well. The power signal is tracked accurately and rapidly, and the operation performance of the SSES system and its energy exchange with the grid are both improved effectively.

Keywords: spiral spring, energy storage, permanent magnet synchronous machine, backstepping control, power control, parameter analysis

1 INTRODUCTION

The exploitation of new energy sources is an effective means for environmental protection and sustainable development, while natural features of intermittence and fluctuation restrict the large scale of the new energy sources connected to the grid (Kumar et al., 2020). Research and investigation of energy storage technologies are increasingly available as an important approach to suppress the adverse effects of new energy sources (Ghaemi and Mirsalim, 2017; Zhang and Zhu, 2018; Gonzalez - Gonzalez et al., 2020). The spiral spring energy storage (SSES) system shown in **Figure 1**, which has been devised and improved in recent years, is paid special attention due to its various merits such as low cost, long lifetime, high safety, high efficiency, environmental friendliness, high power density,

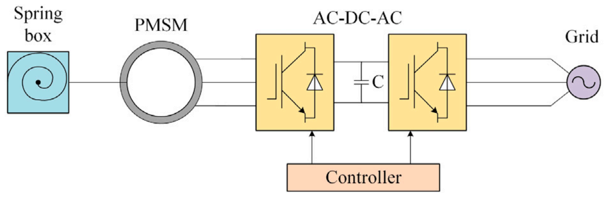

FIGURE 1 | Structural diagram of the mechanical spiral spring energy storage system.

and easy adjustment of energy storage capacity (Yu et al., 2016; Yu et al., 2020). The permanent magnet synchronous machine (PMSM) with full power converters is selected as its energy conversion equipment, owing to a high ratio of torque to inertia and simple structure (Ye et al., 2021).

Basic characteristics of the variable torque and inertia for the spiral spring in operation (Caballero et al., 2018) make the SSES system output decrease in power, and it is difficult for the SSES system to store or release electrical energy, according to the stable power signal from/to the grid with previous control methods. The reversal torque property of the spiral spring (Yu et al., 2018a) also requires the control algorithm to respond quickly and run fast.

For the participation in power regulation of the SSES system with a proper control approach of the full power converters, the control technique for both the grid-side converter (GSC) and the machine-side converter (MSC) should be considered. For the GSC, its power control mainly includes indirect current control, direct current control, and direct power control (DPC) (Gui et al., 2019). In contrast to the indirect current control with a relatively poor dynamic performance, direct current control has the advantages of high precision and good dynamic performance. Active and reactive power could be controlled by changing the d-axis and q-axis currents, respectively. But the proportional–integral (PI)-based double closed-loop control has a relatively slow response and is hard to set the parameters (Mallik et al., 2017). DPC with its fast response can control instantaneous active power and reactive power directly (Kim, 2018). However, the switching frequency in a traditional switching table-based DPC is not fixed. DPC with constant switching frequency is discussed in Gui et al. (2018), and DPC based on model predictive control is proposed in Zhang et al. (2015), but they are both affected by a big computational burden. In view of its simple structure, flexible control, and strong parameter robustness of backstepping control (BC), backstepping control-based DPC is proposed in Wai et al. (2018), which improves the stability of the control system. At present, the GSC is primarily used to stabilize the voltage of the direct current (DC) bus, and few studies have revealed its power control scenario directly responding to the external power signal such as from the grid, which is realized by coordinating with the MSC or the load power. The power control of PMSM is still dominated by DPC. In Zhang and Qu (2015), a switching table-based DPC is investigated through the instantaneous power principle. A fast response DPC with fixed switching frequency under stator current vector orientation is presented by combining SVPWM with the instantaneous reactive power principle in Ali et al. (2017). The references of active power and reactive power obtained by direct calculation are used to replace the PI-based double closed-loop controller in Kwak et al. (2019), and its MSC merely uses the uncontrollable rectification mode. The output power of PMSM under DPC is supplied to the load. If the power signal looked at from the grid side is responded to in this way, the actual power involved in regulation will become inaccurate due to the losses of the machine and converters. Currently, most of the studies focus on bilateral converters from the perspective of isolation and decoupling. To reduce the power imbalance caused by the load fluctuation, it is suitable to increase the coupling capacitor, which leads to a higher cost and lower reliability. Therefore, the coordinated control of the GSC and MSC has been concerned (Yu et al., 2018b).

To achieve good integration and improve the dynamic response speed of the overall system, it is essential to optimize the independent control on both sides of GSC and MSC and target them as a whole to design the coordinated control. A coordinated control scheme based on active power and DC voltage to reduce the oscillation of DC voltage is proposed in Tian et al. (2014), but the PI control is used, and it cannot track the alternating current signal without steady-state error. Coordinated passive control of PMSM based on the dual PWM converter is realized in Li et al. (2018), and it can restrain the fluctuation of the DC bus voltage effectively. In contrast, the passive control is relatively complicated and increases the implementation difficulty in practice. Aiming at the energy relationship of each part in the coordinated control, a mathematical model from the energy viewpoint is established in Bo et al. (2017) to improve the ability of the motor to manage the external energy fluctuation. However, the system still faces the problem of regulating the load power and does not participate in power regulation directly.

BC starts with the control objectives and selects virtual state variables and virtual stability functions to construct the actual controller step-by-step. BC can achieve an accurate and fast tracking of the control targets, and its stability is strictly guaranteed by the Lyapunov stability theory. The application of BC in related fields (Xiong and Sun, 2016; Yang et al., 2020) shows that it is superior to the traditional PI control in control accuracy, control speed, and other performance indexes. In allusion to the variable torque and inertia of the spiral spring, the spring driven by PMSM is realized by BC in Yu et al. (2018b). The results show that BC has a rapid response and small tracking error, so it is also adopted as the control scheme in this research. The choice of the control parameters in BC is an important task and will affect its control performance. The current rule of selecting control parameters is basically based on the theory of Lyapunov stability, which requires that the control parameters satisfy the positive definite condition (Delavari and Naderian, 2019; Achlerkar and Panigrahi, 2020; Li et al., 2020). In Liu et al. (2019), it is pointed out that one of the reasons for the poor dynamic performance of BC is that its control parameters only satisfy the stability condition without considering the convergence rate of the steady-state error and other factors. It can be seen that it is of great significance to select the appropriate backstepping control parameters, but few studies have been involved in the optimization of control parameters. The ability of BC to cope with the change in structural parameters is enhanced in Lu et al. (2015) by adjusting the control parameters. In Jeon et al. (2020), it is further pointed out that the selection of the control parameters in BC should consider the range of the uncertain parameters. The control parameters of BC are optimized and determined in Yu et al. (2016) by the differential evolution algorithm. The control parameters of BC do affect the control performance. But current research optimizes the control parameters mainly through intelligent algorithms and does not directly study the method of parameter selection from the perspective of the control performance.

In summary, a coordinated power control scheme of GSC and MSC for the SSES system based on BC under current vector orientation will be proposed in the research study. Under the current vector orientation, for GSC, the control of the grid current amplitude and power factor angle can ensure the rapid and accurate response to the external power signal; and for PMSM, the coordinated control, including the stability of the DC side voltage, is achieved by regulating the stator current and torque angle. Active coordinated control can greatly simplify the control structure. Meanwhile, for the SSES system with a strong nonlinearity, the control parameters in the designed controller are analyzed and selected in terms of the control performance of the system. Ultimately, through the capacitor in the DC side, the GSC can actively track the power signal from the grid, with the MSC coordinating with it to ensure that the SSES system can participate in power regulation accurately and quickly.

The contribution of this research is reflected in two aspects: First, with the DC-link capacitor to help realize the power coordinated control of the SSES, the coordinated controllers of GSC and MSC are proposed based on BC in the grid current-oriented coordinate system for GSC and in the stator current-oriented coordinate system for MSC, respectively. Second, for multiple control parameters in the proposed control scheme, the determination approach of the control parameters is devised based on the perspective of the control performance. The structure of this context is as follows: **Section 2** introduces the modeling of the SSES system. The formulation and design of the controllers in GSC and PMSM are carried out in **Section 3**. In **Section 4**, the determination of the control parameters is completed. **Section 5** gives the simulation and experimental results. The last section draws the conclusions.

2 MODELING OF THE SSES SYSTEM

The schematic diagram of the SSES system shown in **Figure 1** indicates that the system can be divided into four subsystems: spiral spring, PMSM, AC-DC-AC bidirectional converter, and the controller.

2.1 Modeling of the Spiral Spring

The spiral spring is the energy storage device of the SSES system. According to the knowledge of material mechanics (Yu et al., 2018b), the mathematical model of the spiral spring can be described by the torque characteristic:

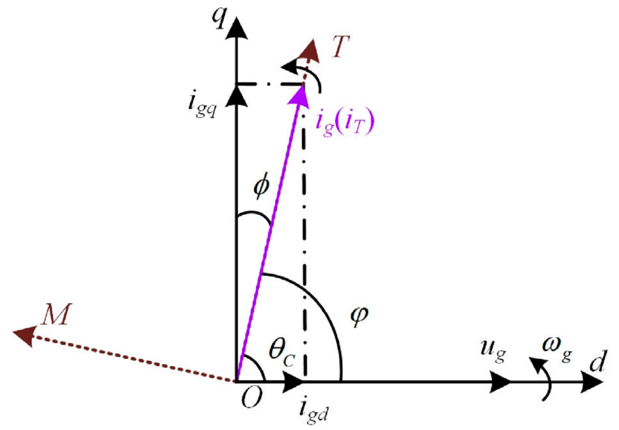

FIGURE 2 | Space vector model of the grid-side converter under the current vector orientation coordinate system.

$$T_{\mathrm{L}} = \frac{Ebh^3}{12L}\delta = \frac{Ebh^3}{12L}\omega_{\mathrm{r}} t, \tag{1}$$

where T_{L} is the output torque, E is the elasticity modulus, b, h, and L are the width, thickness, and length of the spring, respectively, δ is the rotation angle of the motor, ω_{r} is the mechanical angular velocity of the motor, and t is the time.

2.2 Modeling of the Grid-Side Converter Under Grid Current Vector Orientation

Based on the original dqo synchronous rotating coordinate system oriented on the grid voltage vector $\mathbf{u_g}$, a new rotating coordinate system TMo plotted in **Figure 2** is introduced and oriented on the grid current vector $\mathbf{i_g}$, where the T-axis is the real axis, and the M-axis is the imaginary axis. The grid current $\mathrm{i_g}$ overlaps with the T-axis. θ_c is the included angle between T and d axes. ω_g is the angular speed of the grid voltage.

In *TMo*, the state equation of GSC with i_{g} and θ_{C} selected as the state variables can be expressed as follows:

$$\begin{cases} u_{\mathrm{g}T} = R_{\mathrm{g}} i_{\mathrm{g}} + L_{\mathrm{g}} \dfrac{di_{\mathrm{g}}}{dt} + u_T, \\ u_{\mathrm{g}M} = \omega_{\mathrm{g}} L_{\mathrm{g}} i_{\mathrm{g}} + L_{\mathrm{g}} i_{\mathrm{g}} \dfrac{d\theta_{\mathrm{C}}}{dt} + u_M, \end{cases} \tag{2}$$

where $u_{\mathrm{g}T}$ and $u_{\mathrm{g}M}$ are the voltages in T and M axes, u_T and u_M are the output voltages of GSC in T and M axes, and R_g and L_g are the resistance and inductor.

According to **Figure 2**, θ_{C} just represents the power factor angle φ in the *TMo* coordinate system. The response to external power signals can be realized quickly by controlling the amplitude of the grid current i_{g}, and the angle φ. **Eq. 2** also shows that the differential items of i_{g} and θ_{C} only exist in $u_{\mathrm{g}T}$ and $u_{\mathrm{g}M}$, respectively. It means that the control of i_{g} and θ_{C} can be achieved by $u_{\mathrm{g}T}$ and $u_{\mathrm{g}M}$ individually.

2.3 Modeling of PMSM

Another synchronous rotating coordinate system DQo shown in **Figure 3** is established to control PMSM, where DQ axes are the

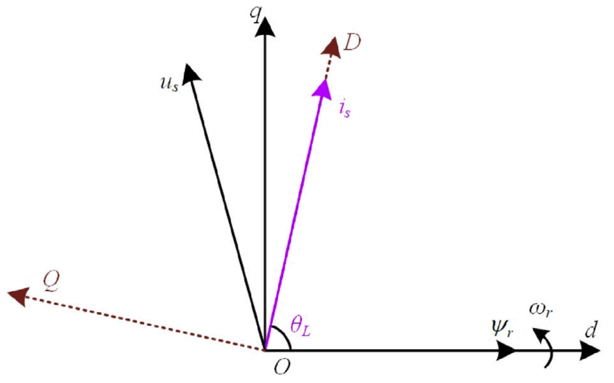

FIGURE 3 | Space vector model of the machine-side converter under the current vector orientation coordinate system.

real and imaginary axes individually. The stator current i_s overlapped with the D-axis. θ_L is the included angle between D and d axes. u_s is the stator voltage, and ψ_r is the permanent magnet flux linkage of PMSM.

Based on the DQo coordinate system, the electromagnetic torque of PMSM is rewritten as follows:

$$T_e = \frac{3}{2} n_p i_s \sin\theta_L \psi_r, \tag{3}$$

where T_e is the electromagnetic torque, n_p is the number of pole pairs, i_s is the amplitude of the stator current, and θ_L is the torque angle.

The rotation equation of PMSM can be written as follows:

$$J\frac{d\omega_r}{dt} = T_e - T_L, \tag{4}$$

where J is the moment of inertia.

In DQo, the control framework of surface-mounted PMSM with i_s and θ_L as the state variables can be expressed as follows (Yu et al., 2018a):

$$\begin{cases} u_{sD} = R_s i_s + L_s \dfrac{di_s}{dt} + n_p \psi_r \omega_r \sin\theta_L, \\ u_{sQ} = L_s i_s \dfrac{d\theta_L}{dt} + n_p \psi_r \omega_r \cos\theta_L + n_p \omega_r L_s i_s, \end{cases} \tag{5}$$

where u_{sD} and u_{sQ} are the stator voltages in the D and Q axes, and R_s and L_s are the resistance and inductor.

Eq. 5 shows that the differential items of i_s and θ_L only exist in u_{sD} and u_{sQ}, respectively. Similarly, with the modeling of GSC, the control of i_s and θ_L can be achieved by u_{sD} and u_{sQ}, respectively. The control framework established in this research can realize the control effect similar to the direct torque control that rapidly improves the response speed.

According to the motor convention, the dynamic equation of the DC-link capacitor is written as follows:

$$C\frac{du_{dc}}{dt} = \frac{P_s}{u_{dc}} - \frac{P_g}{u_{dc}}, \tag{6}$$

where P_g and P_s are the current flowing in and out of the DC-link capacitor respectively, and u_{dc} is the DC-side voltage.

3 COORDINATED CONTROL SCHEME BASED ON BACKSTEPPING CONTROL

The control targets are determined as the following: 1) for GSC, it should regulate the grid current i_g and the angle θ_C to track active and reactive powers from the grid. An indirect current control method employed in the research means that the tracked power signals need to be converted into the expression of i_g and θ_C. 2) For MSC, it should coordinate with the output of GSC and accomplish two jobs. First, the capacitor voltage u_{dc} on the DC side could be stabilized by adjusting the stator current i_s to keep the power of MSC equal to the power of GSC. This objective differs obviously from the power control under the usual voltage vector orientation that stabilizes the DC-link voltage by GSC. Second, based on the determined stator current amplitude, the energy from the grid side can be stored as much as possible when the control torque angle θ_L is π/2, so the angle reference θ_{Lref} is selected as π/2.

3.1 Design of the Grid-Side Converter Controller

It is assumed that active power and reactive power outputted by GSC are P and Q, respectively. They can be expressed as follows:

$$\begin{cases} P = u_{gM} \cdot i_{gM} + u_{gT} \cdot i_{gT} = u_{gT} \cdot i_{gT} \\ \quad = u_{gT} \cdot i_g = u_g \cos\varphi \cdot i_g, \\ Q = u_{gT} \cdot i_{gM} - u_{gM} \cdot i_{gT} = -u_{gM} \cdot i_{gT} \\ \quad = -u_{gM} \cdot i_g = -u_g \sin\varphi \cdot i_g. \end{cases} \tag{7}$$

If the references of active power and reactive power are P_{ref} and Q_{ref}, the references of the grid current i_{gref} and power factor angle θ_{Cref} can be calculated as follows:

$$\begin{cases} i_{gref} = \sqrt{P_{ref}^2 + Q_{ref}^2} \Big/ u_g, \\ \theta_{Cref} = \arctan\left(-Q_{ref}/P_{ref}\right). \end{cases} \tag{8}$$

e_{ig} is defined as the tracking error of i_g, which means $e_{ig} = i_{gref} - i_g$. Based on BC, the derivative of e_{ig} is calculated as follows:

$$\begin{aligned} \dot{e}_{ig} &= \dot{i}_{gref} - \dot{i}_g \\ &= \dot{i}_{gref} - \frac{1}{L_g}\left(u_g \cos\theta_C - R_g i_g - u_T\right). \end{aligned} \tag{9}$$

The first actual control variable u_T is designed as follows:

$$u_T = u_g \cos\theta_C - R_g i_g - L_g k_{ig} e_{ig} - L_g \dot{i}_{gref}, \tag{10}$$

where k_{ig} is a positive control gain and will be determined in the following section.

Substituting **Eq. 10** into **Eq. 9**, we obtain the following:

$$\dot{e}_{ig} = -k_{ig} e_{ig}. \tag{11}$$

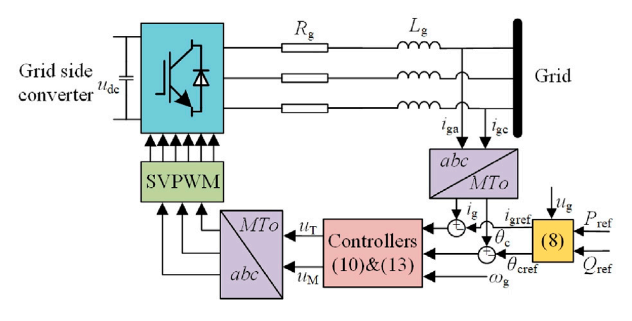

FIGURE 4 | Control diagram block of the grid-side converter.

$e_{\theta c}$ is defined as the tracking error of θ_C, which means $e_{\theta c} = \theta_{Cref} - \theta_C$. The derivative of $e_{\theta c}$ is calculated as follows:

$$\begin{aligned}\dot{e}_{\theta c} &= \dot{\theta}_{Cref} - \dot{\theta}_C \\ &= \dot{\theta}_{Cref} - \frac{1}{L_g i_g}\Big(- u_g \sin\theta_C - \omega_g L_g i_g - u_M\Big).\end{aligned} \tag{12}$$

The second actual control variable u_M is designed as follows:

$$u_M = -u_g \sin\theta_C - \omega_g L_g i_g - L_g i_g k_{\theta c} e_{\theta c} - L_g i_g \dot{\theta}_{Cref}, \tag{13}$$

where $k_{\theta c}$ is a positive control gain of the power factor angle and will also be determined in the following section.

Substituting **Eq. 13** into **Eq. 12**, we obtain the following:

$$\dot{e}_{\theta c} = -k_{\theta c} e_{\theta c}. \tag{14}$$

For e_{ig} and $e_{\theta c}$, a Lyapunov function V_1 is selected as

$$V_1 = \frac{1}{2}e_{ig}^2 + \frac{1}{2}e_{\theta c}^2. \tag{15}$$

The derivative of V_1 is calculated as follows:

$$\dot{V}_1 = e_{ig}\dot{e}_{ig} + e_{\theta c}\dot{e}_{\theta c} = -k_{ig}e_{ig}^2 - k_{\theta c}e_{\theta c}^2 \le 0. \tag{16}$$

Due to V_1 being bounded and k_{ig} and $k_{\theta c}$ being larger than zero, according to the Barbalat theorem, $\lim_{t\to\infty} V_1(t) = 0$ can be obtained. Therefore, the closed-loop system is asymptotically stable.

Eqs 10, **13** give the controllers of the grid current and the power factor angle in GSC. The control block diagram of GSC can be drawn in **Figure 4**, where u_{dc} can be regarded as an equivalent DC voltage source, and the power factor angle can be obtained through active power and reactive power.

3.2 Design of the PMSM-Side Converter Controller

According to **Eq. 6**, the square of DC voltage is chosen as the control variable in order to make the expression simplified, which can be referred as u_2.

$$\frac{du_2}{dt} = \frac{2}{C}\Big(i_g u_T - i_s u_{sD}\Big). \tag{17}$$

e_u is defined as the tracking error of u_2, which means that $e_u = u_{2ref} - u_2$; the derivative of e_u is calculated as follows:

$$\begin{aligned}\dot{e}_u &= \dot{u}_{2ref} - \dot{u}_2 \\ &= \dot{u}_{2ref} - \frac{2}{C}\Big(i_g u_T - i_s u_{sD}\Big).\end{aligned} \tag{18}$$

In accordance with **Eq. 18**, the first actual control variable u_{sD} is designed as follows:

$$u_{sD} = -\frac{C}{2i_s}k_u e_u - \frac{C}{2i_s}\dot{u}_{2ref} + \frac{i_g u_T}{i_s}, \tag{19}$$

where k_u is a positive control gain and will be chosen in the following section.

Substituting **Eq. 19** into **Eq. 18**, we obtain the following:

$$\dot{e}_u = -k_u e_u. \tag{20}$$

$e_{\theta l}$ is defined as the tracking error of θ_L, which means that $e_{\theta l} = \theta_{Lref} - \theta_L$; the derivative of $e_{\theta l}$ is calculated as follows:

$$\begin{aligned}\dot{e}_{\theta l} &= \dot{\theta}_{Lref} - \dot{\theta}_L \\ &= \dot{\theta}_{Lref} + \frac{1}{L_s i_s}\Big(u_{sQ} + n_p\psi_r\omega_r\cos\theta_L + n_p\omega_r L_s i_s\Big).\end{aligned} \tag{21}$$

In accordance with **Eq. 21**, the second actual control variable u_{sD} is designed as follows:

$$u_{sQ} = -n_p\psi_r\omega_r\cos\theta_L - L_s i_s\Big(n_p\omega_r + \dot{\theta}_{Lref} + k_{\theta l}e_{\theta l}\Big), \tag{22}$$

where $k_{\theta l}$ is a positive control gain and will be chosen in the following section.

Substituting **Eq. 22** into **Eq. 21**, we obtain the following:

$$\dot{e}_{\theta l} = -k_{\theta l}e_{\theta l}. \tag{23}$$

For e_u and $e_{\theta l}$, the selection of a Lyapunov function V_2 could be written as follows:

$$V_2 = \frac{1}{2}e_u^2 + \frac{1}{2}e_{\theta l}^2. \tag{24}$$

The derivative of V_2 is calculated as follows:

$$\begin{aligned}\dot{V}_2 &= e_u\dot{e}_u + e_{\theta l}\dot{e}_{\theta l} \\ &= -k_u e_u^2 - k_{\theta l}e_{\theta l}^2 \le 0.\end{aligned} \tag{25}$$

Because V_2 is bounded and e_u and $e_{\theta l}$ values are larger than zero, according to the Barbalat theorem, $\lim_{t\to\infty} V_2(t) = 0$ can be obtained. Hence, the closed-loop system is asymptotically stable.

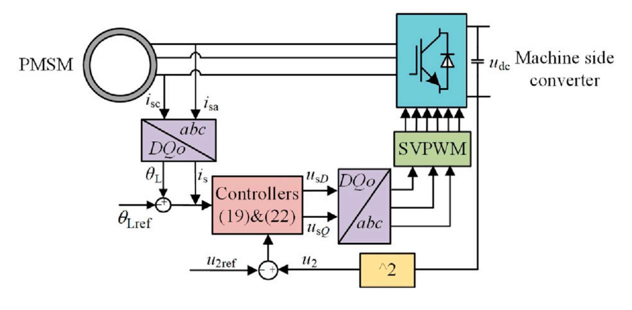

FIGURE 5 | Control diagram block of the machine-side converter.

The DC-side voltage controller shown in **Eq. 19** and the torque angle controller shown in **Eq. 22** are completed based on BC. Thus, the control block diagram of MSC proposed in the research can be drawn in **Figure 5**.

4 CONTROL PARAMETER ANALYSIS

4.1 Analysis of System Performance

By substituting the controller designed by BC into the original differential equation of the system, the following error functions can be obtained:

$$\dot{\boldsymbol{e}}_X = -\boldsymbol{K}\boldsymbol{e}_X, \tag{26}$$

where $\boldsymbol{e}_X$ is the error matrix, and $\boldsymbol{K}$ is the gain matrix, $\boldsymbol{e}_X = [\, e_{\mathrm{ig}} \quad e_{\mathrm{\theta c}} \quad e_{\mathrm{u}} \quad e_{\mathrm{\theta l}} \,]^T$, and $\boldsymbol{K} = diag[k_{\mathrm{ig}}\, k_{\mathrm{\theta c}}\, k_{\mathrm{u}}\, k_{\mathrm{\theta l}}]$.

In terms of **Eq. 26**, the following equation can be obtained:

$$\begin{bmatrix} \dot{i}_{\mathrm{g}} \\ \dot{\theta}_{\mathrm{C}} \\ \dot{u}_2 \\ \dot{\theta}_{\mathrm{L}} \end{bmatrix} = -\begin{bmatrix} k_{\mathrm{ig}} i_{\mathrm{g}} \\ k_{\mathrm{\theta c}} \theta_{\mathrm{C}} \\ k_{\mathrm{u}} u_2 \\ k_{\mathrm{\theta l}} \theta_{\mathrm{L}} \end{bmatrix} + \begin{bmatrix} k_{\mathrm{ig}} i_{\mathrm{gref}} \\ k_{\mathrm{\theta c}} \theta_{\mathrm{Cref}} \\ k_{\mathrm{u}} u_{\mathrm{2ref}} \\ k_{\mathrm{\theta l}} \theta_{\mathrm{Lref}} \end{bmatrix} + \begin{bmatrix} \dot{i}_{\mathrm{gref}} \\ \dot{\theta}_{\mathrm{Cref}} \\ \dot{u}_{\mathrm{2ref}} \\ \dot{\theta}_{\mathrm{Lref}} \end{bmatrix}. \tag{27}$$

If θ_{Lref} could be controlled in π/2 and i_{gref} and θ_{Cref} will not change when power signals remain the same, then, $\dot{\theta}_{\mathrm{Lref}}$, $\dot{i}_{\mathrm{gref}}$, and $\dot{\theta}_{\mathrm{Cref}}$ are all zero. Eq. 27 can be rewritten as follows:

$$\begin{bmatrix} \dot{i}_g \\ \dot{\theta}_C \\ \dot{u}_{dc} \\ \dot{\theta}_L \end{bmatrix} = -\begin{bmatrix} k_{ig} & & & \\ & k_{\theta c} & & \\ & & k_u & \\ & & & k_{\theta l} \end{bmatrix} \begin{bmatrix} i_g \\ \theta_C \\ u_2 \\ \theta_L \end{bmatrix} + \begin{bmatrix} k_{ig} & & & \\ & k_{\theta c} & & \\ & & k_u & \\ & & & k_{\theta l} \end{bmatrix} \times \begin{bmatrix} i_{gref} \\ \theta_{Cref} \\ u_{2ref} \\ \theta_{Lref} \end{bmatrix}. \tag{28}$$

Eq. 28 can be expressed as $\dot{\boldsymbol{X}} = \boldsymbol{AX} + \boldsymbol{BU}$, then

$$\boldsymbol{X}(s) = (s\boldsymbol{I} - \boldsymbol{A})^{-1}\boldsymbol{BU}(s). \tag{29}$$

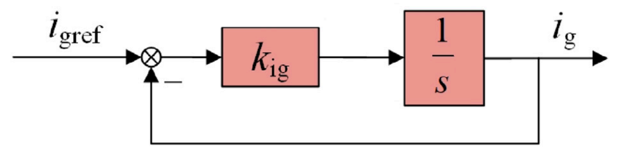

FIGURE 6 | Signal flow diagram of the grid current controller.

Supposing $\boldsymbol{G}(s) = (s\boldsymbol{I} - \boldsymbol{A})^{-1}\boldsymbol{B}$, (29) can be simplified as follows:

$$\boldsymbol{X}(s) = \boldsymbol{G}(s)\boldsymbol{U}(s). \tag{30}$$

$\boldsymbol{G}(s)$ is the system transfer function matrix, which can be calculated in **Eq. 31**. It indicates that the step responses of the grid current, power factor angle, and torque angle are all first-order, and the step response of the DC-link voltage is second-order. Meanwhile, the output of the stator current is relevant to the grid current and DC-link voltage. Then, the various control gains will be analyzed.

$$\begin{aligned} \boldsymbol{G}(s) &= (s\boldsymbol{I} - \boldsymbol{A})^{-1}\boldsymbol{B} \\ &= \begin{bmatrix} s + k_{\mathrm{ig}} & & & \\ & s + k_{\mathrm{\theta c}} & & \\ & & s + k_{\mathrm{u}} & \\ & & & s + k_{\mathrm{\theta l}} \end{bmatrix}^{-1} \begin{bmatrix} k_{\mathrm{ig}} & & & \\ & k_{\mathrm{\theta c}} & & \\ & & k_{\mathrm{u}} & \\ & & & k_{\mathrm{\theta l}} \end{bmatrix} \\ &= \begin{bmatrix} \frac{k_{\mathrm{ig}}}{s + k_{\mathrm{ig}}} & & & \\ & \frac{k_{\mathrm{\theta c}}}{s + k_{\mathrm{\theta c}}} & & \\ & & \frac{k_{\mathrm{u}}}{s + k_{\mathrm{u}}} & \\ & & & \frac{k_{\mathrm{\theta l}}}{s + k_{\mathrm{\theta l}}} \end{bmatrix}. \end{aligned} \tag{31}$$

TABLE 1 | Simulation parameters.

	Parameter	Value
Parameters of spring	Spring modulus of elasticity E (N/m^2)	2×10^{11}
	Spring width b (m)	0.05
	Spring thickness h (m)	0.0018
	Spring length L (m)	14.639
Parameters of PMSM	Moment of inertia J (kg·m^2)	0.51
	Permanent magnet flux linkage ψ_r (Wb)	0.38
	R_s (Ω)	2.875
	L_s (H)	0.033
	n_p	10
Parameters of the converter and grid	R_g (Ω)	0.106
	L_g (H)	0.01
	Grid frequency f (Hz)	50
	C (mF)	1
	DC voltage(V)	400
	Grid voltage(V)	380

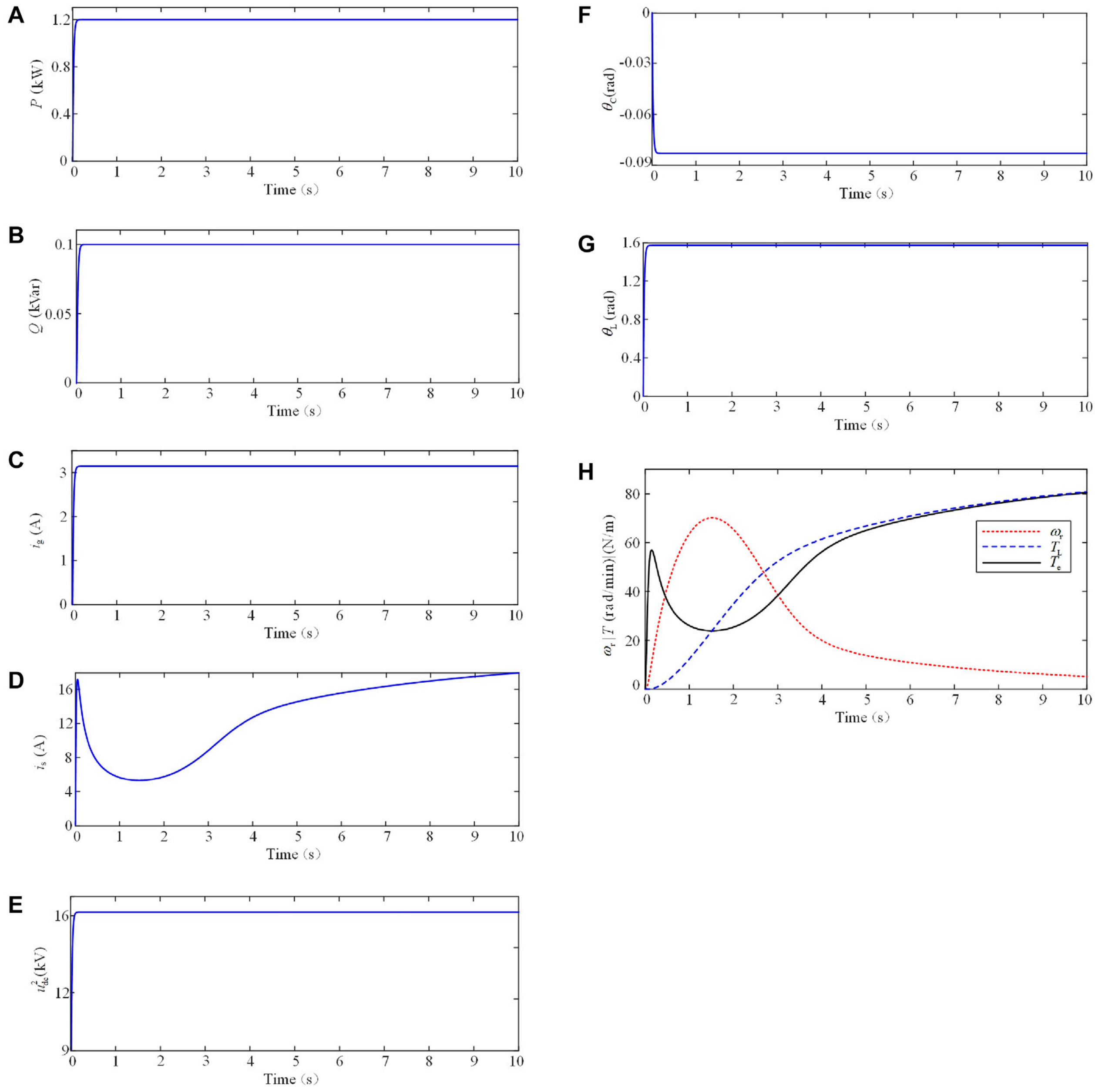

FIGURE 7 | Demonstration of steady control performance. **(A)** Active power. **(B)** Reactive power. **(C)** Grid current. **(D)** Stator current. **(E)** Square of the DC-side voltage. **(F)** Power factor angle. **(G)** Torque angle. **(H)** Rotating speed and torque of PMSM.

4.2 Selection of Control Parameters

First, the grid current, power factor angle, and torque angle are all classical first-order systems. The control gain of the grid current is determined and taken as an instance.

Based on **Eqs 9**, **11**, the signal flow diagram of the grid current controller can be shown in **Figure 6**.

According to the signal flow diagram, the transfer function of the grid current can be calculated as follows:

$$\mathbf{G}_{\mathrm{ig}}(s) = \frac{1}{\frac{s}{k_{\mathrm{ig}}} + 1}. \tag{32}$$

For a first-order inertia system, its time constant is $T_{\mathrm{ig}} = 1/k_{\mathrm{ig}}$. If the response curve reaches 95% of the steady-state value, the adjustment process could be considered completed, and the time required to reach the response value will be $3T_{\mathrm{ig}}$. If the adjustment time of the active power is set to 0.06 s, we can determine $T_{\mathrm{ig}} = 0.02$s. It means that the control gain k_{ig} can be chosen as

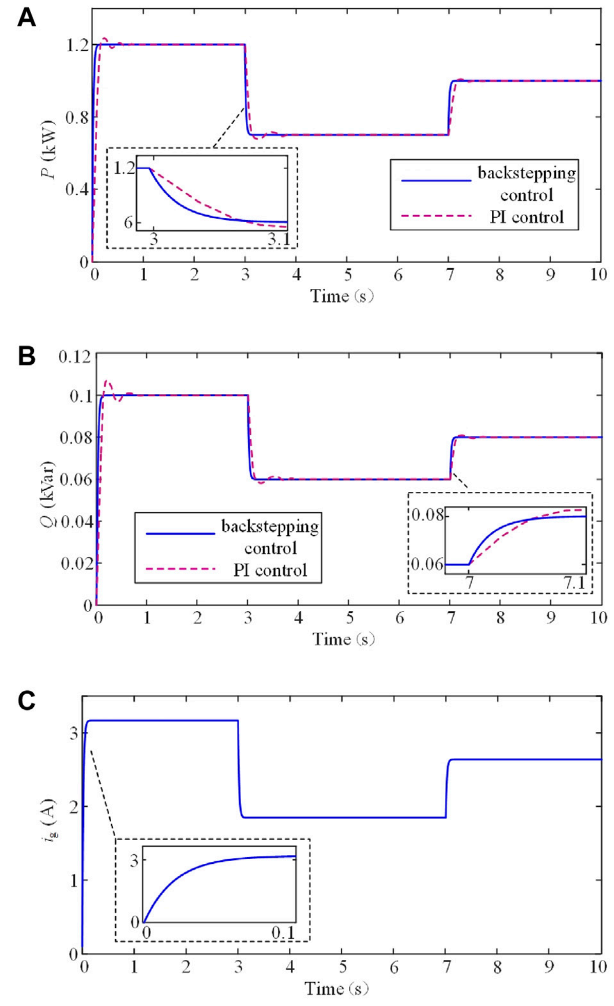

FIGURE 8 | Demonstration of dynamic control performance. **(A)** Active power. **(B)** Reactive power. **(C)** Grid current.

50. The selection of the control parameters in reactive power control is similar to this and will not be described repeatedly.

5 SIMULATION AND EXPERIMENTAL ANALYSIS

5.1 Simulation Analysis

To verify the effectiveness of the proposed power coordinated control scheme for the SSES system, three groups of simulations are carried out on MATLAB software. The solver used in simulation is the Runge–Kutta algorithm, and the time step is 0.1 ms. The controller performance is observed through the tracking effects of active power and reactive power, and the stability of the system is investigated by the grid current amplitude, stator current amplitude, power factor angle, torque angle, and DC-link voltage. The simulation parameters

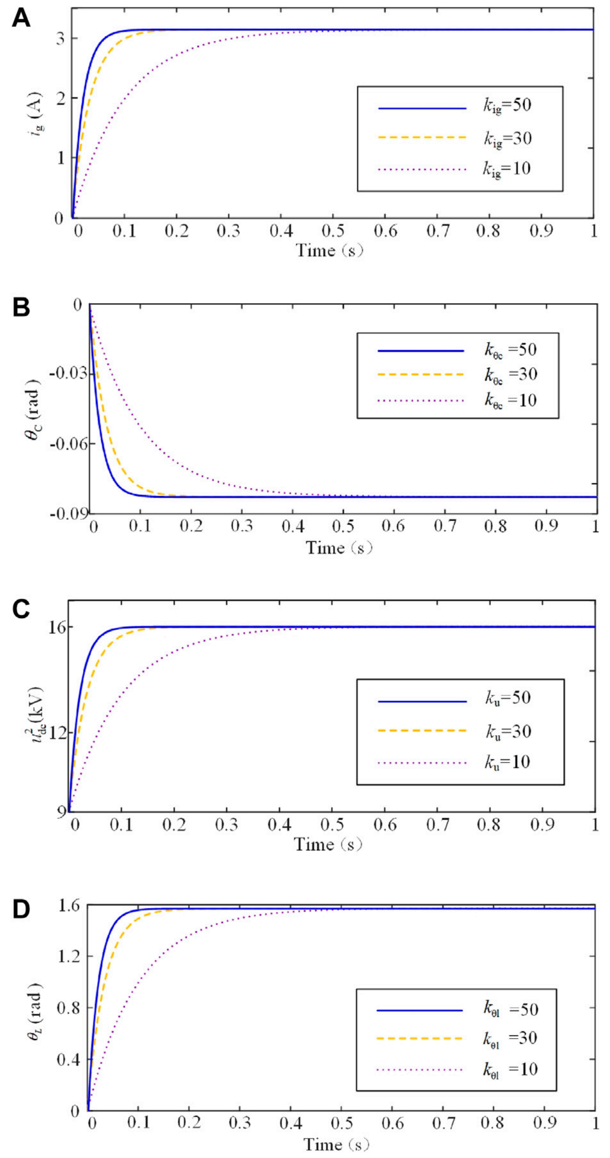

FIGURE 9 | Control gain comparison in a first-order system. **(A)** Grid current. **(B)** Power factor angle. **(C)** Square of the DC-side voltage. **(D)** Torque angle.

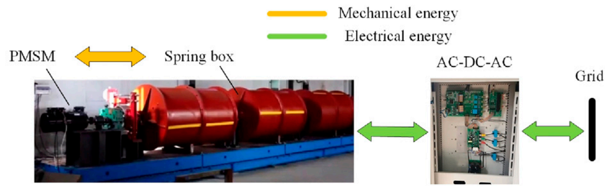

FIGURE 10 | Hardware setup.

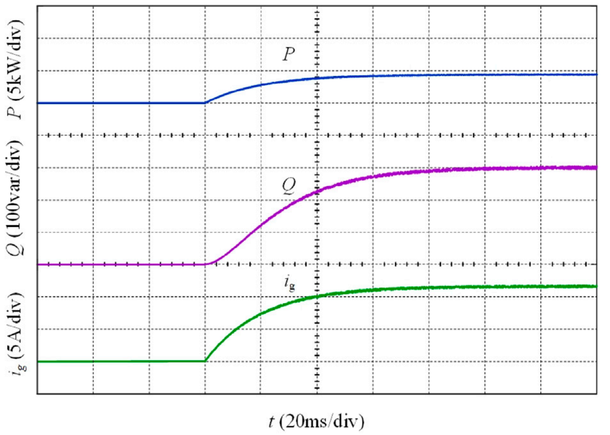

FIGURE 11 | Experimental result.

are given in **Table 1**, and the control gains determined by the method described in **Section 4** are $k_{ig} = 50$, $k_{\theta c} = 50$, $k_u = 50$, and $k_{\theta l} = 50$.

5.1.1 Simulation for Steady Operation

The simulation for an entire cycle of energy storage lasts for 10 s. The active power signal is 4.5 kW, while the reactive power signal is 0.3 kVar.

The simulation results of the steady operation are shown in **Figure 7** and indicate that the SSES system can accurately track the power signals in a short time. The grid current amplitude, power factor angle, torque angle, and DC-link voltage can all reach their stable states within the given time. **Figure 7H** shows that the speed of PMSM increases first with the sudden increase in the electromagnetic torque T_e. When the load torque T_L increases similarly to the electromagnetic torque T_e, the speed of PMSM will begin to decrease. If the speed reduces to zero, the energy stored in the spiral spring will be terminated.

5.1.2 Simulation for Dynamic Operation

To test the dynamic tracking performance of the controller, the proposed backstepping control is compared with the PI control, and it is assumed that the active power and reactive power signal changes start at 4.5 kW and 0.3 kVar, respectively. Then, after 3 s, the active power signal and reactive power signals change to 2 kW and 0.15 kVar, respectively. Finally, at 7 s, the active power signal becomes 5 kW, and the reactive power signal turns into 0.4 kVar. The simulation results are displayed in **Figure 8**. **Figures 8A,B** demonstrate that the active and reactive power with the proposed controller can track their power references faster than the PI control and without oscillation. Even when the power signals change, active power and reactive power regulated by the proposed controller experience almost no power oscillation. The amplitude of the grid current shown in **Figure 8C** also adjusts and enters the steady-state quickly. It indicates that the coordinated control has a good tracking performance. Additionally, by observing the grid current, it can be found that the current can reach stability within the given time of 0.06s, which verifies the correctness of the control parameter's determination approach in **Section 4**.

5.1.3 Comparison of the Control Parameters

To further check the correctness and superiority of the control parameters determined by the control performance, three groups of simulations are conducted for each control parameter. **Figure 9** demonstrates that the time for the system to enter into the steady-state reduces along with the increase in the control parameter in the first-order system.

5.2 Hardware experiment

To further verify the control algorithm proposed in the research, the experimental platform shown in **Figure 10** is set up, and the hardware experiment is carried out. The system parameters are consistent with the simulation.

The control signals for active power and reactive power are 4.5 kW and 0.3 kVar, respectively. The experimental results are displayed in **Figure 11**. It can be seen that both active power and reactive power can reach the steady-state within the designated time of 0.06 s and are well consistent with the simulation results.

In summary, both the simulation and experimental results show that the proposed power coordinated control scenario and control parameter's determination approach for the SSES system based on BC is feasible and effective, which can ensure that the SSES system responds to the power signal of the grid accurately and quickly. Ultimately, the conversion between mechanical energy and electrical energy can be realized well.

6 CONCLUSION

The power coordinated control scheme and corresponding control parameter's determination method are devised for the spiral spring energy storage system based on backstepping control under current vector orientation. Both the simulation and hardware experiments verify the correctness and effectiveness of the proposed control scheme. The conclusions are drawn as follows:

1) The proposed power control scheme can coordinate the grid-side converter with the machine-side converter of the spiral spring energy storage system to regulate the power signal accurately and rapidly.
2) The designed backstepping control under current vector orientation improves static-state and dynamic control performance and simplifies the control difficulty.
3) The determined control parameters improve the control performance effectively.

DATA AVAILABILITY STATEMENT

The original contributions presented in the study are included in the article/Supplementary Material; further inquiries can be directed to the corresponding author.

AUTHOR CONTRIBUTIONS

YY: Methodology, conception, writing—review and editing, and project administration. MW: software, writing, and formal analysis. RZ: software and data analysis. ZM: conduction and supervision. XZ: validation.

FUNDING

This work was supported in part by the National Natural Science Foundation of China under the Grant No. 52077078 and in part by the Natural Science Foundation of Hebei Province in China under Grant E2019502163.

REFERENCES

Achlerkar, P. D., and Panigrahi, B. K. (2020). Robust Backstepping Output Voltage Controller for Standalone Voltage-sourced Converters. *IET Renew. Power Gener.* 14 (12), 2211–2220. doi:10.1049/iet-rpg.2020.0023

Ali, Z. H., Zhao, J., Manla, E., Ma, J., and Song, W. (2017). "Novel Direct Power Control of Single-phase Three-Level SVPWM Inverter for Photovoltaic Generation," in 2017 IEEE Power & Energy Society Innovative Smart Grid Technologies Conference (ISGT), 1–5. doi:10.1109/ISGT.2017.8085959

Bo, F., Bowen, D., Ning, G., and Weiwei, Z. (2017). Double PWM Coordinated Control Based on Energy Mathematic Model. *Chin. Autom. Congr. (CAC)* 2017, 4301–4306. doi:10.1109/CAC.2017.8243536

Caballero, D. F., Guijosa, J. M. M., and de la Cruz, V. R. (2018). Generalized Spiral Torsion Spring Energetic Model. *Arch. Appl. Mech.* 88 (6), 999–1008. doi:10.1007/s00419-018-1354-1

Delavari, H., and Naderian, S. (2019). Backstepping Fractional Sliding Mode Voltage Control of an Islanded Microgrid. *IET Gener. Transm. & Distrib.* 13 (12), 2464–2473. doi:10.1049/iet-gtd.2018.5909

Ghaemi, E., and Mirsalim, M. (2017). Design and Prototyping of a New Flywheel Energy Storage System. *IET Electr. Power Appl.* 11 (9), 1517–1526. doi:10.1049/iet-epa.2017.0074

Gonzalez-Gonzalez, J. M., Martin, S., Lopez, P., and Aguado, J. A. (2020). Hybrid Battery-ultracapacitor Storage System Sizing for Renewable Energy Network Integration. *IET Renew. Power Gener.* 14 (13), 2367–2375. doi:10.1049/iet-rpg.2019.1310

Gui, Y., Kim, C., Chung, C. C., Guerrero, J. M., Guan, Y., and Vasquez, J. C. (2018). Improved Direct Power Control for Grid-Connected Voltage Source Converters. *IEEE Trans. Ind. Electron.* 65 (10), 8041–8051. doi:10.1109/TIE.2018.2801835

Gui, Y., Wang, X., and Blaabjerg, F. (2019). Vector Current Control Derived from Direct Power Control for Grid-Connected Inverters. *IEEE Trans. Power Electron.* 34 (9), 9224–9235. doi:10.1109/TPEL.2018.2883507

Jeon, B.-J., Seo, M.-G., Shin, H.-S., and Tsourdos, A. (2020). Understandings of Classical and Incremental Backstepping Controllers with Model Uncertainties. *IEEE Trans. Aerosp. Electron. Syst.* 56 (4), 2628–2641. doi:10.1109/TAES.2019.2952631

Kim, S. K. (2018). Robust Output Voltage Tracking Algorithm for Three-phase Rectifier with Variable Sliding Surface. *IET Power Electron.* 11 (6), 1119–1127. doi:10.1049/iet-pel.2017.0866

Kumar, S., Saket, R. K., Dheer, D. K., Holm-Nielsen, J. B., and Sanjeevikumar, P. (2020). Reliability Enhancement of Electrical Power System Including Impacts of Renewable Energy Sources: a Comprehensive Review. *IET Gener. Transm. & Distrib.* 14 (10), 1799–1815. doi:10.1049/iet-gtd.2019.1402

Kwak, B., Um, J.-H., and Seok, J.-K. (2019). Direct Active and Reactive Power Control of Three-phase Inverter for AC Motor Drives with Small Dc-Link Capacitors Fed by Single-phase Diode Rectifier. *IEEE Trans. Ind. Appl.* 55 (4), 3842–3850. doi:10.1109/TIA.2019.2915061

Li, J., Guo, Y.-N., Zhang, L.-H., and Shi, W.-T. (2018). "Coordinated Passivity Control of Permanent Magnet Synchronous Generator Based on Dual PWM Converter," in 2018 IEEE International Conference on Industrial Electronics for Sustainable Energy Systems (IESES), 94–99. doi:10.1109/IESES.2018.8349856

Li, L., Xiao, J., Zhao, Y., Liu, K., Peng, X., Luan, H., et al. (2020). Robust Position Anti-interference Control for PMSM Servo System with Uncertain Disturbance. *Trans. Electr. Mach. Syst.* 4 (2), 151–160. doi:10.30941/CESTEMS.2020.00020

Liu, Y., Cheng, S., Ning, B., and Li, Y. (2019). Performance Enhancement Using Durational Model Predictive Control Combined with Backstepping Control and Disturbance Observer for Electrical Drives. *J. Vib. Control* 25 (4), 946–959. doi:10.1177/1077546318807018

Lu, P., van Kampen, E.-J., and Chu, Q. P. (2015). "Robustness and Tuning of Incremental Backstepping Approach," in AIAA Guidance, Navigation, and Control Conference, Kissimmee, USA (Kissimmee, FL: AIAA), 2780–2794. doi:10.2514/6.2015-1762

Mallik, A., Ding, W., Shi, C., and Khaligh, A. (2017). Input Voltage Sensorless Duty Compensation Control for a Three-phase Boost PFC Converter. *IEEE Trans. Ind. Appl.* 53 (2), 1527–1537. doi:10.1109/TIA.2016.2626247

Tian, Y., Chen, Z., Deng, F., Sun, X., and Hu, Y. (2014). "Coodinative Control of Active Power and DC-link Voltage for Cascaded Dual-Active-Bridge and Inverter in Bidirectional Applications," in 2014 IEEE Energy Conversion Congress and Exposition (ECCE), 2249–2256. doi:10.1109/ECCE.2014.6953703

Wai, R.-J., Yang, Y., and Wang, Y.-Q. (2018). "Design of Backstepping Control for Direct Power Control of Three-phase PWM Rectifier," in 2018 3rd International Conference on Intelligent Green Building and Smart Grid (IGBSG), 1–4. doi:10.1109/IGBSG.2018.8393555

Xiong, P., and Sun, D. (2016). Backstepping-based DPC Strategy of a Wind Turbine-Driven DFIG under Normal and Harmonic Grid Voltage. *IEEE Trans. Power Electron.* 31 (6), 4216–4225. doi:10.1109/TPEL.2015.2477442

Yang, T., Cai, Z., and Xun, Q. (2020). Adaptive Backstepping-Based H${_{\infty}}$ Robust Controller for Photovoltaic Grid- Connected Inverter. *IEEE Access* 8, 17263–17272. doi:10.1109/ACCESS.2019.2962280

Ye, S., Zhou, D., Yao, X., and Blaabjerg, F. (2021). Component-level Reliability Assessment of a Direct-Drive PMSG Wind Power Converter Considering Two Terms of Thermal Cycles and the Parameter Sensitivity Analysis. *IEEE Trans. Power Electron.* 36 (9), 10037–10050. doi:10.1109/TPEL.2021.3064363

Yu, Y., Chang, D., Zheng, X., Mi, Z., Li, X., and Sun, C. (2018). A Stator Current Oriented Closed-Loop $I\text{--} F$ Control of Sensorless SPMSM with Fully Unknown Parameters for Reverse Rotation Prevention. *IEEE Trans. Power Electron.* 33 (10), 8607–8622. doi:10.1109/TPEL.2017.2780191

Yu, Y., Cong, L., Tian, X., Mi, Z., Li, Y., Fan, Z., et al. (2020). A Stator Current Vector Orientation Based Multi-Objective Integrative Suppressions of Flexible Load Vibration and Torque Ripple for PMSM Considering Electrical Loss. *Trans. Electr. Mach. Syst.* 4 (3), 161–171. doi:10.30941/CESTEMS.2020.00021

Yu, Y., Mi, Z., Guo, X., Xu, Y., and Zhao, T. (2016). Low Speed Control and Implementation of Permanent Magnet Synchronous Motor for Mechanical Elastic Energy Storage Device with Simultaneous Variations of Inertia and Torque. *IET Electr. Power Appl.* 10 (3), 172–180. doi:10.1049/iet-epa.2015.0159

Yu, Y., Mi, Z., Mi, Z., Guo, X., Zheng, X. X., and Sun, C. (2018). Control Design and Implementation of a Spiral Spring Energy Storage System Connected to a Grid via PMSG. *Csee Jpes* 4 (3), 339–351. doi:10.17775/CSEEJPES.2016.00860

Zhang, S. Q., and Zhu, Y. Q. (2018). Pumped-storage Power Generation System Based on Wave Energy. *J. Eng.* 2017 (13), 2334–2338. doi:10.1049/joe.2017.0748

Zhang, Y., Peng, Y., and Qu, C. (2015). "Comparative Study of Model Predictive Control and Direct Power Control for PWM Rectifiers with Active Power Ripple Minimization," in 2015 IEEE Energy Conversion Congress and Exposition (ECCE), 3823–3830. doi:10.1109/ECCE.2015.7310200

Zhang, Y., and Qu, C. (2015). Table-Based Direct Power Control for Three-phase AC/DC Converters under Unbalanced Grid Voltages. *IEEE Trans. Power Electron.* 30 (12), 7090–7099. doi:10.1109/TPEL.2014.2387694

Conflict of Interest: The authors declare that the research was conducted in the absence of any commercial or financial relationships that could be construed as a potential conflict of interest.

frontiers | Frontiers in Energy Research

METHODS
published: 14 July 2022
doi: 10.3389/fenrg.2022.943946

A Fast and Accurate Calculation Method of Line Breaking Power Flow Based on Taylor Expansion

Shuaihu Li, Xiang Zhao, Wenju Liang, Md Tanjid Hossain and Zhidan Zhang*

Changsha University of Science and Technology, Changsha, China

In order to quickly obtain the voltage value of each node after the power system line is disconnected, a fast and accurate calculation method of breaking voltage based on Taylor series expansion is proposed in this study, which can calculate the value of nodal voltage of the system in a short time. At first, a breaking parameter is introduced into the admittance of the disconnected line, and a nonlinear disconnection function is constructed about the breaking parameter. After the line is disconnected, the voltage of each node and the admittance matrix of each node are functions of the relevant parameters, and then, the Taylor series is used to expand. The voltage of each node of the system before breaking is considered as the initial value of the Taylor series, and the first, second, and third derivatives of the node voltage with respect to the parameter are considered as the correction term; the voltage of each node of the system is calculated after the line is disconnected. Finally, the simulation results of the IEEE 14-node system are used to verify the correctness of the proposed method.

Keywords: power system, static safety analysis, breaking power flow, fast and accurate calculation, nonlinear breaking function

Edited by:
Tianguang Lu,
Shandong University, China

Reviewed by:
Gaurav Dhiman,
Government Bikram College of Commerce Patiala,(Punjab) India
Ning Li,
Xi'an University of Technology, China
Mao Tan,
Xiangtan University, China

****Correspondence:***
Shuaihu Li
lishuaihu2010@126.com

Specialty section:
This article was submitted to Smart Grids, a section of the journal Frontiers in Energy Research

Received: *14 May 2022*
Accepted: *07 June 2022*
Published: *14 July 2022*

Citation:
Li S, Zhao X, Liang W, Hossain MT and Zhang Z (2022) A Fast and Accurate Calculation Method of Line Breaking Power Flow Based on Taylor Expansion. Front. Energy Res. 10:943946. doi: 10.3389/fenrg.2022.943946

INTRODUCTION

As the scale of the power grid continues to expand, the probability of power grid failures also increases. In order to ensure the safe operation of the power grid and reduce the impact of power grid failures on the operation of power system, it is particularly important to find a method that can perform static security analysis online (Peyghami et al., 2020; Liu et al., 1109). N-1 safety check is one of the most common static safety assessment methods, which is designed to anticipate the aftermath of an accident, sort according to the voltage limit violation or transmission power overload degree. Therefore, the serious accident set can be found to provide help for follow-up preventive control, but its essence is the problem of breaking power flow calculation for the system (Lu et al., 2017; Dhiman and Kaur, 2019; Kaur et al., 2020; Chatterjee, 2021; Kumar and Dhiman, 2021).

The traditional power flow algorithms currently used in the N-1 safety verification of the power system are the DC power flow method (Shukla et al., 2022), compensation method (Fliscounakis et al., 2013), sensitivity method (Li et al., 2021) etc. Among them, the DC power flow method is a simple and fast static safety analysis method, but its calculation results contain large errors and can only calculate the active power flow of each branch after the line is disconnected. The nodal voltage amplitude and branch reactive power cannot be calculated. Generally, it is mostly used in the development planning of the long-term power system network. The PQ decomposition method for breaking line verification can give active power, estimation of reactive power flow, and voltage deviation. But in order for the accuracy of the calculation result to be acceptable, iteration must be performed. Otherwise, the calculation result, especially the error of voltage and reactive power flow, is too large. For example, Capitanescu et al. (2007) made full use of the sensitivity matrix obtained by the Newton method in the normal operation mode. The corresponding disconnection is simulated with the increment of the injected power node, which better solves the problem of disconnection calculation in power flow calculation. The key to the method in Vargas and Quintana (1990) is to find the nodal injection power increment after the simulated line is disconnected. In order to obtain the power increment caused by the disconnection, a multiplication operation of a 4×2 second-order matrix and a 2×4-second order matrix is required. Moreover, the elements also need to be calculated from state variables and power system network parameters, which affects the computational efficiency.

The abovementioned methods use the approximate breaking power flow algorithm to calculate the line breaking of the power system; using a linear calculation to solve nonlinear problems can improve the speed. However, there is still a large error in accuracy, and the calculation results can only be used to screen serious faults and the expected accident severity; so it is unavoidable to perform a secondary accurate calculation of severe failures, and there may also be shadowing, resulting in disordering of expected accidents. To address the aforementioned problems, Vargas and Quintana (1990) and Sachdev and Ibrahim (1974) proposed an accurate and fast power flow breaking algorithm. Its basic principle is a mathematical problem with the node voltage as a function and the open and disconnected branch admittance as a variable, and the Taylor series expansion is a very effective method to solve this kind of mathematical problem (Padiyar and Rao, 1996; Meng et al., 2006; Kaplunovich and Turitsyn, 2013; Zhou, 2015; Li et al., 2018). However, when the open branch is continuously removed, that is to say, when the open branch admittance is considered to be a linear function, there is a strong nonlinear relationship between the node voltage and the open branch admittance; the voltage Taylor series converges very slowly, and a higher order series is required to fit the nodal voltage function. Due to the strong nonlinearity of the node voltage and the admittance of the disconnected branch after the line is disconnected, the expression of the disconnection function is very complicated, and the Taylor series can expand the nonlinear function into a very simple power function for calculation, and the calculation error also decreases as the number of expansion increases (Li et al., 2018; Yun et al., 2019; England and Alouani, 2020; Duan et al., 2022).

To address the abovementioned defects in the existing power flow breaking algorithm, a fast and accurate breaking power flow calculation method is proposed in this study. The main contributions of this study are listed as follows:

1) A nonlinear breaking function is established by introducing a breaking parameter; therefore, the node voltage and the breaking branch admittance are both functions of the parameter. Then, the nonlinear function can be fitted by the Taylor series on the premise of the first, second, and third derivatives of the node voltage, so the node voltage of the power system can be expressed by the third-order Taylor series expansion of the admittance of the breaking branch.
2) The optimization selection method of the nonlinear breaking function is proposed to determine the optimal breaking coefficient. Therefore, the nonlinear breaking function can improve the linear relationship between the node voltage and the parameters of the breaking function. Meanwhile, the convergence speed and calculation accuracy of Taylor series are improved.
3) The proposed method can directly judge whether there is a breaking power flow under the expected accident, which makes sure to meet the online safety analysis requirements of the power system. The IEEE14 node system is taken as an example to conduct simulation calculations to verify the effectiveness and rapidity of the proposed method.

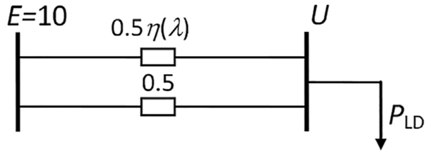

FIGURE 1 | Calculation principle of the breaking voltage of the branch of a simple DC circuit.

The remainder of this study is organized as follows. In **Section 2**, the mechanism of the fast and accurate calculation method is proposed. **Section 3** verifies the accuracy, effectiveness, and solution efficiency of the proposed methods through the IEEE14 node system. The conclusions are drawn in **Section 4**.

FAST AND ACCURATE CALCULATION METHOD OF THE NETWORK INTERRUPTION POWER FLOW

Basic Principle of the Network Branch Breaking Voltage Calculation

In order to clearly illustrate the branch breaking power flow calculation problem in the power system, the branch breaking power flow calculation of the simple DC circuit shown in **Figure 1** is analyzed.

The branch parameter in **Figure 1** is the admittance (e.g., 0.5), and $\eta(\lambda)$ is the breaking function. λ is assumed as the parameter of the branch circuit breaking process. The admittance of one of the branches is multiplied by the breaking function $\eta(\lambda)$, and $0.5\eta(\lambda)$ indicates that the branch is to be disconnected. If the branch admittance is zero, the corresponding branch state is disconnected. Among them, the continuous variation interval of λ is [0,1].

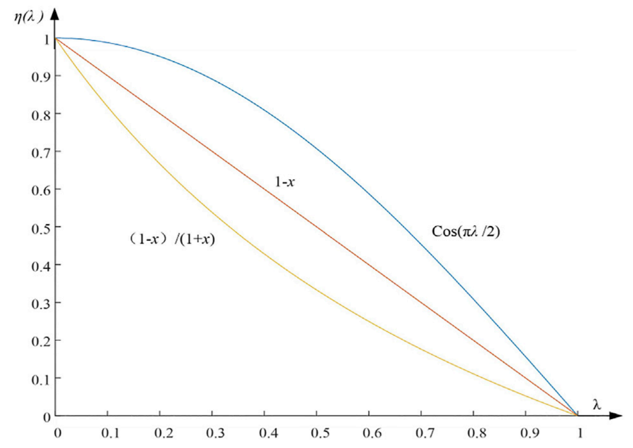

FIGURE 2 | Variation curve of the continuous interruption function η(λ).

The physical meaning of the disconnection function is the transition method selected by the branch from normal operation to disconnection, and its function value describes the degree to which this process is carried out. Now suppose that there is a breaking function $\eta(\lambda)$, as described in Wu et al. (2020), then the continuous breaking function can be set as the following:

$$n(\lambda) = 1 - \lambda, \tag{1a}$$

$$n(\lambda) = (1 - \lambda)/(1 + \lambda). \tag{1b}$$

Obviously, when $\lambda = 0$ and $\eta(0) = 1$, it corresponds to the normal state of the system; otherwise, if $\lambda = 1$ and $\eta(1) = 0$, it corresponds to open a branch. If $(1\text{-}\lambda)$ in **Eq. 1a** is adopted, it is a linear breaking function. In **Eq. 1b**, $(1\text{-}\lambda)/(1+\lambda)$ is a nonlinear breaking function. Suppose the nonlinear function conforms to the $\cos(\pi\lambda/2)$ nonlinear relationship, then the change curve of the continuous breaking function $\eta(\lambda)$ is as shown in **Figure 2**.

It can be seen from **Figure 2** that the change rules of different breaking functions are different.

Their initial and final values are consistent. The function $\eta(\lambda) = \cos(\pi\lambda/2)$ can also play the role of continuous breaking. But it has no practical value and is only used for curve comparison. Therefore, the power equation can be listed from the circuit.

$$P_{\mathrm{LD}} = (10 - U)[0.5 + 0.5\eta(\lambda)]U. \tag{2}$$

Equation 2 can be organized into the following form:

$$P_{\mathrm{LD}} = f(U, \lambda) = (5U - 0.5U^2)[1 + \eta(\lambda)]. \tag{3}$$

From **Eq. 3**, we know that when $\lambda = 0 \rightarrow 1$, U is a composite function with respect to the parameter λ, that is, $U = U(\eta(\lambda))$.

Then, we analyzed a branch broken first in **Figure 1**. Assuming load power is constant (PLD = constant). We expand the voltage U into the Taylor series of the parameter λ, which combined with the nonlinear breaking function $\eta(\lambda)$. Just taking the second-order Taylor series as an example, **Eq. 3** is the second derivative of λ, then we have

$$\begin{cases} 0 = (5 - U)[1 + \eta]\dfrac{\mathrm{d}U}{\mathrm{d}\lambda} + (5U - 0.5U^2)\eta', \\ 0 = (5 - U)[1 + \eta]\dfrac{\mathrm{d}^2U}{\mathrm{d}\lambda^2} - [1 + \eta]\left(\dfrac{\mathrm{d}U}{\mathrm{d}\lambda}\right)^2 \\ \quad +2(5 - U)\dfrac{\mathrm{d}U}{\mathrm{d}\lambda}\eta' + (5U - 0.5U^2)\eta''. \end{cases} \tag{4}$$

In **Figure 1**, when $\lambda = 0$, let the initial state of the system be: $PLD = 9$ and $U0 = 9$. It can be solved by the following formula:

$$\begin{cases} a_1 = \left.\dfrac{\mathrm{d}U}{\mathrm{d}\lambda}\right|_{\substack{\lambda=0 \\ U_0=9}} = \dfrac{4.5}{8}\eta'(0), \\ a_2 = \left.\dfrac{\mathrm{d}^2U}{\mathrm{d}\lambda^2}\right|_{\substack{\lambda=0 \\ U_0=9}} = \dfrac{4.5}{8}\eta''(0) - a_1\eta'(0) - \dfrac{1}{4}a_1^2. \end{cases} \tag{5}$$

In addition, the third-order Taylor series coefficient $a3$ can be obtained according to the abovementioned analogy. Then, the third-order Taylor series of U concerning λ is obtained as follows:

$$U = U_0 + a_1(\lambda - 0) + \frac{a_2}{2}(\lambda - 0)^2 + \frac{a_3}{6}(\lambda - 0)^3. \tag{6}$$

In **Eq. 6**, let $\lambda = 1$, then the breaking voltage can be obtained immediately.

$$U(1) = U_0 + a_1 + \frac{a_2}{2} + \frac{a_3}{6}. \tag{7}$$

Specifically, the different breaking function $\eta(\lambda)$ is selected, which has been largely affected by the convergence rate of the Taylor series. The influence of the calculation results of the breaking voltage under different breaking functions analyzed as follows is shown in **Table 1**.

It can be seen from **Table 1** that the voltage calculation result error reaches 3.73% by applying the linear breaking function $(1\text{-}\lambda)$, obviously far from meeting the precise calculation requirements. After applying the nonlinear breaking function $(1\text{-}\lambda)/(1+\lambda)$, voltage accuracy improved by more than one order of magnitude, and the calculation error of the three-stage number is only$|\Delta| = 0.35\%$. It is proved that the choice of the breaking function has a great influence on the accuracy of the calculation result. Therefore, the nonlinear breaking function of **Eq. 1b** is used in the following text, which is the important significance of the

TABLE 1 | Influence of two typical breaking functions on the convergence accuracy of Taylor series.

η(λ)	η′(0)	η′′(0)	η′′(0)	U calculated value		U accurate value	Error |Δ|	|Δ|/%
				Second order	Third order			
1-λ	−1	0	0	8.1167	7.9310	7.6458	0.2852	3.7297
(1-λ)/(1+λ)	−2	4	−12	7.7168	7.6723	7.6458	0.0265	0.3472

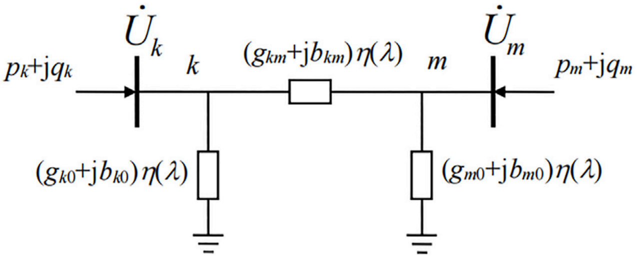

FIGURE 3 | Equivalent circuit of type *k-m* for the grid breaking line.

nonlinear breaking function proposed in this study. In the actual system, especially the larger scale power system with the stronger actual nonlinear characteristics, there are different requirements on the choice of breaking function. Research on how to choose a better breaking function will be carried out in the follow-up studies.

Calculation Method of the Network Disconnection Line Power Flow

Break analysis of any branch of the power system, such as the case of the grid breaking one line and the analysis process of breaking two or more grid lines, is completely consistent with this. Let the continuous breaking function be $\eta(\lambda)=(1-\lambda)/(1+\lambda)$, then the breaking line is $L_{k\text{-}m}$. Then, the ∏-type equivalent circuit for breaking the line is shown in **Figure 3**.

From **Figure 3**, breaking one line is equivalent to breaking three branches at the same time, and each branch admittance is a function of the breaking parameter λ. In the process of line disconnection, since four elements in the admittance matrix ***Y*** are functions of λ, the power flow equation also includes the parameter λ, which is as follows:

$$Y = \begin{bmatrix} Y_{11} & Y_{12} & \cdots & & Y_{1n} \\ Y_{k1} & Y_{km}\eta(\lambda) + (Y_{kk} - Y_{km}) & \cdots & Y_{km}\eta(\lambda) & Y_{kn} \\ \vdots & \vdots & \cdots & \vdots & \vdots \\ Y_{m1} & Y_{mk}\eta(\lambda) & \cdots & Y_{mm}\eta(\lambda) + (Y_{mm} - Y_{km}) & Y_{mn} \\ Y_{n1} & Y_{n2} & \cdots & & Y_{nn} \end{bmatrix}. \tag{8}$$

Since four elements in the network admittance matrix ***Y*** are functions of λ, then in the elements of the power flow Jacobian matrix ***J***, four elements in corresponding positions have both voltage variables and breaking functions $\eta(\lambda)$, which is as follows:

$$\boldsymbol{J}' = \begin{bmatrix} \boldsymbol{J}_{11} & \boldsymbol{J}_{12} & \cdots & & \boldsymbol{J}_{1n} \\ \boldsymbol{J}_{k1} & \boldsymbol{J}_{kk}\eta(\lambda) & \cdots & \boldsymbol{J}_{km}\eta(\lambda) & \boldsymbol{J}_{kn} \\ \vdots & \vdots & & \vdots & \vdots \\ \boldsymbol{J}_{m1} & \boldsymbol{J}_{mk}\eta(\lambda) & \cdots & \boldsymbol{J}_{mm}\eta(\lambda) & \boldsymbol{J}_{mn} \\ \boldsymbol{J}_{n1} & \boldsymbol{J}_{n2} & \cdots & & \boldsymbol{J}_{nn} \end{bmatrix}. \tag{8a}$$

The Jacobian matrix ***J'*** can be equivalently added to two matrices, by which we can get

$$\boldsymbol{J}' = \boldsymbol{J}_1\eta(\lambda) + \boldsymbol{J}_2. \tag{9}$$

In the formula, ***J₁*** and ***J₂*** are, respectively,

$$\boldsymbol{J}_1 = \begin{bmatrix} \boldsymbol{0} & & \cdots & & & \boldsymbol{0} \\ & \boldsymbol{J}_{kk} & \boldsymbol{0} & \cdots & \boldsymbol{J}_{km} & \\ \vdots & \boldsymbol{0} & \boldsymbol{0} & \cdots & \boldsymbol{0} & \vdots \\ & \vdots & \vdots & & \vdots & \\ & \boldsymbol{J}_{mk} & \boldsymbol{0} & \cdots & \boldsymbol{J}_{mm} & \\ \boldsymbol{0} & & \cdots & & & \boldsymbol{0} \end{bmatrix}, \tag{10}$$

$$\boldsymbol{J}_2 = \begin{bmatrix} \boldsymbol{J}_{11} & & \cdots & & & \boldsymbol{J}_{1n} \\ & \boldsymbol{0} & & \cdots & \boldsymbol{0} & \\ \vdots & & & \cdots & & \vdots \\ & \vdots & \vdots & & \vdots & \\ & \boldsymbol{0} & & \cdots & \boldsymbol{0} & \\ \boldsymbol{J}_{n1} & & \cdots & & & \boldsymbol{J}_{nn} \end{bmatrix}. \tag{11}$$

It should be noted that only when $\lambda = 0$ and $\eta(0) = 1$, then $\boldsymbol{J}' = \boldsymbol{J}_1 + \boldsymbol{J}_2$.

For the convenience of description, the power flow equation in polar coordinates is used to deduce the calculation of the breaking power flow. Similarly, the power flow equation in rectangular coordinates can also be used for derivation. The power flow equation of the power system is as follows:

$$\boldsymbol{W} = \boldsymbol{F}(\boldsymbol{X}, \lambda). \tag{12}$$

In **Eq. 12**,

$$\begin{aligned} \boldsymbol{W} &= \begin{bmatrix} P_{1s} & Q_{1s} & \cdots & P_{(n-1)s} & U^2_{(n-1)s} \end{bmatrix}^{\mathrm{T}} \\ \mathbf{X} &= \begin{bmatrix} \delta_1 & \delta_2 & \cdots & \delta_{n-1} & U_1 & U_2 & \cdots U_m \end{bmatrix}^{\mathrm{T}}. \end{aligned} \tag{12a}$$

It can be seen from **Eq. 12** that the phase angle δ and voltage ***U*** of each node in the system are functions of the parameter λ, so **Eq. 12** can be derived from λ. Here,

$$\frac{\mathrm{d}\boldsymbol{W}}{\mathrm{d}\lambda} = \eta' \boldsymbol{H} + (\boldsymbol{J}_1\eta + \boldsymbol{J}_2)\frac{\mathrm{d}X}{\mathrm{d}\lambda}. \tag{13}$$

In **Eq. 13**, when $\lambda = 0$ and $\eta(0) = 1$.

At this time, ***J₁+J₂*** = ***J***, ***J*** is the Jacobian matrix that was obtained before the line was broken and no need to recalculate; therefore,

$$\frac{\mathrm{d}\boldsymbol{W}}{\mathrm{d}\lambda} = \eta'(0)\boldsymbol{H} + \boldsymbol{J}\frac{\mathrm{d}\boldsymbol{X}}{\mathrm{d}\lambda}. \tag{14}$$

In addition, ***H*** is

$$\boldsymbol{H} = \begin{bmatrix} 0 & \cdots & p_k & q_k & 0 & \cdots & p_m & q_m & \cdots & 0 \end{bmatrix}^{\mathrm{T}}. \tag{15}$$

In **Eq. 15**, the elements p_k, q_k, p_m, and q_m happen to be the power injected into each end of the breaking line, respectively (*see* **Figure 3**). The calculation formula is shown in Appendix A.

Therefore, the first derivative of ***X*** to λ before the line is disconnected (i.e., $\lambda = 0$) and is as follows:

$$\frac{\mathrm{d}X}{\mathrm{d}\lambda} = -\boldsymbol{J}^{-1}\left[\eta'(0)\boldsymbol{H}\right]. \tag{16}$$

Eq. 13 continues to take the derivative of λ:

$$\frac{\mathrm{d}^2\boldsymbol{W}}{\mathrm{d}\lambda^2} = \eta''\boldsymbol{H} + \eta'\left(\frac{\mathrm{d}\boldsymbol{H}}{\mathrm{d}\lambda} + \boldsymbol{J}_1\frac{\mathrm{d}X}{\mathrm{d}\lambda}\right) + \frac{\mathrm{d}\boldsymbol{J}}{\mathrm{d}\lambda}\frac{\mathrm{d}\boldsymbol{X}'}{\mathrm{d}\lambda} + \left(\boldsymbol{J}_1\eta + \boldsymbol{J}_2\right)\frac{\mathrm{d}^2\boldsymbol{X}}{\mathrm{d}\lambda^2}. \tag{17}$$

Since $J_1 = \partial H/\partial X$, there are two terms in **Eq. 17** that are completely equal, but the expressions are different.

$$\frac{\mathrm{d}\boldsymbol{H}}{\mathrm{d}\lambda} = \boldsymbol{J}_1\frac{\mathrm{d}\boldsymbol{X}}{\mathrm{d}\lambda}. \tag{18}$$

Therefore, when $\lambda = 0$ and $\eta(0) = 1$, **Eq. 17** can be simplified as follows:

$$\frac{\mathrm{d}^2\boldsymbol{W}}{\mathrm{d}\lambda^2} = \eta''(0)\boldsymbol{H} + 2\eta'(0)\frac{\mathrm{d}\boldsymbol{H}}{\mathrm{d}\lambda} + \frac{\mathrm{d}\boldsymbol{J}}{\mathrm{d}\lambda}\frac{\mathrm{d}\boldsymbol{X}}{\mathrm{d}\lambda}|\lambda = 0 + \boldsymbol{J}\frac{\mathrm{d}^2\boldsymbol{X}}{\mathrm{d}\lambda^2}. \tag{19}$$

Specifically, *dJ'/dλ* in **Eq. 17** and *dJ/dλ* in **Eq. 19** are, respectively,

$$\begin{cases} \dfrac{\mathrm{d}\boldsymbol{J}'}{\mathrm{d}\lambda} = \dfrac{\mathrm{d}\boldsymbol{J}_1}{\mathrm{d}\lambda}\eta(\lambda) + \dfrac{\mathrm{d}\boldsymbol{J}_2}{\mathrm{d}\lambda} & \lambda \neq 0, \\ \dfrac{\mathrm{d}\boldsymbol{J}}{\mathrm{d}\lambda} = \dfrac{\mathrm{d}\boldsymbol{J}_1}{\mathrm{d}\lambda} + \dfrac{\mathrm{d}\boldsymbol{J}_2}{\mathrm{d}\lambda} & \lambda = 0. \end{cases} \tag{20}$$

Therefore, the second derivative of $\boldsymbol{X}$ concerning λ is as follows:

$$\frac{\mathrm{d}^2\boldsymbol{X}}{\mathrm{d}\lambda^2} = -\boldsymbol{J}^{-1}\left[\eta''(0)\boldsymbol{H} + 2\eta'(0)\frac{\mathrm{d}\boldsymbol{H}}{\mathrm{d}\lambda} + \frac{\mathrm{d}\boldsymbol{J}}{\mathrm{d}\lambda}\frac{\mathrm{d}\boldsymbol{X}}{\mathrm{d}\lambda}\right]. \tag{21}$$

After considering **Eqs 17** and **19**, re-expression of **Eq. 14**, and the third derivative of the voltage U concerning λ, *see* Appendix ***C***. After calculating the derivatives of $\boldsymbol{X}$ concerning λ from **Eqs 18** and **21**, the voltage of each node after the disconnection of line can be calculated according to the Taylor expansion:

$$\begin{cases} A_{i1} = \dfrac{\mathrm{d}U_i}{\mathrm{d}\lambda}, \\ A_{i2} = \dfrac{\mathrm{d}^2U_i}{\mathrm{d}\lambda^2}, \\ A_{i3} = \dfrac{\mathrm{d}^3U_i}{\mathrm{d}\lambda^3}. \end{cases} \tag{22}$$

In the Taylor series, let $\lambda = 1$, the calculation expressions of the voltage amplitude and phase angle of each node are obtained as follows:

$$\begin{cases} \boldsymbol{U}(1) = \boldsymbol{U}(0) + \dfrac{\mathrm{d}\boldsymbol{U}}{\mathrm{d}\lambda}(1-0) + \dfrac{1}{2}\dfrac{\mathrm{d}^2\boldsymbol{U}}{\mathrm{d}\lambda^2}(1-0)^2 + \dfrac{1}{6}\dfrac{\mathrm{d}^3\boldsymbol{U}}{\mathrm{d}\lambda^3}(1-0)^3, \\ \boldsymbol{\delta}(1) = \boldsymbol{\delta}(0) + \dfrac{\mathrm{d}\boldsymbol{\delta}}{\mathrm{d}\lambda_{|\lambda=0}} + \dfrac{1}{2}\dfrac{\mathrm{d}^2\boldsymbol{\delta}}{\mathrm{d}\lambda^2{}_{|\lambda=0}} + \dfrac{1}{6}\dfrac{\mathrm{d}^3\boldsymbol{\delta}}{\mathrm{d}\lambda^3{}_{|\lambda=0}}. \end{cases} \tag{23}$$

It can be seen that since J is exactly the Jacobian matrix of the convergence of power flow calculation before line interruption, its inverse matrix already exists, and various interruption power flow calculations use the inverse of the same Jacobian matrix, so its calculation amount is equivalent to that of traditional interruption, like the DC method or compensation method for load flow calculation.

TABLE 2 | Calculation result of the voltage under breaking branches 3–4 in the IEEE14 node system.

Node	N–R accurate value		FTS-calculated value		Error	
	U_i/pu	δ_i/°	U_i/pu	δ_i/°	$\lvert\Delta U_i\rvert$	$\Delta\delta i$/°
1	1.06	0	1.06	0	0	0
2	1.045	−4.9826	1.045	−4.5145	0	0.4681
3	1.01	−12.7251	1.01	−13.4766	0	−0.7515
4	1.0203	−10.3129	1.0214	−11.8877	0.001	−1.5748
5	1.0216	−8.7739	1.0226	−9.8178	0.001	−1.0439
6	1.07	−14.2209	1.07	−15.5426	0	−1.3217
7	1.0628	−13.3596	1.0634	−14.8789	0.0005	−1.5193
8	1.09	−13.3596	1.09	−14.8789	0	−1.5193
9	1.0574	−14.9385	1.0580	−16.4187	0.0006	−1.4802
10	1.0522	−15.0973	1.0527	−16.5516	0.0005	−1.4544
11	1.0576	−14.7906	1.0579	−16.185	0.0003	−1.3944
12	1.0552	−15.0756	1.0553	−16.4174	0.0001	−1.3418
13	1.0506	−15.1563	1.0507	−16.501	0.0001	−1.3447
14	1.0364	−16.0336	1.0369	−17.4603	0.0005	−1.4267

TABLE 3 | Calculation result of power under breaking branches 3–4 in the IEEE14 node system.

Node	Before breaking		After breaking	
	P	Q	P	Q
1	2.323933	−0.16549	2.326768	−0.18337
2	0.183	0.308571	0.183	0.334627
3	−0.942	0.060753	−0.942	0.112413
4	−0.478	0.039	−0.478	0.039
5	−0.076	−0.016	−0.076	−0.016
6	−0.112	0.052309	−0.112	0.040205
7	−4.59E−16	1.09E−16	4.61E−16	−1.02E−16
8	−4.72E−16	0.176235	4.02E−16	0.16806
9	−0.295	−0.166	−0.295	−0.166
10	−0.09	−0.058	−0.09	−0.058
11	−0.035	−0.018	−0.035	−0.018
12	−0.061	−0.016	−0.061	−0.016
13	−0.135	−0.058	−0.135	−0.058
14	−0.149	−0.05	−0.149	−0.05

Power Flow Calculation for Power Interruption

During the disconnection process of the power supply branch, the node admittance matrix of the power system remains unchanged, but the injected power of the node changes. The analysis results showed that the calculation accuracy of the Taylor series method does not depend strongly on the power interruption function $\eta(\lambda)$. When $\eta(\lambda)=(1-\lambda)/(1+\lambda)$, the interrupted power flow results with higher accuracy can also be obtained by fitting the third-order Taylor series. This is because the interruption of the power supply will not affect the system network structure but will only change the initial value of the power flow equation. By applying

TABLE 4 | Calculation results of branch breaking power flow of the Newton–Raphson method and comparison with the proposed method.

	Voltage amplitude			Node m voltage		
Branch (*k*-*m*)	Node *k*	Node m	Maximum error with N−R method results	Node *k*	Node m	Maximum error with N−R method results
1–2	1.060 0	1.045	0.0102	0	−0.6322	0.0088
2–3	1.045 0	1.01	0.0015	−0.0808	−0.4023	0.0036
2–4	1.045 0	1.0082	0.0003	−0.0774	−0.2123	0.0015
1–5	1.060 0	1.0074	0.0011	0	−0.2554	0.0044
2–5	1.045 0	1.0113	0.0002	−0.0755	−0.1654	0.0006
4–9	1.018 1	1.0541	0	−0.1566	−0.2703	0
9–10	1.063 9	1.0254	0.0001	−0.2435	−0.2633	0.0008
9–14	1.063 9	0.9969	0.0002	−0.2465	−0.3002	0.0004

the method in this study, the expected accident set can be scanned accurately and quickly, to directly judge whether the breaking power flow meets the safety requirements, and the precise correction process with a large amount of calculation is omitted.

SIMULATION CALCULATION AND ANALYSIS

Power Flow Calculation for Breaking Branches

In this study, the IEEE14 node calculation example is used to calculate the voltage value of each node after the line is disconnected. One result is according to the Taylor expansion-based breaking power flow method (FTS) proposed in this work It was compared with the real value calculated by the Newton–Raphson method (N–R). The comparison results are shown in **Table 2**. The system power changes before and after the disconnection of lines 3–4 and is shown in **Table 3**.

According to **Table 2** and **Table 3**, it can be observed that when compared with the N–R power flow method, the breaking power flow calculation method based on Taylor series fitting proposed in this study differs in the voltage value and phase angle of each node after the calculation system line is broken very small, and the difference in voltage value is 0–0.005 p.u, the difference between the power angle is 0–1.5°, the active and reactive values are the same, and it is proved that the proposed method has high accuracy in calculating the power flow distribution of the system after the line is disconnected. Moreover, the method in this study does not need to correct the calculation process of precise matrix elements, which greatly speeds up the analysis and calculation speed, and its theoretical significance and application value are very significant.

N-1 Static Security Rapid Analysis

In particular, the method in this study can be easily extended to the case of k-circuit breaking and realizes the static safety and fast analysis of the power system N-k. **Table 4** shows the calculation of the power flow of the N–R method after branch N-1 and the comparison results with the method in this study.

From the results in **Table 4**, it can be found that the error between the breaking power flow calculated by the method in this study and that calculated by the N–R method is very small, the node voltage amplitude error and voltage phase angle error are in the ranges of 0–0.01 and 0–0.0095, respectively, and the calculation error will not affect the estimation of the system operating state. In addition, the N–R method takes 2.9607 s to calculate the breaking power flow for all branches, the total time consumption of this method is 0.3312 s, and the total analysis calculation time is only 11.2% of the traditional method. It can be seen that the calculation speed of the method in this study is greatly accelerated. Therefore, this method is more suitable for application and rapid fault scanning to identify the degree of impact of faults on system stability.

CONCLUSION

This study proposed a breaking power flow calculation method based on Taylor series fitting. Compared with the DC power flow method, this method has advantages such as precise calculation results and the ability to obtain voltage amplitude and reactive power faster. Furthermore, the proposed method can also be generalized to the case of breaking multiple loops and realize the fast and accurate calculation of the power system N-k breaking power flow. Compared with the traditionally expected accident set scanning based on the N–R method, using this method to scan the accident set does not need an iterative solution. It only needs scanning to obtain the accurate data of the fault severity ranking and the node voltage after breaking the line. Therefore, the calculation speed meets the requirements of online static security analysis.

DATA AVAILABILITY STATEMENT

The original contributions presented in the study are included in the article/Supplementary Materials; further inquiries can be directed to the corresponding author.

AUTHOR CONTRIBUTIONS

SL: Find out the problems, conceive the overall framework of the article and put forward the main points. XZ: Process data and develop simulation programs, and analyze simulation results. WL: Revising the critical content for the selection of breaking function and the allowable range of node voltage calculation error. Md TH: Consult the literature to find the relevant materials of the article and participate in the writing of the first draft of the manuscript. ZZ: Oversight and leadership responsibility for the research activity planning and execution.

REFERENCES

Capitanescu, F., Glavic, M., Ernst, D., and Wehenkel, L. (2007). Contingency Filtering Techniques for Preventive Security-Constrained Optimal Power Flow. *IEEE Trans. Power Syst.* 22 (4), 1690–1697. doi:10.1109/tpwrs.2007.907528

Chatterjee, I. (2021). Artificial Intelligence and Patentability: Review and Discussions. *Int. J. Mod. Res.* 1, 15.

Dhiman, G., and Kaur, A. (2019). STOA: a Bio-Inspired Based Optimization Algorithm for Industrial Engineering Problems. *Eng. Appl. Artif. Intell.* 82, 148–174. doi:10.1016/j.engappai.2019.03.021

Duan, N., Huang, C., Sun, C. -C., and Min, L. (2022). Smart Meters Enabling Voltage Monitoring and Control: The Last-Mile Voltage Stability Issue. *IEEE Trans. Industrial Inf.* 1 (18), 677–687. doi:10.1109/tii.2021.3062628

England, B. S., and Alouani, A. T. (2020). Real Time Voltage Stability Prediction of Smart Grid Areas Using Smart Meters Data and Improved Thevenin Estimates. *Int. J. Electr. Power & Energy Syst.* 122, 106189. doi:10.1016/j.ijepes.2020.106189

Fliscounakis, S., Panciatici, P., Capitanescu, F., and Wehenkel, L. (2013). Contingency Ranking with Respect to Overloads in Very Large Power Systems Taking into Account Uncertainty, Preventive, and Corrective Actions. *IEEE Trans. Power Syst.* 28 (4), 4909–4917. doi:10.1109/tpwrs.2013.2251015

Kaplunovich, P. A., and Turitsyn, K. S. (2013). Fast Selection of N−2 Contingencies for Online Security Assessment. in *2013 IEEE Power & Energy Society General Meeting* (New York, NY), 1–5.

Kaur, S., Awasthi, L. K., Sangal, A. L., and Dhiman, G. (2020). Tunicate Swarm Algorithm: A New Bio-Inspired Based Metaheuristic Paradigm for Global Optimization. *Eng. Appl. Artif. Intell.* 90, 103541. doi:10.1016/j.engappai.2020.103541

Kumar, R., and Dhiman, G. (2021). A Comparative Study of Fuzzy Optimization through Fuzzy Number. *Int. J. Mod. Res.* 1, 1.

Li, S., Hou, J., and Li, J.. DNN-based Distributed Voltage Stability Online Monitoring Method for Large-Scale Power Grids. *Front. Energy Res.* 33 (4), 4189. doi:10.3389/fenrg.2021.625914

Li, S., Tan, Y., Li, C., Cao, Y., and Jiang, L.. A Fast Sensitivity-Based Preventive Control Selection Method for Online Voltage Stability Assessment. *IEEE Trans. Power Syst.* 33 (4), 4189. doi:10.1109/TPWRS.2017.2776968

Liu, H., Xie, X., Zhang, C., Li, Y., Liu, H., and Hu, Y. Quantitative SSR Analysis of Series-Compensated DFIG-Based Wind Farms Using Aggregated RLC Circuit Model. *IEEE Trans. Power Syst.* 32, 474–483. doi:10.1109/tpwrs.2016.2558840

Lu, T., Wang, Z., Ai, Q., and Lee, W.-J. (2017). Interactive Model for Energy Management of Clustered Microgrids. *IEEE Trans. Ind. Appl.* 53 (3), 1739–1750. doi:10.1109/tia.2017.2657628

Meng, Z. J., Xue, Y., and Lo, K. L. (2006). A New Approximate Load Flow Calculation Method for Contingency Selection. in *2006 IEEE PES Power Systems Conference and Exposition* (Nanjing), 1601. doi:10.1109/PSCE.2006.296152

Padiyar, K., and Rao, S. S. (1996). Dynamic Analysis of Small Signal Voltage Instability Decoupled from Angle Instability. *Electr. Power &Energy Syst.* 18 (7), 445.

Peyghami, S., Palensky, P., and Blaabjerg, F. (2020). An Overview on the Reliability of Modern Power Electronic Based Power Systems. *IEEE Open J. Power Electron.* 1 (1), 34–50. doi:10.1109/ojpel.2020.2973926

Sachdev, M. S., and Ibrahim, S. A. (1974). A Fast Approximate Technique for Outage Studies in Power System Planning and Operation. *IEEE Trans. Power Apparatus Syst.* (4), 1133. doi:10.1109/TPAS.1974.294059

Shukla, S. K., Gupta, V. K., Joshi, K., Gupta, A., and Singh, M. K. (2022). Self-aware Execution Environment Model (SAE2) for the Performance Improvement of Multicore Systems. *Int. J. Mod. Res.* 2 (1), 17.

Vargas, L., and Quintana, V. H. (1990). A Fast and Reliable Decoupled Load Flow Method in Rectangular Coordinates." in Proceedings of the Twenty-Second Annual North American Power Symposium, 94.

Wu, C., Fei, L. I., and Liu, G. (2020). Breaking Power Flow Calculation Based on Linear Voltage Function and Breaking Function Selection, *Electr. Power Autom. Equip.* 40, 211. doi:10.16081/j.epae.202008026

Yun, Z., Cui, X., and Ma, K. (2019). Online Thevenin Equivalent Parameter Identification Method of Large Power Grids Using LU Factorization. *IEEE Trans. Power Syst.* 34 (6), 4464. doi:10.1109/TPWRS.2019.2920994

Zhou, G. (2015). "The Static Security Analysis in Power System Based on Spark Cloud Computing Platform," in *2015 IEEE Innovative Smart Grid Technologies-Asia* (Beijing: IEEE), 1–6. doi:10.1109/isgt-asia.2015.7387102

ACKNOWLEDGMENTS

The authors are grateful to Hongying He and Hu Pengyu for providing basic data and simulation software for this article. In addition, the authors are also grateful for the financial support from the National Natural Science Foundation of China (Grant No.51777179) and the State Grid Hunan Electric Power Co., Ltd. Science and Technology Project (No. 5216A521003C).

Conflict of Interest: The authors declare that the research was conducted in the absence of any commercial or financial relationships that could be construed as a potential conflict of interest.

frontiers | Frontiers in Energy Research

TYPE Brief Research Report
PUBLISHED 17 August 2022
DOI 10.3389/fenrg.2022.974682

OPEN ACCESS

EDITED BY
Tianguang Lu,
Shandong University, China

REVIEWED BY
Zhenyuan Zhang,
University of Electronic Science and Technology of China, China
Zhaohao Ding,
North China Electric Power University, China

*CORRESPONDENCE
HongYing He,
lhx20070322@sina.com
FangYu Fu,
fangyufu@hnu.edu.cn

SPECIALTY SECTION
This article was submitted to Smart Grids,
a section of the journal
Frontiers in Energy Research

RECEIVED 21 June 2022
ACCEPTED 13 July 2022
PUBLISHED 17 August 2022

CITATION
He H, Fu F and Luo D (2022), Multiplex parallel GAT-ALSTM: A novel spatial-temporal learning model for multi-sites wind power collaborative forecasting.
Front. Energy Res. 10:974682.
doi: 10.3389/fenrg.2022.974682

Multiplex parallel GAT-ALSTM: A novel spatial-temporal learning model for multi-sites wind power collaborative forecasting

HongYing He*, FangYu Fu* and DianSheng Luo

College of Electrical and Information Engineering, Hunan University, Changsha, China

In order to improve the accuracy of wind power output forecasting and ensure reliability of the power grid, multiplex parallel GAT-ALSTM, a spatial-temporal learning model for multi-sites wind power collaborative forecasting is proposed in this study. Topography was generated by using geographic information (longitude and latitude) obtained from the wind power generation sites. The GAT layer was used to capture the spatial correlation characteristics of multi-sites wind power. Feature dimension enhancement of each wind power generation site was achieved by aggregating the information from the adjacent sites. The ALSTM layer was used to capture the temporal correlation of each power output time series. The multiplex parallel structure of the model is designed to provide fast prediction of large-scale distributed wind power generation. The validity of the proposed multiplex parallel GAT-ALSTM was confirmed by comparison with the forecast results obtained by RNN, LSTM, ALSTM, and GNN-ALSTM. The testing results showed that, compared to RNN, LSTM, ALSTM, and GNN-ALSTM, the forecast results of the multiplex parallel GAT-ALSTM had the lowest mean absolute value error and the highest accuracy.

KEYWORDS

wind power forecast, multi-sites, multiplex parallel, graph attention network, attention-based LSTM

1 Introduction

With the sharp increase in wind farms and installed capacity, the proportion of wind power in the total power grid capacity is also increasing. However, due to the intermittence and volatility of wind power, it will bring challenges to the safety and stable operation of the power grid (Yan et al., 2018; Li, 2022). Accurate forecasting of wind power can relieve the pressure of peak shaving and frequency modulation and effectively improve wind power accommodation capability on the power grid (Li et al., 2022; Liu et al., 2022).

Wind power prediction has been widely used and extensively researched recently. Wind power prediction algorithms are mainly divided into two categories: one based on a statistical model and the other on a deep learning algorithm. Tan et al. (2021) proposed a method to use an improved LSTM network with a new gating mechanism to build a prediction model for ultra-short-term wind power. González-Sopeña et al. (2020) introduced a multi-step wind power prediction model using variational mode decomposition and an extreme learning machine. Verma et al. (2018) proposed a short-term wind power model enhanced by support vector machines. Cao and Gui (2018) combined an LSTM algorithm based on deep learning with a LightGBM algorithm based on a statistical model for wind power prediction. Yatiyana et al. (2017) established wind power generation prediction technology based on an ARIMA statistical model. Peng et al. (2016) proposed a new ultra-short-term wind power prediction method based on numerical weather forecasting and an error correction method. These methods have advantages and applicability in different wind power forecasting situations; however, most of them only focus on the data of a single site, and ignore the correlation of data between adjacent sites. At the same time, if it is necessary to predict the wind power of a large-scale station, model training should be carried out separately, which is inefficient.

A graph neural network is a deep learning algorithm based on the topological relationships of nodes to extract their spatial correlation. In the field of traffic, Tang et al. (2020) proposed the use of a GAGCN network to predict traffic flow speed. In the field of communication, He and Zhao (2020) proposed a fault diagnosis scheme for a telecommunication network based on a graph neural network. At present, the most widely used and effective graph neural network is the graph attention network (GAT) (Hu et al., 2021; Tian et al., 2022). The GAT introduces an attention mechanism in the process of the graph neural network, which makes the net pay more attention to neighboring nodes with large correlations and can achieve better results (Dong et al., 2022; Xu et al., 2022).

In this study, we propose a collaborative forecasting model for multi-sites wind power forecasting with strong generalization ability and greater accuracy. The proposed model was termed the multiplex parallel GAT-ALSTM, which aimed to simultaneously capture the spatial-temporal correlations in multi-sites wind power systems and achieve multi-sites wind power multiplex parallel forecasts. In this model, the spatial correlation feature of wind power was extracted by a multi-channel parallel graph attention network. After that, the temporal features of multi-sites wind power were extracted by a multi-channel parallel ALSTM network. The efficiency and accuracy of the forecast were improved by the aforementioned method. The rest of this article is organized as follows: Section 2 describes the prerequisite knowledge for the graph attention network and attention-based short- and long-term networks; Section 3 introduces the concrete realization scheme of multiplex parallel GAT-ALSTM; Section 4 provides experimental simulation and results analysis; and, Section 5 discusses the experimental conclusions.

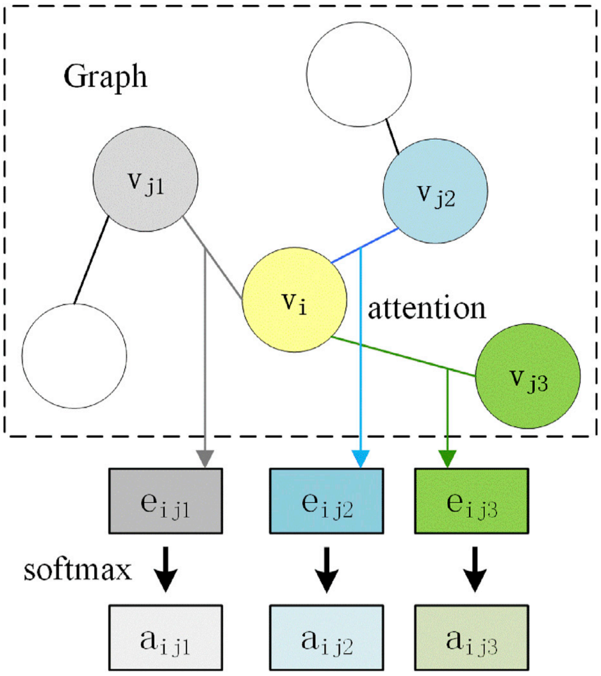

FIGURE 1
GAT network attention coefficient calculation diagram.

2 Preliminaries

To interpret the multiplex parallel GAT-ALSTM model, some basic knowledge of GAT and ALSTM is essential.

2.1 Graph attention network

The graph attention network is a variant and improvement of the traditional graph neural network, which considers the topological relationship between the target node and the neighbor node from spatial dimension, and can adaptively assign different weight coefficients to the surrounding nodes in the aggregation process, which improves the learning and expression ability of the graph neural network for non-Euclidean data.

The key of GAT lies in the attention mechanism, and the attention mechanism is defined as follows:

$$e_{ij} = attention\left(h_i, h_j\right) \tag{1}$$

$$attention = \begin{cases} < h_i, h_j > \\ OR \quad LeakyReLU\left(a^T\left[Wh_i, Wh_j\right]\right) \end{cases} \tag{2}$$

where h_i represents the feature vector of node v_i, h_j represents the feature vector of node v_j, and e_{ij} represents attention coefficients that indicate the importance of node j's features to node i. Attention refers to the attention mechanism layer, which can be in a form without

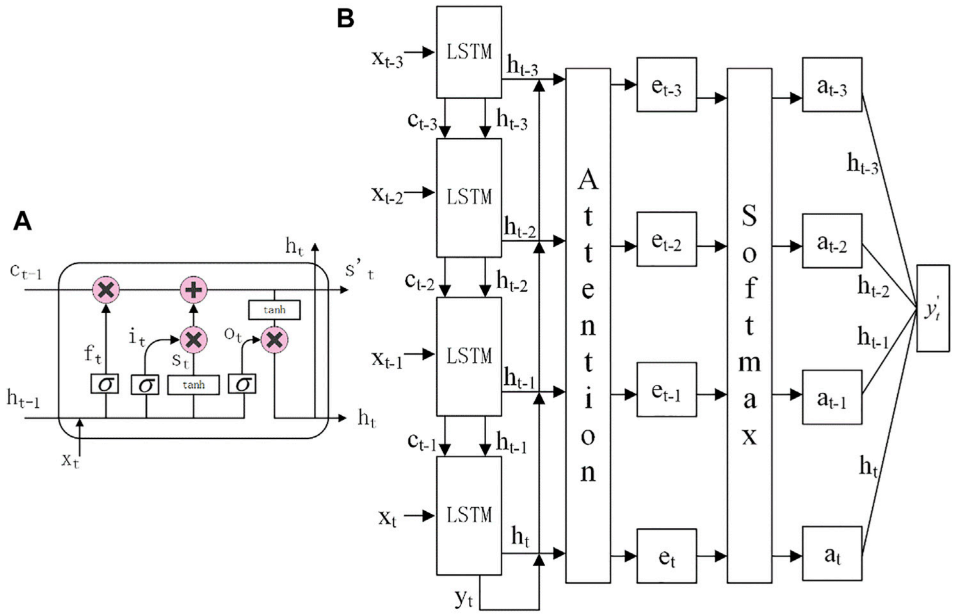

FIGURE 2
Single LSTM model diagram and ALSTM model diagram. **(A)** Single LSTM model. **(B)** ALSTM model.

parameters, such as the inner product of two vectors, or in a form with parameters, such as a single-layer linear fully connected layer.

To make attention coefficients easily comparable among different nodes, we normalized them with the softmax function, and obtained the normalized attention coefficient a_{ij}:

$$a_{ij} = soft\max\left(e_{ij}\right) = \frac{\exp\left(e_{ij}\right)}{\sum \exp\left(e_{ik}\right)} \tag{3}$$

Figure 1 shows the process of computing the attention coefficients of the nodes in a graph attention network. In order to simplify the calculation, we only compute e_{ij} for nodes $j \in N_i$, where N_i is some neighborhood of node i in the graph. In all our experiments, they are exactly the first-order neighbors of i. The attention coefficients of n-order neighbor nodes also can be obtained by overlaying and n-layer attention mechanism.

After the attention coefficients have been calculated, the features of all neighboring nodes are weighted and summed up to obtain the new feature vector of node v_i, Where h_i' represents the new feature vector of node v_i , W represents the linear transformation weight matrix, and σ represents the activation function:

$$h_i' = \sigma\left(\sum a_{ij} W h_j\right) \tag{4}$$

The features of first-order neighbor nodes can be extracted by a single layer network, while the features of second-order or multi-order neighbor nodes can be extracted by stacking multiple GATs. The attention mechanism is introduced in the graph attention network when updating the node information, which makes the graph neural network focus more on the useful feature information of the neighbor node to easily capture the spatial correlations of the neighboring node according to the topology structure, which largely improves the generalization and learning ability of the network.

2.2 Attention-based long short-term memory network

A long short-term memory network (LSTM) is a popular and effective deep learning model for processing time series data. The gating mechanism introduced in LSTM solves the problem of gradient disappearance in the training process of a recurrent neural network. The LSTM model is shown in Figure 2A, and the transfer function of each unit is given by:

$$\begin{bmatrix} S_t \\ O_t \\ i_t \\ f_t \end{bmatrix} = \begin{bmatrix} \tanh \\ \sigma \\ \sigma \\ \sigma \end{bmatrix} \left(W \begin{bmatrix} x_t \\ h_{t-1} \end{bmatrix} + b \right) \tag{5}$$

$$S_t' = f_t \cdot S_{t-1}' + i_t \cdot S_t \tag{6}$$

$$h_t = O_t \cdot \tanh\left(S_t'\right) \tag{7}$$

where, O_t, i_t and f_t represent the output information of the three gating mechanisms, S_t' represents the new LSTM unit status information at time t, and h_t represents the output of the LSTM unit at time t.

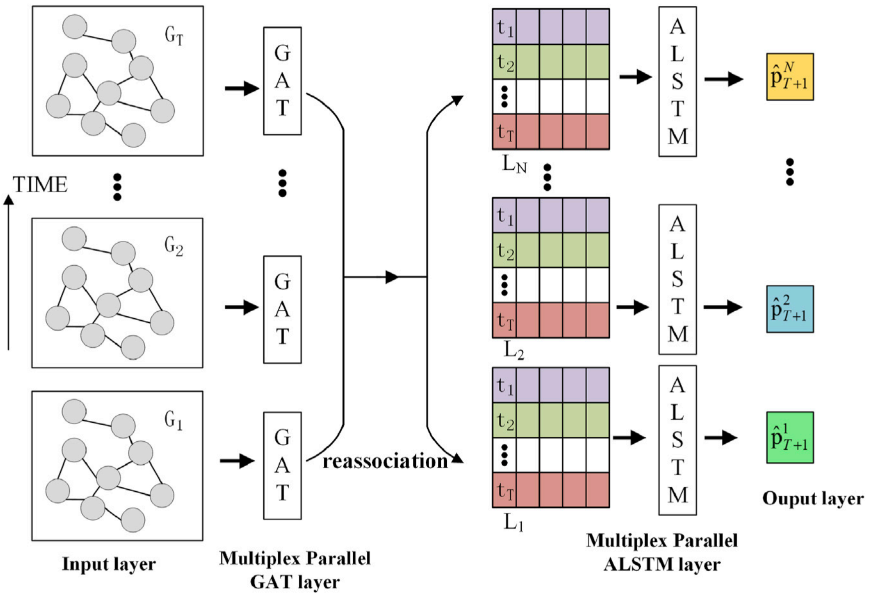

FIGURE 3
GAT—ALSTM model diagram.

When LSTM processes a time series, there is a problem that the input information in front of the time series will be diluted by the later input information. The longer the input time series is, the more obvious this phenomenon becomes. Therefore, in order to solve this problem, an attention mechanism is added to the LSTM model. The attention mechanism makes the LSTM network focus on the more important part of the time series, so as to improve the accuracy and efficiency of the network. The attention mechanism is given by:

$$e_i = at(h_i, y_t) = \tanh\left(h_i^T W_i y_t\right) \tag{8}$$

$$a_i = soft\max(e_i) \tag{9}$$

$$y_t' = \sum a_i h_i \tag{10}$$

where, h_i represents the output of the ith LSTM unit, y_t represents the initial output of LSTM, and y_t' is the final output of the LSTM with attention mechanism. Figure 2B shows the schematic diagram of the ALSTM model.

3 Implementation of multi-sites wind power collaborative forecasting based on a multiplex parallel GAT-ALSTM model

3.1 Model design

Figure 3 shows the structure of the multiplex parallel GAT-ALSTM model. It consists of an input layer, a multiplex parallel GAT layer, a multiplex parallel ALSTM layer, and an output layer.

(1) Input layer: Using the geographic information (longitude and latitude) of the wind sites, a topology graph G with N nodes is generated. Each node corresponds to a wind site. The input of the GAT-ALSTM model is the wind power generation of N sites at T slots before the prediction time, $T + 1$. The wind power generation is embedded into the topology graph G as node features.
(2) Multiplex parallel GAT layer: T parallel GAT networks are used to simultaneously learn the correlation of wind power between different sites at T slots from the spatial dimension. GAT uses different weights to aggregate the information of neighbor nodes according to the learned correlation among sites. The features of each site are dynamically updated.
(3) Multiplex parallel ALSTM layer: A multiplex parallel ALSTM layer is used to capture the temporal correlation of time series.
(4) Output layer: uses a linear transform layer to predict wind power at all sites at time, $T + 1$.

3.2 Prediction based on a multi-channel parallel GAT-ALSTM model

A set of wind power data of model input is denoted as:

$$\{\mathrm{p}_t^n | n = 1, 2, \cdots, N; t = 1, 2, \cdots, T\} \quad (11)$$

where, $\mathrm{p}_t^n \in R$ means the nth wind power of N wind sites at time t, N represents the number of wind sites, and T is the input time window of the model. The input sequences of the nth wind site are written as:

$$\mathrm{P}^n = \left(p_1^n, p_2^n, \ldots, p_T^n\right) \in \mathbf{R}^T \quad (12)$$

The model input matrix is denoted as:

$$P = \left(\mathrm{P}^1, \mathrm{P}^2, \ldots, \mathrm{P}^N\right)^T \in \mathbf{R}^{N \times T} \quad (13)$$

A one-step ahead forecast is applied in the model, which inputs the content sequences of N wind sites from time 1 to time T, and outputs the predicted wind power of N wind sites at time $(T + 1)$, which is denoted as:

$$\hat{P} = \left(\hat{\mathrm{p}}_{T+1}^1, \hat{\mathrm{p}}_{T+1}^2, \cdots, \hat{\mathrm{p}}_{T+1}^N\right)^{\mathrm{T}} \in \mathbf{R}^{N \times 1} \quad (14)$$

The prediction model can be described as follows:

$$\hat{P} = F(\mathrm{P}, \boldsymbol{\theta}), \quad (15)$$

where, θ is the parameter set and F is the multiplex parallel GAT-ALSTM model.

In order to achieve wind power prediction at multiple sites based on the multiplex parallel GAT-ALSTM model, the specific steps are as follows:

Step 1: Data preprocessing, such as data cleaning and normalization, is performed first, then the history power data of the selected N wind turbines are divided into training sets and test sets for model training and testing.

Step 2: Generate topography by using the geographic information (longitude and dimension) of the sites. The history power data of the selected N wind turbines and the wind power of N stations at the same time are used as features of nodes in each topological structure graph. T GAT networks are used for parallel computation. Finally, the characteristic matrix of n sites of T moments that aggregate the information of neighbor node is output by the GAT.

Step 3: Use the output of the GAT network as the input to the ALSTM. After processing by the GAT network, the initial features of the n sites at each time are increased from one dimension to high dimensions. Finally, the ALSTM uses enhanced feature data to output the wind power at N sites.

Step 4: Train the neural network.

Step 5: Use the model obtained by the aforementioned steps to make predictions on the test set sample and analyze the results.

4 Application and results

The wind power of seven adjacent sites from January to March 2013 was collected from NREL West. The training data set was from January 1 to March 20. The test data set was from March 21 to March 31. The data is in the form of csv files containing power values at 10-min resolution for seven wind sites.

4.1 Data preprocessing

Due to measurement errors or data storage errors in the data sampling equipment, there may be random errors in the original sampling data. These erroneous values will interfere with the efficacy of the model in wind power forecasting. In order to improve the speed of the machine learning model gradient descent to find the optimal solution, it is also necessary to preprocess the original data. The formula is as follows, where x_t represents the wind power at a certain moment, and X represents the wind power sequence:

$$x_t = \frac{x_t - \min(X)}{\max(X) - \min(X)}$$

For wind power generators with a capacity of 1.5 MW, the reasonable range of power outputs is 0–1.5 MW. Data beyond this range are regarded as abnormal and are eliminated and replaced with interpolated data. Lastly, all data are normalized.

4.2 Evaluation methods

To evaluate the accuracy of the prediction results, the mean absolute error (MAE) is used to evaluate the forecast results accuracy and the correlation coefficient (CC) is used to evaluate the time lag. The formula is as follows:

$$\mathrm{MAE}\left(\mathrm{P}^n, \hat{\mathrm{P}}^n\right) = \frac{1}{T} \sum_{t=t_1}^{t_1+T} \left| p_t^n - \hat{p}_t^n \right| \quad (16)$$

$$CC = \frac{\mathrm{cov}\left(\mathrm{P}^n, \hat{\mathrm{P}}^n\right)}{\sqrt{\sigma_{\mathrm{P}^n}} \cdot \sqrt{\sigma_{\hat{\mathrm{P}}^n}}} \quad (17)$$

where T represents the number of consecutive one-step-ahead forecasts from time $\mathbf{t}_1$, $\mathrm{cov}(\mathrm{P}^n, \hat{\mathrm{P}}^n)$represents the covariance, and σ_{P^n} $\sigma_{\hat{\mathrm{P}}^n}$ represent standard deviation.

4.3 Experimental results

To verify the validity of the proposed model in an actual wind power forecasting task, the multiplex parallel GAT-ALSTM

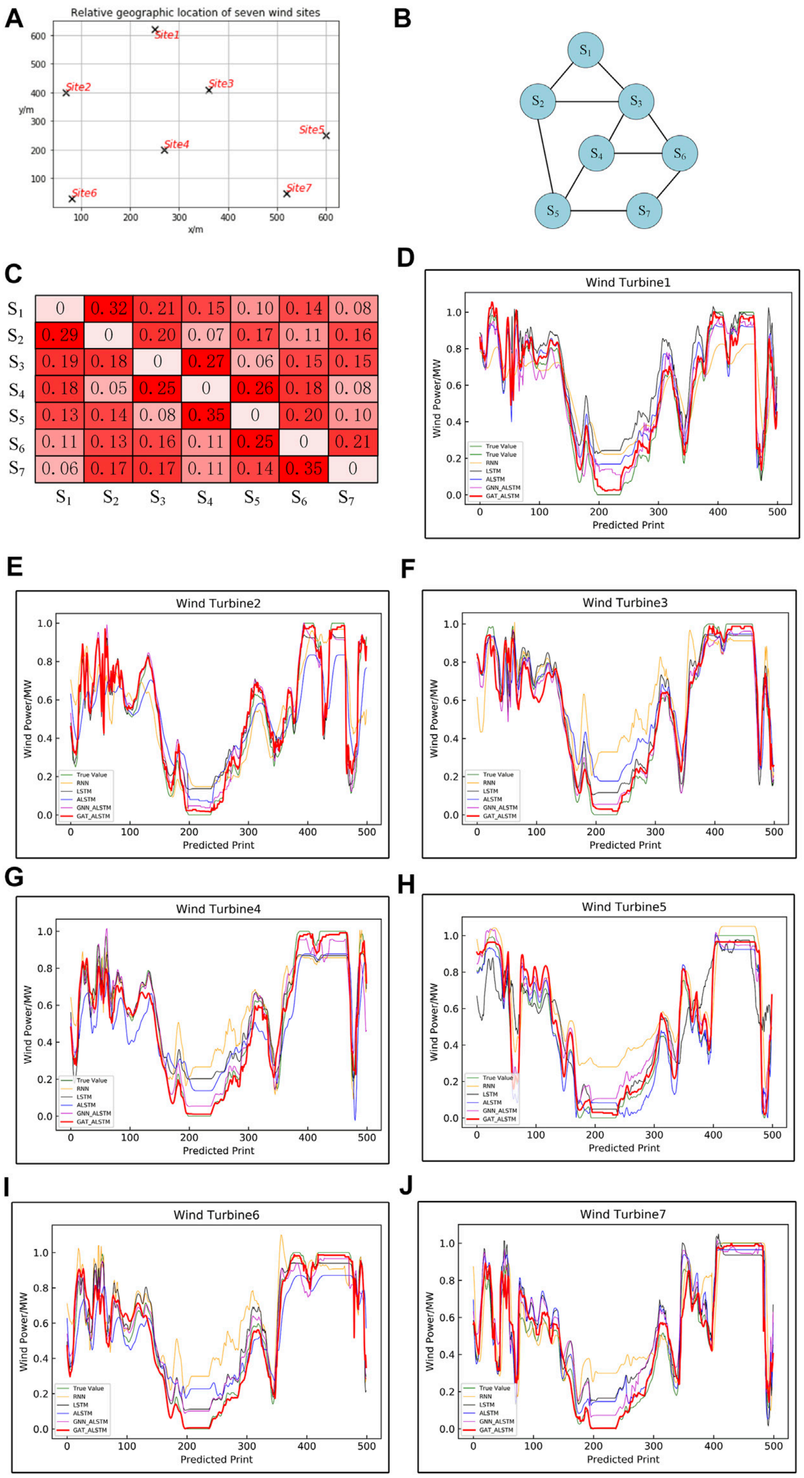

	S_1	S_2	S_3	S_4	S_5	S_6	S_7
S_1	0	0.32	0.21	0.15	0.10	0.14	0.08
S_2	0.29	0	0.20	0.07	0.17	0.11	0.16
S_3	0.19	0.18	0	0.27	0.06	0.15	0.15
S_4	0.18	0.05	0.25	0	0.26	0.18	0.08
S_5	0.13	0.14	0.08	0.35	0	0.20	0.10
S_6	0.11	0.13	0.16	0.11	0.25	0	0.21
S_7	0.06	0.17	0.17	0.11	0.14	0.35	0

FIGURE 4
Experimental result diagram. **(A)** Relative geographical locations of seven wind sites. **(B)** Topology graph of seven wind sites. **(C)** Site weight coefficient diagram learned by the GAT layer. **(D)** Wind power forecast chart of Site 1. **(E)** Wind power forecast chart of Site 2. **(F)** Wind power forecast chart of Site 3. **(G)** Wind power forecast chart of Site 4. **(H)** Wind power forecast chart of Site 5. **(I)** Wind power forecast chart of Site 6. **(J)** Wind power forecast chart of Site 7.

TABLE 1 Performance comparisons of five models for predicting wind power generation at sites 1 and 5.

Model Indicators	RNN (%)	LSTM (%)	ALSTM (%)	GNN-ALSTM	Multiplex parallel GAT-ALSTM (%)
MAE of site 1	9.21	8.77	8.47	8.02%	7.41
CC of site 1	94.32	94.58	95.38	96.97%	98.56
MAE of site 2	9.32	9.02	8.76	8.32%	7.67
CC of site 2	94.12	94.65	95.33	95.98%	97.24
MAE of site 3	9.06	8.85	8.31	7.98%	7.32
CC of site 3	94.43	94.87	95.43	96.11%	98.04
MAE of site 4	9.51	8.54	8.29	8.01%	7.58
CC of site 4	94.69	95.01	96.59	97.55%	98.43
MAE of site 5	9.10	8.64	8.32	8.11%	7.52
CC of site 5	94.07	94.87	95.33	96.86%	98.06
MAE of site 6	9.10	8.21	8.07	7.89%	7.44
CC of site 6	94.76	95.01	95.78	97.32%	98.10
MAE of site 7	9.11	8.91	8.41	7.99%	7.36
CC of site 7	94.76	95.11	96.78	97.33%	98.21

model and other associated models were used for wind power forecast experiments. The RNN and LSTM networks are common time series prediction models, and the ALSTM and GNN-ALSTM networks are used to verify the effectiveness of the attention mechanism. The experiment consists of one-step ahead forecasting of wind power. Figure 4A shows the location of each site. Figure 4B shows the topology graph of the seven wind sites. Figure 4C shows the attention weight coefficient between the wind sites learned by the GAT layer. It can be seen that the attention coefficient basically conforms to the rule of “near large and far small” in the spatial dimension. Figure 4D–J shows a comparison diagram of wind power forecasts at wind sites 1 to site 7 using five network models. Table 1 shows the evaluation index values of five network models for wind power forecast at sites 1 to 5.

It can be seen from the experimental results that, compared to the RNN network, theMAEof LSTM was reduced due to the introduction of the gating mechanism. ALSTM introduced a time attention mechanism into LSTM, and the CC of site one was increased by 0.8%, which indicates that a temporal attention mechanism can improve the time lag in time series prediction to a certain extent. Compared with ALSTM and GNN-ALSTM, the multiplex parallel GAT-ALSTM can fully utilize the information of adjacent sites, and theMAEof site 1 and site 5 decreased by 0.45% and 0.84%, respectively. Lastly, by comparing the forecast results of GNN-ALSTM with those from multiplex parallel GAT-ALSTM, the MAEof multiplex parallel GAT-ALSTM for site 1 was 0.39% lower than that of GNN-ALSTM, and the *CC* of multiplex parallel GAT-ALSTM for site 1 was 0.26% higher than that of GNN-ALSTM. It can be concluded from Table 1 that multiplex parallel GAT-ALSTM had the best prediction results among the five models because it introduced the attention mechanism for both temporal and spatial dimensions.

5 Conclusion

This study has proposed multiplex parallel GAT-ALSTM, a spatial-temporal learning model for multi-sites wind power collaborative forecasting. Leveraging the geographical information and historical power output data of adjacent wind sites, the model simultaneously captured the spatial-temporal correlation in multi-sites wind power by two attention mechanisms. Based on the learned spatial-temporal correlation, it improved the accuracy of the forecast. The multiplex parallel structure of the model is suitable for fast prediction of large-scale distributed wind power generation. The validity of the proposed multiplex parallel GAT-ALSTM is confirmed by comparing its forecast results with those obtained from RNN, LSTM, ALSTM, and GNN-ALSTM. It was found that forecast errors were minimized by the proposed model; hence, the proposed model shows good performance in forecasting wind power.

In potential future work, we plan to incorporate atmospheric factors such as wind speed and temperature as exogenous variables in the learning process to further enhance the forecasting ability.

Data availability statement

The original contributions presented in the study are included in the article/supplementary material. Further inquiries can be directed to the corresponding authors.

Author contributions

HH: conceptualization, methodology, validation, and writing—review. FF: software, visualization, and writing—original draft. DL: methodology and experimental verification.

Funding

This work was supported by the National Key Research and Development Plan, China, 2017, under Grant 2017YFB0903403.

Conflict of interest

The authors declare that the research was conducted in the absence of any commercial or financial relationships that could be construed as a potential conflict of interest.

Publisher's note

References

Cao, Y., and Gui, L. (2018). "Multi-step wind power forecasting model using LSTM networks, similar time series and LightGBM," in 2018 5th International Conference on Systems and Informatics (ICSAI), 10-12 Nov. 2018 (Nanjing, China: IEEE), 192–197. doi:10.1109/ICSAI.2018.8599498

Dong, Y., Liu, Q., Du, B., and Zhang, L. (2022). Weighted feature fusion of convolutional neural network and graph attention network for hyperspectral image classification. *IEEE Trans. Image Process.* 31, 1559–1572. doi:10.1109/TIP.2022.3144017

González-Sopeña, J. M., Pakrashi, V., and Ghosh, B. (2020). "Multi-step ahead wind power forecasting for Ireland using an ensemble of VMD-ELM models," in 2020 31st Irish Signals and Systems Conference (ISSC), 11-12 June 2020 (Letterkenny, Ireland: IEEE), 1–5. doi:10.1109/ISSC49989.2020.9180155

He, J., and Zhao, H. (2020). "fault diagnosis and location based on graph neural network in telecom networks," in 2020 International Conference on Networking and Network Applications (NaNA), 10-13 Dec. 2020 (Haikou City, China: IEEE), 304–309. doi:10.1109/NaNA51271.2020.00059

Hu, B., Guo, K., Wang, X., Zhang, J., and Zhou, D. (2022). RRL-GAT: Graph attention network-driven multilabel image robust representation learning. *IEEE Internet Things J.* 9, 9167–9178. doi:10.1109/JIOT.2021.3089180

Li, H. (2022). Short-term wind power prediction via spatial temporal analysis and deep residual networks. *Front. Energy Res.* 10. doi:10.3389/fenrg.2022.920407

Li, Y., Tang, F., Gao, X., Zhang, T., Qi, J., Xie, J., et al. (2022). Numerical weather prediction correction strategy for short-term wind power forecasting based on bidirectional gated recurrent unit and XGBoost. *Front. Energy Res.* 9. doi:10.3389/fenrg.2021.836144

Liu, S., Wang, L., Jiang, H., Liu, Y., and You, H. (2022). Wind farm Energy storage system based on cat swarm optimization-backpropagation neural network wind power prediction. *Front. Energy Res.* 10. doi:10.3389/fenrg.2022.850295

Peng, X., Deng, D., Wen, J., Xiong, L., Feng, S., and Wang, B. (2016). "A very short term wind power forecasting approach based on numerical weather prediction and error correction method," in 2016 China International Conference on Electricity Distribution (CICED), 10-13 Aug. 2016 (Xi'an, Chinadio: IEEE), 1–4. doi:10.1109/CICED.2016.7576362

Tan, B., Ma, X., Shi, Q., Guo, M., Zhao, H., and Shen, X. (2021). "Ultra-short-term wind power forecasting based on improved LSTM," in 2021 6th International Conference on Power and Renewable Energy (ICPRE), 17-20 Sept. 2021 (Shanghai, China: IEEE), 1029–1033. doi:10.1109/icpre52634.2021.9635314

Tang, C., Sun, J., Sun, Y., Peng, M., and Gan, N. (2020). A general traffic flow prediction approach based on spatial-temporal graph attention. *IEEE Access* 8, 153731–153741. doi:10.1109/ACCESS.2020.3018452

Tian, Y., Zhang, C., Metoyer, R., and Chawla, N. V. (2022). Recipe recommendation with hierarchical graph attention network. *Front. Big Data* 4, 778417. doi:10.3389/fdata.2021.778417

Verma, S. M., Reddy, V., Verma, K., and Kumar, R. (2018). "Markov models based short term forecasting of wind speed for estimating day-ahead wind power," in 2018 International Conference on Power, Energy, Control and Transmission Systems (ICPECTS), 22-23 Feb. 2018 (Chennai, India: IEEE), 31–35. doi:10.1109/ICPECTS.2018.8521645

Xu, X., Gao, T., Wang, Y., and Xuan, X. (2022). Event temporal relation extraction with attention mechanism and graph neural network. *Tsinghua Sci. Technol.* 27, 79–90. doi:10.26599/TST.2020.9010063

Yan, J., Zhang, H., Liu, Y., Han, S., Li, L., Lu, Z., et al. (2018). Forecasting the high penetration of wind power on multiple scales using multi-to-multi mapping. *IEEE Trans. Power Syst.* 33, 3276–3284. doi:10.1109/TPWRS.2017.2787667

Yatiyana, E., Rajakaruna, S., and Ghosh, A. (2017). "Wind speed and direction forecasting for wind power generation using ARIMA model," in 2017 Australasian Universities Power Engineering Conference (AUPEC), 19-22 Nov. 2017 (Melbourne, VIC, Australia: IEEE), 1–6. doi:10.1109/AUPEC.2017.8282494

frontiers | Frontiers in Energy Research

TYPE Original Research
PUBLISHED 25 August 2022
DOI 10.3389/fenrg.2022.937240

EDITED BY
Fei Wang,
North China Electric Power University,
China

REVIEWED BY
Saeid Jafarzadeh Ghoushchi,
Urmia University of Technology, Iran
Yagang Zhang,
North China Electric Power University,
China

*CORRESPONDENCE
Zhenglin Zhu,
8115403@qq.com

SPECIALTY SECTION
This article was submitted to Smart Grids,
a section of the journal
Frontiers in Energy Research

RECEIVED 06 May 2022
ACCEPTED 06 July 2022
PUBLISHED 25 August 2022

CITATION
Zhu Z, Xu Y, Wu J, Liu Y, Guo J and Zang H (2022), Wind power probabilistic forecasting based on combined decomposition and deep learning quantile regression.
Front. Energy Res. 10:937240.
doi: 10.3389/fenrg.2022.937240

Wind power probabilistic forecasting based on combined decomposition and deep learning quantile regression

Zhenglin Zhu[1]*, Yusen Xu[2], Junzhao Wu[2], Yiwen Liu[2], Jianwei Guo[2] and Haixiang Zang[2]

[1]School of Energy and Power Engineering, Nanjing Institute of Technology, Nanjing, China, [2]College of Energy and Electrical Engineering, Hohai University, Nanjing, China

With the expansion of scale of the grid-connected wind power, wind power forecasting plays an increasing important role in ensuring the security and steady operation and instructing the dispatch of power systems. In consideration of the randomness and intermittency of wind power, the probabilistic forecasting is required in quantifying the uncertainty of wind power. This study proposes a probabilistic wind power prediction method that combines variational modal decomposition (VMD), singular spectrum analysis (SSA), quantile regression (QR), convolutional neural network (CNN) and bidirectional gated neural network (BGRU). Firstly, a combination decomposition method VMDS combining VMD and SSA is proposed to decompose wind power sequence to reduce the complexity of the sequence. Next, a feature extractor based on CNN and BGRU (CBG) is used to extract complex dynamic features of NWP data and high-frequency components. Then, the QR is performed by the BGRU based on the high-order features to obtain the predicted values for different quantiles. Finally, the kernel density estimation (KDE) is employed to estimate the probability density curve of wind power. The proposed model can achieve reliable probabilistic prediction while achieving accurate deterministic prediction. According to comparisons with related prediction models, the effectiveness of the proposed method is verified with the example test using datasets from the wind farm in China.

KEYWORDS

probabilistic forecasting, combination decomposition, quantile regression, convolutional neural network, bidirectional gated neural network

1 Introduction

The limitation of fossil fuels and the environmental degradation caused by fossil fuels have restricted the increasing global demand for electricity. Countries around the world are promoting the rapid development of clean energy represented by wind energy. In 2021, the newly installed wind power capacity in the world exceeded 94 GW (Global Wind Energy Council (GWEC), 2022). Due to the randomness, volatility and intermittent of wind power, the large-scale grid connection of wind power brings great uncertainty and risks to the supply side of the power system (Georgilakis, 2008). Therefore, accurate and reliable wind power forecasting is important to the safe operation of the power system and the utilization of wind energy (Jin et al., 2021).

Wind power prediction methods are mainly divided into deterministic prediction and probabilistic prediction (Zhou et al., 2021). Deterministic prediction is achieved through point prediction models which have three types: statistical models, machine learning models, and deep learning models. Many statistical models have been applied to wind power prediction, such as kalman filter (KF) (Liu and Liang, 2021), auto regressive moving average (ARMA) (Erdem and Shi, 2011), auto regressive integrated average (ARIMA) (Amini et al., 2016), etc. Commonly used machine learning models include artificial neural network (ANN) (Ren et al., 2014), support vector machine (SVM) (Demolli et al., 2019), etc.

Compared with statistical and machine learning models, deep learning models have stronger nonlinear mapping capabilities. With the development of deep learning technology, some deep neural network (DNN) models have been applied to renewable energy prediction, including deep belif network (DBN) (Wang et al., 2018), convolutional neural network (CNN) (Oh et al., 2019; Hong and Satriani, 2020; Huang et al., 2022), recurrent neural network (RNN) (Yu et al., 2018) etc. Ordinary RNN models suffering from the gradient vanishment and gradient explosion are rarely used to predict wind power (Zang et al., 2021), while its variants long short term memory neural network (LSTM) (Yuan et al., 2019; Wang et al., 2020; Zang et al., 2021) and gated recurrent unit (GRU) (Niu et al., 2020; Peng et al., 2020; Kisvari et al., 2021) can deal with the long-term dependency through specific internal structures.

The models mentioned above are all point prediction models. The expected values of wind power are obtained while the results are incapable of quantifying the uncertainty. Especially when the wind power fluctuates strongly, the point prediction may be less reliable and cannot meet the actual scheduling requirements. Therefore, the probability density and interval prediction of wind power have more significance in practical application and become a hot research direction recently (Wang et al., 2017; Zhang et al., 2019; Zhou et al., 2021).

Wind power probabilistic prediction can provide the probability density functions of wind power at the future time or the fluctuation interval under a certain degree of confidence (Zhang et al., 2016). Commonly used probabilistic prediction methods include error analysis method (Lv et al., 2021), upper and lower bound estimation method (Liu et al., 2020), quantile regression method (QR) (He and Li, 2018), etc. QR can construct the relationship between the input and the output of different quantiles, combined with the kernel density estimation (KDE) can achieve probabilistic prediction. QR is essentially a linear model, and its ability to express nonlinear data is poor. Some variants of QR models such as neural network QR solve this problem by combining QR with BP neural network (He and Li, 2018). In Ref. (Zhang et al., 2019), a framework combining the point prediction model with QR was proposed to achieve probabilistic prediction. QRLSTM, QRGRU and QRMGM were proposed to prove the effectiveness of the proposed framework. In Ref. (Peng et al., 2021), a model called EALSTM-QR was designed, which combined QR, LSTM, Encoder and Attention to improve the non-linear expression of data. Yao et al. (He and Wang, 2021) combined the LASSO regression with the QRNN model, and used ensemble empirical mode decomposition (EEMD) to reduce the complexity of the wind power sequence, which effectively improved the prediction accuracy. In Ref. (Sun et al., 2022), a quantile regression forest interval prediction model is proposed for multiple fluctuation processes for ultra-short-term time scales.

Many scholars have proposed hybrid models that combine data decomposition technology and prediction model to further improve the accuracy of wind power prediction (Zhang et al., 2021). Common data decomposition methods include empirical mode decomposition (Bokde et al., 2018) (EMD), EEMD (Santhosh et al., 2018), empirical wavelet transform (Hu and Wang, 2015) (EWT), variational mode decomposition (Dragomiretskiy and Zosso, 2014) (VMD), singular spectrum analysis (Yu et al., 2017a) (SSA), etc. In Ref. (Han et al., 2019), a prediction method combining VMD and LSTM (VMD-LSTM) is proposed to improve the accuracy of multi-step wind power prediction. Similar to other combined models, VMD is used to decompose wind power data into trend, periods and random components; then, LSTM is used to deeply learn the characteristics of the three components. Some studies combine different decomposition methods to improve the overall prediction performance. Sun et al. (Sun et al., 2021) proposes a secondary decomposition strategy, which combines EWT and VMD to comprehensively filter out the instability and noise of the wind power sequence. In Ref. (Yu et al., 2017b), a hybrid model that combines EMD, SSA and Elman uses SSA to reprocess the highest-frequency component of the EMD component to improve the accuracy of prediction.

Data of numerical weather prediction (NWP) includes forecast data such as wind speed, wind direction, humidity, etc., which including features related to wind power (Wu et al., 2021). Using NWP data as a feature input can improve the prediction performance of wind power (Wang et al., 2021). The information contained in NWP data is complex and diverse. Effective methods need to be used to extract the dynamic features of NWP data as input to the predictive model. Hao et al. (Yin et al., 2021) designed a feature extractor called CNNs-LSTM, which uses CNN and LSTM to extract meteorological and temporal features of wind farms. Zang et al. (Zang et al., 2020b) proposed a CNN-LSTM model, which applies CNN to extract spatial features from meteorological data, and LSTM extracts temporal features from historical solar irradiance time series data. In (Cheng et al., 2022), a model based on CNN and LSTM is proposed for prediction of satellite-derived solar irradiance and improves its learning ability relative to traditional learning models. In Ref. (Wang et al., 2022), a load probability density forecasting model based on convolutional long short-term memory (ConvLSTM) is proposed to capture the deep information. CNN has powerful capabilities of feature extraction and non-linear expression, which can effectively extract important information from input data (Zang et al., 2020a). GRU has powerful capabilities of time series analysis and learning, and can effectively extract the time series features of the sequence. This study uses the feature extraction module that combines CNN and Bi-directional GRU (BGRU) to extract features from NWP data.

There are many studies based on wind power point forecasting, but there is a lack of wind power probability forecasting models that combine the advantages of combinatorial decomposition techniques and deep neural networks. Reliable probabilistic predictions and accurate point predictions of wind power need to be achieved simultaneously. Based on the above analysis, this study proposes a novel wind power probabilistic prediction model combining VMD, SSA, QR, CNN, and BGRU (VMDS-QR-CBG). First, wind power history sequence is processed by VMDS, where the SSA improves VMD though making further operation on the high-frequency components of the VMD. Next, the BGRU extracts the timing features of the low-frequency components of the wind power; CBG is used to extract the complex dynamic features of high-frequency components and NWP data respectively. Then, BGRU further extracts deep time-series features of all the extracted features, and establishes a QR model to obtain predicted values at different quantile conditions. Finally, the probability density function curve (PDF) of wind power is obtained by kernel density estimation (KDE) to achieve probabilistic prediction. The model can also achieve reliable point and interval prediction. According to the discussions above, the main contributions of this study can be summarized as follows:

- A novel combined data decomposition method called VMDS is proposed, which combines VMD and SSA to reduce the complexity of the original wind power sequence and further extract the high-frequency trend components. The input data processed by VMDS helps to improve the accuracy of the prediction model.
- A feature extractor called CBG that combines CNN and BGRU is used to extract features from complex data, including meteorological data and high-frequency data.
- A hybrid VMDS-QR-CBG model with three input channels is developed by combining VMDS and CBG and QR to achieve reliable wind power point and probabilistic prediction.

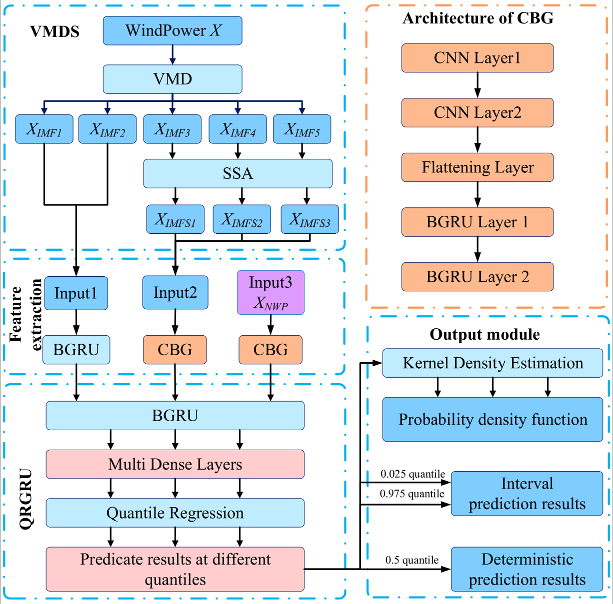

FIGURE 1
Structure diagram of VMDS-QRCNN-BGRU.

2 Proposed methodology

2.1 General process of the proposed method

This section introduces the proposed model of wind power probabilistic prediction. The flow chart of VMDS-QR-CBG is shown in Figure 1, where the forecasting process can be summarized as follows:

- VMDS for data decomposition.

The wind power sequence is decomposed into several components using the proposed data decomposition method VMDS. The low-frequency components and high-frequency trend components are used as inputs to different channels.

- Feature extraction.

The input of the proposed model has three kinds of data, namely VMD components X_{IMF}, SSA components X_{IMFS} and NWP data X_{NWP}. The features of the data are extracted by different modules. The features extracted by each module are combined into X_f, which is used as the input of subsequent modules.

- Probabilistic forecasting.

A probability prediction module based on QR and BGRU is constructed, and prediction values under different quantiles are obtained according to fusion features X_f. At the same time, deterministic forecast results and interval forecast results are obtained. KDE is used to obtain the PDF curve of the predicted value.

2.2 Combination decomposition VMDS

VMDS is a combined decomposition method composed of VMD and SSA. Considering the degree of data utilization and the training cost of the model, VMDS is used to decompose the wind power data into 5 components. The main process is:

- VMD is used to decompose the wind power sequence X into sub-sequences, X_{IMF1} to X_{IMF5}, where X_{IMF1}, and X_{IMF2} are low-frequency components, X_{IMF3} to X_{IMF5} are high frequency-components.
- SSA is used to extract trend components of X_{IMF3} to X_{IMF5} to reduce the complexity of the sequence and highlight the timing feature of the sequence. The trend components are defined as X_{IMFS1}, X_{IMFS2}, and X_{IMFS3}.

The principles of VMD and SSA are as follows.

2.2.1 Variational mode decomposition

VMD technology is a non-recursive signal multi-resolution decomposition technology, which can decompose a complex signal S into q modal functions with different center frequencies (Hu and Wang, 2015). The specific steps of VMD are as follows:

Calculate the unilateral frequency spectrum of each mode based on the Hilbert transform method. Perform exponential correction for each modal component to shift its phase to the center frequency of the modal itself.

According to the Gaussian smoothness of the frequency-shifted signal, the bandwidth is estimated to minimize the sum of the estimated bandwidth of each sub-signal.

$$\begin{aligned} &\min_{u_k,\omega_k}\left\{\sum_k\left\|\partial t\left[\left(\delta(t)+\frac{j}{\pi t}\right)*u_k(t)\right]e^{-j\omega_k t}\right\|_2\right\} \\ &s.t.\ \ S(t)=\sum_k u_k(t) \end{aligned} \tag{1}$$

The augmented Lagrangian function is introduced to turn the constrained variational problem into an unconstrained problem:

$$\begin{aligned} &L(u_k,\omega_k,\lambda)=\beta\sum_k\left\|\partial t\left[\left(\delta(t)+\frac{j}{\pi t}\right)*u_k(t)\right]e^{-j\omega_k t}\right\|_2 \\ &+\left\|S(t)-\sum_k u_k(t)\right\|_2+<\lambda(t),S(t)-\sum_k u_k(t)> \end{aligned} \tag{2}$$

Solve the Eq. 2 by the alternating direction multiplier method, obtain the required q modal components u_k, and the center frequency ω_k.

2.2.2 Singular spectrum analysis

SSA constructs a trajectory matrix based on the observed time series, and decomposes and reconstructs the trajectory matrix, thereby extracting sub-sequences representing different components of the original time series (Dragomiretskiy and Zosso, 2014). The specific steps of SSA are as follows:

Select the appropriate embedding dimension L to transform the time series $X_n = (x_1, ..., x_n)$ into the trajectory matrix A.

$$A=\begin{pmatrix} x_1 & x_2 & x_3 & \cdots & x_{M-L+1} \\ x_2 & x_3 & x_4 & \cdots & x_{M-L+2} \\ \vdots & \vdots & \vdots & \cdots & \vdots \\ x_L & x_{L+1} & x_{L+2} & \cdots & x_M \end{pmatrix} \tag{3}$$

Perform singular value decomposition (SVD) on matrix A, and the SVD formula is as follows:

$$A=\sum_{i=1}^{rank(X)}\sqrt{\lambda_i}U_iV_i^T \tag{4}$$

Use the diagonal averaging method to transform the decomposition matrix A into a matrix of length M. The formula for diagonal averaging is as follows:

$$x_k^*=\begin{cases} \dfrac{1}{k}\displaystyle\sum_{m=1}^{k}x^*_{m,k-m+1} & 1\le k<L^* \\ \dfrac{1}{L^*}\displaystyle\sum_{m=1}^{L^*}x^*_{m,k-m+1} & L^*\le k<Q^* \\ \dfrac{1}{M-k+1}\displaystyle\sum_{m=k-Q^*+1}^{M-k+1}x^*_{m,k-m+1} & Q^*\le k<M \end{cases} \tag{5}$$

Where the number of vectors $Q = M - L + 1$, $L^* = \min(L, Q)$, $Q^* = \max(L, Q)$.

2.3 Feature extraction based on deep neural network

The DNNs mainly used in the model are CNN and BGRU. Construct different feature extraction modules for different inputs:

- The feature extraction of X_{IMF} mainly considers the trend component X_{IMF1} and the periodic component X_{IMF2}. Their fluctuation frequency is low and the trend is obvious. Therefore, a two-layer BGRU is used to extract the features of X_{IMF}.
- The fluctuation frequency of X_{IMFS} is high and the trend is not obvious. Therefore, the feature extraction module that combines CNN and BGRU (CBG) is used to extract the

complex dynamic features of X_{IMFS}. The structure of CBG is cascaded, mainly including two layers of CNN and two layers of BGRU.

- X_{NWP} contains many non-linear and low-correlation factors. The CBG module is used to extract the spatiotemporal features of the impact of X_{NWP} on wind power.

The principles of CNN and BGRU are as follows.

2.3.1 Convolutional neural network

CNN is a DNN with pooling operation, local connection, and weight sharing based on convolution operation. It is widely used to extract high-order features from complex data. 1D-CNN structure mainly includes convolutional layer, pooling layer, and fully connected layer (Huang et al., 2022).

The function of the convolutional layer is to extract features from the input data by scanning through the convolution kernel. The convolution formula is shown in Eq. 6. The function of the pooling layer is to extract the convolutional layer. The features of the feature vector are sampled, and while retaining the main information of the feature vector, it can reduce the dimension of the feature vector and the complexity of the network. The fully connected layer is mainly used to integrate the features extracted by the network, and then output the final feature vector of a specific dimension after processing methods such as activation functions. The overall calculation formula is shown in Eq. 7.

$$y_p^l = r\left(\sum_{q\in T_{l-1}} x_q^{l-1} * v_p^l + b_p^l\right),\quad p \in T_l \tag{6}$$

$$y_j^l = \sigma\left(\sum_{i=1}^{N_{l-1}} W_{ij} x_i^{l-1} + b_j^l\right) \tag{7}$$

2.3.2 Bi-directional gated recurrent unit

GRU optimizes and improves LSTM, reduces network complexity, and maintains a learning performance equivalent to LSTM (Peng et al., 2020). The gated loop unit in GRU has two gate structures: an update gate and a reset gate. The update gate controls the degree of retention of the state at the previous moment in the current state, and the reset gate controls the degree of combination of the current input and the state at the previous moment. The calculation formula of the hidden layer state h_t of GRU is as follows:

$$z_t = \sigma\left(W_{zx}x_t + W_{zh}h_{t-1} + b_z\right) \tag{8}$$

$$r_t = \sigma\left(W_{rx}x_t + W_{rh}h_{t-1} + b_r\right) \tag{9}$$

$$\tilde{h}_t = \tanh\left(W_{\tilde{h}h}\left(r_t \odot h_{t-1}\right) + W_{\tilde{h}x}x_t + b_{\tilde{h}}\right) \tag{10}$$

$$h_t = \left(1 - z_t\right) \odot h_{t-1} + z_t \odot \tilde{h}_t \tag{11}$$

GRU can make full use of the information of the current and previous moments, but cannot obtain the unit information after the current moment. BGRU combines two GRU networks with opposite timings to fully obtain the hidden information before and after the current unit, and further mine timing features.

2.4 Probabilistic prediction module

According to the fusion features obtained by the feature extraction module, a prediction model based on BGRU and QR is constructed.

Use BGRU to extract deeper timing features of X_f, and send the results to the multi dense layers for processing. The process can be expressed as:

$$y = f\left(W, b, X_{in}\right) \tag{12}$$

Construct the quantile loss function as in Eq. 13 to realize quantile regression.

$$\tilde{W}(\tau), \tilde{b}(\tau) = \arg\min_{W,b} \sum_{t=1}^{n} \rho_\tau\left(y_t - f\left(W(\tau), b(\tau), X_t\right)\right) \tag{13}$$

$$\rho_\tau(\mu) = \mu\left(\tau - I(\mu)\right),\quad I(\mu) = \begin{cases} 1, & \mu < 0 \\ 0, & \mu \geq 0 \end{cases} \tag{14}$$

Where the quantile τ is continuously taken in the range of (0,1), the Adam gradient descent algorithm is used to optimize Eq. 13 to obtain the optimal estimated values of network parameters $W(\tau)$ and $b(\tau)$ under different quantile conditions. Furthermore, the predicted value of wind power at different quantile conditions can be obtained according to Eq. 14.

$$\tilde{y}(\tau) = f\left(\tilde{W}(\tau), \tilde{b}(\tau), X_{in}\right) \tag{15}$$

After obtaining the predicted values at different quantiles, the deterministic prediction results and interval prediction results can be obtained, which are $\tilde{y}(0.5)$ and $[\tilde{y}(\tau_{down}), \tilde{y}(\tau_{up})]$ respectively. τ_{down} and τ_{up} are determined by the confidence of the prediction interval. $\tau_{down} = 0.5\alpha$ and $\tau_{up} = 1 - 0.5\alpha$ while the prediction interval confidence is $1 - \alpha$.

KDE is a classic non-parametric estimation method that does not require prior assumptions (Zhang et al., 2019). Provided at a given point y, the prediction value of the prediction model at each quantile is $\hat{y} = [\hat{y}_1, \hat{y}_2, \ldots, \hat{y}_N]$, the probability density function of y at a formula:

$$P(y) = \frac{1}{nB}\sum_{i=1}^{n} K\left(\frac{y_i - y}{B}\right) \tag{16}$$

Where B is the bandwidth, using grid search with cross-validation to select the appropriate bandwidth. This study uses the Epanechnikov as kernel function, the formula is as follows:

$$K(\mu) = \begin{cases} \frac{3}{4}\left(1 - \mu^2\right), & \mu \in [-1, 1] \\ 0, & \mu \notin [-1, 1] \end{cases} \tag{17}$$

TABLE 1 The basic information of data set.

Numbers	Mean (MW)	Std (MW)	Max (MW)	Min (MW)
1,440	11.15	7.67	48.44	0

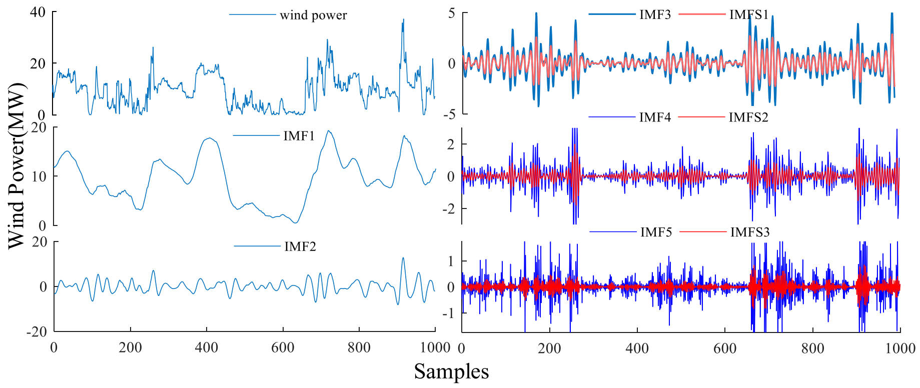

FIGURE 2
Original wind power and VMDS decomposition results.

KDE is used to fit the predicted values at different quantiles to obtain the final PDF to achieve probability density prediction.

3 Performance indicators

3.1 Evaluation metrics of deterministic prediction

This study uses root mean square error (RMSE) and normalized mean absolute percentage error (NMAPE) to evaluate the deterministic prediction performance of the prediction model (Zhang et al., 2019). The formulas are as follow:

$$RMSE = \sqrt{\frac{1}{n}\sum_{i=1}^{n}(y_i - \hat{y}_i)^2} \tag{18}$$

$$NMAPE = \frac{1}{n}\sum_{i=1}^{n}\frac{|y_i - \hat{y}_i|}{\max\limits_{i=1}^{n} y_i} \times 100\% \tag{19}$$

The smaller the RMSE and NMAPE values, the better the performance of the deterministic prediction model.

TABLE 2 The main parameter settings of VMDS-QR-CBG.

Algorithm	Parameter	Value
CNN1 of CBG	kernel size	2 × 2
	Number of kernel	16
CNN2 of CBG	kernel size	2 × 2
	Number of kernel	32
BGRU of CBG	number of hidden layer nodes	32
BGRU of QRGRU	number of hidden layer nodes	64
Dense	number of hidden layer nodes	128,64
Dropout	rate	0.2

3.2 Evaluation metrics of interval prediction

This study uses average coverage error (ACE), prediction interval normalized average width (PINAW), and interval sharpness (IS) to evaluate interval prediction performance (Zhang et al., 2019). The formula is as follows:

$$ACE = \left(\frac{1}{n}\sum_{i=1}^{n}\begin{cases}1, & y_i \in [l_i^{\alpha}, u_i^{\alpha}]\\ 0, & y_i \notin [l_i^{\alpha}, u_i^{\alpha}]\end{cases} - (1-\alpha)\right) \times 100\% \tag{20}$$

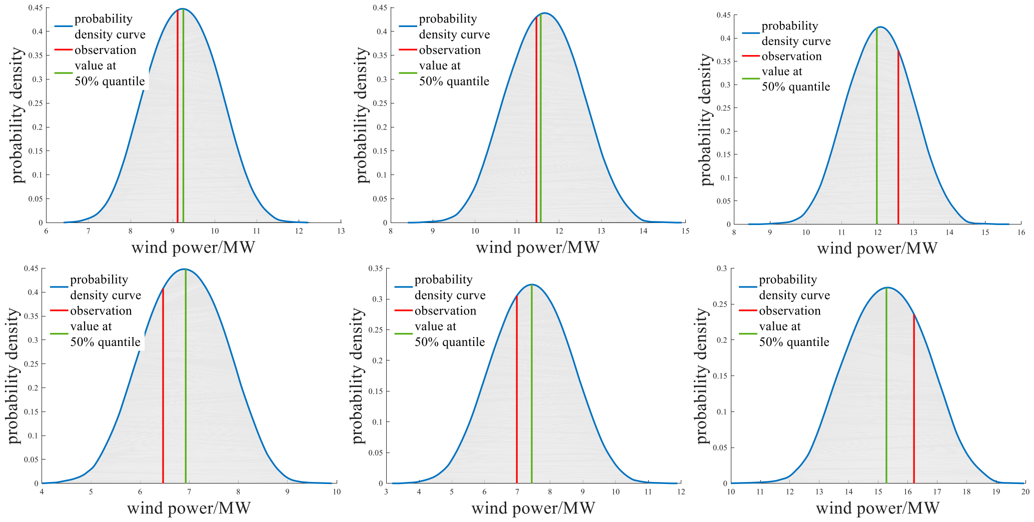

FIGURE 3
PDF at different moments predicted by VMDS-QR-CBG.

TABLE 3 The values of the CRPS of different models.

VMDS-QR-CBG	VMD-QRCNN-BGRU	VMDS-BGRU	QRCNN-BGRU	QRGRU	QRCNN
0.621	0.713	0.686	0.696	0.716	0.722

$$PINAW = \frac{1}{ns}\sum_{i=1}^{n}\left(u_i^\alpha - l_i^\alpha\right) \tag{21}$$

$$IS = \frac{1}{n}\sum_{i=1}^{n}\begin{cases} -2\alpha\left(u_i^\alpha - l_i^\alpha\right), & y_i \in \left[l_i^\alpha, u_i^\alpha\right] \\ -2\alpha\left(u_i^\alpha - l_i^\alpha\right) - 4\left(l_i^\alpha - y_i\right), & y_i < l_i^\alpha \\ -2\alpha\left(u_i^\alpha - l_i^\alpha\right) - 4\left(y_i - u_i^\alpha\right), & y_i > u_i^\alpha \end{cases} \tag{22}$$

ACE represents the coverage of the actual value in the prediction area under a given confidence interval, and reflects the reliability of the interval prediction. PINAW is used to measure the width of the prediction interval and reflects the acuity of interval prediction. IS measures the comprehensive performance of interval prediction, because ACE and PINAW are a pair of contradictory indicators.

3.3 Evaluation metrics of probabilistic prediction

This study uses continuous ranked probability score (CRPS) to evaluate probabilistic prediction performance (Peng et al., 2021). The formula is as follows:

$$CRPS = \frac{1}{n}\sum_{i=1}^{n}\int_{-\infty}^{+\infty}\left[F\left(y_i\right) - I\left(\hat{y}_i - y_i\right)\right]^2 \mathrm{d}y_i \tag{23}$$

$$F\left(y_i\right) = \int_{-\infty}^{y_i} P\left(x_i\right)dx_i \tag{24}$$

The smaller the CRPS, the better the overall performance of the model's probabilistic prediction and the higher the reliability.

4 Testing results and discussions

4.1 Datasets

The original data comes from a wind farm in Jiangsu, China, which contains the wind power series data and NWP data for the whole year of 2017. Wind power data is collected every 15 min, so there are 96 data points in a day. Table 1 shows the basic information of the data set. The dataset has strong nonlinearity and non-stationarity. NWP data includes wind speed at different heights, wind direction at different heights, temperature, air pressure, humidity, etc.

In the experiment of this study, the input dimensions of wind power data and NWP data are both set to 10. The first 80% of each data set is used as the training set, and the last 20% is used as the test set.

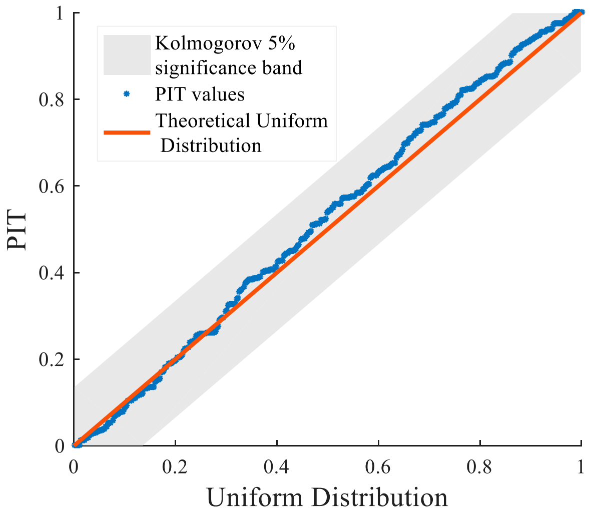

FIGURE 4
QQ plot of probability prediction results of VMDS-QR-CBG.

4.2 Result of VMDS

The wind power sequence is processed by VMDS to obtain two low-frequency components and three high-frequency components. The partial decomposition result of Dataset is shown in Figure 2, where IMF1 to IMF5 are the results of VMD, and IMFS1 to IMFS3 are the results of further processing by SSA. VMD parameters are set as: penalty parameter is 1,000; initial center frequency is 0; convergence criterion is 10^{-6}. SSA parameters are set as: Embedded window length is 10.

4.3 Models and parameter settings

Several predictive models were proposed as comparison models to verify the superiority of the comprehensive predictive performance of VMDS-QR-CBG. The models are VMD-QR-CBG, VMDS-QRGRU, QRCNN-GRU, QRLSTM, QRGRU. VMD-QR-CBG is used to illustrate the superiority of VMDS. VMDS-QRGRU is used to reflect the effect of proposed module of multi-source feature extraction. QRCNN-GRU, QRLSTM, QRGRU are common deep learning models that do not use data decomposition technology, which reflect the overall performance of the proposed combined model.

The main layer design and hyperparameter settings of VMDS-QR-CBG are shown in Table 2. The setting of the model parameters is obtained through multiple experiments and is suitable for the scale of the dataset. The settings of the hyperparameters of the comparison models are kept as uniform as possible to reflect the superiority of the proposed combined model under a unified hyperparameter setting. The training configuration of the five models is the same: the training round is 200, the optimizer is Adam, the early stop waiting round is 10, and the validation set ratio is 0.1. The model proposed in this study sets 199 quantile points, and quantile points $\tau = [0.005, 0.01, \ldots, 0.99, 0.995]$.

4.4 Analysis of prediction result

4.4.1 Probability density prediction results

The predicted value at different quantiles obtained by the models using QR, can estimate the PDF of each observation point through KDE. Figure 3 shows the PDFs of six randomly selected observation points for the dataset. Figure 3 shows that most of the actual values are close to the peak of the PDF and close to the predicted median. This shows that the proposed probabilistic prediction model is effective.

Table 3 shows the value of the CRPS of the probabilistic prediction results of different models. Among them, the CRPS of VMDS-QR-CBG is the smallest, indicating that the comprehensive performance of the probabilistic prediction of VMDS-QR-CBG is the highest.

By calculating the probability integral transformation (PIT) of the predicted value and analyzing whether it obeys a uniform distribution, the reliability of the probabilistic prediction model can be verified. The QQ chart is used to visually analyze whether the PIT value of the prediction model result obeys a uniform distribution.

Figure 4 is the QQ plot of the PIT values of the probabilistic prediction results of VMDS-QR-CBG. The red straight line is the uniform distribution of the theoretical situation, and the blue is the probability distribution of the

TABLE 4 Interval predication error statistics of different models.

Indicators	VMDS-QR-CBG	VMD-QRCNN-BGRU	VMDS-BGRU	QRCNN-BGRU	QRGRU	QRCNN
PINAW95%	0.137	0.161	0.172	0.189	0.236	0.219
ACE95%	1.197	1.283	2.972	2.297	2.253	1.621
IS95%	−0.249	−0.307	−0.291	−0.321	−0.432	−0.401

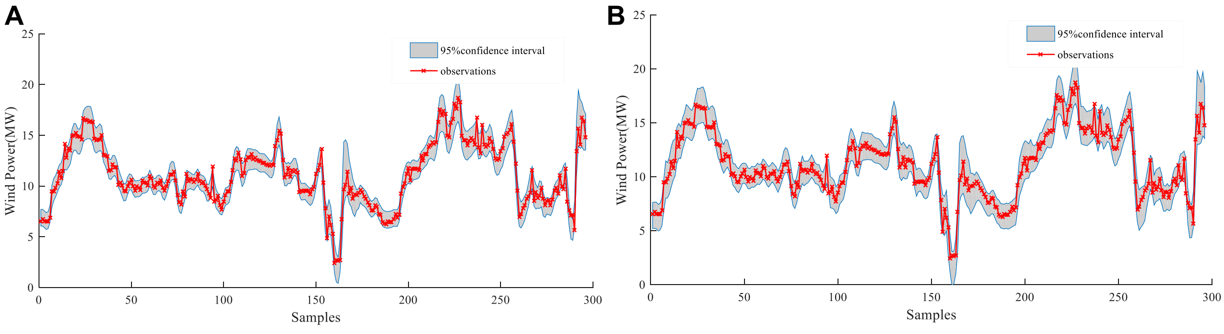

The interval prediction result of VMDS-QR-CBG

The interval prediction result of VMD-QRCNN-BGRU

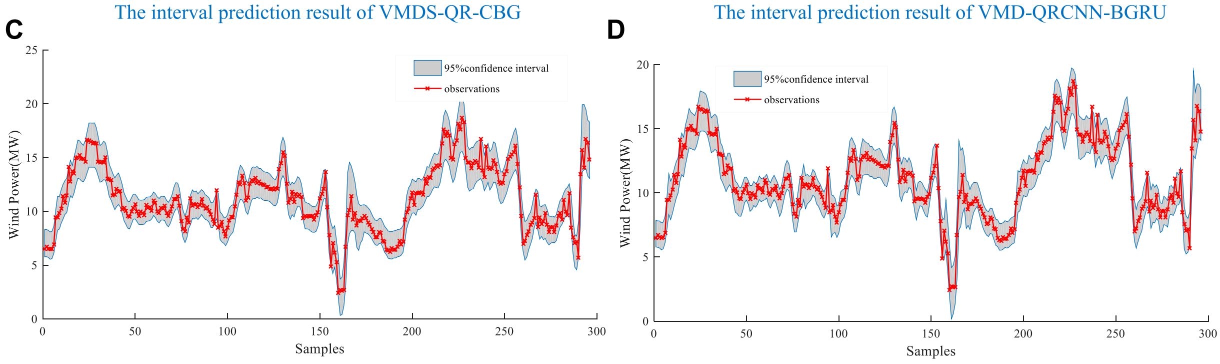

The interval prediction result of VMDS-BGRU

The interval prediction result of QRCNN-BGRU

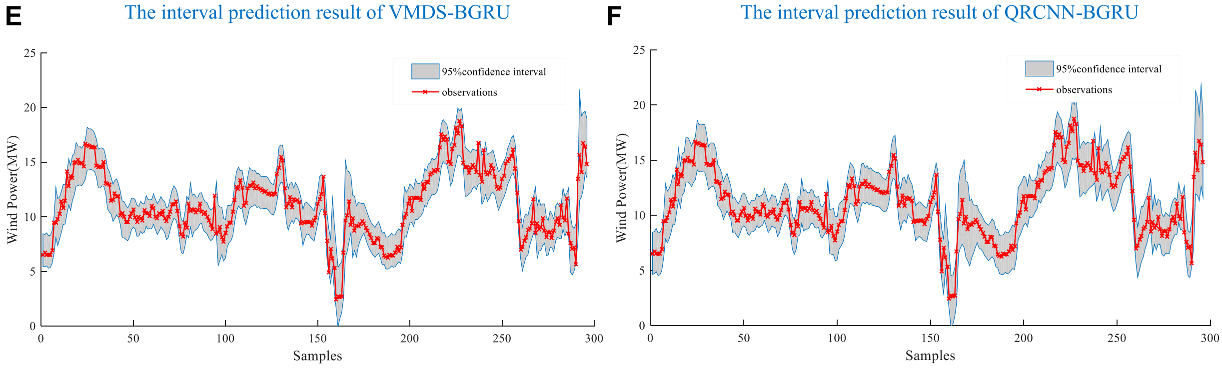

The interval prediction result of QRGRU

The interval prediction result of QRCNN

FIGURE 5
Interval prediction results of Datast1 of different models.

predicted value of the PIT value. It can be seen from Figure 4 that the distribution of the PIT values are in the Kolmogorov 5% significant band, which shows that the probabilistic prediction results of VMDS-QR-CBG are reliable.

4.4.2 Analysis of interval prediction results

Excellent interval prediction performance requires that the acuity of prediction should be improved as much as possible

TABLE 5 Deterministic predication error statistics of different models.

Indicators	VMDS-QR-CBG	VMD-QRCNN-BGRU	VMDS-BGRU	QRCNN-BGRU	QRGRU	QRCNN
RMSE/MW	0.492	0.570	0.538	0.587	0.718	0.726
NMAPE/%	1.940	2.240	2.116	2.261	2.639	2.713

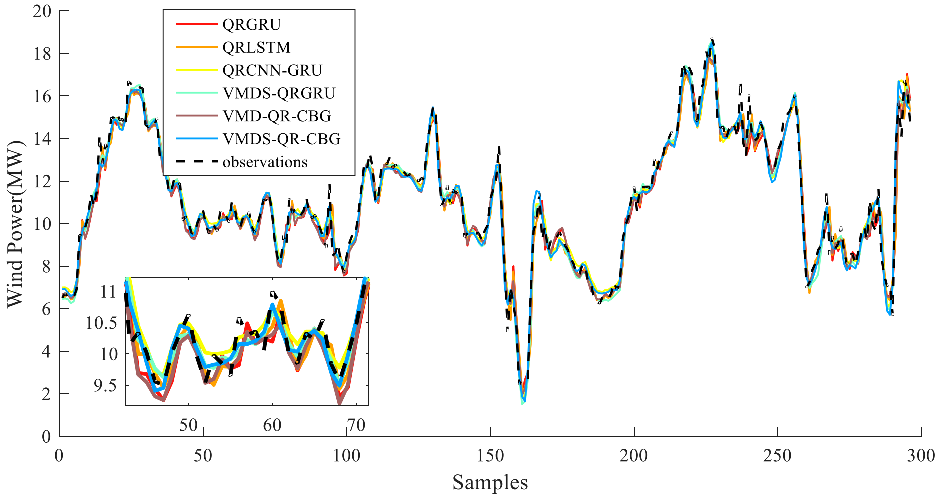

FIGURE 6
Point prediction results of Datast1 of different models.

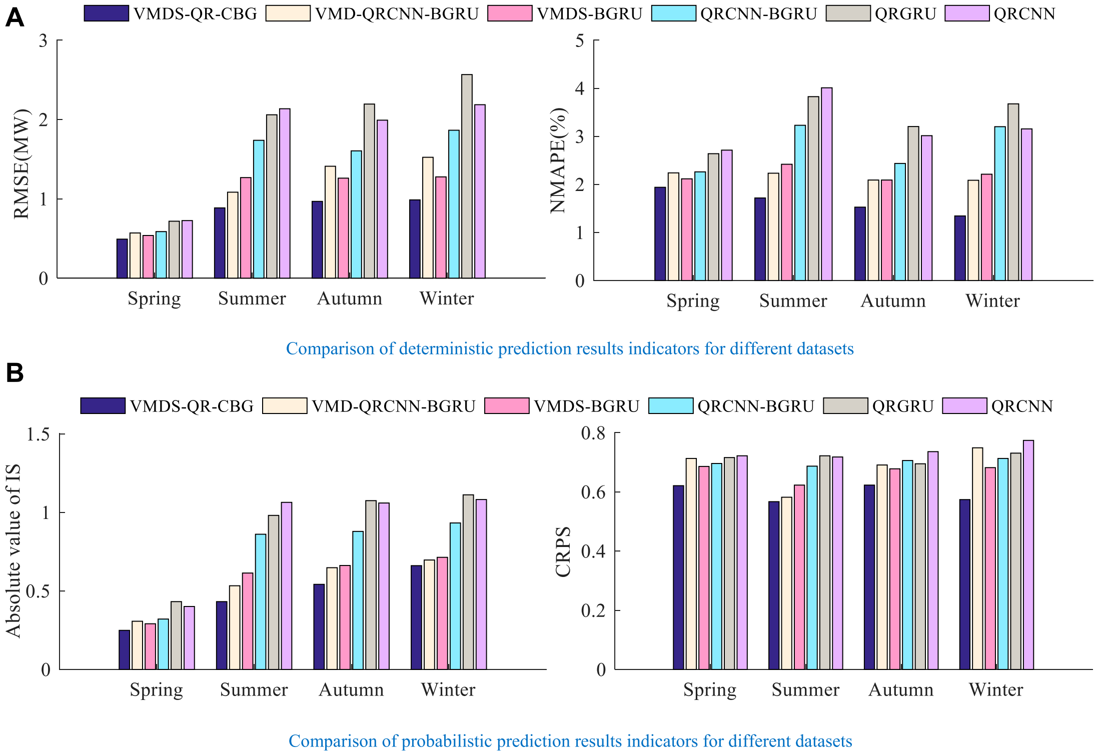

FIGURE 7
Comparison of prediction results indicators for different datasets.

while ensuring the reliability of prediction. Table 4 shows the error statistics of the interval prediction of each model, including evaluation indicators: PINAW, ACE, IS. The following conclusions can be drawn: Compared with models using data decomposition technology, the evaluation indicators of QRCNN-GRU, QRLSTM, QRGRU models are much inferior. The ACE value of the models without the decomposition technology is generally higher than that of the model using the decomposition technology. However, the PINAW value is much lower than the model using decomposition technology. This shows that the prediction interval of models such as QRCNN-GRU is relatively wide, so that the reliability of prediction is improved, but the acuity of prediction is reduced, thereby reducing the overall performance of interval prediction. The IS values of the model using VMD or VMDS are 0.1–0.5 lower than the IS value of models such as QRCNN-GRU. In summary, compared to traditional models that do not use data decomposition technology, the interval prediction of VMDS-QR-CBG has better performance.

The comparison of the interval prediction performance of VMDS-QR-CBG and VMD-QR-CBG is to verify the effectiveness of the proposed VMDS. The ACE value of VMDS-QR-CBG is lower than that of VMD-QR-CBG, which shows that the reliability of VMD-QR-CBG is slightly higher than that of VMDS-QR-CBG. However, the PINAW value of VMDS-QR-CBG is respectively lower than VMD-QR-CBG by 14.9%. The IS value of VMDS-QR-CBG is respectively higher than VMD-QR-CBG by 18.8%. The above analysis shows that the proposed VMDS method is helpful to the improvement of the model's interval prediction performance.

The comparison between the interval prediction performance of VMDS-QR-CBG and VMDS-QR-GRU is to verify the effectiveness of the proposed combined model. The PINAW value of VMDS-QR-CBG is respectively lower than VMDS-QR-GRU by 20.3%. Moreover, the IS value of VMDS-QR-CBG is respectively higher than VMDS-QR-GRU by 14.4%. The above analysis can show that the proposed combination method using CBG to extract the dynamic features of the NWP data and SSA components is effective.

The interval prediction results are shown in Figure 5. All models have good prediction performance, but the interval width of VMDS-QR-CBG is significantly narrower than that of other models. VMDS-QR-CBG can both ensure reliability and high sensitivity in wind power with large fluctuations.

4.4.3 Analysis of deterministic prediction results

This study selects the median of the probabilistic prediction results of each model as the deterministic prediction result of wind power.

Table 5 shows that the RMSE and NMAPE of VMDS-QR-CBG are the lowest. RMSE decreased by 13.6, 8.6, 16.2, 31.5 and 32.2% respectively compared with other models. NMAPE decreased by 0.300, 0.176, 0.312, 0.699 and 0.773 respectively compared with other models.

Figure 6 is a comparison diagram between the predicted values of each model and the actual value of wind power. Figure 6 shows that each model can accurately predict the change trend of wind power, and the predicted value of the VMDS-QR-CBG model is the closest to the actual value of wind power. In summary, VMDS-QR-CBG can better ensure accurate deterministic prediction of wind power.

4.4.4 Generality verification

Data sets of different seasons are selected as the prediction objects to verify the versatility of the model in different meteorological conditions. Figure 7 shows the index comparison of the prediction results of different models for the four datasets. Both point predictors and probabilistic indicators of the proposed model are optimal in different datasets, which indicates that the proposed model has high generality.

5 Conclusion

This study proposes a combined model of wind power probabilistic prediction based on combined decomposition and QR and CBG, namely VMDS-QR-CBG. The multi-channels input data of the model is constructed by VMDS, which can reduce the complexity of the data and improve the prediction ability of the model. CBG has powerful feature extraction ability, which can improve the accuracy of the whole model compared with the traditional model. Finally, QR and KDE combine VMDS and CBG to realize probabilistic prediction. Compared with the traditional model, VMDS-QR-CBG has better comprehensive performance in wind power prediction. The proposed combined model can achieve high reliability and acuity interval prediction and reliable and effective probabilistic prediction while ensuring the accuracy of point prediction. The proposed model combines a variety of methods, and the structure of the model is complex. The model can attempt to be optimized for larger scale wind power forecasts.

Data availability statement

The raw data supporting the conclusions of this article will be made available by the authors, without undue reservation.

Author contributions

Conceptualization, ZZ; methodology, ZZ and YX; original draft preparation, ZZ, YX, and JW; review and editing, ZZ, YL, and JG; supervision, HZ; project administration, ZZ, and HZ;

funding acquisition, ZZ All authors have read and agreed to the published version of the manuscript.

Conflict of interest

The authors declare that the research was conducted in the absence of any commercial or financial relationships that could be construed as a potential conflict of interest.

Publisher's note

References

Amini, M. H., Kargarian, A., and Karabasoglu, O. (2016). ARIMA-based decoupled time series forecasting of electric vehicle charging demand for stochastic power system operation. *Electr. Power Syst. Res.* 140, 378390. doi:10.1016/j.epsr.2016.06.003

Bokde, N., Feijoo, A., and Kulat, K. (2018). Analysis of differencing and decomposition preprocessing methods for wind speed prediction. *Appl. Soft Comput.* 71, 926938. doi:10.1016/j.asoc.2018.07.041

Cheng, L., Zang, H., Wei, Z., Ding, T., Xu, R., and Sun, G. (2022). Short-term solar power prediction learning directly from satellite images with regions of interest. *IEEE Trans. Sustain. Energy* 13 (1), 629639. doi:10.1109/TSTE.2021.3123476

Demolli, H., Dokuz, A. S., Ecemis, A., and Gokcek, M. (2019). Wind power forecasting based on daily wind speed data using machine learning algorithms. *Energy Convers. Manag.* 198, 111823. doi:10.1016/j.enconman.2019.111823

Dragomiretskiy, K., and Zosso, D. (2014). Variational mode decomposition. *IEEE Trans. Signal Process.* 62, 531544. doi:10.1109/TSP.2013.2288675

Erdem, E., and Shi, J. (2011). ARMA based approaches for forecasting the tuple of wind speed and direction. *Appl. Energy* 88, 14051414. doi:10.1016/j.apenergy.2010.10.031

Georgilakis, P. (2008). Technical challenges associated with the integration of wind power into power systems. *Renew. Sustain. Energy Rev.* 12, 852863. doi:10.1016/j.rser.2006.10.007

Global Wind Energy Council (GWEC) (2022). Global wind report 2022. Available at: https://gwec.net/global-wind-report-2022 (Accessed June 30, 2022).

Han, L., Zhang, R. C., Wang, X. S., Bao, A., and Jing, H. (2019). Multi-step wind power forecast based on VMD-LSTM. *IET Renew. Power Gener.* 13, 16901700. doi:10.1049/iet-rpg.2018.5781

He, Y. Y., and Li, H. Y. (2018). Probability density forecasting of wind power using quantile regression neural network and kernel density estimation. *Energy Convers. Manag.* 164, 374384. doi:10.1016/j.enconman.2018.03.010

He, Y. Y., and Wang, Y. (2021). Short-term wind power prediction based on EEMD-LASSO-QRNN model. *Appl. Soft Comput.* 105, 107288. doi:10.1016/j.asoc.2021.107288

Hong, Y. Y., and Satriani, T. R. A. (2020). Day-ahead spatiotemporal wind speed forecasting using robust design-based deep learning neural network. *Energy* 209, 118441. doi:10.1016/j.energy.2020.118441

Hu, J. M., and Wang, J. Z. (2015). Short-term wind speed prediction using empirical wavelet transform and Gaussian process regression. *Energy* 93, 14561466. doi:10.1016/j.energy.2015.10.041

Huang, R., Wang, X., Fei, F., Li, H., and Wu, E. (2022). Forecast method of distributed photovoltaic power generation based on EM-WS-CNN neural networks. *Front. Energy Res.* 10, 902722. doi:10.3389/fenrg.2022.902722

Jin, H. P., Shi, L. X., Chen, X. G., Qian, B., and Yang, B. (2021). Probabilistic wind power forecasting using selective ensemble of finite mixture Gaussian process regression models. *Renew. Energy* 174 (1), 1. doi:10.1016/j.renene.2021.04.028

Kisvari, A., Lin, Z., and Liu, X. L. (2021). Wind power forecasting - a data-driven method along with gated recurrent neural network. *Renew. Energy* 163, 18951909. doi:10.1016/j.renene.2020.10.119

Liu, L. J., and Liang, Y. J. (2021). Wind power forecast optimization by integration of CFD and Kalman filtering. *Energy Sources Part A Recovery Util. Environ. Eff.* 43, 1880-1896. doi:10.1080/15567036.2019.1668080

Liu, F. J., Li, C. S., Xu, Y. H., Tang, G., and Xie, Y. (2020). A new lower and upper bound estimation model using gradient descend training method for wind speed interval prediction. *Wind Energy* 24, 290304. doi:10.1002/we.2574

Lv, J. Q., Zheng, X. D., Pawlak, M., Mo, W., and Miskowicz, M. (2021). Very short-term probabilistic wind power prediction using sparse machine learning and nonparametric density estimation algorithms. *Renew. Energy* 177, 181192. doi:10.1016/j.renene.2021.05.123

Niu, Z. W., Yu, Z. Y., Tang, W. H., Wu, Q., and Reformat, M. (2020). Wind power forecasting using attention-based gated recurrent unit network. *Energy* 196, 117081. doi:10.1016/j.energy.2020.117081

Oh, B. K., Glisic, B., Kim, Y., and Park, H. S. (2019). Convolutional neural network-based wind-induced response estimation model for tall buildings. *Comput.-Aided. Civ. Inf. Eng.* 34, 843858. doi:10.1111/mice.12476

Peng, Z. Y., Peng, S., Fu, L. D., Lu, B., Tang, J., Wang, K., et al. (2020). A novel deep learning ensemble model with data denoising for short-term wind speed forecasting. *Energy Convers. Manag.* 207, 112524. doi:10.1016/j.enconman.2020.112524

Peng, X. S., Wang, H. Y., Lang, J. X., Li, W., Xu, Q., Zhang, Z., et al. (2021). EALSTM-QR: Interval wind-power prediction model based on numerical weather prediction and deep learning. *Energy* 220, 119692. doi:10.1016/j.energy.2020.119692

Ren, C., An, N., Wang, J. Z., Li, L., Hu, B., and Shang, D. (2014). Optimal parameters selection for BP neural network based on particle swarm optimization: a case study of wind speed forecasting. *Knowledge-Based Syst.* 56, 226239. doi:10.1016/j.knosys.2013.11.015

Santhosh, M., Venkaiah, C., and Kumar, D. M. V. (2018). Ensemble empirical mode decomposition based adaptive wavelet neural network method for wind speed prediction. *Energy Convers. Manag.* 168, 482493. doi:10.1016/j.enconman.2018.04.099

Sun, Z. X., Zhao, M. Y., Dong, Y., Cao, X., and Sun, H. (2021). Hybrid model with secondary decomposition, randomforest algorithm, clustering analysis and long short memory network principal computing for short-term wind power forecasting on multiple scales. *Energy* 221, 119848. doi:10.1016/j.energy.2021.119848

Sun, Y., Huang, Y., and Yang, M. (2022). Ultra-short-term wind power interval prediction based on fluctuating process partitioning and quantile regression forest. *Front. Energy Res.* 10, 867719. doi:10.3389/fenrg.2022.867719

Wang, H. Z., Li, G. Q., Wang, G. B., Peng, J. c., Jiang, H., and Liu, Y. T. (2017). Deep learning based ensemble approach for probabilistic wind power forecasting. *Appl. Energy* 188, 5670. doi:10.1016/j.apenergy.2016.11.111

Wang, K. J., Qi, X. X., Liu, H. D., and Song, J. (2018). Deep belief network based k-means cluster approach for short-term wind power forecasting. *Energy* 165, 840852. doi:10.1016/j.energy.2018.09.118

Wang, F., Xuan, Z., Zhen, Z., Li, K., Wang, T., and Shi, M. (2020). A day-ahead PV power forecasting method based on LSTM-RNN model and time correlation modification under partial daily pattern prediction framework. *Energy Convers. Manag.* 212, 112766. doi:10.1016/j.enconman.2020.112766

Wang, F., Lu, X., Mei, S., Su, Y., Zhen, Z., Zou, Z., et al. (2021). A satellite image data based ultra-short-term solar PV power forecasting method considering cloud information from neighboring plant. *Energy* 238, 121946. doi:10.1016/j.energy.2021.121946

Wang, Y., Wang, T., Chen, X., Zeng, X. J., Huang, J. J., and Tang, X. F. (2022). Short-term probability density function forecasting of industrial loads based on ConvLSTM-MDN. *Front. Energy Res.* 10, 891680. doi:10.3389/fenrg.2022.891680

Wu, Y. K., Wu, Y. C., Hong, J. S., Phan, L. H., and Phan, Q. D. (2021). Probabilistic forecast of wind power generation with data processing and numerical weather predictions. *IEEE Trans. Ind. Appl.* 57, 3645. doi:10.1109/TIA.2020.3037264

Yin, H., Ou, Z., Fu, J. J., Cai, Y., Chen, S., and Meng, A. (2021). A novel transfer learning approach for wind power prediction based on a serio-parallel deep learning architecture. *Energy* 234, 121271. doi:10.1016/j.energy.2021.121271

Yu, C. J., Li, Y. L., and Zhang, M. J. (2017b). Comparative study on three new hybrid models using elman neural network and empirical mode decomposition based technologies improved by singular spectrum analysis for hour-ahead wind speed forecasting. *Energy Convers. Manag.* 147, 7585. doi:10.1016/j.enconman.2017.05.008

Yu, C. J., Li, Y. L., and Zhang, M. J. (2017a). An improved wavelet transform using singular spectrum analysis for wind speed forecasting based on elman neural network. *Energy Convers. Manag.* 148, 895-904. doi:10.1016/j.enconman.2017.05.063

Yu, C. J., Li, Y. L., Bao, Y. L., Tang, H., and Zhai, G. (2018). A novel framework for wind speed prediction based on recurrent neural networks and support vector machine. *Energy Convers. Manag.* 178, 137145. doi:10.1016/j.enconman.2018.10.008

Yuan, X. H., Chen, C., Jiang, M., and Yuan, Y. (2019). Prediction interval of wind power using parameter optimized Beta distribution based LSTM model. *Appl. Soft Comput.* 82, 105550. doi:10.1016/j.asoc.2019.105550

Zang, H., Cheng, L., Ding, T., Cheung, K. W., Wei, Z., and Sun, G. (2020a). Day-ahead photovoltaic power forecasting approach based on deep convolutional neural networks and meta learning. *International Journal of Electrical Power and Energy Systems* 118, 105790. doi:10.1016/j.ijepes.2019.105790

Zang, H., Liu, L., Sun, L., Cheng, L., Wei, Z., and Sun, G. (2020b). Short-term global horizontal irradiance forecasting based on a hybrid CNN-LSTM model with spatiotemporal correlations. *Renew. Energy* 160, 2641. doi:10.1016/j.renene.2020.05.150

Zang, H., Xu, R., Cheng, L., Ding, T., Liu, L., Wei, Z., et al. (2021). Residential load forecasting based on LSTM fusing self-attention mechanism with pooling. *Energy* 229, 120682. doi:10.1016/j.energy.2021.120682

Zhang, Y. C., Liu, K. P., Qin, L., and An, X. (2016). Deterministic and probabilistic interval prediction for short-term wind power generation based on variational mode decomposition and machine learning methods. *Energy Convers. Manag.* 112, 208219. doi:10.1016/j.enconman.2016.01.023

Zhang, Z. D., Qin, H., Liu, Y. Q., Yao, L., Yu, X., Lu, J., et al. (2019). Wind speed forecasting based on quantile regression minimal gated memory network and kernel density estimation. *Energy Convers. Manag.* 196, 13951409. doi:10.1016/j.enconman.2019.06.024

Zhang, Y. G., Han, J. Y., Pan, G. F., Xu, Y., and Wang, F. (2021). A multi-stage predicting methodology based on data decomposition and error correction for ultra-short-term wind energy prediction. *J. Clean. Prod.* 292, 125981. doi:10.1016/j.jclepro.2021.125981

Zhou, M., Wang, B., Guo, S., and Watada, J. (2021). Multi-objective prediction intervals for wind power forecast based on deep neural networks. *Inf. Sci.* 550, 207220. doi:10.1016/j.ins.2020.10.034

Nomenclature

Indices

$\boldsymbol{k}$ Index of sub-sequence

$\boldsymbol{t}$ Index of time

$\boldsymbol{l}$ Index of layer

$\boldsymbol{\tau}$ The quantile point

$\boldsymbol{i}$ Index of sample

$\boldsymbol{p}/\boldsymbol{q}$ Index of channel

Parameters

$\boldsymbol{X_{IMF}}/\boldsymbol{X_{IMFS}}/\boldsymbol{X_{NWP}}$ The VMD components, SSA components and NWP data

$\boldsymbol{X}$ The historical wind power data input

$\boldsymbol{X_f}$ The fusion features

$u_k(t)$ The discrete sub-signal with different frequencies obtained by VMD

ω_k The center frequencies of sub-signal

$\delta(t)$ The unit impulse function

$S(t)$ The original complex signal to be decomposed

$\lambda(t)$ The Lagrangian multiplier value at time t

β The weight coefficient to ensure the accuracy of the reconstructed signal

$L(\cdot)$ The joint objective function

$\|\cdot\|_2$ The two-norm function

λ_i The i-th eigenvalue

$\boldsymbol{U_i}$ The eigenvector corresponding to the i-th eigenvalue

$\boldsymbol{V_i}$ The i-th principal component

y_p^l The output vector of the p-th channel of the l-th layer

x_q^{l-1} Input vector for the q-th channel of the l-1-th layer

T_l / T_{l-1} Number of channels for l-th layer and l-1-th layer

v_n^l The l-th layer the n-th convolution kernel vector

$r(\cdot)$ Activation function: rectified linear unit function

W_{ij} The weight between the i-th neuron and the j-th neuron

N_{l-1} The number of neurons in the l-1-th layer

b_j^l The bias of the j-th neuron

$\sigma(\cdot)$ Sigmoid activation function

z_t / r_t Output of update gate and reset gate

h_t The state of the hidden layer at time t

W_{zx} / W_{zh}/ b_z Weights and biases of update gate

W_{rx} / W_{rh}/ b_r Weights and biases of reset gate

tanh Hyperbolic tangent function

$\boldsymbol{X_{in}}$ The historical data input

$\boldsymbol{y}$ The wind power forecast output

$\boldsymbol{W}/\boldsymbol{b}$ The network weight and bias

$f(\cdot)$ A nonlinear function reflecting the relationship between X_{in} and y

$\boldsymbol{X_t}$ The input of the t-th sample

$\boldsymbol{y_t}$ The actual value of the wind power of the t-th sample

$\boldsymbol{f(W(\tau),b(\tau),X_i)}$ The predicted value of wind power at τ-quantile

$\boldsymbol{W(\tau)/b(\tau)}$ The network parameters related to τ-quantile

$\rho_\tau(\cdot)$ The check function

$I(\cdot)$ The indicative function

$\tilde{y}(\tau)$ The predicted value of wind power at the τ-quantile

$\boldsymbol{B}$ The bandwidth

$K(\cdot)$ The kernel function

$\boldsymbol{n}$ The number of test samples

$\hat{y}_i$ The predicted values output by the i-th sample

u_i^α / l_i^α The lower and upper bounds of the prediction of the i-th sample

α The significance level

$\boldsymbol{s}$ The difference between the max value and the min value of the actual value

$P(\cdot)$ The probability density function

$F(\cdot)$ The cumulative density function

frontiers | Frontiers in Energy Research

TYPE Original Research
PUBLISHED 06 September 2022
DOI 10.3389/fenrg.2022.965812

OPEN ACCESS

EDITED BY
Fei Wang,
North China Electric Power University,
China

REVIEWED BY
Taskin Jamal,
Ahsanullah University of Science and
Technology, Bangladesh
Haifeng Dai,
Tongji University, China

*CORRESPONDENCE
Jing Zhang,
opkl_5606@163.com

SPECIALTY SECTION
This article was submitted to Smart Grids,
a section of the journal
Frontiers in Energy Research

RECEIVED 10 June 2022
ACCEPTED 09 August 2022
PUBLISHED 06 September 2022

CITATION
Zhang J, Hou L, Diao X, Yang X, Tang P and Cao X (2022), Power allocation method of battery energy storage system considering state balance in smoothing photovoltaic power fluctuations.
Front. Energy Res. 10:965812.
doi: 10.3389/fenrg.2022.965812

Power allocation method of battery energy storage system considering state balance in smoothing photovoltaic power fluctuations

Jing Zhang[1]*, Lei Hou[2], Xiaohong Diao[1], Xin Yang[2], Panpan Tang[1] and Xiaobo Cao[2]

[1]China Electric Power Research Institute, Beijing Engineering Technology Research Center of Electric Vehicle Charging/Battery Swap, Beijing, China, [2]State Grid Hebei Electric Power Co., Ltd. Xiongan New District Power Supply Company, Baoding, Hebei, China

Aiming at the imbalances of SOC (state of charge, SOC) and SOH (state of health, SOH) for battery energy storage system (BESS) in smoothing photovoltaic power fluctuations, a power allocation method of BESS is proposed. Firstly, the hierarchical structure of the power allocation method is given, including acquisition of the grid-connected photovoltaic power reference and double-layer power allocation strategy for BESS. Secondly, a swing door trend algorithm optimized by the improved Aquila optimizer is devised and used to deal with the raw photovoltaic power to obtain the grid-connected signal. Next, the dynamic grouping principle considering the SOC and SOH of battery units is devised, and the double-layer power allocation method of BESS is designed in terms of the dynamic grouping results of battery units. Finally, the proposed power allocation method is simulated through actual data, and the results compared with other methods show that it can smooth photovoltaic power fluctuations more effectively, and the SOC and SOH can be balanced more quickly and accurately, which verifies its effectiveness.

KEYWORDS

smoothing photovoltaic power fluctuations, battery energy storage system, improved Aquila optimizer, state balance of battery units, power allocation

1 Introduction

Photovoltaic power generation has the characteristics of no pollution, no noise, and renewability, and it has attracted more and more attention around the world (Sharadga et al., 2020). The fluctuations of photovoltaic power caused by the random variations of solar radiation and ambient temperature will bring a significant challenge to the reliable and stable operation of the power system (De la Parra et al., 2015) (Dong et al., 2020). At the same time, it is not conducive to the increase in renewable energy consumption (Jaszczur et al., 2021) (Jaszczur and Hassan, 2020). The battery energy storage system

(BESS) has a fast and flexible capability in power regulation. Configuring a BESS for a photovoltaic power station can suppress the fluctuations of grid-connected photovoltaic power effectively. It can also increase the grid-connected capacity of photovoltaic energy and reduce the operating pressure of the power system (Rana et al., 2022) (Khezri et al., 2020).

To reduce the fluctuations of grid-connected photovoltaic power, it is first necessary to obtain the grid-connected photovoltaic power reference in terms of the grid-connected standard on the photovoltaic power. The current research is carried out mainly based on various filtering algorithms and other algorithms. The moving average algorithm and the double moving average algorithm are used in (Jiang and Hong, 2012) and (Prasad et al., 2022), respectively. The low-pass filtering algorithm considering the state of charge (SOC) of the energy storage system is designed in (Huixiang et al., 2020) and (Syed et al., 2020). However, the low-pass filtering algorithm has a delay problem that is difficult to overcome. Another difficulty directly affecting the inhibition of the power fluctuations is the selection of the time constant in the low-pass filter. A fixed-order empirical mode decomposition is devised in Liu et al., 2022, but it does not fully consider the volatility of the photovoltaic power, and the large fluctuations exist sometimes. An optical storage model is proposed to suppress the power fluctuations and corresponding control methods is devised to solve the intermittent output of new energy for grid connection. In the model, the constraints of charging and discharging the energy storage module fail to take the battery units SOC into account, which is not conducive to protecting the energy storage device (Abdalla et al., 2021) (Othman et al., 2020). Therefore, the above studies based on various filtering algorithms only have a relatively limited effect on suppressing the fluctuations of photovoltaic power. More importantly, the imbalances of SOC and state of health (SOH) among battery units have not yet been considered, which weakens the schedulable potential and is unable to reduce the life loss of BESS in power regulation.

Aiming at the problem of the SOC imbalance of battery units when BESS smoothing the fluctuations of photovoltaic power, most of the existing studies are to achieve the SOC balance by changing the power regulated by the battery units (Ali et al., 2021) (Morstyn et al., 2014). An energy management scheme considering the SOC balance is proposed in Ali et al., 2021 based on a multi-agent system, where each energy storage unit is used as a controllable agent, and the active power reference of each energy storage unit is adjusted in proportion to the level of the SOC to reduce the SOC imbalance. A distributed cooperative control method is designed in Morstyn et al., 2014. It changes the charging and discharging behaviors of multiple battery units to ensure that the SOC among all battery units tends to be consistent. Although the above solutions have made outstanding contributions to the balance of the SOC among battery units, there is still a problem of the low balance in SOC.

Additionally, achieving the balance of SOH among battery units can prolong the lifetime of BESS. A life cycle model for the battery unit is established in Weng et al., 2013. It is optimized by a public dataset, and a balancing system is constructed based on the model. The power allocation scheme redistributing the output current into each battery unit according to their SOH state is designed in Goh et al., 2022 to achieve the balance in SOH. A SOH-awareness balancing scheme is devised in Azimi et al., 2022 by reducing the load current of the battery units with lower SOH. A prediction model and SOH balancing scheme are created in Shili et al., 2016 to compensate for the aging difference of the battery units by generating the voltage dispersion and balancing the aging speed of each battery unit. Finally, the maximization of the lifetime through balancing the SOH is achieved. Although the composite control system of the combined power generation system proposed in the literature can adjust the output of the energy storage system according to the demand, the strategy is limited to the degree of mitigation of photovoltaic fluctuations, and the battery units SOH is not considered (Shen et al., 2020) (Parlikar et al., 2021). The optimization strategy of the optical storage model proposed in the literature is based on the charge and discharge protection of the energy storage module, but it does not consider the number of charge and discharge times and costs of the energy storage module, and it does not improve the system's consumption of photovoltaic resources (Kroposki et al., 2020) (Victoria et al., 2021). A simplified SOH balancing topology is proposed in Farahani, 2021 to achieve the balance of the SOH in the battery units within a battery group. However, the SOH balancing scheme as mentioned earlier can only achieve the SOH balance among the battery units inside a single battery group. It cannot achieve SOH balance of all battery units for the whole BESS.

Based on the analysis above, few studies have considered reducing the life loss through the simultaneous improvement of the consistencies of SOC and SOH among battery units in smoothing the fluctuations of photovoltaic power with BESS. The main contributions of the research can be summarized as follows:

1) For the relatively weak performance of the current research to reduce the fluctuations of the photovoltaic power, a Swing Door Trending (SDT) algorithm optimized by the improved Aquila Optimizer (IAO) algorithm is proposed, which is called the IAO-SDT algorithm. The IAO-SDT algorithm is used to extract the characteristic data points of the photovoltaic power to obtain the grid-connected power reference of the photovoltaic power station.
2) Aiming at the low consistencies of SOC and SOH among all battery units during operation, a dynamic grouping method that considers SOC and SOH in all battery units simultaneously is proposed. The dynamic grouping time is determined by the standard deviation of the SOC among the battery units. Whether the SOH of each battery unit deviating

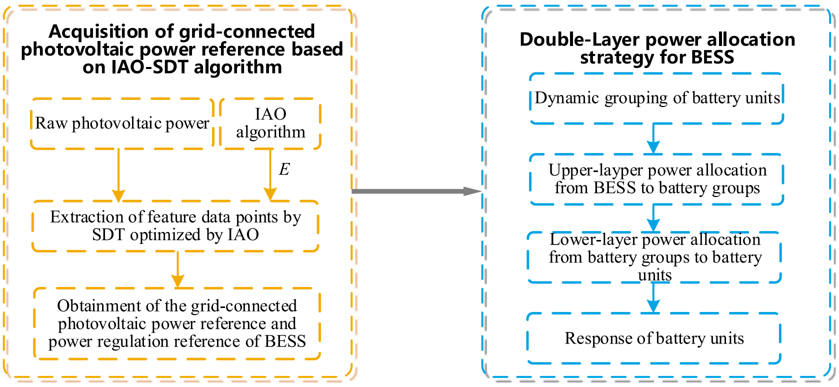

FIGURE 1
Hierarchical structure and implementation process of this study.

from the predetermined range is used to divide the battery group. If the SOH of one or more battery units deviates from the predetermined range, the battery units are divided into three groups: The priority charging group, the priority discharge group, and the outlier group. Otherwise, they are divided into two groups: The priority charging group and the priority discharging group.

3) Based on the dynamic grouping results of battery units, the double-layer power allocation method of BESS is designed. The action sequence of the battery groups depends on the positive and negative values of the power regulation reference of BESS. Then, the power regulation reference undertaken by each battery group is distributed from the power regulation reference of BESS, where the power allocation in upper-layer from BESS to the battery groups is achieved; then, the power regulation reference of the battery groups is allocated to the battery units inside the battery groups in terms of the principle of maximum charge/discharge power or the principle of SOC balance, and the power allocation in the lower-layer from the battery groups to the battery units is conducted.

The operating data of a photovoltaic power station is used to verify the proposed method. The simulated results show that the proposed method, compared with other approaches, minimizes the fluctuation rate of the grid-connected photovoltaic power, and further improves the balances of SOC and SOH among battery units.

The organizational structure of the rest of this study: Section 2 introduces the hierarchical structure and the implementation process of the proposed method; Section 3 presents the IAO-SDT algorithm to obtain the grid-connected photovoltaic power reference; Section 4 devises a double-layer power allocation strategy based on the dynamic grouping technology; Section 5 conducts the simulation verification; Section 6 summarizes the main conclusion.

2 Hierarchical structure and implementation process

Figure 1 gives the hierarchical structure and the implementation process of this study. It shows that this study includes the two main contents:

1) Acquisition of the grid-connected photovoltaic power reference: The IAO algorithm is presented to speed up the convergence speed and enhance the optimization accuracy, and it is used to optimize the compression offset of the SDT algorithm; the IAO-SDT algorithm is applied to extract the characteristic data points from the raw photovoltaic power; the grid-connected photovoltaic power reference is obtained by connecting these feature data and it is also used to be compared with the raw photovoltaic power to get the power regulation reference of BESS.
2) Double-layer power allocation strategy for BESS: The dynamic grouping time is determined by the standard deviation of the SOC among the battery units, and the SOH of each battery unit deviating from the predetermined range is used to divide the battery group; the action sequence of the battery group is determined by the power regulation reference of BESS, and then double-layer power allocation from BESS to battery units is realized; eventually, every battery unit responds to its power regulation reference, and the whole process of the power regulation of BESS assisting the photovoltaic station is completed.

3 Acquisition of grid-connected photovoltaic power reference based on IAO-SDT algorithm

3.1 Principle and deficiency of SDT algorithm

The SDT algorithm proposed by Bristol in 1990 (Bristol, 1990) has been effectively applied in the wind power ramp events and the SCADA system data compression due to its high compression ratio, fast execution speed, and controllable error (Cui et al., 2015) (Mah et al., 1995). SDT is a linear segmented algorithm, simple in calculation, small in compression and reconstruction, small in storage space and fast in operation, so it is widely used in industrial engineering practice. When processing the field data, the use of SDT algorithm can significantly decrease the demand for storage space and reduce the possibility of congestion in the network. Meanwhile, it can measure the value of some points and improve the performance of the control system. The implementation steps of the SDT algorithm are as follows:

Step 1: Initialization.

$$\begin{cases} k_{1d} = \dfrac{x_1 - (x_0 + E)}{t_1 - t_0} \\ k_{2d} = \dfrac{x_1 - (x_0 - E)}{t_1 - t_0} \end{cases} \tag{1}$$

where t_0 and x_0 are the initial moment and the corresponding data value, respectively; $t_1$and $x_1$are the first moment and the corresponding data value, respectively; $k_{1d}$and k_{2d} are the initial values of the upper and lower pivot gate slopes, respectively; E is the compression offset.

Step 2: Calculation of the slope.

$$\begin{cases} k_1 = \dfrac{x_i - (x_k + E)}{t_j - t_k} \\ k_2 = \dfrac{x_j - (x_k - E)}{t_j - t_k} \\ k_j = \dfrac{x_j - x_k}{t_j - t_k} \end{cases} \tag{2}$$

where $t_j$and x_j are the jth moment and the corresponding data value, respectively; t_k and x_k are the kth moment and the corresponding data value, respectively.

Step 3: Updating the slope.

$$\begin{cases} k_{1d} = \max\{k_1, k_{1d}\} \\ k_{2d} = \max\{k_2, k_{2d}\} \end{cases} \tag{3}$$

Step 4: Extraction of feature data.

$$k_{1d} \geq k_{2d} \tag{4}$$

If Eq. 4 is satisfied, the data value at the last moment is recorded as the feature data, and it returns to step 2; otherwise, it returns to Step 3.

In this study, the raw grid-connected photovoltaic power data at 5 min intervals over one-day-ahead 24 h is selected. The SDT algorithm is used to extract the feature data, and the grid-connected photovoltaic power reference curve is obtained by connecting the extracted feature data. It is worth noting that the compression offset E in the SDT algorithm directly affects the extraction result of the feature data. If selecting a larger E, fewer feature data will be extracted. Therefore, a suitable E is so essential that the IAO is used to find the optimal value E.

3.2 Improved aquila optimizer

The Aquila Optimizer (AO) was proposed in 2021 (Abualigah et al., 2021), and it is inspired by the behavior of the eagles in capturing prey in nature. The optimization process of the AO is represented by four methods: the search space selected by the high soaring of vertical diving, the exploration within the diverging search space by the profile flight of the short glide attack, the exploitation of the convergent search space by the low flight of the slow descent attack, and finally diving on foot and catching the prey. The specific steps are as follows:

Step 1: Selection of a search space.

$$X_1(n+1) = X_{\text{best}}(n) \times \left(1 - \frac{n}{N_{\max}}\right) + \left(X_M(n) - X_{\text{best}}(n) \times rand\right) \tag{5}$$

$$X_M(n) = \frac{1}{N}\sum\nolimits_{i=1}^{N} X_{il}(n), \forall j = 1, 2, \ldots, D \tag{6}$$

where n is the number of iterations; $X_1(n+1)$ is the solution of the next iteration of n, generated by the first search method; $X_{\text{best}}(n)$ is the optimal solution at the nth iteration; n and $N_{\max}$ are the current iteration and the maximum number of iterations, respectively; N is the number of Aquila individuals; $X_M(n)$ is the average value of the current solutions of all Aquila individuals at the nth iteration; *rand* is a random value between 0 and 1; D is the search variable dimension.

Step 2: Global search.

$$X_2(n+1) = X_{\text{best}}(n) \times \text{Levy}(D) + X_R(n) + (y - x) \times rand \tag{7}$$

where $X_2(n+1)$ is the solution of X_2 for the next iteration of n, generated by the second search method; $X_R(n)$ is to take the current solution in any Aquila individual in the nth iteration;

$Levy(D)$ is the $Levy$ flight distribution function, and the calculation equation is as follows:

$$\begin{cases} Levy(D) = s \times \dfrac{\boldsymbol{u} \times \boldsymbol{\sigma}}{|\boldsymbol{v}|^{1/\beta}} \boldsymbol{X}_{\mathbf{R}}(\boldsymbol{n}) + (\boldsymbol{y} - \boldsymbol{x}) \times \boldsymbol{rand} \\ \sigma = \dfrac{\boldsymbol{\Gamma}(1+\boldsymbol{\beta}) \times \mathbf{sin}(\boldsymbol{\pi\beta}/2)}{\boldsymbol{\Gamma}[(1+\boldsymbol{\beta})/2] \times \boldsymbol{\beta} \times 2^{(\beta-1)/2}} \end{cases} \tag{8}$$

where the parameter s is selected as 0.01; u and v are random numbers between 0 and 1, and the parameter β is 1.5; y_1 and y_2 are used to represent the spiral shape in the search, and the calculation is as follows:

$$\boldsymbol{y}_1 = \boldsymbol{r} \times \mathbf{cos}(\boldsymbol{\theta}) \tag{9}$$

$$\boldsymbol{y}_2 = \boldsymbol{r} \times \mathbf{sin}(\boldsymbol{\theta}) \tag{10}$$

where r and θ are calculated as follows:

$$\boldsymbol{r} = \boldsymbol{r}_1 + \boldsymbol{U} \times \boldsymbol{D}_1 \tag{11}$$

$$\boldsymbol{\theta} = -\boldsymbol{\omega} \times \boldsymbol{D}_1 + \boldsymbol{\theta}_1 \tag{12}$$

$$\boldsymbol{\theta}_1 = \frac{3\boldsymbol{\pi}}{2} \tag{13}$$

where r_1 is a random value between 1 and 20; U is 0.00565; D_1 is an integer between 1 and the dimension D of the search variable, and ω is 0.005.

Step 3: Local mining.

$$\begin{aligned} \boldsymbol{X}_3(\boldsymbol{n}+1) = {} & (\boldsymbol{X}_{\mathbf{best}}(\boldsymbol{n}) - \boldsymbol{X}_{\mathbf{M}}(\boldsymbol{n})) \times \boldsymbol{\delta}_1 - \boldsymbol{rand} \\ & + ((\boldsymbol{UB} - \boldsymbol{LB}) \times \boldsymbol{rand} + \boldsymbol{LB}) \times \boldsymbol{\delta}_2 \end{aligned} \tag{14}$$

where $\boldsymbol{X}_3(n+1)$ is the solution of the next iteration of n, generated by the third method; δ_1 and δ_2 are both 0.1; LB is the lower limit of the variables, and UB is the upper limit of the variables.

Step 4: Reduction of the search area.

$$\begin{aligned} \boldsymbol{X}_4(\boldsymbol{n}+1) = {} & \boldsymbol{QF} \times \boldsymbol{X}_{\mathbf{best}}(\boldsymbol{n}) - (\boldsymbol{G}_1 \times \boldsymbol{X}(\boldsymbol{n}) \times \boldsymbol{rand}) \\ & - \boldsymbol{G}_2 \times \mathbf{Levy}(\boldsymbol{D}) + \boldsymbol{rand} \times \boldsymbol{G}_1 \end{aligned} \tag{15}$$

$$\boldsymbol{QF}(\boldsymbol{n}) = \boldsymbol{n}^{\frac{2 \times \boldsymbol{rand} - 1}{(1 - N\, \boldsymbol{max})}} \tag{16}$$

where $\boldsymbol{X}_4(n+1)$ is the solution for the next iteration of n, generated by the fourth search method; QF is the quality function to balance the search strategy; G_1 is the various movement of the eagle tracking the prey during hunting, and $X(n)$ is the current solution at the nth iteration. To speed up the optimization speed, the modified step size is shown below:

$$\boldsymbol{G}_1 = 2 \times \boldsymbol{rand} - 1 \tag{17}$$

$$\boldsymbol{\mu} = \boldsymbol{a}_1 + \boldsymbol{a}_2 \times \boldsymbol{ln}\left[\boldsymbol{a}_3 - \boldsymbol{a}_4 \times \boldsymbol{n} + \sqrt{\boldsymbol{a}_5 + (\boldsymbol{a}_3 - \boldsymbol{a}_4 \times \boldsymbol{n})^2}\right] \tag{18}$$

where a_1, a_2, a_3, a_4 and a_5 are the step size parameters, and their values are selected as 1.1, 0.2, 30, 1.5, and 1, respectively.

Compared with existing optimization algorithms such as Whale Optimization Algorithm (WOA), Sine Cosine Algorithm (SCA), Slime Mould Algorithm (SMA), the AO optimizer has faster optimization speed and higher convergence accuracy under the same conditions (Abualigah et al., 2021). Specifically, in the first and second steps of the AO optimization algorithm, the larger search range makes it possible to lock the optimal solution in a shorter time, and the third and fourth steps make the AO optimizer obtain higher optimization accuracy than other optimization algorithms in a shorter time.

3.3 Acquisition of grid-connected photovoltaic power reference

Firstly, the compression ratio Y_a, the sum of the errors C_{az}, the power fluctuation rate V_a, and the power reference $P_{\mathrm{r \cdot b}}$ tracked by BESS are defined as follows:

$$\boldsymbol{Y}_{\boldsymbol{a}} = \frac{\boldsymbol{N}_1}{\boldsymbol{N}_2} \tag{19}$$

$$\boldsymbol{C}_{\boldsymbol{az}} = \frac{1}{\boldsymbol{N}_2} \sum_{\boldsymbol{t}=1}^{N_2} \left| \boldsymbol{P}_{\mathbf{b}}(\boldsymbol{t}) - \boldsymbol{P}_{\mathbf{y}}(\boldsymbol{t}) \right| \tag{20}$$

$$\begin{aligned} \boldsymbol{V}_{\boldsymbol{a}} = {} & \frac{1}{\boldsymbol{T}_1} \sum_0^{\mathrm{T}_1} \{ \mathbf{max}_{t_i \le t \le t_i + 10\,\mathbf{min}} \{ \boldsymbol{P}_{\mathbf{b}}(\boldsymbol{t}) \} \\ & - \mathbf{min}_{t_i \le t \le t_i + 10\,\mathbf{min}} \{ \boldsymbol{P}_{\mathbf{b}}(\boldsymbol{t}) \} \} \Big/ \boldsymbol{P}_{\mathbf{vN}} \end{aligned} \tag{21}$$

$$\boldsymbol{P}_{\mathbf{r \cdot b}}(\boldsymbol{t}) = \boldsymbol{P}_{\mathbf{y}}(\boldsymbol{t}) - \boldsymbol{P}_{\mathbf{g}}(\boldsymbol{t}) \tag{22}$$

where N_1 is the number of extracted feature data points; N_2 is the number of raw photovoltaic power data points; $P_{\mathrm{g}}(t)$, $P_{\mathrm{y}}(t)$, and $P_{\mathrm{r \cdot b}}(t)$ are the reference of grid-connected photovoltaic power, the original power value, and the power reference of BESS at the time t, respectively; t_i is the ith time interval (10min for each interval), and T_1 is the scheduling period. Y_a reflects the ability of the SDT algorithm to compress the data; C_{az} characterizes the demand for the capacity of BESS, and V_a expresses the power fluctuation rate of the photovoltaic power.

Then, combined with the requirement of evaluating the fluctuations in Zilong Yang et al., 2019, the grid-connected power at every 10min interval should not exceed 1/3. The fitness function to solve the optimal compression offset of the SDT algorithm optimized by the IAO algorithm is designed in Eq. 23, and the constraint conditions are shown in Eq. 24:

$$\mathbf{min}\, \boldsymbol{f} = \boldsymbol{\alpha}_1 \cdot \boldsymbol{Y}_{\boldsymbol{a}} + \boldsymbol{\alpha}_2 \cdot \boldsymbol{C}_{\boldsymbol{az}} + \boldsymbol{\alpha}_3 \cdot \boldsymbol{V}_{\boldsymbol{a}} \tag{23}$$

$$\left\{ \mathbf{max}_{t_i \le t \le t_i + 10\,\mathbf{min}} \left\{ \boldsymbol{P}_{\boldsymbol{g}}(\boldsymbol{t}) \right\} - \mathbf{min}_{t_i \le t \le t_i + 10\,\mathbf{min}} \left\{ \boldsymbol{P}_{\boldsymbol{g}}(\boldsymbol{t}) \right\} \right\} \le (1/3) \boldsymbol{P}_{\boldsymbol{vN}} \tag{24}$$

where α_1, α_2, and α_3 are the weights; P_{vN} is the installed capacity of the photovoltaic power station. In this study, the values of α_1, α_2, and α_3 determined by the repeated experiments takes 110,

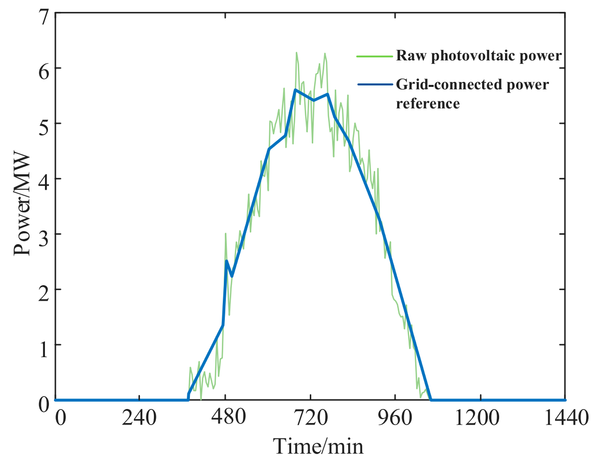

FIGURE 2
Extracted grid-connected power signals based on IAO-SDT algorithm.

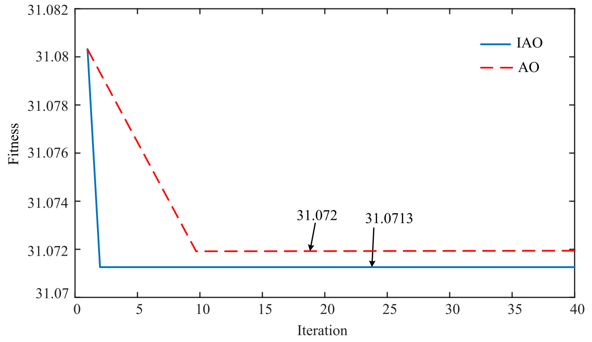

FIGURE 3
Comparison of optimization process between IAO algorithm and AO algorithm.

TABLE 1 Result comparison between IAO-SDT algorithm and AO-SDT algorithm.

Index	IAO	AO
Y_a/%	11	10
C_{az}/MW	0.1474	0.1689
V_a/%	0.14	0.16

600, and 80, respectively. The output of the fitness function P_g is the grid-connected photovoltaic power reference.

To verify the superiority of the SDT algorithm optimized by the IAO algorithm, the raw photovoltaic power is dealt with by the proposed algorithm. The result is shown in Figure 2. It shows that the maximum deviation between the raw power and grid-connected power optimized by the SDT algorithm is 0.1474 MW and meets the requirements of the fluctuations in Lixing L V et al., 2021, which means that the maximum charge/discharge power of BESS is 0.1474 MW every time. It reduces the need of the capacity for the BESS. The compression ratio Y_a of the SDT algorithm is 10%, because there are many zero-power data in the raw photovoltaic power curve. The power fluctuation rate V_a of the raw photovoltaic power data is 0.61%, but the power fluctuation rate V_a of the grid-connected power reference is 0.14%. It indicates that the IAO-SDT algorithm has a significant effect on reducing the fluctuations.

The optimization process of the IAO algorithm and the AO algorithm to search for the optimal solution is compared and shown in Figure 3. It indicates that the IAO algorithm takes less time than the AO algorithm to find a better optimal result. Moreover, the comparative indexes between these the proposed IAO-SDT algorithm and the AO-SDT algorithm are shown in Table 1. It displays that the SDT algorithm optimized by the IAO algorithm outputs a lower fluctuation rate and reduces the requirement of the capacity of BESS as well. Ultimately, the IAO-SDT algorithm has a good optimization performance.

4 Dual-layer power allocation strategy based on dynamic grouping for BESS

4.1 Dynamic grouping technique

For BESS, when responding to the power signal, the power signal is usually divided equally or distributed under a certain proportion to the battery units. The coordination allocation of battery units is not adequately considered (Lixing et al., 2021). Furthermore, the current methods require every battery unit in the battery group to participate in the response. So the dynamic grouping approach of the BESS is designed to solve this problem.

When charging the BESS, the battery units with lower SOC should be charged first. Contrarily, battery units with higher SOC should discharge first. Consequently, the SOC of each battery unit tends to be gradually consistent, and the charge/discharge power and the left available capacity of the BESS could both be maintained in good condition for the next cycle. The dynamic grouping approach is designed as follows.

1) Determination of grouping time

After running for some time, the SOC of the battery unit may change, so the grouping of the BESS will be adjusted after some fixed time as usual. To improve the SOC consistency among the battery units, the battery units in the battery groups are dynamically updated in this study when the SOC standard deviation δ_1 of one or more battery units is greater than the threshold value γ_1 as shown in Eq. 25. γ_1 could be flexibly set to satisfy the various working conditions.

$$\delta_1 > \gamma_1 \tag{25}$$

2) Determination of grouping principle

Moreover, when dividing the BESS into the battery groups, the dynamic grouping principle adopted by the current research is designed only according to the SOC of battery units. But the SOH of some battery unis may be gradually reduced to its lifetime limitation, such as 80%, and these battery units will have to be out of service (Chen et al., 2020). Hence, the grouping of the BESS in the study considers the SOC and the SOH concurrently.

At the time of dynamic grouping, the SOH of the battery units is first judged as whether deviating from the predetermined range shown in Eq. 26. If the SOH of one or more battery units deviates from the predetermined range, the battery units are divided into three battery groups: the priority charging group, the priority discharge group, and the outlier group. These battery units whose SOH deviates from the predetermined range belong to the outlier group. The remaining battery units are ordered by the SOC from low to high. The battery units with lower SOC are given to the priority charging group, and the battery units with higher SOC are assigned to the priority discharging group. The number of battery units assigned to the priority charging group and the priority discharge group is the same. If the SOH in any battery unit does not diverge from the predetermined range, all battery units are divided into two battery groups: the priority charging group and the priority discharge group. The method of how to assign the battery units into the two battery groups is the same as above.

$$\mu_t - \gamma_2\delta_{2,t} \le SOH_{n,t} \le \mu_t + \gamma_2\delta_{2,t} \tag{26}$$

where μ_t is the average value of the SOH at the time t; $\delta_{2,t}$ is the standard deviation of the SOH at the time t; γ_2 is the weight coefficient. With a larger γ_2, the SOH consistency among the battery units will be worsen, and the SOC consistency among the battery units will be better. Therefore, γ_2 could be appropriately determined under different working conditions.

3) Calculation of SOH

Currently, the calculation of the SOH can use the estimation methods based on the capacity degradation or the internal resistance increase (Guha and Patra, 2017). Since the capacity change of the battery unit is easier to be measured during operation (Meng et al., 2020), the calculation accuracy with the method based on the capacity degradation is higher than the latter, and it is used in the study to calculate the SOH of the battery unit as follows (Li et al., 2017):

$$SOH = \frac{C_{mM}}{C_N} \times 100\% \tag{27}$$

where C_N is the nominal capacity of the battery unit, andC_{mM} is the discharging capacity measured at the mth measurement.

The estimation methods based on capacity degradation and internal resistance increase are the most used in SOH estimation. The residual capacity method is the SOH estimation method used in the research, and it is also a widely used SOH estimation method for battery units. In practice, the aging process of batteries is quite complex, related to various factors such as ambient temperature, discharge rate, and depth of discharge (DOD). The literature (Ma et al., 2020) gives a specific method for estimating SOH in practical engineering. The calculation of SOH is as follows:

$$\mathrm{SOH}_{i,t} = \frac{\Delta \mathrm{SOC}_{\mathrm{all\_min}}}{\Delta \mathrm{SOC}_{i,t}} \tag{28}$$

where $\Delta\mathrm{SOC}_{all\_min}$ is the minimum value among all average SOC variation rates during relative SOH estimation progress, and $\Delta\mathrm{SOC}_{i,t}$ is the SOC change rate of the ith battery cell at the time t.

4) Calculation of SOC and its constraints

SOC represents the remaining capacity of the battery units. Accurate estimation of the SOC is of great importance in describing the state of the battery units (Jiang et al., 2021). Numerous methods could be used to estimate of the SOC of the battery units, such as the open-circuit voltage method, ampere-hour integral method, neural network, and Kalman filter (Yu and Gao, 2013). Since the ampere-hour integral method is simple in principle and easy to calculate, it is used to estimate the SOC of the battery units in the study:

$$SOC_{n,t} = SOC_{n,t-1} + \frac{\int P_{\mathrm{bn},t}dt}{C_n} \tag{29}$$

where $SOC_{n,t}$ is the SOC of the nth battery unit at the time t; $P_{\mathrm{bn},t}$ is the charge/discharge power of the nth battery unit at the time t, and it is positive when charging and negative when discharging; C_n is the maximum energy storage capacity of the nth battery unit.

4.2 Double-layer power allocation strategy

When the BESS responds to the power reference, the existing methods generally ignore the state difference of each battery unit, which leads to overcharge and over-discharge of some battery units and affects the lifetime of the battery units. In addition, the frequent and irregular response of the BESS may also reduce the sustainable regulation ability in the next period. To minimize the loss of lifetime and maintain the reasonable sustainably schedulable potential for the BESS, this study designs a double-layer power allocation strategy for BESS in response to its power reference. The sustainably schedulable potential means that the SOC of the battery units in each battery group should be kept within an optimal range to ensure that the charge/discharge power of the BESS reaches the maximum in the next schedulable cycle (Yu et al., 2011).

4.2.1 Battery group action sequence determination and upper-layer power allocation

1) For the power allocation without the outlier group

When the SOH of all battery units stays within the predetermined range, the battery units are divided into the priority charging group, and the priority discharge group. The operating state of the BESS is judged by the power regulation reference $P_{\text{r-b}}$, and the action sequence of the battery group could also be determined. The power regulation reference $P_{\text{r-b}}$ is distributed into the battery groups according to the maximum charge/discharge power of the battery group and the action sequence.

1) Power allocation in charge

If $P_{\text{r-b}} > 0$, the BESS needs to be charged, and the action sequence of the two battery groups is from the priority charging group to the priority discharging group. The maximum charging powers of the priority charging group and the priority discharging group are written as P_{gcmax} and P_{gdmax}, respectively.

When $P_{\text{r-b}} \le P_{\text{gcmax}}$, only the priority charging group is responsible for regulating the power reference. Then, the secondary distribution of the power reference in the battery units inside the priority charging group is realized according to the principle of SOC balance, and the priority discharging group do not need to run, where the principle of SOC balance will be introduced in Section 4.2.2.

When $P_{\text{r-b}} > P_{\text{gcmax}}$, the priority charging group works with the maximum charge power, and the priority discharging group undertaking the left power adopts the principle of SOC balance for power distribution in the battery units within the group.

2) Power allocation in discharge

If $P_{\text{r-b}} < 0$, the BESS needs to be discharged, and the action sequence of the two battery groups is from the priority discharging group to the priority charging group.

When $P_{\text{r-b}} \ge -P_{\text{gdmax}}$, only the priority discharging group undertakes the power regulation reference of BESS, and the power distribution of the battery units inside the discharging group is conducted by the principle of SOC balance. The priority charging group does not need to run.

When $P_{\text{r-b}} < -P_{\text{gdmax}}$, the priority discharging group works with the maximum discharge power, and the priority charging group adopts the principle of SOC balance to complete the remaining power distribution in the battery units within the group.

2) For the power allocation with the outlier group

When the SOH of one or more battery units deviates from the predetermined range, the battery units are divided into the priority charging group, the priority discharge group, and the outlier group. The operating state of the BESS is also judged by the power regulation reference $P_{\text{r-b}}$, and the action sequence of the battery group can be determined. The power regulation reference $P_{\text{r-b}}$ is distributed into the battery groups according to the maximum charge/discharge power of the battery group and the action sequence.

1) Power allocation in charge

If $P_{\text{r-b}} > 0$, the BESS needs to be charged, and the action sequence of the three battery groups is arranged as follows: the priority charging group, the priority discharging group, and the outlier group. The maximum charging powers of the priority charging group and the priority discharging group are also written as P_{gcmax} and P_{gdmax}, respectively.

When $P_{\text{r-b}} \le P_{\text{gcmax}}$, only the priority charging group undertakes the power regulation reference of the BESS, and the secondary power distribution into the battery units inside it according to the principle of SOC balance; the remaining two battery groups do not operate.

When $P_{\text{r-b}} \le P_{\text{gcmax}} + P_{\text{gdmax}}$, the priority charging group works with the maximum charge power, and the priority discharging group adopts the principle of SOC balance for power distribution within the group; the outlier group does not operate.

When $P_{\text{r-b}} > P_{\text{gcmax}} + P_{\text{gdmax}}$, the priority charging group and the priority discharging group both work with its maximum charge power, and the outlier group adopts the principle of SOC balance for left power distribution within its group.

2) Power allocation in discharge

If $P_{\text{r-b}} < 0$, the BESS needs to be discharged, and the action sequence of the three battery groups is arranged as follows: The priority discharging group, the priority charging group, and the outlier group.

When $P_{\text{r-b}} \ge -P_{\text{gdmax}}$, only the priority discharging group undertakes the power regulation reference of the BESS, and the power distribution inside its battery units according to the principle of SOC balance; the remaining battery groups do not operate.

When $P_{\text{r-b}} \ge -(P_{\text{gcmax}} + P_{\text{gdmax}})$, the priority discharging group works with the maximum discharge power, and the priority charging group adopts the principle of SOC balance

TABLE 2 Power distribution principle for battery units in each battery group with different states.

Outlier group	State	Condition	Priority charge group	Priority discharge group	Outlier group
No existence	Charge ($P_{r\text{-}b}>0$)	$P_{r\text{-}b} \le P_{gcmax}$	SOC balance	Idle	—
		$P_{r\text{-}b} > P_{gcmax}$	Max. charge power	SOC balance	—
	Discharge ($P_{r\text{-}b}<0$)	$P_{r\text{-}b} \ge -P_{gdmax}$	Idle	SOC balance	—
		$P_{r\text{-}b} < -P_{gdmax}$	SOC balance	Max. discharge power	—
Existence	Charge ($P_{r\text{-}b}>0$)	$P_{r\text{-}b} \le P_{gcmax}$	SOC balance	Idle	Idle
		$P_{r\text{-}b} \le P_{gcmax} + P_{gdmax}$	Max. charge power	SOC balance	Idle
		$P_{r\text{-}b} > P_{gcmax} + P_{gdmax}$	Max. charge power	Max. charge power	SOC balance
	Discharge ($P_{r\text{-}b}<0$)	$P_{r\text{-}b} \ge -P_{gdmax}$	SOC balance	Idle	Idle
		$P_{r\text{-}b} \ge -(P_{gcmax} + P_{gdmax})$	Max. discharge power	SOC balance	Idle
		$P_{r\text{-}b} < -(P_{gcmax} + P_{gdmax})$	Max. discharge power	Max. discharge power	SOC balance

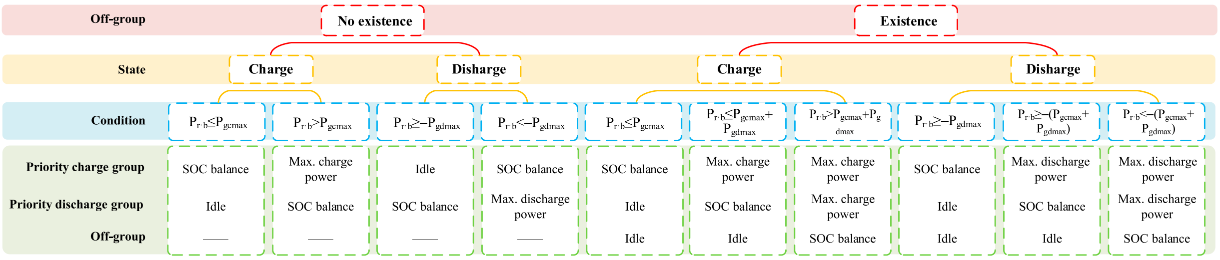

FIGURE 4
Power distribution principle for battery units in each battery group with different states.

to complete the left power distribution within the group; the outlier group does not operate.

When $P_{r\text{-}b} < -(P_{gcmax} + P_{gdmax})$, the priority charging group and the priority discharging group both work with their maximum discharge powers, and the outlier group adopts the principle of SOC balance to complete the left power distribution within the group.

The power distribution principles that the battery groups should adopt under different conditions are summarized in Table 2 and Figure 4, respectively.

4.2.2 Lower-layer power allocation

The lower-layer power allocation from the battery group to the battery units inside it is completed by both the power allocation results in the upper-layer and the power distribution principle adopted by each battery group.

1) Principle of maximum charge/discharge power

The maximum charge/discharge power allocation means that the battery unit participates in the power regulation with its full charge/discharge power under reasonable constraints.

2) Principle of SOC balance

Since the SOC of the battery units in a battery group may differs greatly from each other during operation, it is anticipated that the battery units with lower SOC will be charged firstly. The battery units with higher SOC will be discharged firstly to realize the relative balance of the SOC among the battery units. For this reason, the arctan function is used to describe the charge/discharge process of the battery unit to characterize its charge/discharge capacity (Vicidomini et al., 2017). In this study, the charge function f_{ch} and discharge function f_{dis} are set as follows:

$$f_{ch}\left(SOC_{n,t}\right) = 0.5 - 0.33 \cdot \mathbf{arctan}\left(2 \cdot \left(SOC_{n,t} - 0.5\right)\right) \tag{30}$$

$$f_{dis}\left(SOC_{n,t}\right) = 0.5 + 0.33 \cdot \mathbf{arctan}\left(2 \cdot \left(SOC_{n,t} - 0.5\right)\right) \tag{31}$$

When the battery group needs to be charged, the power allocation approach of SOC balance is depicted as follows:

TABLE 3 Comparison of various power allocation approaches.

Index	Proposed method (%)	Approach-I (%)	Approach-II (%)	Approach-III (%)	Approach-IV (%)	Approach-V (%)
β	99.9	97.9	98.7	98.2	98.5	98.1

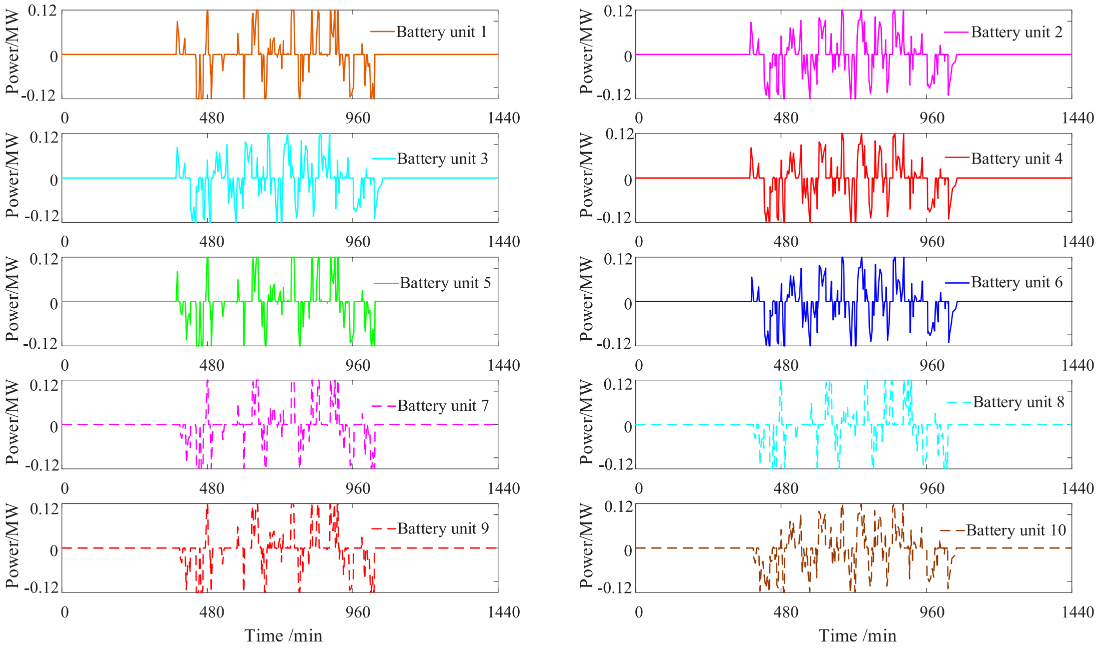

FIGURE 5
Power allocation result for battery units.

TABLE 4 Comparison of SOC and SOH regulated by various approaches.

Index	Proposed method	Approach-I	Approach-II	Approach-III	Approach-IV	Approach-V
SOC standard deviation	0.0087	0.0102	0.0111	0.0116	0.0108	0.0110
SOC average value	0.304	0.322	0.312	0.309	0.308	0.310
SOH standard deviation	6.8817e-05	7.46e-05	8.42e-05	8.82e-05	7.35e-05	8.10e-05
SOH average value	0.9999	0.9999	0.9999	0.9999	0.9999	0.9999

$$\frac{P_{\mathrm{r\cdot b}i,t}}{f_{\mathrm{ch}}\left(SOC_{i,t-1}\right)} = \frac{P_{\mathrm{r\cdot b}j,t}}{f_{\mathrm{ch}}\left(SOC_{j,t-1}\right)} \forall i,j \in N \tag{32}$$

where $P_{\mathrm{r\cdot b}i,t}$ and $P_{\mathrm{r\cdot b}j,t}$ is the power reference assigned into the ith battery unit and the jth battery unit at the time t, respectively.

When the battery group requires to be discharged, the power allocation approach of SOC balance is written as follows:

$$\frac{P_{\mathrm{r\cdot b}i,t}}{f_{\mathrm{dis}}\left(SOC_{i,t-1}\right)} = \frac{P_{\mathrm{r\cdot b}j,t}}{f_{\mathrm{dis}}\left(SOC_{j,t-1}\right)} \forall i,j \in N^{*} \tag{33}$$

4.2.3 Battery unit responding to power reference

After the power regulation reference is assigned to the battery units, they should respond to the power reference separately under some constraints.

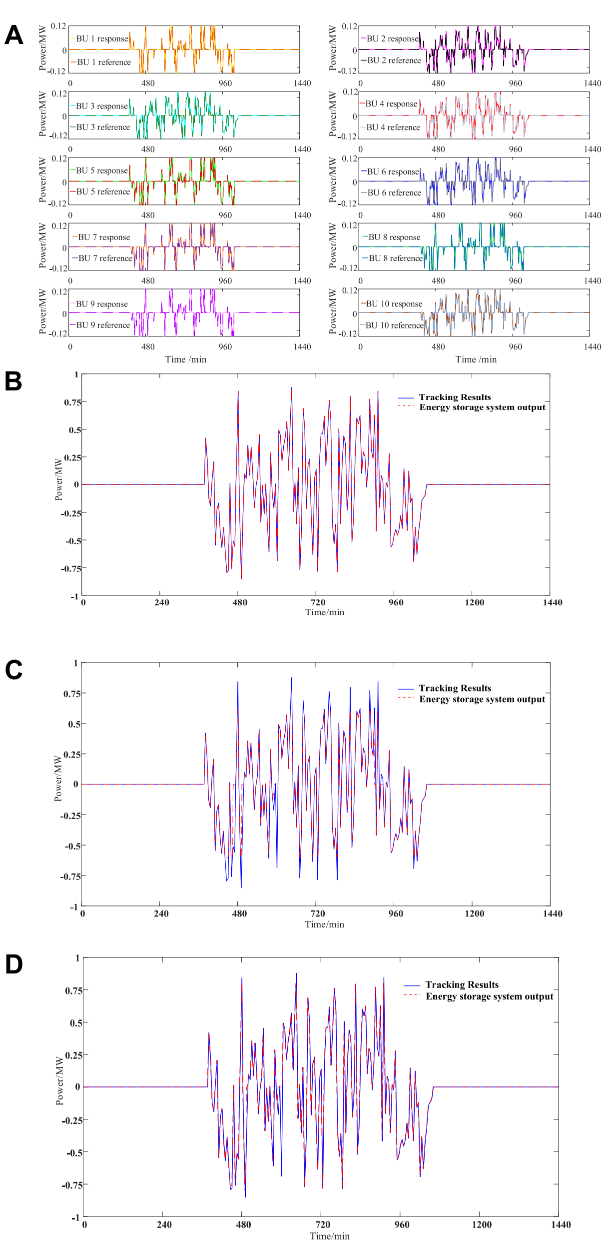

FIGURE 6
(A) Tracking results of the power references by the battery units. **(B)** Tracking result of the power reference by BESS for proposed approach. **(C)** Tracking result of the power reference by BESS for approach-IV. **(D)** Tracking result of the power reference by BESS for approach-V.

1) Maximum charge/discharge power limitation

When the battery unit participates in the power regulation, the high-rate charge/discharge method is generally not used, so the power allocated to the battery units must meet the following constraints:

$$P_{bn,t} = \begin{cases} P_{\mathrm{bmax}\,n}, & P_{\mathrm{r}\text{-}bn} > P_{\mathrm{bmax}\,n} \\ P_{\mathrm{r}\text{-}bn}, & P_{\mathrm{bmin}\,n} \le P_{\mathrm{r}\text{-}bn} \le P_{\mathrm{bmax}\,n} \\ P_{\mathrm{bmin}\,n}, & P_{\mathrm{r}\text{-}bn} < P_{\mathrm{bmin}\,n} \end{cases} \tag{34}$$

where $P_{\mathrm{r}\text{-}bn}$ is the power allocated to the lower-layer of the nth battery unit; $P_{\mathrm{bmax}\,n}$ and $P_{\mathrm{bmin}\,n}$ are the maximum charging power and the maximum discharging power of the nth battery unit, respectively.

2) SOC limitation

During the operation of the battery units, it is necessary to avoid overcharge and over-discharge. The SOC is used to characterize the capacity limit of the BESS (Christensen and Newman, 2003), and the corresponding constraint is:

$$SOC_{\min i} \le SOC_{i,t} \le SOC_{\max i} \tag{35}$$

where $SOC_{\max i}$ and $SOC_{\min i}$ are the upper limit and lower limit of the SOC for the ith battery unit, respectively.

3) Charge/discharge states limitation

The simultaneous charge state and discharge state are impossible for a battery unit and should be avoided, so the constraint is:

$$u_{i,t}^{\mathrm{charge}} + u_{i,t}^{\mathrm{discharge}} \le 1 \tag{36}$$

where $u_{i,t}^{charge}$ and $u_{i,t}^{discharge}$ are the charge flag and the discharge flag of the ith battery unit at the time t, respectively. For charging, $u_{i,t}^{charge}$ is selected as 1 and $u_{i,t}^{discharge}$ is selected as 0. For discharging, $u_{i,t}^{discharge}$ is chosen as 1 and $u_{i,t}^{charge}$ is selected as 0. For other states they are also chosen as 0.

5 Simulation verification and analysis

5.1 Simulated data

The simulation verification is carried out in an actual 6.6 MW photovoltaic power station at high-speed railway station in China. The scale of the BESS equipped for the photovoltaic power station is 1.2MW/1.8 MWh. Ten battery units is included in the BESS, and the initial SOC is given as: 0.4, 0.42, 0.46, 0.47, 0.48, 0.5, 0.52, 0.54, 0.57, and 0.6. The initial SOH is given as: 1, 0.99999, 0.99998, 0.99996, 0.9995, 0.99985, 0.99983, 0.99982, 0.99981, and 0.99980. The initial SOH standard deviation is 8.3327e-05. The maximum charge/discharge power of every battery unit is 0.12 MW.

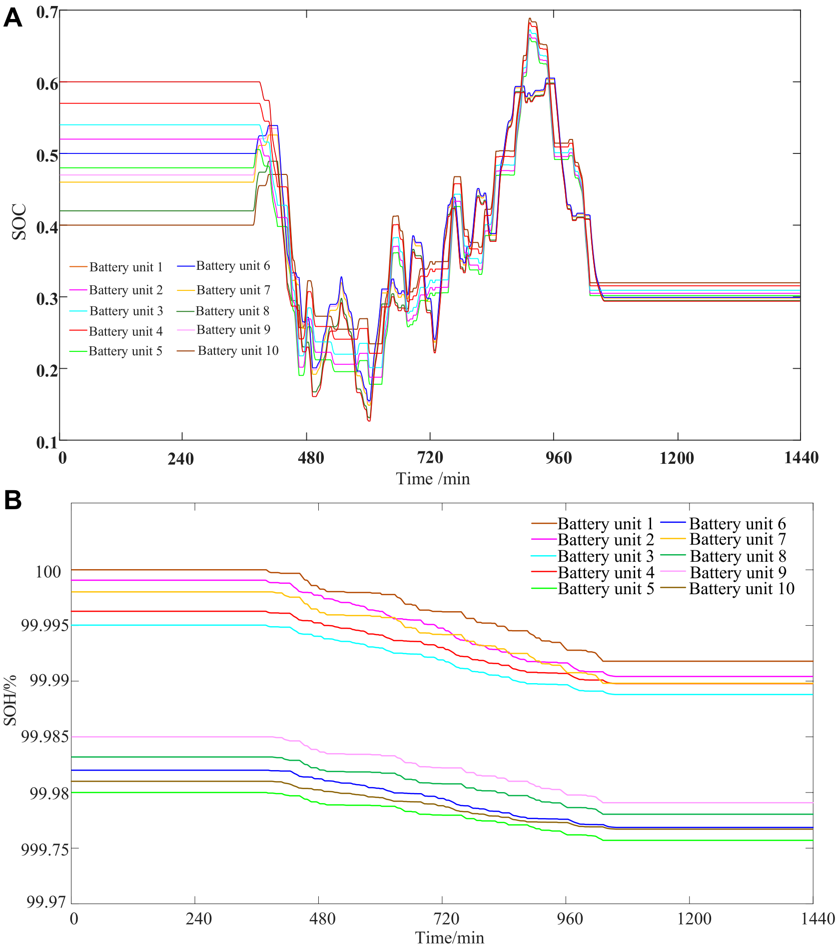

FIGURE 7
(A) Variation of SOC for battery units. **(B)** Variation of SOH for battery units.

5.2 Results and analysis of dynamic grouping

To reflect the superiority of the power allocation method proposed in this research, it is compared with the other three approaches, which are called approach-I, approach-II, and approach-III. Approach-I adopts the dynamic grouping algorithm, but the power reference is equally shared within the group. Approach-II does not use the grouping algorithm, and the power reference is equally shared in the battery units. The power reference of BESS under Approach-III is responded to by the battery unit one by one. Approach-IV comes from the reference (Wang et al., 2021). Approach-V comes from the reference (Li et al., 2018).

The ratio of the tracking power reference is calculated as Eq. 37:

$$\boldsymbol{\beta} = \frac{\boldsymbol{N}_3}{\boldsymbol{N}_2} \tag{37}$$

where N_3 is the number of data points that can track the power reference, and β is the proportion of the power reference that can be well followed.

Table 3 shows the comparative result of the ratio β under different approaches. It indicates that β is the highest in the proposed method. Therefore, the performance of tracking the power reference under the proposed method is also the best.

The power allocation result in the ten battery units is shown in Figure 5. It displays that the allocated power references in all the battery units do not exceed their maximum charge/discharge powers, and the effect of the power allocation is satisfactory.

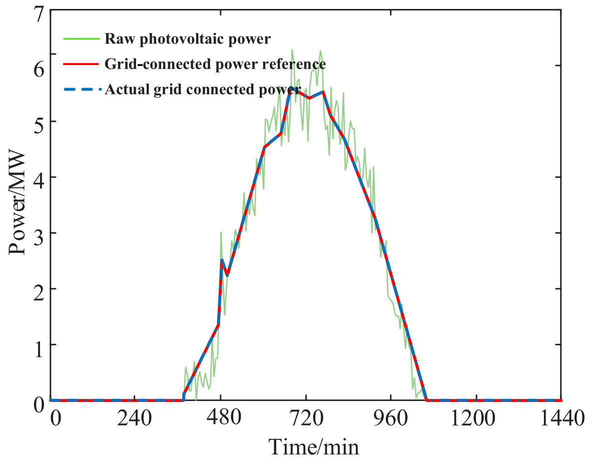

FIGURE 8
Raw and actual grid-connected powers for photovoltaic power station.

5.3 Results and analysis of battery units to track power references

To verify that the proposed power allocation method can improve the consistencies of the SOC and SOH effectively, the average value and standard deviation of SOC and SOH are calculated at the end of the regulation for the battery units, and the results are shown in Table 4. It can be seen from the comparison that compared with other control strategies, the standard deviation of SOC and SOH in the proposed method is the smallest, and the average value of SOC and SOH in the proposed method is at a low level as well. The results show that the power allocation method improves the uniformity of SOC and SOH significantly, thereby avoiding premature withdrawal of the battery units and improving the sustainable scheduling capability of BESS.

The tracking performance of the battery units and the BESS is shown in Figures 6A,B, respectively. Figure 6A indicates that the battery units respond to their assigned power reference smoothly, and Figure 6B the BESS can basically track the power reference. For these points without being fully tracked, the reason is that the power reference in these points exceeds the charge/discharge power limit of the BESS, and only about 1% of the data cannot be tracked. since the SOC of all battery units shown in Figure 7A does not exceed the limit, and the regulation performance is also acceptable. Figure 7B also manifests that the proposed method can further improve the consistency of the SOH among the battery units, and the standard deviation of the SOH among the battery units is only 6.8817e-05.

As shown in the above simulation diagrams, the approaches IV and V both have tracking errors when tracking the same photovoltaic grid-connected power signal, but the proposed method can achieve the high-precision tracking in the whole process. So the regulation performance of the proposed mthod is more acceptable.

5.4 Result of grid-connected photovoltaic power

The raw grid-connected power and actual grid-connected power regulated by the BESS are compared and shown in Figure 8. It manifests that the output of the photovoltaic station aided the BESS is able to track the grid-connected power reference well. Hence, the validity of the proposed power allocation method is testified.

6 Conclusion

Aiming at the low consistencies of SOC and SOH in smoothing the fluctuations of the photovoltaic power through the BESS, a power allocation method considering the state balance of the battery units is presented for the BESS. The research conclusions can be summarized as follows:

1) An approach based on the SDT algorithm optimized by IAO algorithm is designed to acquire the grid-connected photovoltaic power reference. The original AO algorithm is improved to speed up its convergence speed and enhance the optimization accuracy. The IAO-SDT algorithm finds the optimal compression offset of the SDT algorithm more quickly, and the optimization accuracy is higher. The result of the raw photovoltaic power data processed by the IAO-SDT algorithm shows that the grid-connected photovoltaic power reference is effectively extracted, and its fluctuation rate is reduced to satisfy the grid-connected standard better.
2) The dynamic grouping algorithm of the battery units is devised. The dynamic grouping time is determined by the standard deviation of the SOC of the battery units. The dynamic grouping principle is designed according to their SOH and SOC. The grouping status of the battery units is dynamically updated at the dynamic grouping time. Compared with the existing fixed grouping scheme, the consistency of SOC and SOH is guaranteed to a greater extent with the designed dynamic grouping method.
3) A double-layer power allocation strategy for the battery units is proposed. The power regulation reference that each battery group should undertake is determined, and its internal power allocation method is designed to complete the upper-layer power distribution. The lower-layer power distribution of the battery units is also intended to ensure that the power regulation reference

allocated by the battery units does not exceed its maximum charge/discharge power. The simulation results show that the proposed double-layer power allocation strategy can help the BESS track the power reference effectively, and ensure that the SOC and SOH of the battery units are both gradually balanced to be consistent.

In the future, the proposed power allocation method can be further improved by considering the benefit of the photovoltaic station.

Data availability statement

The original contributions presented in the study are included in the article/Supplementary Material; further inquiries can be directed to the corresponding author.

Author contributions

JZ contributed to conception and design of the study. LH organized the database. PPT performed the statistical analysis. JZ wrote the first draft of the manuscript. XBC wrote sections of the manuscript. XY made substantial contributions to the conception or design of the updated work, and interpreted data for the updated work. XHD made substantial contributions to the conception or design of the updated work, interpreted data for the updated work, and revised it for important intellectual content. All authors contributed to manuscript revision, read, and approved the submitted version.

Funding

State Grid Science and Technology Project “Multi energy collaborative optimization and intelligent management and control technology of high proportion clean energy high-speed railway stations”. Item code: 5204XQ21N001.

Conflict of interest

Authors LH, XY, and XC were employed by the company State Grid Hebei Electric Power Co., Ltd. Xiongan New District Power Supply Company.

The remaining authors declare that the research was conducted in the absence of any commercial or financial relationships that could be construed as a potential conflict of interest.

Publisher’s note

References

Abdalla, A. N., Nazir, M. S., Tao, H., Cao, S., Ji, R., Jiang, M., et al. (2021). Integration of energy storage system and renewable energy sources based on artificial intelligence: An overview. *J. Energy Storage* 40, 102811. doi:10.1016/j.est.2021.102811

Abualigah, L., Yousri, D., Abd Elaziz, M., Ewees, A. A., Al-qaness, M. A., and Gandomi, A. H. (2021). Aquila optimizer: A novel meta-heuristic optimization algorithm. *Comput. Industrial Eng.* 157, 107250. doi:10.1016/j.cie.2021.107250

Ali, Z., Putrus, G., Marzband, M., Bagheri Tookanlou, M., Saleem, K., Ray, P. K., et al. (2021). Heuristic multi-agent control for energy management of microgrids with distributed energy sources[C]//2021 56th international universities power engineering conference (UPEC). *IEEE*, 1–6. doi:10.1109/upec50034.2021.9548152

Azimi, V., Allam, A., and Onori, S. (2022). *Extending life of lithium-ion battery packs by taming heterogeneities via an optimal control-based active balancing strategy[J]*. arXiv preprint arXiv:2203.04226.

Bristol, E. H. (1990). Swing door trending: Adaptive trend recording. *ISA Natl. Conf. Proc.*, 749–753.

Chen, X., Tang, J., Li, W., and Xie, L. (2020). Operational reliability and economy evaluation of reusing retired batteries in composite power systems. *Int. J. Energy Res.* 44 (5), 3657–3673. doi:10.1002/er.5147

Christensen, J., and Newman, J. (2003). Effect of anode film resistance on the charge/discharge capacity of a lithium-ion battery. *J. Electrochem. Soc.* 150 (11), A1416. doi:10.1149/1.1612501

Cui, M., Zhang, J., Florita, A. R., Hodge, B. M., Ke, D., Sun, Y., et al. (2015). An optimized swinging door algorithm for wind power ramp event detection[C]//2015. *IEEE Power & Energy Soc. General Meet.*, 1–5. doi:10.1109/pesgm.2015.7286272

De la Parra, I., Marcos, J., García, M., and Marroyo, L. (2015). Control strategies to use the minimum energy storage requirement for PV power ramp-rate control. *Sol. Energy* 111, 332–343. doi:10.1016/j.solener.2014.10.038

Dong, J., Olama, M. M., Kuruganti, T., Melin, A. M., Djouadi, S. M., Zhang, Y., et al. (2020). Novel stochastic methods to predict short-term solar radiation and photovoltaic power. *Renew. Energy* 145, 333–346. doi:10.1016/j.renene.2019.05.073

Farahani, G. (2021). DC–DC Series-resonant converter with multi-stage current-driven for balance charger of series-connected lithium-ion batteries. *IET Power Electron.* 14 (5), 992–1007. doi:10.1049/pel2.12081

Goh, H. H., Lan, Z., Zhang, D., Dai, W., Kurniawan, T. A., and Goh, K. C. (2022). Estimation of the state of health (SOH) of batteries using discrete curvature feature extraction. *J. Energy Storage* 50, 104646. doi:10.1016/j.est.2022.104646

Guha, A., and Patra, A. (2017). State of health estimation of lithium-ion batteries using capacity fade and internal resistance growth models. *IEEE Trans. Transp. Electrific.* 4 (1), 135–146. doi:10.1109/tte.2017.2776558

Huixiang, L., Caixue, C., and Zhigang, X. (2020). A wavelet packet-dual fuzzy control method for hybrid energy storage to suppress wind power fluctuations[J]. *Appl. Energy* 279, 115776.

Jaszczur, M., Hassan, Q., Abdulateef, A. M., and Abdulateef, J. (2021). Assessing the temporal load resolution effect on the photovoltaic energy flows and self-consumption. *Renew. Energy* 169, 1077–1090. doi:10.1016/j.renene.2021.01.076

Jaszczur, M., and Hassan, Q. (2020). An optimisation and sizing of photovoltaic system with supercapacitor for improving self-consumption. *Appl. Energy* 279, 115776. doi:10.1016/j.apenergy.2020.115776

Jiang, C., Wang, S., Wu, B., Fernandez, C., Xiong, X., and Coffie-Ken, J. (2021). A state-of-charge estimation method of the power lithium-ion battery in complex conditions based on adaptive square root extended Kalman filter. *Energy* 219, 119603. doi:10.1016/j.energy.2020.119603

Jiang, Q., and Hong, H. (2012). Wavelet-based capacity configuration and coordinated control of hybrid energy storage system for smoothing out wind power fluctuations. *IEEE Trans. Power Syst.* 28 (2), 1363–1372. doi:10.1109/tpwrs.2012.2212252

Khezri, R., Mahmoudi, A., and Haque, M. H. (2020). Optimal capacity of solar PV and battery storage for Australian grid-connected households. *IEEE Trans. Ind. Appl.* 56 (5), 5319–5329. doi:10.1109/tia.2020.2998668

Kroposki, B., Bernstein, A., King, J., Vaidhynathan, D., Zhou, X., Chang, C. Y., et al. (2020). Autonomous energy grids: Controlling the future grid with large amounts of distributed energy resources. *IEEE Power Energy Mag.* 18 (6), 37–46. doi:10.1109/mpe.2020.3014540

Li, N., Gao, F., Hao, T., Ma, Z., and Zhang, C. (2017). SOH balancing control method for the MMC battery energy storage system. *IEEE Trans. Ind. Electron.* 65 (8), 6581–6591. doi:10.1109/tie.2017.2733462

Li, Y., Li, X., Jia, X., Ma, R., and Hui, D. (2018). Monitoring and control for hundreds megawatt scale battery energy storage station based on multi-agent: Methodology and system design[C]//2018 IEEE international conference of safety produce informatization (IICSPI). *IEEE*, 765–769. doi:10.1109/iicspi.2018.8690406

Liu, D., Chen, H., Tang, Y., Liu, C., Cao, M., Gong, C., et al. (2022). Slope micrometeorological analysis and prediction based on an ARIMA model and data-fitting system. *Sensors* 22 (3), 1214. doi:10.3390/s22031214

Lixing, L. V., Shaohua, C., and Xiaobai, Z. (2021). Control strategy for secondary frequency regulation of power system considering SOC consensus of large-scale battery energy storage[J]. *Therm. power Gener.* 50 (7), 108–117.

Ma, Z., Gao, F., Gu, X., Li, N., Wu, Q., Wang, X., et al. (2020). Multilayer SOH equalization scheme for MMC battery energy storage system. *IEEE Trans. Power Electron.* 35 (12), 13514–13527. doi:10.1109/tpel.2020.2991879

Mah, R. S. H., Tamhane, A. C., Tung, S. H., and Patel, A. (1995). Process trending with piecewise linear smoothing. *Comput. Chem. Eng.* 19 (2), 129–137. doi:10.1016/0098-1354(94)e0042-l

Meng, J., Cai, L., Stroe, D. I., Ma, J., Luo, G., and Teodorescu, R. (2020). An optimized ensemble learning framework for lithium-ion Battery State of Health estimation in energy storage system. *Energy* 206, 118140. doi:10.1016/j.energy.2020.118140

Morstyn, T., Hredzak, B., and Agelidis, V. G. (2014). Distributed cooperative control of microgrid storage. *IEEE Trans. Power Syst.* 30 (5), 2780–2789. doi:10.1109/tpwrs.2014.2363874

Othman, M. H., Mokhlis, H., Mubin, M., Talpur, S., Ab Aziz, N. F., Dradi, M., et al. (2020). Progress in control and coordination of energy storage system-based VSG: A review. *IET Renew. Power Gener.* 14 (2), 177–187. doi:10.1049/iet-rpg.2019.0274

Parlikar, A., Truong, C. N., Jossen, A., and Hesse, H. (2021). The carbon footprint of island grids with lithium-ion battery systems: An analysis based on levelized emissions of energy supply. *Renew. Sustain. Energy Rev.* 149, 111353. doi:10.1016/j.rser.2021.111353

Prasad, E. N., Dash, P. K., and Sahani, M. (2022). Diagnosing utility grid disturbances in photovoltaic integrated DC microgrid using adaptive multiscale morphology with DFA analysis. *Sustain. Energy, Grids Netw.* 29, 100574. doi:10.1016/j.segan.2021.100574

Rana, M. M., Uddin, M., Sarkar, M. R., Shafiullah, G., Mo, H., and Atef, M. (2022). A review on hybrid photovoltaic – battery energy storage system: Current status, challenges, and future directions. *J. Energy Storage* 51, 104597. doi:10.1016/j.est.2022.104597

Sharadga, H., Hajimirza, S., and Balog, R. S. (2020). Time series forecasting of solar power generation for large-scale photovoltaic plants. *Renew. Energy* 150, 797–807. doi:10.1016/j.renene.2019.12.131

Shen, L., Cheng, Q., Cheng, Y., Wei, L., and Wang, Y. (2020). Hierarchical control of DC micro-grid for photovoltaic EV charging station based on flywheel and battery energy storage system. *Electr. power Syst. Res.* 179, 106079. doi:10.1016/j.epsr.2019.106079

Shili, S., Hijazi, A., Sari, A., Lin-Shi, X., and Venet, P. (2016). Balancing circuit new control for supercapacitor storage system lifetime maximization. *IEEE Trans. Power Electron.* 32 (6), 4939–4948. doi:10.1109/tpel.2016.2602393

Syed, M. A., Abdalla, A. A., Al-Hamdi, A., and Muhammad, K. (2020). Double moving average methodology for smoothing of solar power fluctuations with battery energy storage[C]//2020 International Conference on Smart Grids and Energy Systems (SGES). *IEEE*, 291–296.

Vicidomini, G., Petrone, G., Monmasson, E., and Spagnuolo, G. (2017). FPGA based implementation of a sliding-mode observer for battery state of charge estimation[C]//2017 IEEE 26th International Symposium on Industrial Electronics (ISIE). *IEEE*, 1268–1273. doi:10.1109/isie.2017.8001427

Victoria, M., Haegel, N., Peters, I. M., Sinton, R., Jager-Waldau, A., del Canizo, C., et al. (2021). Solar photovoltaics is ready to power a sustainable future. *Joule* 5 (5), 1041–1056. doi:10.1016/j.joule.2021.03.005

Wang, W., Han, X., Wu, Y., Li, H., Li, X., Wang, S., et al. (2021). Energy management of battery energy storage station considering system operation efficiency[C]//2021 International Conference on Power System Technology (POWERCON). *IEEE*, 1100–1104. doi:10.1109/powercon53785.2021.9697503

Weng, C., Cui, Y., Sun, J., and Peng, H. (2013). On-board state of health monitoring of lithium-ion batteries using incremental capacity analysis with support vector regression. *J. Power Sources* 235, 36–44. doi:10.1016/j.jpowsour.2013.02.012

Yang, Zilong, Song, Zhenhao, pan, Jing, Chen, Zhuo, and Wang, Yibo (2019). Multi-mode coordinated control strategy of distributed PV and energy storage system[J]. *Proc. CSEE* 39 (08), 2213–2220+4. doi:10.13334/j.0258-8013.pcsee.182342

Yu, D. X., and Gao, Y. X. (2013). SOC estimation of Lithium-ion battery based on Kalman filter algorithm[C]//Applied Mechanics and Materials. *Trans. Tech. Publ. Ltd.* 347, 1852–1855. doi:10.4028/www.scientific.net/amm.347-350.1852

Yu, Z., Zinger, D., and Bose, A. (2011). An innovative optimal power allocation strategy for fuel cell, battery and supercapacitor hybrid electric vehicle. *J. Power Sources* 196 (4), 2351–2359. doi:10.1016/j.jpowsour.2010.09.057

frontiers | Frontiers in Energy Research

TYPE Brief Research Report
PUBLISHED 19 September 2022
DOI 10.3389/fenrg.2022.973736

EDITED BY
Tianguang Lu,
Shandong University, China

REVIEWED BY
Tao Chen,
Southeast University, China
Licheng Wang,
Zhejiang University of Technology,
China

*CORRESPONDENCE
DianSheng Luo,
lhx20070322@hnu.edu.cn

SPECIALTY SECTION
This article was submitted to Smart Grids,
a section of the journal
Frontiers in Energy Research

RECEIVED 20 June 2022
ACCEPTED 15 August 2022
PUBLISHED 19 September 2022

CITATION
Luo D, Xi R, Che L and He H (2022),
Health condition assessment of transformers based on cross message passing graph neural networks.
Front. Energy Res. 10:973736.
doi: 10.3389/fenrg.2022.973736

Health condition assessment of transformers based on cross message passing graph neural networks

DianSheng Luo[1]*, RuiYao Xi[1], LiXuan Che[2] and HongYing He[1]

[1]College of Electrical and Information Engineering, Hunan University, Changsha, China, [2]Weifang Vocational College, Weifang, China

A method is proposed to assess the health condition of transformers based on cross message passing graph neural networks (CMPGNNs) in this paper. In order to improve the accuracy of transformer health condition assessment, multiple indicators and their strong correlation are taken into account. The evaluation indicators are divided into four comprehensive state categories, and each category has several indicators. First, the correlation between indicators of a state category is extracted by the health index method and the importance of criteria is analyzed through the inter-criteria correlation (CRITIC) method, and the health index of comprehensive indicators is obtained. Then, a diagram of comprehensive indicators is constructed, and the correlation between indicators of different state categories is extracted. Finally, CMPGNN is constructed to achieve the health assessment. The experimental results show that the proposed method can improve the accuracy of transformer health condition assessment.

KEYWORDS

power transformer, health condition assessment, health index, cross message passing graph neural network, correlation of indicators

1 Introduction

A power transformer is one of the most important parts of the power system (Xie et al., 2020), and the health of a power transformer plays a vital role in the safe operation of power grids and the development of national economy (Wang et al., 2022). Accurate health condition assessment helps detect potential faults and reduce maintenance costs by 20–50% (Sun et al., 2022).

A power transformer is a large system with a complex structure. The selection of indicators is important for the assessment of the transformer health condition. Zhang et al., 2021 select dissolved gases in oil as the evaluation indicator. With the operation of the transformer, the aging of the pressboard will produce furfural. Therefore, furfural content can effectively reflect the aging of insulation (Lin et al., 2019). In Benhmed et al., 2018, indicators of dissolved gases and oil tests are selected to construct an evaluation system. However, in the above methods, only indicators of preventive tests are considered, and indicators of other information, such as the basic information, operating information, and fault maintenance information, are ignored.

At present, the health condition assessment methods include not only single algorithms such as an expert system (Purkait and Chakravorti, 2002), fuzzy theory (Abu-Elanien et al., 2012; Arshad et al., 2014), the Bayesian network (Quan et al., 2013), and the artificial neural network (Pengju and Birtwhistle, 2001) but also the collaborative algorithm of multiple methods (Liao et al., 2011). The mapping between seven dissolved gases and the transformer health condition is established by linear models and nonlinear models (Zeinoddini-Meymand et al., 2021). In reference Islam et al., 2018, the general regression neural network (GRNN) is used to quantify the operating state of each component of the transformer. In reference Ashkezari et al., 2013, a fuzzy support vector machine (FSVM) is constructed to predict the health condition of the transformer insulation system by using the indicators of dissolved gases and oil tests. In fact, there are correlations between indicators. If correlations are not taken into account, the accuracy of evaluation results will be reduced.

Aiming at the problems existing in the transformer health condition assessment method, a method is proposed to assess the health condition of the transformer based on cross message passing graph neural networks (CMPGNNs) in this paper. In this method, the evaluation system of the transformer is established by selecting the indicators of various state information. The health index method and criteria importance through the inter-criteria correlation (CRITIC) method are used to consider the correlation between indicators of a state category. Aiming at the correlation between indicators of different state categories, a diagram of comprehensive indicators is established, and a graph neural network (GNN) based on the cross message passing mechanism is constructed to mine the relationship between indicators and achieve health condition assessment. The experimental results show that it is beneficial to evaluate the health condition of the transformer by using the indicators of multiple state information. The correlation between indicators is fully considered by utilizing CRITIC and CMPGNN, which makes the evaluation results more accurate. In addition, GNN based on the cross message passing mechanism can improve the accuracy of the graph classification task.

2 Health index of comprehensive indicators

2.1 The construction of the transformer evaluation system

Load rate and operating environment are two important factors affecting the insulation performance of power transformers (Muthanna et al., 2006). A preventive test is an effective method to detect the aging of the transformer. In addition, the number of transformer faults is directly related to the health condition (En-Wen and Bin, 2014). In order to consider the state information as much as possible, indicators of four comprehensive state categories, including basic operational information, dissolved gas analysis, oil tests, and electrical tests, are selected to build an evaluation system, as shown in Figure 1A. Each state category includes several sub-state indicators, which are regarded as the low-level indicators.

2.2 Health index of basic operational information

Health index (HI) is the representation of transformer aging degree, and its value ranges from 0 to 10. The larger the health index, the worse the health condition of the transformer.

Four low-level indicators including operating time, designed life, load rate, and operating environment are used to obtain the health index of basic operational information. The health index of basic operational information is expressed as

$$HI_1 = HI_0 * e^{B*(T_2 - T_1)} \tag{1}$$

where HI_0 is the initial health index of the transformer, which is generally taken as 0.5. (T_2-T_1) is the operating time. B is the aging coefficient, which can be expressed as

$$B = \frac{\ln HI_t - \ln HI_0}{T_d} * f_L * f_E \tag{2}$$

where HI_t is the health index corresponding to the time when the transformer has a high probability of failure, which is generally taken as 7. T_d is the designed life. f_L and f_E are the correction coefficients of load and environment, respectively. Their values are shown in Table 1.

2.3 Preprocessing of low-level indicators of the preventive test

The preventive test includes dissolved gas analysis, oil tests, and electrical tests. The low-level indicators of the preventive test are divided into positive and negative indicators. The positive indicator is the indicator that the larger the value, the better the health condition of the transformer, such as breakdown voltage. The negative indicator is the indicator that the larger the value, the worse the health condition of the transformer, such as water content. Positive indicators and negative indicators are preprocessed by Eq. 3 and Eq. 4, respectively.

$$y = \begin{cases} 10 & 0 \le x \le a \\ 5 - 5\sin\left[\frac{\pi}{b-a} * \left(x - \frac{a+b}{2}\right)\right] & a \le x \le b \\ 0 & x > b \end{cases} \tag{3}$$

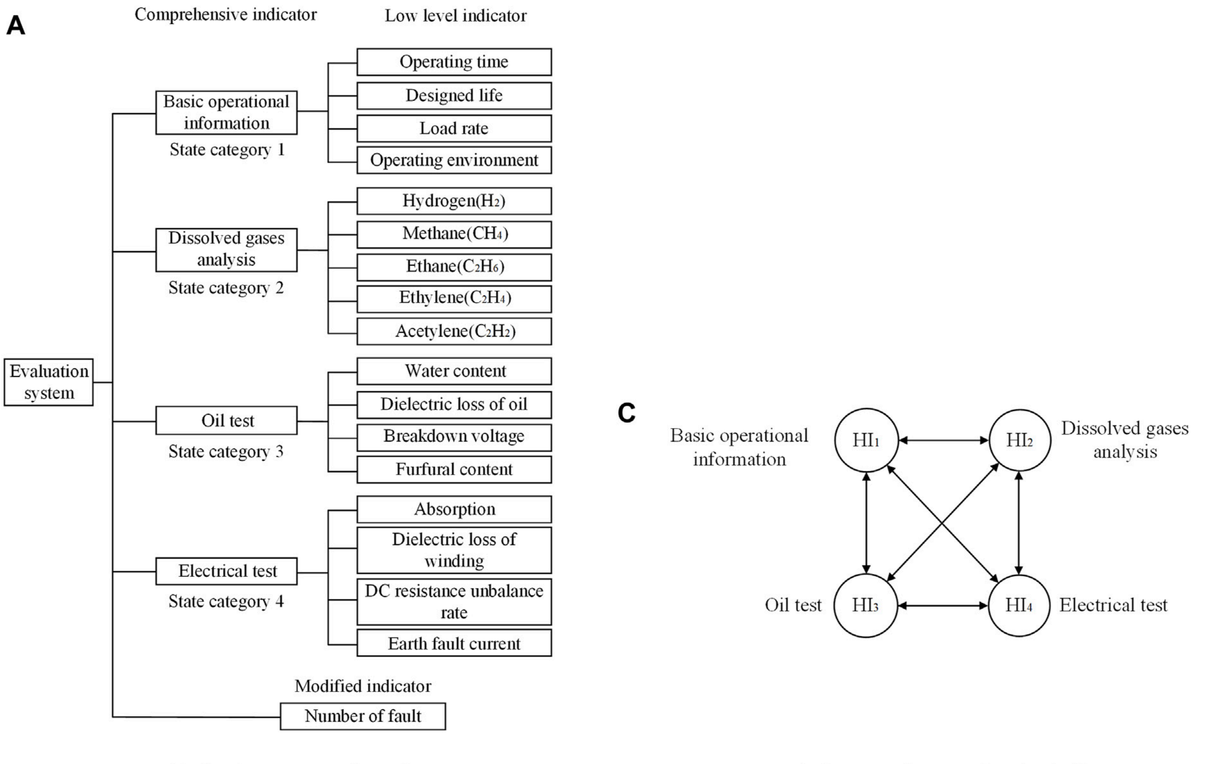

Evaluation system of transformer

A diagram of comprehensive indicators

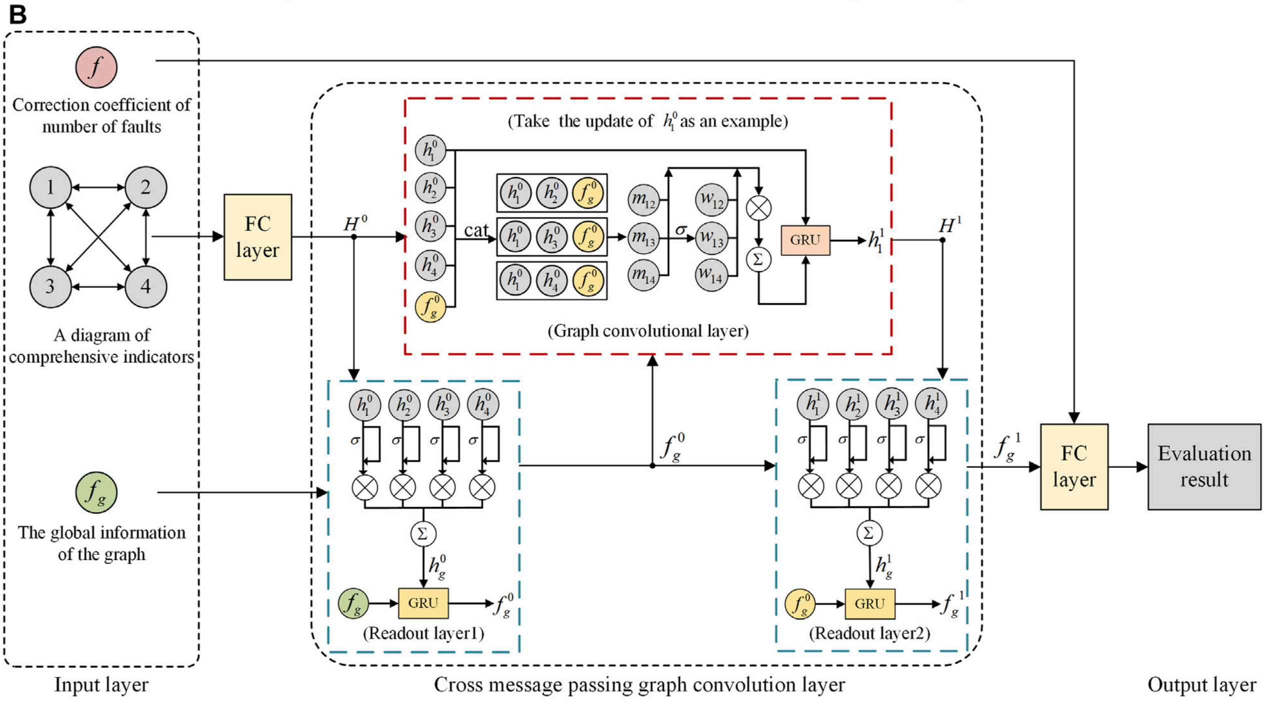

The assessment model of transformer health condition based on CMPGNN

FIGURE 1
Evaluation system and model of health condition assessment.

TABLE 1 Correction coefficient for load, environment, and number of faults.

Load rate (%)	f_L	Environment grade	f_E	Number of faults	Correction coefficient of number of faults
[0–40)	1	0	1	0–1	0.96
[40–60)	1.05	1	1	2–4	1.04
[60–70)	1.1	2	1.05	5–10	1.2
[70–80)	1.25	3	1.15	>10	1.4
[80–150)	1.6	4	1.3	-	-

TABLE.2 Thresholds and pretreatment methods of low-level indicators.

Low-level indicator	*a*	*b*	Formula of pretreatment
H_2 (μL/L)	10	150	Eq. 3
CH_4 (μL/L)	0	60	Eq. 3
C_2H_6 (μL/L)	0	40	Eq. 3
C_2H_4 (μL/L)	0	70	Eq. 3
C_2H_2 (μL/L)	0	5	Eq. 3
Water content (mg/L)	20	35	Eq. 3
Dielectric loss of oil (%)	0	4	Eq. 3
Breakdown voltage (kV)	35	50	Eq. 4
Furfural content (mg/L)	0	4	Eq. 3
Absorption	1.3	2	Eq. 4
Dielectric loss of winding (%)	0	0.8	Eq. 3
DC resistance unbalance rate (%)	0	2	Eq. 3
Earth fault current (mA)	0	100	Eq. 3

$$y = \begin{cases} 0 & 0 \le x \le a \\ 5 + 5\sin\left[\dfrac{\pi}{b-a} * \left(x - \dfrac{a+b}{2}\right)\right] & a \le x \le b \\ 10 & x > b \end{cases} \tag{4}$$

where *a* and *b* are thresholds for indicators. *x* is the measured value. *y* is the preprocessed value, which means the health index of each low-level indicator. In this paper, 110 kV power transformer is taken as an example. The thresholds and pretreatment methods of low-level indicators are shown in Table 2.

2.4 Weight of low-level indicators of the preventive test

The CRITIC method uses the contrast intensity and conflict of the samples to obtain the weights of indicators. Contrast intensity refers to the volatility of the value of an indicator in different samples. The greater the volatility, the stronger the contrast intensity and the higher the weight of the indicator. Conflict refers to the correlation between different indicators. The greater the correlation, the less the conflict and the lower the weight of the indicator. In this paper, the CRITIC method is used to obtain the correlation between indicators of a state category and assign weights to each indicator. With *n* samples and *m* evaluation indicators, the state evaluation matrix is

$$X = \begin{bmatrix} x_{11} & x_{12} & \cdots & x_{1j} & \cdots & x_{1m} \\ x_{21} & x_{22} & \cdots & x_{2j} & \cdots & x_{2m} \\ \vdots & \vdots & \vdots & \vdots & \cdots & \vdots \\ x_{i1} & x_{i2} & \cdots & x_{ij} & \cdots & x_{im} \\ \vdots & \vdots & \vdots & \vdots & \cdots & \vdots \\ x_{n1} & x_{n2} & \cdots & x_{nj} & \cdots & x_{nm} \end{bmatrix} \tag{5}$$

where x_{ij} is the value of the *j*th indicator of the *i*th sample. Positive indicators and negative indicators are normalized by Eq. 6 and Eq. 7, respectively.

$$x_{ij}^{'} = \frac{x_{ij} - \min\limits_{1\le i\le n}\left\{x_{ij}\right\}}{\max\limits_{1\le i\le n}\left\{x_{ij}\right\} - \min\limits_{1\le i\le n}\left\{x_{ij}\right\}} \tag{6}$$

$$x'_{ij} = \frac{\max\limits_{1\le i\le n}\left\{x_{ij}\right\} - x_{ij}}{\max\limits_{1\le i\le n}\left\{x_{ij}\right\} - \min\limits_{1\le i\le n}\left\{x_{ij}\right\}} \tag{7}$$

In this paper, the standard deviation is used to measure the contrast intensity of the low-level indicators, which can be expressed as follows:

$$\bar{x}_j = \frac{1}{n}\sum_{i=1}^{n} x'_{ij} \tag{8}$$

$$P_j = \sqrt{\frac{\sum\limits_{i=1}^{n}\left(x'_{ij} - \bar{x}_j\right)^2}{n}} \tag{9}$$

where $\bar{x}_j$ represents the average value of indicator j. P_j is the standard deviation of indicator j. In this paper, the Spearman correlation coefficient is used to measure the conflict between the low-level indicators, which is expressed as follows:

$$d_i = z_{i(s)} - z_{i(j)} \tag{10}$$

$$r_{sj} = 1 - \frac{6*\sum\limits_{i=1}^{n} d_i^2}{n*(n^2-1)} \quad (s, j \in m) \tag{11}$$

where $z_{i(s)}$ and $z_{i(j)}$ represent the new index of the ith sample after the sample sequences of indicator s and indicator j are, respectively, arranged in descending order. d_i represents the difference of the new index. r_{sj} represents the correlation coefficient between indicator s and indicator j, and $r_{sj} = r_{js}$.

The conflict of indicator j is expressed as follows:

$$Q_j = \sum_{s=1}^{m}\left(1 - r_{sj}\right) \tag{12}$$

Therefore, the information provided by indicator j is expressed as follows:

$$T_j = P_j * Q_j \tag{13}$$

Then the weight of indicator j is expressed as follows:

$$w_j = T_j \Big/ \sum_{j=1}^{m} T_j \tag{14}$$

2.5 Health index of dissolved gas analysis, oil tests, and electrical tests

The health index of dissolved gas analysis, oil tests, and electrical tests can be expressed as follows:

$$HI_i = \sum_{j=1}^{o} y_j w_j \tag{15}$$

where i is equal to 2, 3, and 4, and the corresponding HI_i is the health index of dissolved gas analysis, oil tests, and electrical tests, respectively. o is the number of low-level indicators. o is equal to 5, 4, and 4.

3 Assessment of the transformer health condition based on cross message passing graph neural networks

The assessment model of the transformer health condition based on CMPGNN is shown in Figure 1B. According to the figure, the model includes an input layer, a cross message passing graph convolution layer, and an output layer.

3.1 Input and output of the model

The input layer consists of three parts, namely, the correction coefficient of the number of faults, a diagram of comprehensive indicators, and the global information of the graph. The correction coefficient of the number of faults is determined by the number of faults, as shown in Table 1.

In order to mine the correlation between indicators of different state categories, this paper constructs a diagram of comprehensive indicators as shown in Figure 1C. Each node on the graph represents a comprehensive indicator. The characteristic information of the node is the health index of the comprehensive indicator. The edges between nodes represent the possible correlations between comprehensive indicators.

When mining the correlation between indicators and updating the characteristic information of each indicator, not only the local information but also the global information of the graph should be taken into account. The global information of the graph is the centralized representation of the diagram of comprehensive indicators, which contains the important information of each node and the correlation between nodes.

Transformer health condition types include excellent, good, average, poor, and serious. Therefore, these five health conditions are selected as the output of the model. In addition, the health level for each health condition is set to 0, 1, 2, 3, and 4, respectively.

3.2 Working principle of the cross message passing graph convolution layer

The message passing mechanism is the framework followed by the GNN, including the message passing stage and readout stage. It completes the learning task on the graph according to the correlation between nodes on the graph. The GNN based on the traditional message passing mechanism only performs the readout operation after the message passing stage, and the dynamic features of the graph are ignored during the running time step. In addition, in the process of message generation in the message passing stage, only the information of its own node and neighbor node is considered, and the global information of the graph is not considered. To solve the above problems, a cross message passing mechanism is proposed.

The readout layer is used to realize the readout operation and complete the extraction of the global information of the graph. The sigmoid function is introduced to retain important information of each node and remove redundant information. Then, the aggregation of important information of all nodes on the graph $h_g^{\,t}$ can be expressed as follows:

$$h_g^t = \sum_{i\in G}\left(h_i^t \odot \text{sigmoid}\left(v_1\left(h_i^t\right)\right)\right) \tag{16}$$

where v_1 ( ) is a linear function. t is the running time step. $h_i^{\,t}$ is the information of node i in time step t. G is the set of all nodes on the graph.

The gated recurrent neural network (GRU) includes a reset gate and update gate. The reset gate is used to forget part of the information from the previous time and generate candidate information by combining the selected important historical information with the new input information. The update gate is used to retain part of the information of the previous time and generate the information of the current time by combining the retained historical information with the candidate information. Compared with feed forward neural networks, GRU has memory functions. In addition, compared with long short-term memory networks, GRU has fewer parameters, which can reduce the risk of overfitting.

Therefore, GRU is used to synthesize the global information of the graph at the previous time $f_g^{\,t-1}$ and aggregation of important information of all nodes $h_g^{\,t}$ and update the global information of the graph at current time $f_g^{\,t}$ in this paper,

$$f_g^t = GRU\left(f_g^{t-1}, h_g^t\right) \tag{17}$$

The graph convolution layer is used to realize the message passing stage, which completes message generation, message aggregation, and node embedding update. First, a nonlinear neural network is constructed to generate messages between nodes with correlation, and its principle is formulated as

$$e_{ij}^{t+1} = u\left(v_2\left(h_i^t \parallel h_j^t \parallel f_g^t\right)\right) \tag{18}$$

where v_2 ( ) is a linear function. ‖ is the concatenation operation, which concatenates the i node information, the j node information, and the global information of the graph with time step t. u( ) is a nonlinear activation function. By constructing the nonlinear relationship, the message generated from node j to node i in time step (t+1) is obtained.

In the message aggregation, in order to avoid assigning the same weight to each neighbor node, the sigmoid function is used to assign different passing coefficients for the generated messages. By multiplying the corresponding coefficients with the generated messages and adding them, the aggregation of messages generated by the neighbor node can be obtained, which can be expressed by the formula

$$u_i^{t+1} = \sum_{j\in\mathcal{N}(i)}\left(e_{ij}^{t+1} \odot \text{sigmoid}\left(v_3\left(e_{ij}^{t+1}\right)\right)\right) \tag{19}$$

where v_3 ( ) is a linear function. N(i) is the set of neighbor nodes of node i.

In the updating of the node embedding, not only the aggregation of messages generated by neighbor nodes is used but also the previous information of its own node is used. GRU can selectively retain and forget some historical information and realize update, which is expressed as

$$h_i^{t+1} = GRU\left(h_i^t, u_i^{t+1}\right) \tag{20}$$

Finally, the health condition of the transformer is obtained by a full connection layer which is constructed by using the output of the cross message graph convolution layer and the correction coefficient of the number of the faults.

4 Experiment

4.1 Experimental process

Based on Python language, the model is built on the Spyder platform. The virtual environment is Python 3.7 built by Anaconda.

The training set is used to train the transformer health condition assessment model based on CMPGNN. Figure 2A shows the curve of training loss with the number of iterations. As can be seen from the figure, when the number of trainings reaches 100 times, the loss curve changes slowly and tends to be stable.

Figure 2B is the confusion matrix of the test set. It can be seen from the figure that the model has better performance for transformer health condition evaluation, and there are fewer misjudgments. In addition, the evaluation accuracy of the proposed method in this test set is 95%.

4.2 The influence of the selection of indicators on health condition assessment results

At present, most evaluation methods of the transformer health condition only use the indicators of preventive tests. Therefore, the health condition assessment results using the indicators selected in this paper are compared with those using only indicators of preventive tests. The confusion matrix for the test set using indicators of the preventive test is shown in Figure 2C.

As a large system, there are many factors affecting the health condition of the power transformer, and the preventive

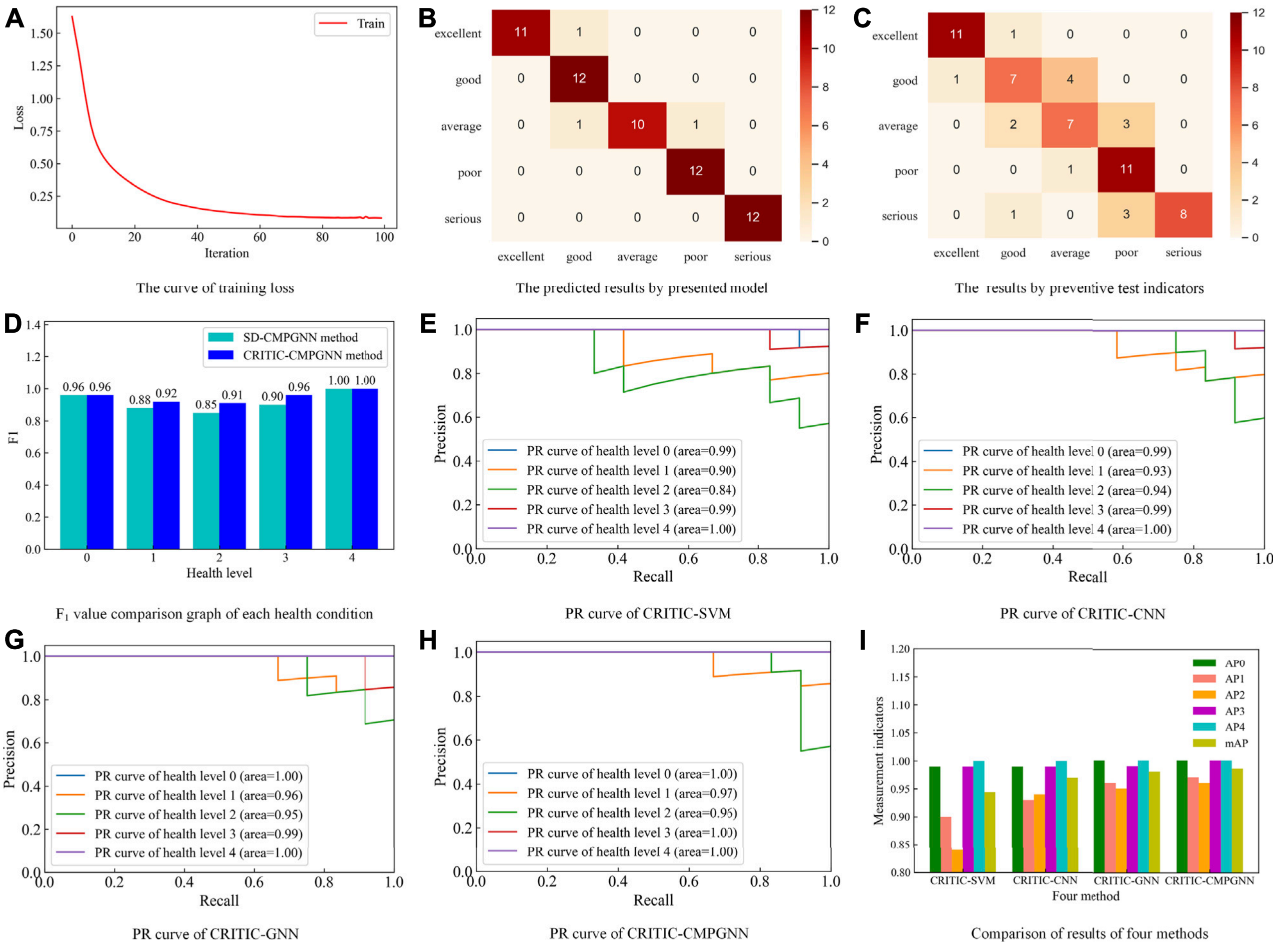

FIGURE 2
Experimental results.

test indicators are only a part of them. Therefore, the health condition of the transformer cannot be accurately obtained by using only the indicators of the preventive test, as shown in Figure 2C.

4.3 The influence of correlation between indicators of a state category on results

The standard deviation method (SD) uses the standard deviation to obtain the sample volatility and assigns weights to each indicator. Compared with the CRITIC method, this method lacks consideration of the correlation between indicators. In this paper, the results of SD-CMPGNN and CRITIC-CMPGNN methods are compared, as shown in Figure 2D.

As can be seen from the figure, the F_1 values obtained by using CRITIC-CMPGNN are 0.04, 0.06, and 0.06 higher than those obtained by SD-CMPGNN when the health condition is “good”, “average”, and “poor”, respectively. This is due to the duplication of information between the low-level indicators. In the SD method, the correlation between indicators is ignored, resulting in more redundant information and less important information provided to comprehensive indicators, thus affecting the accuracy of evaluation results. Therefore, considering the correlation between indicators of a state category can improve the accuracy of results.

4.4 The influence of correlation between indicators of different state categories on results

Figures 2E–H are PR curves of the health condition assessment method based on CRITIC-SVM, CRITIC-CNN, CRITIC-GNN, and CRITIC-CMPGNN, respectively.

The results of the four methods are also shown in Figure 2I. Here, AP_i is the area under the PR curve for the ith health condition. mAP is the average of AP for five health conditions. The larger the value of the above indicators, the better the effect of the model. According to the figure, the effect of CRITIC-SVM is the worst, and the effect of CRITIC-CNN is better than that of CRITIC-SVM. This is due to the inherent shortcomings of SVM in solving multiple classification problems, while CNN has good feature extraction ability. Compared with CRITIC-CNN, the effects of CRITIC-CMPGNN and CRITIC-GNN are improved. This is because CMPGNN and GNN can effectively extract the spatial features of the topology and deeply mine the correlation features of the topology. Therefore, considering the correlation between indicators of different state categories can improve the accuracy of results. In addition, the effect of CRITIC-CMPGNN is better than that of CRITIC-GNN, which indicates that GNN based on the cross message passing mechanism can improve the accuracy.

5 Conclusion

In order to improve the accuracy of transformer health condition assessment, multiple indicators and their strong correlation are taken into account in this paper. CMPGNN is designed to achieve higher accuracy. The conclusions of this paper are as follows:

(1) The accuracy of the result is improved by considering the indicators of multiple state information.
(2) The accuracy of the result is improved by using CRITIC. This is because the correlation between low-level indicators is taken into account, resulting in less redundant information and more important information for comprehensive indicators.
(3) The accuracy of the result is improved by using CMPGNN. This is because the correlation between the comprehensive indicators is deeply excavated.
(4) In the cross message passing mechanism of CMPGNN, the global information of the graph at the previous time is taken into account in subsequent node updates and global information updates of the graph. This is beneficial to improve the accuracy of evaluation results.

Data availability statement

The original contributions presented in the study are included in the article/supplementary material; further inquiries can be directed to the corresponding author.

Author contributions

LD: conceptualization, methodology, validation, writing—review. XR: gathering data, debug programs, writing—original draft. CL: supervision, writing—revise. HH: methodology, supervision, writing—revise and editing.

Funding

This work is supported by the National Key Research and Development Plan, China, 2017, under Grant 2017YFB0903403.

Conflict of interest

The authors declare that the research was conducted in the absence of any commercial or financial relationships that could be construed as a potential conflict of interest.

Publisher's note

References

Abu-Elanien, A. E. B., Salama, M. M. A., and Ibrahim, M. (2012). Calculation of a health index for oil-immersed transformers rated under 69 kV using fuzzy logic. *IEEE Trans. Power Deliv.* 27, 2029–2036. doi:10.1109/TPWRD.2012.2205165

Arshad, M., Islam, S. M., and Khaliq, A. (2014). Fuzzy logic approach in power transformers management and decision making. *IEEE Trans. Dielectr. Electr. Insul.* 21, 2343–2354. doi:10.1109/TDEI.2014.003859

Ashkezari, A. D., Ma, H., Saha, T. K., and Ekanayake, C. (2013). Application of fuzzy support vector machine for determining the health index of the insulation system of in-service power transformers. *IEEE Trans. Dielectr. Electr. Insul.* 20, 965–973. doi:10.1109/TDEI.2013.6518966

Benhmed, K., Mooman, A., Younes, A., Shaban, K., and El-Hag, A. (2018). Feature selection for effective health index diagnoses of power transformers. *IEEE Trans. Power Deliv.* 33, 3223–3226. doi:10.1109/TPWRD.2017.2762920

En-Wen, L., and Bin, S. (20142014). Transformer health status evaluation model based on multi-feature factors. *2014 Int. Conf. Power Syst. Technol.* 20-22, 1417–1422. doi:10.1109/POWERCON.2014.6993723

Islam, M., Lee, G., Hettiwatte, S. N., and Williams, K. (2018). Calculating a health index for power transformers using a subsystem-based GRNN approach. *IEEE Trans. Power Deliv.* 33, 1903–1912. doi:10.1109/TPWRD.2017.2770166

Liao, R., Zheng, H., Grzybowski, S., Yang, L., Zhang, Y., and Liao, Y. (2011). An integrated decision-making model for condition assessment of power transformers using fuzzy approach and evidential reasoning. *IEEE Trans. Power Deliv.* 26, 1111–1118. doi:10.1109/TPWRD.2010.2096482

Lin, Y., Wei, C., Tao, F., and Li, J. (2019). Aging assessment of oil-paper insulation of power equipment with furfural analysis based on furfural generation and partitioning. *IEEE Trans. Power Deliv.* 34, 1626–1633. doi:10.1109/TPWRD.2019.2916254

Muthanna, K. T., Sarkar, A., Das, K., and Waldner, K. (2006). Transformer insulation life assessment. *IEEE Trans. Power Deliv.* 21, 150–156. doi:10.1109/TPWRD.2005.855474

Pengju, K., and Birtwhistle, D. (2001). Condition assessment of power transformer on-load tap-changers using wavelet analysis. *IEEE Trans. Power Deliv.* 16, 394–400. doi:10.1109/61.924817

Purkait, P., and Chakravorti, S. (2002). Time and frequency domain analyses based expert system for impulse fault diagnosis in transformers. *IEEE Trans. Dielectr. Electr. Insul.* 9, 433–445. doi:10.1109/TDEI.2002.1007708

Quan, J., Ruan, L., Xie, Z., Li, X., and Lin, X. (2013), The application of Bayesian network theory in transformer condition assessment. *IEEE PES Asia-Pacific Power Energy Eng. Conf* (Hong Kong, China: APPEEC), 8–11, 1–4. doi:10.1109/APPEEC.2013.6837161

Sun, C., Zhou, Z., Zhang, Y., Jia, Z., Huang, J., and Huang, C. (2022). A dissolved gas assessment model for power transformers according to weighted association rule mining. *Front. Energy Res.* 10. doi:10.3389/fenrg.2022.879869

Wang, J., Zhang, X., Zhang, F., Wan, J., Kou, L., and Ke, W. (2022). Review on evolution of intelligent algorithms for transformer condition assessment. *Front. Energy Res.* 10. doi:10.3389/fenrg.2022.904109

Xie, B., Zhao, D., and Hong, T. (2020). Transformer monitoring and protection in dynamic power systems – a review. *Front. Energy Res.* 8. doi:10.3389/fenrg.2020.00150

Zeinoddini-Meymand, H., Kamel, S., and Khan, B. (2021). An efficient approach with application of linear and nonlinear models for evaluation of power transformer health index. *IEEE Access* 9, 150172–150186. doi:10.1109/ACCESS.2021.3124845

Zhang, P., Qi, B., Shao, M., Li, C., Rong, Z., Chen, J., et al. (2021). Optimal data selection rule mining for transformer condition assessment. *IEEE Access* 9, 156962–156972. doi:10.1109/ACCESS.2021.3126763

frontiers | Frontiers in Energy Research

TYPE Original Research
PUBLISHED 20 September 2022
DOI 10.3389/fenrg.2022.995714

Check for updates

OPEN ACCESS

EDITED BY
Tianguang Lu,
Shandong University, China

REVIEWED BY
Jilei Ye,
Nanjing Tech University, China
Yachen Tang,
Michigan Technological University,
United States

*CORRESPONDENCE
Chong Wang,
chongwang@hhu.edu.cn

SPECIALTY SECTION
This article was submitted to Smart Grids,
a section of the journal
Frontiers in Energy Research

RECEIVED 16 July 2022
ACCEPTED 23 August 2022
PUBLISHED 20 September 2022

CITATION
Ge Y, Wang C, Hao Y, Han G and Lu Y (2022), Robust optimal dispatch of distribution system considering carbon capture and demand response.
Front. Energy Res. 10:995714.
doi: 10.3389/fenrg.2022.995714

Robust optimal dispatch of distribution system considering carbon capture and demand response

Yulin Ge[1], Chong Wang[1]*, Yuchen Hao[2], Guigang Han[3] and Yu Lu[1]

[1]Hohai University, Nanjing, China, [2]State Grid Jiangsu Electric Power Co., Ltd., Nanjing, China, [3]China Electric Power Research Institute, Nanjing, China

Participation of carbon capture power plants and demand response in power system dispatch is an important mean to achieve the carbon-neutral goal. In order to take into account uncertainty of wind power and low-carbon economic operation of the distribution system, a two-stage robust optimal dispatch model of the distribution system considering carbon capture and demand response is proposed in this paper. In the day-ahead stage, the unit commitment plan and the price demand response (PDR) schedule are established. In the intra-day stage, the carbon related cost is included in the optimization objective. The strategies for the generators and the incentive demand response (IDR) are optimized under the worst-case output of wind power based on the results of the day-ahead stage. Karush-Kuhn-Tucker (KKT) conditions and the column-and-constraint generation (C&CG) algorithm are used to solve the proposed two-stage model. A revised IEEE 33-bus distribution system is used to verify the feasibility and effectiveness of the proposed model.

KEYWORDS

carbon capture, demand response, carbon trading, column-and-constraint generation algorithm, two-stage robust optimization

Introduction

With the increasing shortage of traditional fossil energy, the energy crisis is a main problem faced by countries all over the world. On the one hand, the depletion of fossil energy is inevitable with the continuous exploitation of human beings. On the other hand, the massive use of traditional fossil energy is usually accompanied by greenhouse gas emissions, which makes the global temperature rise. In order to solve the environmental problems, China has clearly put forward the goals of “emission peak” in 2030 and “carbon neutrality” in 2060.

The emergence of the carbon capture and storage (CCS) technology provides a new way to achieve the carbon-neutral goal. In carbon-constrained environment, Chen et al. (2010) formulates the process of carbon capture and explores the interaction between carbon capture system and power system. A unit commitment model based on the carbon capture technology is proposed and performance indices affecting the scheduling are derived in (Reddy et al., 2017). Based on the major operating characteristics of the carbon capture power plant, a profit maximization model is proposed in (Chen et al., 2012) and a comprehensive low-carbon power system dispatch model is formulated in (Ji et al., 2013). In (Lou et al., 2015), a multi-period spinning reserve optimization model is proposed based on the flexibility of the operation of the carbon capture power plant. In order to cope with the uncertainty of wind power and load, a multi-objective programming-based economic-emission dispatch model with carbon capture power plants is proposed in (Akbari-Dibavar et al., 2021). In (Li et al., 2015), a stochastic dispatch model of power systems with carbon capture power plants and a robust re-dispatch strategy are proposed to realize the low-carbon operation requirement.

The introduction of the carbon trading mechanism combines the economic benefits and environmental benefits of the power system. It can guide the energy saving and emission reduction of power plants through carbon trading price (Zhou et al., 2020). In (Zhang N. et al., 2016), demand side resources and the carbon trading mechanism are considered and their effect on generation dispatch is analyzed. Wang Y. et al. (2020) proposes a two-stage scheduling model considering the electricity and carbon markets, which provides an important guidance for carbon trading mechanism.

There are many schedulable resources in the distribution network (Wang C. et al., 2020). Demand response is one of them, which plays the role of peak shaving and valley filling. Xiao et al. (2018) considers the uncertainty of the load side and the generation side in the optimal operation of the integrated energy system with distributed generation, demand response and the energy storage system. According to response form, demand response can be divided into price demand response (PDR) and incentive demand response (IDR). PDR changes users' electricity consumption habits by setting electricity prices. IDR encourage users to participate in power system dispatch by means of economic compensation. The PDR is uncertain due to the affection of operating scenarios and types of customers (Liu and Tomsovic, 2015). A multi-stage robust optimization of unit commitment with the uncertainty of PDR and the wind power is developed in (Zhao et al., 2013). Similarly, there is uncertainty in the IDR. In (Bai et al., 2016), an interval optimal dispatch of gas-electricity integrated energy systems considering IDR and wind power uncertainty is proposed and the effect of IDR is investigated.

Due to the influence of the weather, environment and other factors, there are many uncertainties in the power system (Wang et al., 2022). Robust optimization is an important method to deal with the uncertainty. It does not depend on the probability distribution of uncertain parameters, and can be applied to large-scale calculation. Therefore, it can be applied to a variety of optimization scenarios, e.g., the identification of critical switches in distribution systems, the planning and allocation of microgrid defense resource and the location-allocation of the distributed power flow controller (Lei et al., 2018; Lei et al., 2019; Zhu et al., 2022). In (Xu et al., 2019), a cyber-physical system robust routing model considering the interdependent characteristics of cyber networks and physical networks is proposed. Considering the uncertainty of wind power, a robust optimal dispatch model of wind fire energy storage system is established in (Chen et al., 2021), which achieves the optimal robustness and economical operation of the system. Yan et al. (2022) proposes a robust scheduling methodology for the integrated electric and gas systems with blending hydrogen and considers the dynamics of natural gas pipeline. In (Zhang et al., 2018), a two-stage robust optimization for the multi-microgrid is constructed, which describes the discrete characteristics of energy transaction combinations. The multi-microgrids are connected with the smart distribution networks in (Liu et al., 2018). A two-level interactive mechanism is proposed and a two-stage robust model is established to handle the uncertainty in the lower level. Based on the results of the lower level, the operation cost of the distribution network is minimized with the operational quality guaranteed in the upper level. In (Wang et al., 2021), flexible loads are connected to the active distribution networks through load aggregators. Since the load aggregators and the active distribution networks belong to two stakeholders, a robust optimal dispatching model of active distribution networks and an independent optimal scheduling model for load aggregators are constructed. The analytical target cascading method is implemented to solve the problem.

There have been lots of papers considering carbon trading mechanism and carbon capture power plants. However, how to coordinate them is still worth investigating. And the effect of the wind power uncertainty on demand response is rarely mentioned. Based on the background above, a two-stage robust optimal dispatch model of the distribution system considering carbon capture and demand response is proposed to realize the optimal economic and environmental benefits. C&CG algorithm is used to solve the problem by iteration. Case studies investigate the effects of the robust level and demand response on the optimization results. The influences of different demand response form are distinguished. The function of carbon trading mechanism and the interaction between carbon trading mechanism and carbon capture power plants are analyzed.

Mathematical model

Carbon capture power plant model

A thermal power plant can become a carbon capture power plant after introducing the CCS technology.

The carbon dioxide produced by the carbon capture power plants can be expressed as:

$$Q_{ccs}(t) = \mu_{ccsint} P_{ccs}(t) \tag{1}$$

P_{ccs}, μ_{ccsint} and Q_{ccs} are the active power output, carbon emission intensity and actual carbon emissions of the carbon capture power plant, respectively.

Carbon capture power plants can absorb part of carbon dioxide produced by coal combustion through absorption towers. Therefore, the carbon dioxide treated by the carbon capture power plant should meet the following constraint:

$$0 \le Q_{ccs}^{tre}(t) \le Q_{ccs}(t) \tag{2}$$

where Q_{ccs}^{tre} is the amount of carbon dioxide treated by the carbon capture power plant.

Because of the treatment of carbon dioxide, the operation energy consumption caused by the carbon capture device can be expressed as:

$$P_{ccs0}(t) = \gamma_{ccs} Q_{ccs}^{tre}(t) \tag{3}$$

where γ_{ccs} is the operation energy consumption caused by the treatment of unit carbon dioxide; P_{ccs0} is the operation energy consumption of the carbon capture device.

The operation energy consumption of the carbon capture device should be limited in its operating region.

$$P_{ccs0}{}^{min}(t) \le P_{ccs0}(t) \le P_{ccs0}{}^{max}(t) \tag{4}$$

$P_{ccs0}{}^{max}$ and $P_{ccs0}{}^{min}$ are the upper and lower limits of operation energy consumption of the carbon capture device.

Carbon capture power plants also cause some fixed energy consumption which can be regarded as a constant. Therefore, the net output of the carbon capture power plant can be calculated as:

$$P_{ccsnet}(t) = P_{ccs}(t) - P_{ccs0}(t) - P_{ccsfix} \tag{5}$$

where P_{ccsnet} and P_{ccsfix} are the net output and the fixed energy consumption of the carbon capture power plant, respectively.

The carbon dioxide captured by the carbon capture device is given by:

$$Q_{cap}(t) = \beta_{ccs} Q_{ccs}^{tre}(t) \tag{6}$$

where β_{ccs} is the carbon dioxide collection ratio usually taken 0.9; Q_{cap} is amount of carbon dioxide captured by the carbon capture device.

Carbon trading mechanism model

Carbon trading mechanism takes carbon emission as a commodity, which can control the total amount of carbon emissions. The government allocates carbon credits to each carbon emission source. If the actual carbon emissions exceed the carbon credits, the excess amount should be purchased from the carbon trading market. On the contrary, if the actual carbon emissions are less, the remaining credits can be sold in the carbon trading market.

This paper holds that the power purchase from the main network comes from thermal power plants. So, there are three kinds of carbon emission sources including carbon capture power plants, thermal power plants and power purchase. It is assumed that the carbon credits and the actual carbon emissions are proportional to the active power outputs of the carbon emission resources, which can be expressed as:

$$\begin{cases} E_{quo}(t) = E_{ccsquo}(t) + E_{genquo}(t) + E_{buyquo}(t) \\ E_{ccsquo}(t) = \sum_{i \in \Omega_{ccs}} \mu_{i,ccsquo} P_{i,ccs}(t) \\ E_{genquo}(t) = \sum_{i \in \Omega_{gen}} \mu_{i,genquo} P_{i,gen}(t) \\ E_{buyquo}(t) = \mu_{buyquo} P_{buy}(t) \end{cases} \tag{7}$$

where $P_{i,ccs}$, $P_{i,gen}$ and P_{buy} are the active power of the carbon capture power plants, thermal power plants and power purchase, respectively; $\mu_{i,ccsquo}$, $\mu_{i,genquo}$ and $\mu_{i,buyquo}$ are the unit carbon emission quotas; Ω_{ccs} and Ω_{gen} are the set of carbon capture power plants and thermal power plants; E_{ccsquo}, E_{genquo} and E_{buyquo} are the carbon credits of each carbon emission source; E_{quo} is the carbon credits of the distribution system.

Since the carbon capture power plants can absorb part of carbon dioxide, the actual carbon emissions of the distribution system should be reduced by the captured carbon dioxide, which can be calculated as follows:

$$\begin{cases} E_{int}(t) = E_{ccsint}(t) + E_{genint}(t) + E_{buyint}(t) - E_{cap}(t) \\ E_{ccsint}(t) = \sum_{i \in \Omega_{ccs}} Q_{i,ccs}(t) \\ E_{genint}(t) = \sum_{i \in \Omega_{gen}} \mu_{i,genint} P_{i,gen}(t) \\ E_{cap}(t) = \sum_{i \in \Omega_{ccs}} Q_{i,cap}(t) \\ E_{buyint}(t) = \mu_{buyint} P_{buy}(t) \end{cases} \tag{8}$$

where $\mu_{i,genint}$ and μ_{buyint} are the carbon emission intensities of thermal power plants and power purchase; E_{ccsint}, E_{genint} and E_{buyint} are the actual carbon emissions of each carbon emission source; E_{cap} and E_{int} are the total amount of the captured carbon dioxide and the actual carbon emissions of the distribution system.

The volume of carbon trading E_{car} is given by:

$$E_{car}(t) = E_{int}(t) - E_{quo}(t) \tag{10}$$

Demand response model

PDR model

For the PDR model, the elasticity matrix **E** is usually used to express the influence of relative change in electricity prices on the relative change in loads (Kirschen et al., 2000).

$$\mathbf{\Delta q} = \mathbf{E} \cdot \mathbf{\Delta p} \tag{14}$$

where $\mathbf{\Delta q}$ and $\mathbf{\Delta p}$ are the change rate matrix of the loads and electricity prices. The exactly expressions of $\mathbf{\Delta q}$, $\mathbf{\Delta p}$ and $\mathbf{E}$ are as follows:

$$\mathbf{\Delta p} = \begin{bmatrix} \frac{\Delta p(1)}{p(1)} & \frac{\Delta p(2)}{p(2)} & \cdots & \frac{\Delta p(24)}{p(24)} \end{bmatrix}^T \tag{11}$$

$$\mathbf{\Delta q} = \begin{bmatrix} \frac{\Delta q(1)}{q(1)} & \frac{\Delta q(2)}{q(2)} & \cdots & \frac{\Delta q(24)}{q(24)} \end{bmatrix}^T \tag{12}$$

$$\mathbf{E} = \begin{bmatrix} \varepsilon_{1,1} & \varepsilon_{1,2} & \cdots & \varepsilon_{1,24} \\ \varepsilon_{2,1} & \varepsilon_{2,2} & \cdots & \varepsilon_{2,24} \\ \vdots & \vdots & & \vdots \\ \varepsilon_{24,1} & \varepsilon_{24,2} & \cdots & \varepsilon_{24,24} \end{bmatrix} \tag{13}$$

where Δp and p are the variation in electricity prices and the reference value of the electricity prices; Δq and q are the response power of the loads and the reference value of the loads; ε_{ii} and ε_{ij} are the self-elasticity coefficient and the cross-elasticity coefficient, respectively.

After the implementation of PDR, the loads are given by:

$$q_{\text{PDR}}(t) = q^0(t) + \Delta q(t) \tag{14}$$

where q^0 and q_{PDR} is the initial loads and the loads after PDR.

The total loads before and after PDR should remain the same, which can be expressed as:

$$\sum_{t=1}^{T} q_{\text{PDR}}(t) = \sum_{t=1}^{T} q^0(t) \tag{15}$$

Considering the interests of users, the change of electricity prices and loads should be within the limits.

$$0 \le \Delta p(t) \le \Delta p^{\max} \tag{16}$$

$$-\Delta q^{\max} \le \Delta q(t) \le \Delta q^{\max} \tag{17}$$

$\Delta p^{\max}$ and $\Delta q^{\max}$ are the maximum variation of electricity prices and loads, respectively.

IDR model

The loads participating in IDR can be divided into shiftable loads and interruptible loads (Zhang X. et al., 2016). The constraints of the response power of the two kinds of loads Eqs 18, 19 are considered. In the whole dispatching period, the response power of interruptible loads cannot be larger than the maximum shedding power Eq. 20 and the total amount of the shiftable loads should remain unchanged Eq. 21.

$$0 \le P_{\text{IDR,inte}}(t) \le \alpha_{\text{inte}} P_{\text{load}}(t) \tag{18}$$

$$-\alpha_{\text{shif}} P_{\text{load}}(t) \le P_{\text{IDR,shif}}(t) \le \alpha_{\text{shif}} P_{\text{load}}(t) \tag{19}$$

$$0 \le \sum_{t=1}^{T} P_{\text{IDR,inte}}(t) \le P_{\text{IDR,inte}}{}^{\max} \tag{20}$$

$$\sum_{t=1}^{T} P_{\text{IDR,shif}}(t) = 0 \tag{25}$$

$P_{\text{IDR, inte}}$ and $P_{\text{IDR, shif}}$ are the response power of the interruptible loads and shiftable loads, respectively. α_{inte} and α_{shif} are the maximum interruptible load ratio and shiftable load ratio. P_{load} is the total loads. $P_{\text{IDR,inte}}{}^{\max}$ is the maximum shedding power in the whole dispatching period.

In order to avoid the fluctuation of the electricity prices in a short time, the PDR schedule is implemented in the day-ahead stage, and the obtained electricity prices are maintained in the intra-day stage. And the IDR schedule is implemented in the intra-day stage. Therefore, PDR and IDR can schedule loads on different time scales and increase the economy and flexibility of the power system operation.

Two-stage robust optimal dispatch model

With the increase of wind farms accessing the distribution system, it is difficult to obtain the probability distribution of the outputs of each wind farm. And using the probability distribution to represent the uncertainty of wind power will increase the amount of calculation greatly. Robust optimization model is a better choice. The two-stage robust optimization model can reduce some conservatism. The dispatching plan of the power plants and the demand response strategy can be made at two time scales, which gives physical meaning to the two-stage model. So, in this section, a day-ahead and intra-day two-stage robust optimal dispatch model of the distribution system considering carbon capture and demand response is established. The objective function and constraints are introduced as follows.

Objective function

According to the different time scales, the two-stage robust optimal dispatch model divides the decision-making process into two stages which are called the day-ahead stage and the intra-day stage. The cost includes the start up and shut down cost of power plants in the day-ahead stage. And the operation cost of power plants, the carbon trading cost, the cost of storage and transportation of carbon dioxide and the IDR scheduling cost are included in the intra-day stage. To sum up, the objective function is as follows:

$$\min_{\mathbf{x}} \left\{ \sum_{t=1}^{T} \left[C_{\text{up}}(\mathrm{t}) + C_{\text{off}}(t) \right] + \max_{\mathbf{w} \in W} \min_{\mathbf{y}} \sum_{t=1}^{T} \left[C_{\text{run}}(t) + C_{\text{ex}}(t) + C_{\text{car}}(\mathrm{t}) + C_{\text{IDR}}(t) \right] \right\} \tag{22}$$

where C_{up} and C_{off} are the start up and shut down cost of power plants; C_{run}, C_{ex}, C_{car} and C_{IDR} are the operation cost of power plants, the power purchase cost, the carbon related cost and the

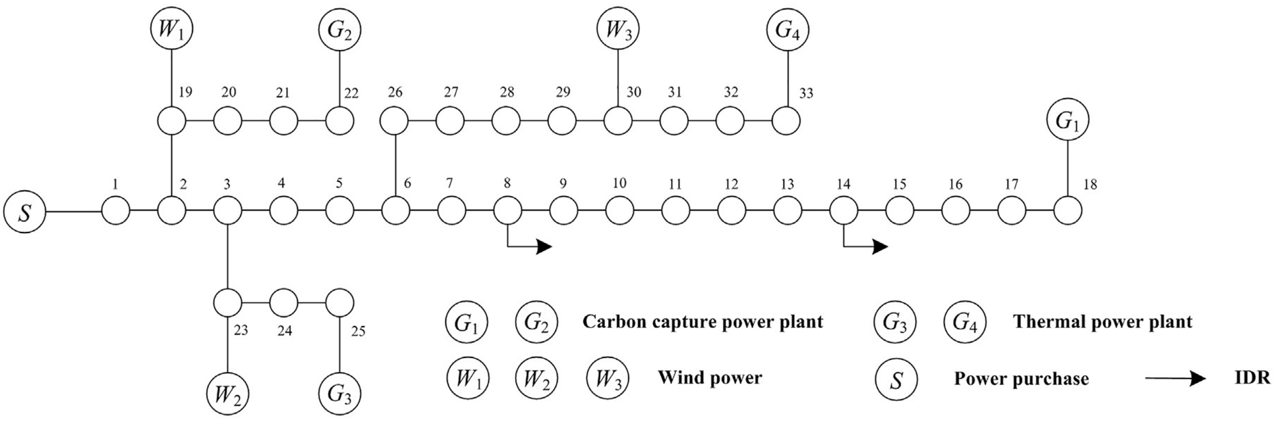

FIGURE 1
The revised IEEE-33 bus distribution system.

IDR scheduling cost, respectively; **x** and **y** represents decision variable vector of the day-ahead stage and the intra-day stage; **w** represents the uncertain variables referring to the output of wind power and W is the uncertainty set of the wind power.

Objective in the day-ahead stage

The start up and shut down cost of power plants should meet the following constraints.

$$C_{\mathrm{up}}(t) \geq \sum_{i\in\Omega} \rho_{i,\mathrm{up}} \left[u_i(t) - u_i(t-1)\right], \quad C_{\mathrm{up}}(t) \geq 0 \tag{22}$$

$$C_{\mathrm{off}}(t) \geq \sum_{i\in\Omega} \rho_{i,\mathrm{off}} \left[u_i(t) - u_i(t-1)\right], \quad C_{\mathrm{off}}(t) \geq 0 \tag{23}$$

u is a binary variable and 0 is taken when the power plant is closed, while 1 means the power plant is started. ρ_{up} and ρ_{off} are the single start up and shut down cost of power plants. Ω is the set of power plants including thermal power plants and carbon capture power plants.

In the day-ahead stage, the unit commitment plan and electricity prices for the next day are optimized. The decision variables involve the start up and shut down status of power plants, the variation in electricity prices and the response power of the loads after PDR, which can be expressed as follows:

$$\mathbf{x} = \left[u, \Delta p, \Delta q\right] \tag{24}$$

Objective in the intra-day stage

The cost in the intra-day stage can be calculated as Eqs 26–35.

$$C_{\mathrm{run}}(t) = C_{\mathrm{ccs}}(t) + C_{\mathrm{gen}}(t) \tag{26}$$

$$C_{\mathrm{ccs}}(t) = \sum_{i\in\Omega_{\mathrm{ccs}}} \left\{\left[a_i P_{i,\mathrm{ccsnet}}(t)^2 + b_i P_{i,\mathrm{ccsnet}}(t) + c_i\right] + \rho_{\mathrm{ccs}}\left[P_{i,\mathrm{ccs0}}(t) + P_{i,\mathrm{ccsfix}}(t)\right]\right\} \tag{27}$$

$$C_{\mathrm{gen}}(t) = \sum_{i\in\Omega_{\mathrm{gen}}} \left[a_i P_{i,\mathrm{gen}}(t)^2 + b_i P_{i,\mathrm{gen}}(t) + c_i\right] \tag{28}$$

$$C_{\mathrm{ex}}(t) = \rho_{\mathrm{ex}} P_{\mathrm{buy}}(t) \tag{29}$$

$$C_{\mathrm{car}}(t) = C_{\mathrm{carex}}(t) + C_{\mathrm{carsto}}(t) \tag{30}$$

$$C_{\mathrm{carex}}(t) = \rho_{\mathrm{car}} E_{\mathrm{car}}(t) \tag{31}$$

$$C_{\mathrm{carsto}}(t) = \rho_{\mathrm{sto}} E_{\mathrm{cap}}(t) \tag{32}$$

$$C_{\mathrm{IDR}}(t) = C_{\mathrm{IDR,inte}}(t) + C_{\mathrm{IDR,shif}}(t) \tag{33}$$

$$C_{\mathrm{IDR,inte}}(t) = \rho_{\mathrm{inte}} P_{\mathrm{IDR,inte}}(t) \tag{34}$$

$$C_{\mathrm{IDR,shif}}(t) = \rho_{\mathrm{shif}} \left|P_{\mathrm{IDR,shif}}(t)\right| \tag{35}$$

C_{ccs} and C_{gen} are the operation cost of carbon capture power plants and thermal power plants, respectively. ρ_{ccs} is the unit operation cost of the carbon capture devices. a, b and c are the fuel consumption coefficient of power plants. ρ_{ex} is the unit power purchase price. C_{carex} and C_{carsto} are the carbon trading cost and the cost of storage and transportation of carbon dioxide. ρ_{car} and ρ_{sto} are the carbon trading price and the cost of storing and transporting unit carbon dioxide. $C_{\mathrm{IDR,\ inte}}$ and $C_{\mathrm{IDR,\ shif}}$ are the scheduling cost of the interruptible loads and the shiftable loads. ρ_{inte} and ρ_{shif} are the unit scheduling cost of the interruptible loads and the shiftable loads.

In the intra-day stage, the outputs of all power plants and IDR schedule are optimized under the worst-case output of wind power based on the results of the day-ahead stage. The decision variables and the uncertain variables in the intra-day stage are given by:

$$\mathbf{y} = \left[P_{\mathrm{ccs}}, P_{\mathrm{gen}}, Q_{\mathrm{ccs}}, Q_{\mathrm{gen}}, P_{\mathrm{branch}}, Q_{\mathrm{branch}}, V, P_{\mathrm{buy}}, Q_{\mathrm{ccs}}^{\mathrm{tre}}, P_{\mathrm{IDR,inte}}, P_{\mathrm{IDR,shif}}\right] \tag{36}$$

$$\mathbf{w} = \left[P_{\mathrm{wind}}\right] \tag{37}$$

where Q_{ccs} and Q_{gen} are the reactive power of carbon capture power plants and thermal power plants; P_{branch} and Q_{branch} are

TABLE 1 The operation parameters of power plants.

Bus	$P^{\max}$ (MW)	$P^{\min}$ (MW)	$Q^{\max}$ (MVar)	$Q^{\min}$ (MVar)	R_{up} (MW/h)	R_{down} (MW/h)	S_{up} (MW/h)	S_{down} (MW/h)	T_{on} (h)	T_{off} (h)
18	1	0.3	0.8	−0.1	0.7	0.7	0.3	0.3	4	4
22	0.8	0.2	0.7	−0.1	0.6	0.6	0.2	0.2	3	3
25	0.6	0.2	0.5	−0.1	0.3	0.3	0.2	0.2	3	3
33	0.3	0.1	0.4	−0.1	0.2	0.2	0.1	0.1	2	2

TABLE 2 The cost parameters of power plants.

Bus	Startup cost (¥)	Shutdown cost (¥)	a (¥/MW^2)	b (¥/MW)	c (¥)
18	6,000	3,000	0.03	100	500
22	5,000	3,000	0.02	80	600
25	4,000	2000	0.015	70	700
33	3,000	2000	0.01	60	800

TABLE 3 The carbon emission factors of carbon emission sources.

Bus	Carbon emission quota (t/MW)	Carbon emission intensity (t/MW)
1	0.8	1
18	0.75	0.95
22	0.7	0.8
25	0.65	0.75
33	0.8	1

the active power and the reactive power flowing on each line; V is the voltage amplitude of buses; P_{wind} is the output of the wind power.

Constraints

Constraints for the day-ahead stage

The constraints of active power and reactive power outputs Eqs 38, 39, ramp rates Eqs 40, 41, and running time Eqs 42, 43 are considered:

$$u(t){P_{\mathrm{gen}}}^{\min} \le P_{\mathrm{gen}}(t) \le u(t){P_{\mathrm{gen}}}^{\max} \tag{38}$$

$$u(t){Q_{\mathrm{gen}}}^{\min} \le Q_{\mathrm{gen}}(t) \le u(t){Q_{\mathrm{gen}}}^{\max} \tag{39}$$

$$P_{\mathrm{gen}}(t) - P_{\mathrm{gen}}(t-1) \le u(t-1)\left(R_{\mathrm{up}} - S_{\mathrm{up}}\right) + S_{\mathrm{up}} \tag{40}$$

$$P_{\mathrm{gen}}(t-1) - P_{\mathrm{gen}}(t) \le u(t)\left(R_{\mathrm{down}} - S_{\mathrm{down}}\right) + S_{\mathrm{down}} \tag{41}$$

$$\sum_{k=t}^{t+T_{\mathrm{off}}-1} [1 - u(k)] \ge T_{\mathrm{off}}[u(t-1) - u(t)] \tag{42}$$

$$\sum_{k=t}^{t+T_{\mathrm{on}}-1} u(k) \ge T_{\mathrm{on}}[u(t) - u(t-1)] \tag{43}$$

where ${P_{\mathrm{gen}}}^{\max}$ and ${P_{\mathrm{gen}}}^{\min}$ are the maximum and minimum active power outputs of the power plants; ${Q_{\mathrm{gen}}}^{\max}$ and ${Q_{\mathrm{gen}}}^{\min}$ are the maximum and minimum reactive power outputs of the power plants; R_{up} and R_{down} are the up ramp rate and down ramp rate; S_{up} and S_{down} are the up ramp rate and down ramp rate when the power plants start and close; T_{on} and T_{off} are the minimum on and off time of the power plants.

The distribution system is usually a radial network. The linearized DistFlow Eqs 44–49 are adopted here (Wang et al., 2019).

$$P_i^{\mathrm{inj}}(t) + \sum_{j<i} P_{ji}(t) = P_i^{\mathrm{d}}(t) + \sum_{k>i} P_{ik}(t) \tag{44}$$

$$Q_i^{\mathrm{inj}}(t) + \sum_{j<i} Q_{ji}(t) = Q_i^{\mathrm{d}}(t) + \sum_{k>i} Q_{ik}(t) \tag{45}$$

$$V_j(t) = V_i(t) - \left[r_{ij}P_{ij}(t) + x_{ij}Q_{ij}(t)\right]\big/V_{\mathrm{r}} \tag{46}$$

$$-{P_{ij}}^{\max} \le P_{ij}(t) \le {P_{ij}}^{\max} \tag{47}$$

$$-{Q_{ij}}^{\max} \le Q_{ij}(t) \le {Q_{ij}}^{\max} \tag{48}$$

$${V_i}^{\min} \le V_i(t) \le {V_i}^{\max} \tag{49}$$

P_i^{inj} and Q_i^{inj} are the injection active power and reactive power of the node i. P_i^{d} and Q_i^{d} are the active load and reactive load of the node i. $\sum_{j<i} P_{ji}$ and $\sum_{j<i} Q_{ji}$ represent the sum of active power and reactive power flows injected into the node i from other nodes. $\sum_{k>i} P_{ik}$ and $\sum_{k>i} Q_{ik}$ represent the sum of active power and reactive power flows

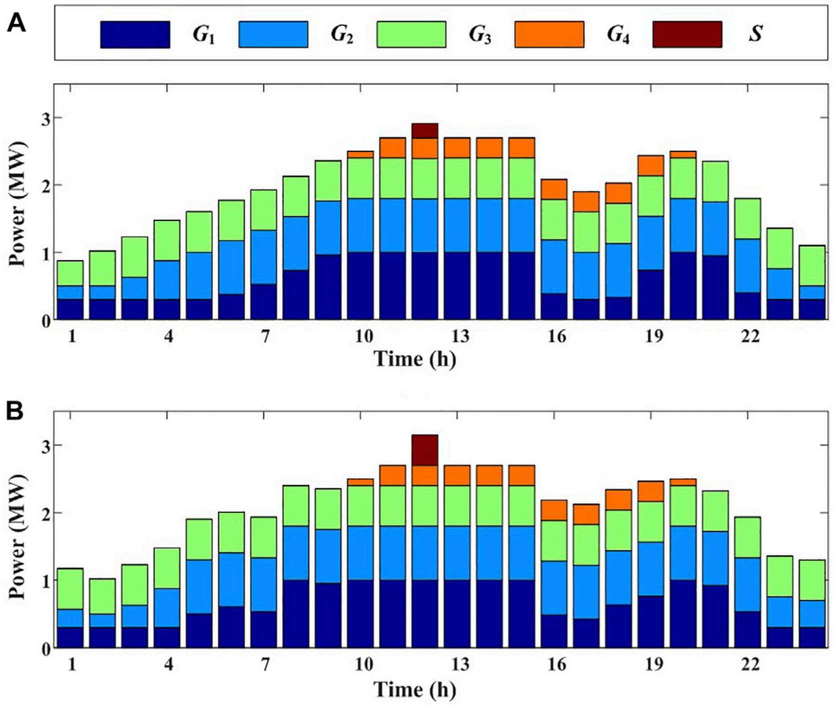

FIGURE 2
Outputs of power plants: **(A)** $\Gamma_{\text{wind}} = 0$ **(B)** $\Gamma_{\text{wind}} = 8$.

from the node i to other nodes. P_{ij} and Q_{ij} represent the active power and reactive power flowing through the line between the node i and the node j. $P_{ij}{}^{\max}$ and $Q_{ij}{}^{\max}$ represent the maximum active power and reactive power transmission capacity. $V_i{}^{\max}$ and $V_i{}^{\min}$ are maximum and minimum voltage of the node i. r_{ij} and x_{ij} are the resistance and reactance of the line. V_{r} is the referenced voltage.

As mentioned above, the power purchase comes from the thermal power plants. Therefore, the upper and lower bound constraints and the ramp constraints should be meet as follows:

$$0 \le P_{\text{buy}}(t) \le P_{\text{buy}}{}^{\max} \tag{50}$$

$$P_{\text{buy}}(t) - P_{\text{buy}}(t-1) \le R_{\text{up}} \tag{51}$$

$$P_{\text{buy}}(t-1) - P_{\text{buy}}(t) \le R_{\text{down}} \tag{52}$$

where $P_{\text{buy}}{}^{\max}$ is the maximum purchasing power.

The carbon dioxide emissions in the whole dispatching period are limited, which can be expressed as:

$$\sum_{t=1}^{T} E_{\text{int}}(t) \le E_{\text{car}}{}^{\max} \tag{53}$$

where $E_{\text{car}}{}^{\max}$ is the maximum carbon dioxide emissions in the dispatching period.

Constraints for the intra-day stage

The constraints in the intra-day stage are basically the same as those in the day-ahead stage. After the optimization in the day-ahead stage, the decision variables in the day-ahead stage are known in the intra-day stage. Therefore, the constraints of running time Eqs 42, 43 are not considered in the intra-day stage.

The uncertainty of wind power is described as follows:

$$W = \begin{cases} P_{\text{wind}}(t) = \tilde{P}_{\text{wind}}(t) + B^{+}_{\text{wind}}(t)\Delta P_{\text{wind}}{}^{\max}(t) - B^{-}_{\text{wind}}(t)\Delta P_{\text{wind}}{}^{\max}(t) \\ B^{+}_{\text{wind}}(t), B^{-}_{\text{wind}}(t) \in \{0,1\} \\ B^{+}_{\text{wind}}(t) + B^{-}_{\text{wind}}(t) \le 1 \\ \sum\limits_{t=1}^{T}\left[B^{+}_{\text{wind}}(t) + B^{-}_{\text{wind}}(t)\right] \le \Gamma_{\text{wind}} \end{cases} \tag{54}$$

where $\tilde{P}_{\text{wind}}$ is the forecast value of the wind power; $\Delta P_{\text{wind}}{}^{\max}$ is the maximum prediction errors of the wind power; B^{+}_{wind} and B^{-}_{wind} are matrixes of binary variables; Γ_{wind} is the budget controlling the maximum number of the wind power deviating from their forecast values. The robustness and economy of the optimization results can be balanced by adjusting Γ_{wind}.

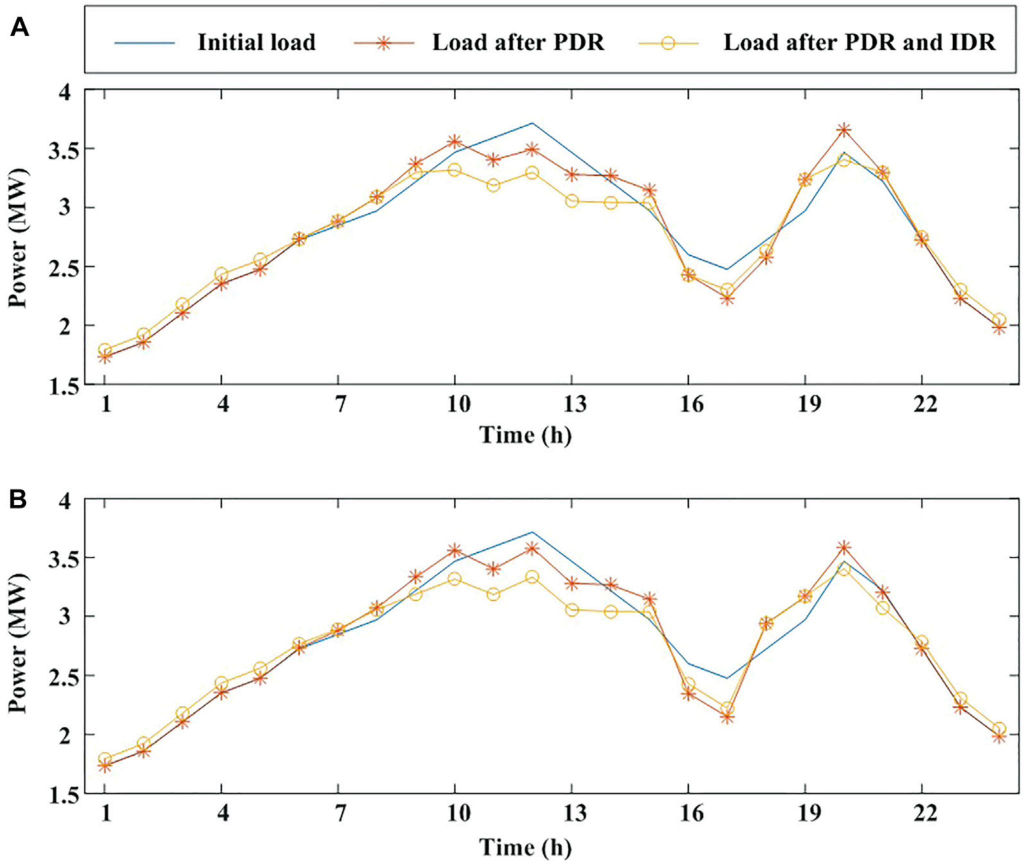

FIGURE 3
Load curves: **(A)** $\Gamma_{\text{wind}} = 0$ **(B)** $\Gamma_{\text{wind}} = 8$.

Solution methodology based on the C&CG algorithm

Linearization of nonlinear terms

There are quadratic terms in the operation cost of power plants. The piecewise linearization method is used to eliminate the quadratic terms and improve the computational efficiency. In Eq. 35, the absolute value is used to represent the shift power of the shiftable loads. By introducing the auxiliary variables $P_{\text{IDR1,shif}}$, $P_{\text{IDR2,shif}}$ and constraints Eqs 56, 57, the scheduling cost of the shiftable loads can be converted to the linear form, which can be expressed as follows:

$$C_{\text{IDR,shif}}(t) = \rho_{\text{shif}}\left[P_{\text{IDR1,shif}}(t) + P_{\text{IDR2,shif}}(t)\right] \tag{55}$$

$$P_{\text{IDR,shif}}(t) + P_{\text{IDR1,shif}}(t) - P_{\text{IDR2,shif}}(t) = 0 \tag{56}$$

$$P_{\text{IDR1,shif}}(t) \geq 0,\ P_{\text{IDR2,shif}}(t) \geq 0 \tag{57}$$

C&CG algorithm

The robust optimal model can be written in the following compact matrix form:

$$\begin{aligned}
&\min_{\mathbf{x}}\left(\mathbf{A}\mathbf{x}^T + \max_{\mathbf{w}\in W}\min_{\mathbf{y}} \mathbf{B}\mathbf{y}^T\right)\\
&\text{s.t.}\mathbf{C}\mathbf{x}^T \leq \mathbf{c}\\
&\mathbf{D}\mathbf{x}^T = \mathbf{d}\\
&\mathbf{E}\mathbf{y}^T \leq \mathbf{e}\\
&\mathbf{F}\mathbf{y}^T = \mathbf{f}\\
&\mathbf{H}\mathbf{x}^T + \mathbf{K}\mathbf{y}^T \leq \mathbf{h}\\
&\mathbf{M}\mathbf{x}^T + \mathbf{N}\mathbf{y}^T = \mathbf{m}\\
&\mathbf{G}\mathbf{x}^T + \mathbf{Q}\mathbf{y}^T + \mathbf{R}\mathbf{w}^T = \mathbf{q}
\end{aligned} \tag{58}$$

The C&CG algorithm is introduced to solve the two-stage robust optimal dispatch model (Zeng and Zhao, 2013). This model is transformed into a master problem (MP) and a subproblem (SP) by C&CG algorithm. They are defined as:

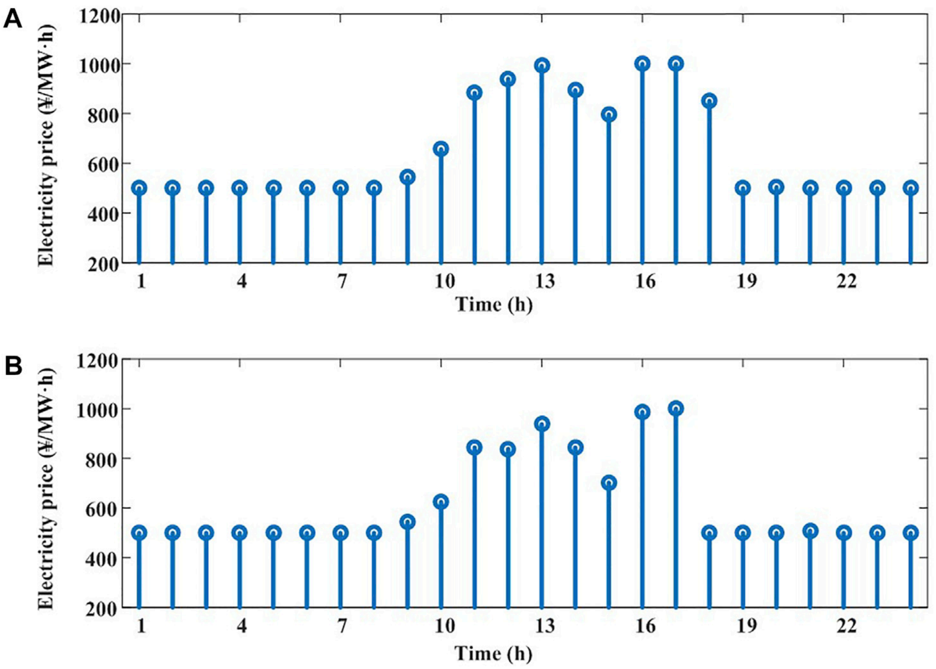

FIGURE 4
Electricity prices: **(A)** $\Gamma_{\text{wind}} = 0$ **(B)** $\Gamma_{\text{wind}} = 8$.

$$\begin{aligned}
&\text{MP: } \min_{\mathbf{x},\mathbf{y}} \mathbf{A}\mathbf{x}^T + \alpha \\
&\text{s.t.}\, \alpha \geq \mathbf{B}\mathbf{y}^T \\
&\mathbf{C}\mathbf{x}^T \leq \mathbf{c} \\
&\mathbf{D}\mathbf{x}^T = \mathbf{d} \\
&\mathbf{E}\mathbf{y}^T \leq \mathbf{e} \\
&\mathbf{F}\mathbf{y}^T = \mathbf{f} \\
&\mathbf{H}\mathbf{x}^T + \mathbf{K}\mathbf{y}^T \leq \mathbf{h} \\
&\mathbf{M}\mathbf{x}^T + \mathbf{N}\mathbf{y}^T = \mathbf{m} \\
&\mathbf{G}\mathbf{x}^T + \mathbf{Q}\mathbf{y}^T + \mathbf{R}\mathbf{w}^T = \mathbf{q}
\end{aligned} \tag{59}$$

$$\begin{aligned}
&\text{SP: } \max_{\mathbf{w}\in W} \min_{\mathbf{y}} \mathbf{B}\mathbf{y}^T \\
&\text{s.t. } \mathbf{E}\mathbf{y}^T \leq \mathbf{e} \\
&\mathbf{F}\mathbf{y}^T = \mathbf{f} \\
&\mathbf{H}\mathbf{x}^T + \mathbf{K}\mathbf{y}^T \leq \mathbf{h} \\
&\mathbf{M}\mathbf{x}^T + \mathbf{N}\mathbf{y}^T = \mathbf{m} \\
&\mathbf{G}\mathbf{x}^T + \mathbf{Q}\mathbf{y}^T + \mathbf{R}\mathbf{w}^T = \mathbf{q}
\end{aligned} \tag{60}$$

Using the above method, the MP is linearized to a mixed integer linear programming. Using KKT conditions, the max-min form in the SP is turned into the max form. The SP can also be converted into a mixed integer linear programming with the big-M method. Therefore, the MP and SP are easy to solve by existing solvers. The SP aims to find the worst-case output of wind power with the given day-ahead stage decision variables and provide an upper bound (*UB*). Then, the new variables and constraints are added to the MP to obtain a lower bound (*LB*). The MP and SP are solved iteratively and the process stops until the gap between the upper and lower bounds is smaller than a pre-set convergence tolerance ε_{CCG}.

The specific steps of the C&CG solution process are as follows:

Step 1. Define the forecast values of the wind power as the initial worst scenario and set $LB = -\infty$, $UB = +\infty$, $\varepsilon_{\text{CCG}} = 0.001$ and the iterations counter $k = 0$.

Step 2. Solve the MP in Eq. 59 based on the worst-case output of the wind power to obtain the decision variables x and update the *LB*.

Step 3. Solve the SP in Eq. 60 with the given decision variables **x** to obtain the decision variables **y** and the uncertain variables **w**. Update the *UB*.

Step 4. If $UB\text{-}LB \leq \varepsilon_{\text{CCG}}$, return the optimal solutions and stop. Otherwise, generate new variables and add corresponding new constraints to the MP. Update $k = k+1$ and go to Step 2.

Case study

Case description

A revised IEEE 33-bus system is used to verify the feasibility and effectiveness of the robust dispatch model proposed in this

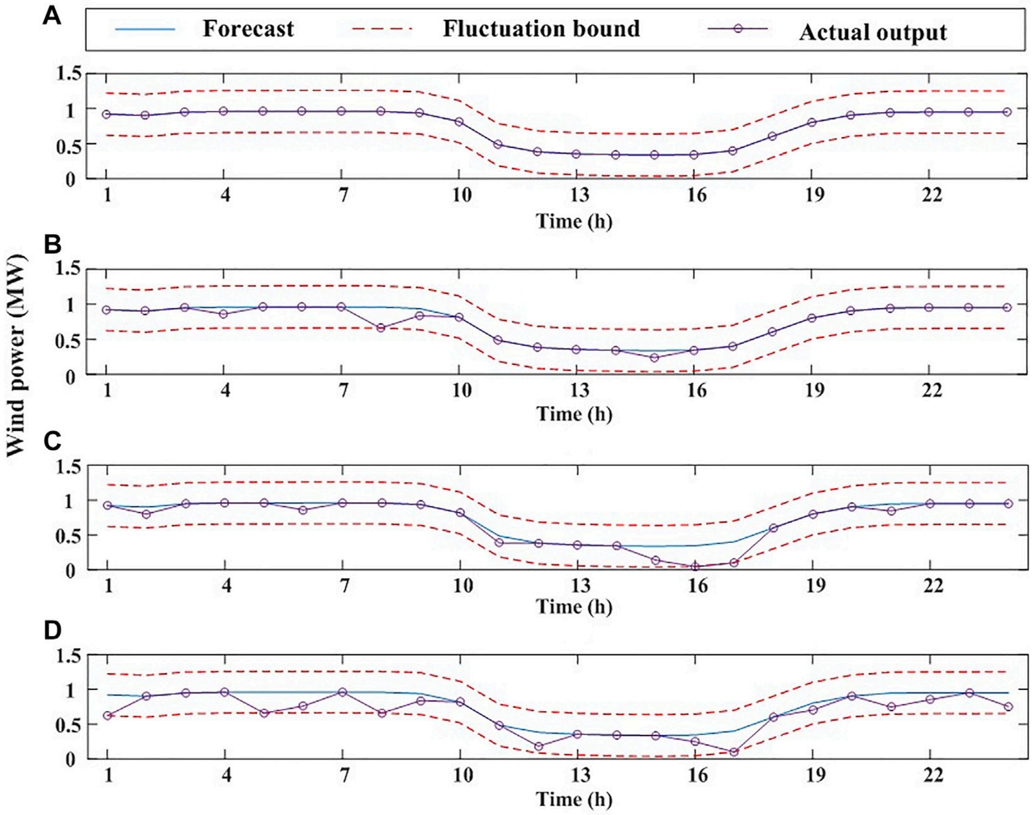

FIGURE 5
Wind power curves: **(A)** $\Gamma_{\text{wind}} = 0$ **(B)** $\Gamma_{\text{wind}} = 2$ **(C)** $\Gamma_{\text{wind}} = 4$ **(D)** $\Gamma_{\text{wind}} = 8$.

TABLE 4 Robust optimization results under different budget Γ_{wind}.

Γ_{wind}	C_{run} (¥)	C_{ex} (¥)	C_{carex} (¥)	C_{carsto} (¥)	C_{IDR} (¥)	Total cost (¥)	Carbon emissions (t)
0	57830.7	331.14	−1971	844.71	862.48	62898	34.2704
2	57874.7	447.34	−1958	844.71	905.85	63115	34.8133
4	57930.7	560.70	−1956	847.86	904.17	63288	35.3465
8	58037.1	674.39	−1941	851.19	979.76	63602	36.4426

paper (Dolatabadi et al., 2021). The topology of the test system is shown in Figure 1. Carbon capture power plants are connected to the buses 18 and 22. Thermal power plants are connected to the buses 25 and 33. Wind power plants are connected to the buses 19, 23 and 30. Electric power can be purchased from the main network at bus 1. We assume that the loads of all nodes participate in the PDR and the loads at buses 8 and 14 participate in the IDR. For the convenience of comparison and more obvious simulation results, we set α_{inte} and α_{shif} to 0.4. The base voltage of the distribution system is 12.66 kV. The maximum and minimum values of bus voltage are 1.05 pu and 0.95 pu. The active power and reactive power transmission capacity of the line is 2 MW and 1 MVar. The operation parameters and cost parameters of power plants are illustrated in Table 1 and Table 2. The carbon emission quotas and carbon emission intensities of carbon emission sources are shown in Table 3. The maximum purchasing power is 1 MW. The power purchase price is 1,500 ¥/MW. The up ramp rate and down ramp rate of purchasing power are 0.7 MW/h. The energy consumption of carbon capture device for capturing unit carbon dioxide is 0.6 MW. The maximum operating energy consumption of carbon capture devices is 0.5 and 0.3 MW,

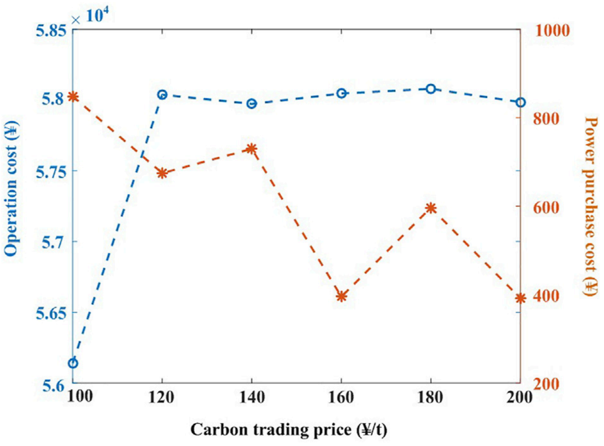

FIGURE 6
Relation curve between operation cost, power purchase cost and carbon trading price.

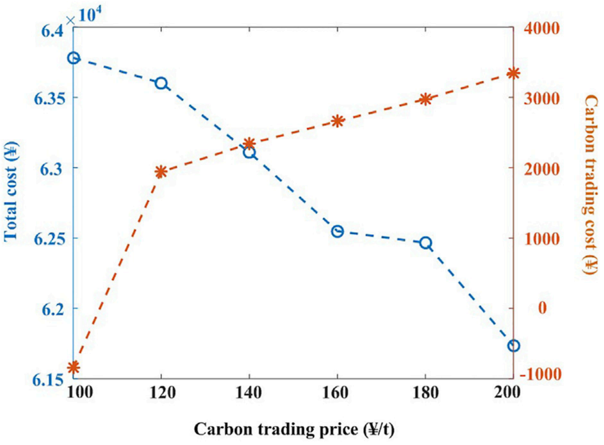

FIGURE 7
Relation curve between total cost, carbon trading cost and carbon trading price.

respectively. The unit operation cost of the carbon capture devices is 100 ¥/MW. The cost of storing and transporting unit carbon dioxide is 30 ¥/t. The carbon trading price is 120 ¥/t. The maximum carbon dioxide emissions is 50t. The reference value of the electricity prices is 500 ¥/MW·h. The maximum variation of electricity prices is 500 ¥/MW·h. Therefore, the electricity prices are between 500 ¥/MW·h and 1,000 ¥/MW·h. The unit scheduling cost of the interruptible loads and the shiftable loads are 500 ¥/MW and 320 ¥/MW, respectively. The maximum prediction errors of the wind power is 0.1 MW. This model is solved by a commercial software CPLEX 12.7.1 in MATLAB 2015b.

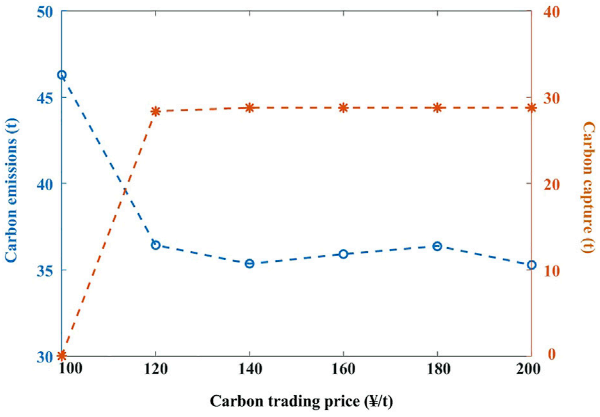

FIGURE 8
Relation curve between carbon emissions, carbon capture and carbon trading price.

Result analysis

Robustness and economy analysis

Due to the low probability of the extreme wind power output, the robustness and economy of the model can be balanced by adjusting the budget Γ_{wind} to avoid the too conservative optimization results. In this case, the budgets Γ_{wind} are set to 0, 2, 4 and 8, respectively. The results of outputs of power plants are shown in Figure 2. The outputs of power plants are indicated by the height of the colored bar. The initial load curve, the load curve after PDR and the load curve after PDR and IDR are presented by different curves in Figure 3. The hourly electricity prices are represented by stems in Figure 4. Figure 5 shows the sum of the forecast value, the output range and the actual output of all wind power. Table 4 shows various costs and the carbon emissions of the distribution system.

In Figure 2, it can be seen the outputs of power plants increase due to the uncertainty of the wind power. Especially, when all power plants reach their maximum power, the purchasing power increases significantly. At this time, power plants have no additional regulation capacity to cope with the uncertainty of the wind power. Therefore, the power balance can only be achieved by purchasing power from the main network. It can be found from Figure 3 that the peak-valley difference of the load curves decreases after the implementation of PDR and IDR. The interruptible loads are interrupted at the peak and the shiftable loads are transferred from the peak to the valley of the loads. The electricity prices are higher at the peak of the loads and lower at the valley of the loads in Figure 4. Because a smoother load curve can avoid the frequent startup and shutdown of the power plants, which can reduce the total cost. In Figure 4B, the electricity prices fluctuate between 10:00 and 13:00 instead of monotone increasing in Figure 4A. And

TABLE 5 Robust optimization results under different cases.

Case	C_{run} (¥)	C_{ex} (¥)	C_{carex} (¥)	C_{carsto} (¥)	C_{IDR} (¥)	Total cost (¥)	Carbon emissions (t)
1	57965.2	2,804.8	−1919	849.86	0	64703	37.1080
2	57922.7	2,853.6	−1922	847.86	0	64701	36.7963
3	57931	1,530.2	−1936	846.62	761.86	64133	36.0406
4	58037.1	674.4	−1941	851.19	979.76	63602	36.4426

the variations of electricity prices from 15:00 to 18:00 are larger. It is reasonable because the uncertainty of the wind power leads to the changes of power plants outputs. In order to minimize the total cost while meeting the load demand, the electricity prices will also change more. Therefore, fluctuating wind power output will lead to significant changes in electricity prices.

According to the uncertainty set, the forecast value of wind power is in the middle of the upper bound and lower bound. When the budget Γ_{wind} is set to 0, this model is transformed into a deterministic optimization. The actual output of wind power is consistent with the forecast value. When the budgets Γ_{wind} are set to 2, 4 and 8, the actual output of wind power tends to locate at the lower bound and reaches the lower bound at some time in Figure 5, which is regarded as the worst-case output of wind power. In Table 4, the various costs have increased with the increase of budget Γ_{wind}. Because the output of wind power is decreased. In order to meet the load demand, all costs are increased. Although the amount of carbon dioxide captured by carbon capture power plants increases, the carbon emissions of the distribution system increase from 34.2704 t to 36.4426 t.

Effect of carbon trading price

The carbon trading mechanism not only imposes economic punishment on high carbon emission power plants, but also rewards energy-saving and environmentally friendly power plants, which makes carbon emissions of great economic value. The change of carbon trading price affects various costs. The relation with the operation cost and power purchase cost is shown in Figure 6. Figure 7 shows the relation with the total cost and the carbon trading cost. When the carbon trading cost is positive, it means the profit generated by the power plants selling carbon emission quotas. When the carbon trading cost is negative, it means the cost generated by the power plant purchasing additional carbon emission quotas. The change of carbon trading price also affects the carbon emissions and the amount of captured carbon dioxide, as shown in Figure 8.

In Figure 6, the operation cost increase at the beginning and then remain stable. When the carbon trading price is 100 ¥/t, the profit generated by carbon capture are low. Therefore, the carbon capture devices operate at a very low power and generate little cost. When the carbon trading price is 120 ¥/t or more, the profit can reduce the total cost greatly. So, carbon capture devices operate at a high power leading to the increase of operation cost. And the operation cost keeps stable when the carbon capture devices operate at the maximum power. The power purchasing cost shows a decreased trend. It is reasonable because the high carbon trading prices encourage the low-carbon power plants. The power purchase from the main network can be regarded as a high pollution thermal power plant. And the purchasing power decreases with the increase of carbon trading price.

It can be observed that the profit generated by the carbon trading increases and the total cost decreases with the increase of the carbon trading price in Figure 7. The carbon capture power plants sell carbon emission quotas to gain profit. The higher carbon trading price, the more profit. And the total cost become less.

It can be found in Figure 8 that the carbon emissions decrease at first and keep stable later. The amount of carbon dioxide captured shows a similar trend with the operation cost when the carbon trading price increase. Because the operation of carbon capture devices is the main factor that affects the operation cost. When the carbon capture devices operate at maximum power, the carbon emissions remain unchanged basically. But the basic carbon emissions are inevitable to meet the load demand.

Therefore, the carbon trading mechanism can promote energy conservation and emission reduction of power plants. Combining the carbon trading mechanism and the CCS technology will release their carbon emission reduction potential and decrease the carbon emissions of the distribution system.

Comparison of demand response

PDR and IDR dispatch loads in different ways. PDR enable user to spontaneously change their consumption habits by setting electricity prices, so the scheduling cost is 0 ¥. And IDR dispatches loads by economic compensation. In order to compare the effects of PDR and IDR, four cases are designed.

Case 1: Demand response doesn't participate in distribution system dispatch.

Case 2: PDR participates in distribution system dispatch.

Case 3: IDR participates in distribution system dispatch.

Case 4: Both PDR and IDR participate in distribution system dispatch.

Optimization results of various costs and carbon emissions are shown in Table 5. The total costs of case 1 and case 2 are basically the same, but the carbon emissions are reduced. It can be seen that PDR can decrease the carbon emissions of distribution system but has little impact on the total cost. Compared case 1 with case 3, the total cost and carbon emissions are reduced significantly. Although there is IDR scheduling cost, IDR has a significant effect on reducing total cost and carbon emissions compared with PDR. When both PDR and IDR participate in distribution system dispatch at the same time, the power purchase cost is reduced greatly so that the total cost are decreased to the minimum in case 4. Because of the participation of demand response, the loads are more easily met by the power plants of the distribution network with no need to purchase power from the main network. And the carbon emissions are the lowest among four cases. Therefore, the participation of PDR and IDR in distribution system can realize the optimization of economic and environmental benefits.

Conclusion

In this paper, a two-stage robust optimal dispatch model of the distribution system considering carbon capture and demand response is proposed. This model takes the uncertainty of wind power into account and realize the low-carbon economic operation of the distribution system. From the results of case studies, the following conclusions can be drawn: 1) With the increasing uncertainty of the wind power, all costs and carbon emissions of the distribution system increase. The robustness and economy of the model can be balanced by adjusting the budget Γ_{wind} to avoid the too conservative optimization results. 2) PDR and IDR can reduce the peak-valley difference of the load curves to realize the optimization of economic and environmental benefits. And the uncertainty of wind power can lead to the fluctuation of electricity prices. 3) The carbon trading mechanism can promote energy conservation and emission reduction of power plants. Carbon capture devices can capture carbon dioxide more by setting carbon trading price reasonably. However, the actual operation process of the carbon capture power plant is complex. Further work will consider a more detailed model of the carbon capture power plant. And a more accurate representation of wind power uncertainty is worthy of study.

Data availability statement

The original contributions presented in the study are included in the article/Supplementary Material, further inquiries can be directed to the corresponding author.

Author contributions

YG contributed to the model, simulation and writing. CW contributed to the method. YH and GH contributed equally to the editing of the article and discussion. YL contributed to the literature analysis and provided a critical review.

Funding

This work was supported by the National Natural Science Foundation of China (52277088 and 51907050).

Conflict of interest

YH was employed by the Company State Grid Jiangsu Electric Power Co., Ltd.

The remaining authors declare that the research was conducted in the absence of any commercial or financial relationships that could be construed as a potential conflict of interest.

Publisher's note

References

Akbari-Dibavar, A., Mohammadi-Ivatloo, B., Zare, K., Khalili, T., and Bidram, A. (2021). Economic-emission dispatch problem in power systems with carbon capture power plants. *IEEE Trans. Ind. Appl.* 57, 3341–3351. doi:10.1109/TIA.2021.3079329

Bai, L., Li, F., Cui, H., Jiang, T., Sun, H., and Zhu, J. (2016). Interval optimization based operating strategy for gas-electricity integrated energy systems considering demand response and wind uncertainty. *Appl. Energy* 167, 270–279. doi:10.1016/j.apenergy.2015.10.119

Chen, Q., Kang, C., Xia, Q., and Kirschen, D. S. (2012). Optimal flexible operation of a CO_2 capture power plant in a combined energy and carbon emission market. *IEEE Trans. Power Syst.* 27, 1602–1609. doi:10.1109/TPWRS.2012.2185856

Chen, Q., Kang, C., and Xia, Q. (2010). Modeling flexible operation mechanism of CO_2 capture power plant and its effects on power-system operation. *IEEE Trans. Energy Convers.* 25, 853–861. doi:10.1109/TEC.2010.2051948

Chen, X., Huang, L., Zhang, X., He, S., Sheng, Z., Wang, Z., et al. (2021). Robust optimal dispatching of wind fire energy storage system based on equilibrium optimization algorithm. *Front. Energy Res.* 9, 754908. doi:10.3389/fenrg.2021.754908

Dolatabadi, S. H., Ghorbanian, M., Siano, P., and Hatziargyriou, N. D. (2021). An enhanced IEEE 33 bus benchmark test system for distribution system studies. *IEEE Trans. Power Syst.* 36, 2565–2572. doi:10.1109/TPWRS.2020.3038030

Ji, Z., Kang, C., Chen, Q., Xia, Q., Jiang, C., Chen, Z., et al. (2013). Low-carbon power system dispatch incorporating carbon capture power plants. *IEEE Trans. Power Syst.* 28, 4615–4623. doi:10.1109/TPWRS.2013.2274176

Kirschen, D. S., Strbac, G., Cumperayot, P., and de Paiva Mendes, D. (2000). Factoring the elasticity of demand in electricity prices. *IEEE Trans. Power Syst.* 15, 612–617. doi:10.1109/59.867149

Lei, H., Huang, S., Liu, Y., and Zhang, T. (2019). Robust optimization for microgrid defense resource planning and allocation against multi-period attacks. *IEEE Trans. Smart Grid* 10, 5841–5850. doi:10.1109/TSG.2019.2892201

Lei, S., Hou, Y., Qiu, F., and Yan, J. (2018). Identification of critical switches for integrating renewable distributed generation by dynamic network reconfiguration. *IEEE Trans. Sustain. Energy* 9, 420–432. doi:10.1109/TSTE.2017.2738014

Li, J., Wen, J., and Han, X. (2015). Low-carbon unit commitment with intensive wind power generation and carbon capture power plant. *J. Mod. Power Syst. Clean. Energy* 3, 63–71. doi:10.1007/s40565-014-0095-6

Liu, G., and Tomsovic, K. (2015). Robust unit commitment considering uncertain demand response. *Electr. Power Syst. Res.* 119, 126–137. doi:10.1016/j.epsr.2014.09.006

Liu, Y., Guo, L., and Wang, C. (2018). A robust operation-based scheduling optimization for smart distribution networks with multi-microgrids. *Appl. Energy* 228, 130–140. doi:10.1016/j.apenergy.2018.04.087

Lou, S., Lu, S., Wu, Y., and Kirschen, D. S. (2015). Optimizing spinning reserve requirement of power system with carbon capture plants. *IEEE Trans. Power Syst.* 30, 1056–1063. doi:10.1109/TPWRS.2014.2341691

Reddy, K. S., Panwar, L. K., Panigrahi, B. K., and Kumar, R. (2017). Modeling of carbon capture technology attributes for unit commitment in emission-constrained environment. *IEEE Trans. Power Syst.* 32, 662–671. doi:10.1109/TPWRS.2016.2558679

Wang, C., Ju, P., Wu, F., Lei, S., and Pan, X. (2022). Long-term voltage stability-constrained coordinated scheduling for gas and power Grids with uncertain wind power. *IEEE Trans. Sustain. Energy* 13, 363–377. doi:10.1109/TSTE.2021.3112983

Wang, C., Lei, S., Ju, P., Chen, C., Peng, C., and Hou, Y. (2020b). MDP-Based distribution network reconfiguration with renewable distributed generation: Approximate dynamic programming approach. *IEEE Trans. Smart Grid* 11, 3620–3631. doi:10.1109/TSG.2019.2963696

Wang, J., Xu, Q., Su, H., and Fang, K. (2021). A distributed and robust optimal scheduling model for an active distribution network with load aggregators. *Front. Energy Res.* 9, 646869. doi:10.3389/fenrg.2021.646869

Wang, X., Shahidehpour, M., Jiang, C., and Li, Z. (2019). Coordinated planning strategy for electric vehicle charging stations and coupled traffic-electric networks. *IEEE Trans. Power Syst.* 34, 268–279. doi:10.1109/TPWRS.2018.2867176

Wang, Y., Qiu, J., Tao, Y., and Zhao, J. (2020a). Carbon-oriented operational planning in coupled electricity and emission trading markets. *IEEE Trans. Power Syst.* 35, 3145–3157. doi:10.1109/TPWRS.2020.2966663

Xiao, H., Pei, W., Dong, Z., and Kong, L. (2018). Bi-level planning for integrated energy systems incorporating demand response and energy storage under uncertain environments using novel metamodel. *CSEE J. Power Energy Sys* 4, 155–167. doi:10.17775/CSEEJPES.2017.01260

Xu, L., Guo, Q., Yang, T., and Sun, H. (2019). Robust routing optimization for smart grids considering cyber-physical interdependence. *IEEE Trans. Smart Grid* 10, 5620–5629. doi:10.1109/TSG.2018.2888629

Yan, D., Wang, S., Zhao, H., Zuo, L., Yang, D., Wang, S., et al. (2022). A robust scheduling methodology for integrated electric-gas system considering dynamics of natural gas pipeline and blending hydrogen. *Front. Energy Res.* 10, 863374. doi:10.3389/fenrg.2022.863374

Zeng, B., and Zhao, L. (2013). Solving two-stage robust optimization problems using a column-and-constraint generation method. *Operations Res. Lett.* 41, 457–461. doi:10.1016/j.orl.2013.05.003

Zhang, B., Li, Q., Wang, L., and Feng, W. (2018). Robust optimization for energy transactions in multi-microgrids under uncertainty. *Appl. Energy* 217, 346–360. doi:10.1016/j.apenergy.2018.02.121

Zhang, N., Hu, Z., Dai, D., Dang, S., Yao, M., and Zhou, Y. (2016a). Unit commitment model in smart grid environment considering carbon emissions trading. *IEEE Trans. Smart Grid* 7, 420–427. doi:10.1109/TSG.2015.2401337

Zhang, X., Shahidehpour, M., Alabdulwahab, A., and Abusorrah, A. (2016b). Hourly electricity demand response in the stochastic day-ahead scheduling of coordinated electricity and natural gas networks. *IEEE Trans. Power Syst.* 31, 592–601. doi:10.1109/TPWRS.2015.2390632

Zhao, C., Wang, J., Watson, J., and Guan, Y. (2013). Multi-stage robust unit commitment considering wind and demand response uncertainties. *IEEE Trans. Power Syst.* 28, 2708–2717. doi:10.1109/TPWRS.2013.2244231

Zhou, Y., Yu, H., Li, Z., Su, J., and Liu, C. (2020). Robust optimization of a distribution network location-routing problem under carbon trading policies. *IEEE Access* 8, 46288–46306. doi:10.1109/ACCESS.2020.2979259

Zhu, X., Wu, J., and Liu, D. (2022). Robust unit commitment for minimizing wind spillage and load shedding with optimal DPFC. *Front. Energy Res.* 10, 877042. doi:10.3389/fenrg.2022.877042

frontiers | Frontiers in Energy Research

TYPE Original Research
PUBLISHED 02 November 2022
DOI 10.3389/fenrg.2022.929113

OPEN ACCESS

EDITED BY
Fei Wang,
North China Electric Power University,
China

REVIEWED BY
Zejun Yang,
University of British Columbia, Canada
Martin P. Calasan,
University of Montenegro, Montenegro

*CORRESPONDENCE
Yang Du,
yang.du@jcu.edu.au

SPECIALTY SECTION
This article was submitted to Smart Grids, a section of the journal Frontiers in Energy Research

RECEIVED 26 April 2022
ACCEPTED 30 September 2022
PUBLISHED 02 November 2022

CITATION
Chang J, Du Y, Chen X, Lim E, Wen H, Li X and Jiang L (2022), Frequency regulation in adaptive virtual inertia and power reserve control with high PV penetration by probabilistic forecasting.
Front. Energy Res. 10:929113.
doi: 10.3389/fenrg.2022.929113

Frequency regulation in adaptive virtual inertia and power reserve control with high PV penetration by probabilistic forecasting

Jiaming Chang[1], Yang Du[2]*, Xiaoyang Chen[1], Enggee Lim[1], Huiqing Wen[1], Xingshuo Li[3] and Lin Jiang[4]

[1]Xi'an Jiaotong-Liverpool University, Suzhou, Jiangsu, China, [2]James Cook University, Townsville, QLD, Australia, [3]Nanjing Normal University, Nanjing, Jiangsu, China, [4]University of Liverpool, Liverpool, North West England, United Kingdom

The large-scale deployment of sustainable energy sources has become a mandatory goal to reduce pollution from electricity production. As photovoltaic (PV) plants replace conventional synchronous generators (SGs), their significant inherent rotational inertia characteristics are reduced. The high penetration of PV results in reduced system inertia, leading to system frequency instability. Virtual inertial control (VIC) technology has attracted increasing interest because of its ability to mimic inertia. Adoption of the energy storage system (ESS) is hindered by the high cost, although it can be used to provide virtual inertia. The determined forecast gives PVs the ability to reserve power before shading and compensate the power when a system power drop occurs, which can increase system inertia. Nevertheless, it has forecast errors and energy waste in a stable state. To improve the stability of the microgrid and improve the ESS efficiency, this study proposes an adaptive forecasting-based (AFB) VIC method using probabilistic forecasts. The adaptive power reserve and virtual inertia control are proposed to reduce energy waste and increase system inertia. The simulation results reveal that the proposed method has adaptive system inertia to reduce the reserved power, required ESS power capacity, and battery aging.

KEYWORDS

micro-grid, frequency regulation, virtual inertial control, forecasting, power reserve

1 Introduction

Local loads, energy storage systems (ESS), and distributed generators (DGs) comprise a micro-grid. Due to the clean, sustainable, and environmentally friendly nature of solar energy sources, photovoltaic power generation has seen rapid growth in remote areas as one of the most promising renewable energy sources (Woodhouse et al., 2011). The amount of energy obtained from renewable energy has increased exponentially over the last decade, making distributed generation a viable scheme for mainstream power generation (Askarian et al., 2018). The evolution of the global power generation mode has changed and will continue to change the prospects of the power system. The adaptability of micro-grids allows for rapid tracking of fluctuations in renewable energy power generation. It has the potential to reduce demand from large grid power systems (Zhang et al., 2020a).

For the 2030 scenario, the Australian Energy Market Operator (AEMO) has proposed a 100% renewable power system (RPS) composition (Gu et al., 2018). The RPS of the national electricity market (NEM) generation mix projection is expected. The PV power ratio accounts for 22% of total power while providing 51% of the peak demand power. Thus, with the increasing PV penetration level, the intermittent nature of solar energy poses new challenges for the conventional grid. Non-dispatchable PV power may result in a loss of system inertia and increased frequency deviation. Mararakanye and Bekker (2019) specified two conditions for frequency control in the NEM: ±0.5 Hz/s RoCoF and ±0.15 Hz frequency deviations.

Because of the high penetration of PVs, system inertia is reduced, resulting in an unstable system frequency in micro-grids (Dreidy et al., 2017). Due to the high penetration of PVs, many researchers have considered the impact of low inertia on the stability and operation of grid systems (Gu et al. 2018; Tielens and Van Hertem, 2016; Ulbig et al. 2014). For the response to system contingencies, frequency regulation actions must be implemented multiple times. The problem of reducing system inertia and the challenges of system operation are investigated in Tielens and Van Hertem (2016). The main challenge for Australia is to maintain enough inertia in the system to ensure safe operation (Gu et al., 2018). Ulbig et al. (2014) investigates the impact of low inertia on the operation and stability of micro-grids at high PV penetration levels. It is demonstrated that in a micro-grid with low inertia, it may result in rapid frequency changes and overshoot the frequency policy limitations. Because of the high penetration of PVs in the micro-grid, the generator may not increase power in time to regulate frequency when the frequency drops. As a result, the low inertia issues are widely acknowledged.

The low inertia issues in a micro-grid system can be improved by virtual inertial control (VIC). In Tielens and Van Hertem (2016), the rate of change of frequency (RoCoF) is increased to a higher level. Iit uses the VIC technique to increase system inertia by simulating the properties of traditional synchronous generators (SGs). Most VIC strategies necessitate the use of additional ESS energy, such as a battery or super capacitor. Hammad et al. (2019) proposed an efficient virtual inertial measurement method. It is suitable for actuated ESS. Although the ESS efficiently provides enough power for VIC, it results in higher capital and operating costs.

The PV-based VIC method is comparable to other ESS-VIC technologies. A sufficient power supply for the VIC can be provided by reserving PV power (Crăciun et al., 2014; Hua et al., 2017; Yan et al., 2018). This approach is provided by the development of active power reserves (Hoke and Maksimović, 2013; Yang et al. 2016). However, to provide sufficient power buffers to the VIC when frequency deviations occur, the aforementioned method usually necessitates a constant power reduction, such as 10% of the maximum available power. This study describes the process of modeling the PV small signal with VIC and implements the details of simulating the dynamic properties of SGs (Li et al., 2019). As a result, once the micro-grid system is stabilized, there is a constant waste of energy.

Algorithms for determining forecasting PV power using historical solar irradiance data are proposed in the literature reports (Chen et al., 2019; Mahmud et al., 2021; da Luz et al., 2020; Han et al., 2019; Wang et al., 2020). The impact of data normalization on forecast performance is introduced in Mahmud et al. (2021) using a variety of performance indicators. Han et al. (2019) proposed a reserve method in which the optimal operation plan of a controllable generator is used to deal with the forecast error uncertainty. The methods described earlier typically require forecast information about the PV power drop. The reserve method, known as local curtailment (LC), is used at the local PV power station. Forecasting errors are unavoidable. With forecast errors, PV may not provide the required virtual inertia. It may cause a frequency deviation that exceeds the grid limit.

Coordinate control is proposed in Chang et al. (2021) to reduce the effect of forecast error. In a large distributed area, the PV stations have a geographical distance. When power is changed at one local PV station, using other remote PV station's reserve power can provide constant virtual inertia. The remote reserve has improved frequency stability *via* probabilistic forecasting. However, it works in a transient state with constant virtual inertia and cannot limit the frequency deviation in policy. As a result, it is challenging to limit frequency deviations in any limitations. Given the policy constraints in continuous operation, an adaptive virtual inertia parameter and a power reserve control strategy are required.

The contribution of this study is listed as follows:

1) The proposed reserve strategy is capable of filtering and determining the working point in quantile regression results. It reduces reserve power in stable irradiance and improves the efficiency of reserved power in the regulating frequency.
2) The ESS capacity and charge/discharge times are reduced by improved virtual inertia control for the remote reserve using adaptive inertia parameters. The virtual inertia is changed to be suitable for different scenarios of the PV power drop. The system frequency and RoCoF variation are reduced in the continuous control throughout the single daytime.
3) Considering the policy of RoCoF and frequency nadir limitation to the virtual inertia control, coordinated control of PV and ESS helps micro-grids improve the system stability.

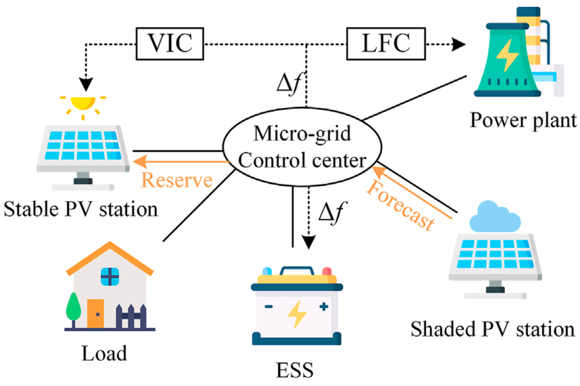

FIGURE 1
Framework of the islanded micro-grid.

The remainder of this study is structured as follows. The framework and islanded micro-grid components are described in Section 2. The system inertia and control strategies are defined in Section 3. The simulation results are presented and discussed in Section 4. Conclusion is provided in Section 5.

2 System configuration

The proposed framework of the AFB-VIC strategy, including PV, load, SG, and ESS connected to a micro-grid controlled by a micro-grid control center, is depicted in Figure 1. There is a geographical distance between PV stations where the irradiance changes asynchronously. The forecast information from the shaded PV station is used to generate reserve power demand in the stable station, shown as the orange arrow. When one of the PV stations is expected to be shaded, the other stable PV begins to reserve power. Following a power drop in a shaded PV station, the ESS and reserved power can be released to provide VIC. For load frequency control (LFC), SG provides constant inertia. Figure 2 shows a simple mathematical schematic representation of an islanded micro-grid. The system's inertia is divided into two parts. The governor (GOV) of the power plant provides the constant inertia. The virtual inertia is controlled by PV and ESS. The parameters of virtual inertia can be adaptively changed according to the forecasting information. The RoCoF and frequency nadir methods are used to control the value of virtual inertia. The following sections follow the specifics of the proposed control strategy.

2.1 Synchronous generators

An SG module to regulate the system frequency with feedback control is proposed in Liu et al. (2016). The constant inertia is provided by SGs in the micro-grid. The control system of the SG is shown in Figure 2; the GOV is used to change the shaft power P_m when angular frequency deviation occurs. The difference between the SG output angular frequency ω_0 and the rated angular frequency ω_r is the angular frequency deviation. The GOV droop coefficient is k_p. In control, a first-order equation is added to represent inertia, where t_d is the inertial response of the governor. The automatic voltage regulator (AVR) is shown in Figure 3. It consists of a power calculation, root-mean-square (RMS), and proportional–integral (PI) control. The excitation system provides the DC to regulate the SG voltage, where k_q is the AVR droop coefficient.

2.2 Photovoltaic

A maximum power point (MPP) estimation method for PV power sources is proposed in Belhachat and Larbes (2019). The maximum available power is estimated by irradiance G and temperature T, which is represented as

$$P_{mp} = \frac{25°\mathrm{C} \cdot G}{T} \cdot \frac{K}{\frac{\sqrt{A}}{2\pi \cdot 0.02}s+1}, \tag{1}$$

where K is a constant parameter and A is the PV panel area. Here, s represents the continuous domain. As shown in Figure 4, PV reserve power means changing the working point from A to B. V_{cmd} is the reserved voltage to regulate the PV voltage. Figure 5 depicts the PV power control strategy that employs MPP estimation and reserve control. P_r is the PV working away from the MPP to reserve power for VIC. The controlled power is limited to less than the reserve power. It ensures PV will not over-regulate. The control strategy of VIC is shown in the PV-controlled power in Figure 2. PVs can compensate the power with virtual inertia when frequency deviation occurs. The VIC function is determined by

$$D_p \cdot \Delta\omega = \left(2H_{pv}s + D_{pv}\right) \cdot P_c, \tag{2}$$

where D_p is p_ω droop coefficient, H_{pv} is the virtual inertia, and D_{pv} is the virtual damping. The ramp-rate violations are considered in power-reserved processing. The PV power change rate should be suitable for the forecast horizon. The ramp rate limits R_s will help grid stability in the reserve strategy. It limits the reserve speed before the stable PV provides the virtual inertia.

$$R_s = |\frac{dP_{PV}}{dt}|. \tag{3}$$

2.3 Energy storage system

The frequency deviation in the power system is caused by a mismatch between supply and demand as a result of a generator

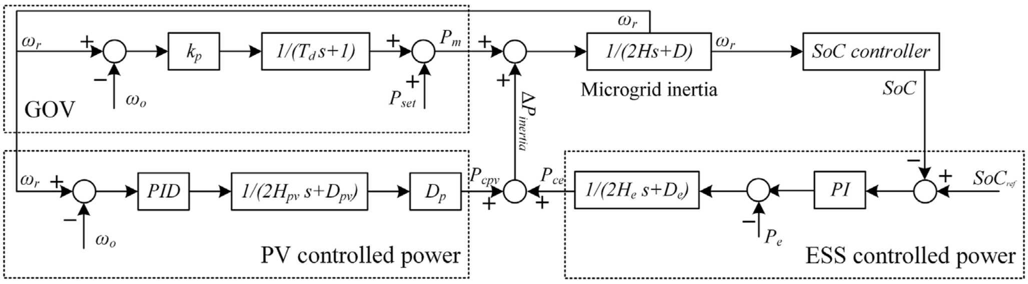

FIGURE 2
Schematic representation of the micro-grid plant model.

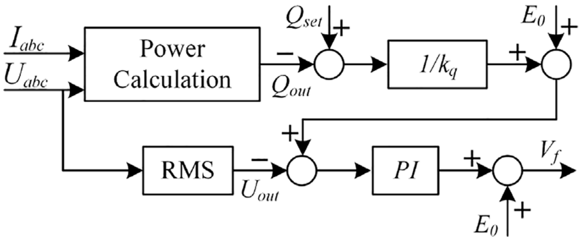

FIGURE 3
Control system of the automatic voltage regulator.

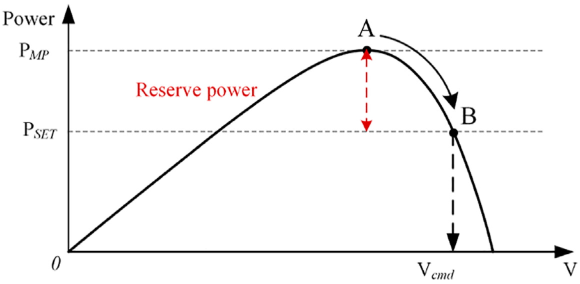

FIGURE 4
Movement of PV power reserves by the operating point away from the MPP.

fault. Furthermore, frequency deviation exists in the forecasting system as a result of forecasting errors. Keeping the ESS state of charge (SOC) in the middle of its capacity can increase delivered energy while decreasing its capacity. Figure 6 illustrates the ESS charge and discharge control strategy. It is stable in the middle of the SOC and is only affected by minor frequency deviations.

The virtual inertia and damping components of the ESS recovery control are similar to the grid forming control for VIC of PVs. When there is a frequency deviation, the ESS compensates the power to the system except for the no-action region. The following Figure 2 illustrates ESS control, which consists of energy recovery control and virtual inertia-damping emulation. It is similar to the VIC of the PV. The ESS virtual inertia is H_e, and damping is D_e.

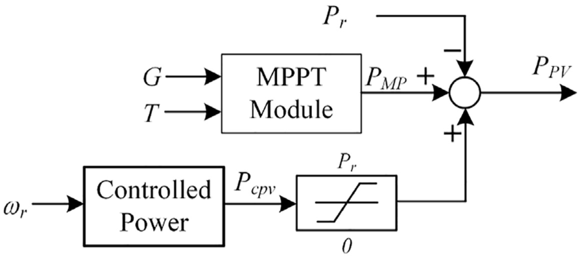

FIGURE 5
Power reserve and the VIC strategy of the PV.

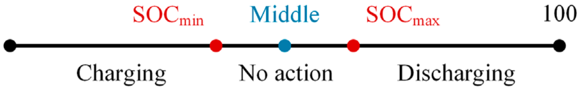

FIGURE 6
SOC control and limitation to charging.

3 Proposed control strategy

For the evaluated adaptive virtual inertia, forecasting results must be transformed into system inertia demand. As a result, the PV and ESS can share the inertia demand with their respective energy capacities. For frequency regulation, the control strategy employs a two-part strategy that includes forecasted reserve control and inertia control.

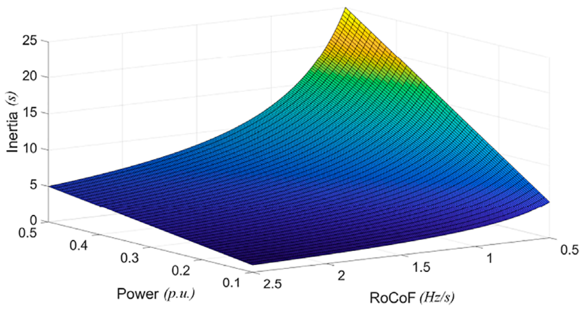

FIGURE 7
Relationships of inertia and power in different RoCoF limitations.

3.1 Inertia

A sudden change in irradiance causes PV power deviations, which may lead to a generation-demand disequilibrium. Initially, the inertia prevents the system's frequency drop. The primary control is to operate the output power of generators to compensate for the frequency deviations. The inertia could be provided by SG, ESS, and reserved power in the PV.

The instantaneous RoCoF is determined by system inertia, and the power of contingency size is expressed by

$$RoCoF_{max} = \frac{f_0 P_d}{2H_{sys}}, \tag{4}$$

where P_d is the contingency size, f_0 is the nominal system frequency, and H_{sys} is the total system inertia. If the permissible RoCoF is determined, the required minimum system inertia can be formulated as

$$H_{min} = \frac{f_0 P_d}{2RoCoF_{max}}. \tag{5}$$

Figure 7 shows the relationship between the contingency size, maximum RoCoF, and minimum system inertia. It can be seen that the minimum system inertia and contingency size have a positive relationship. On the contrary, there is an inverse relationship between minimum system inertia and maximum RoCoF. When the maximum RoCoF is determined, the contingency size determines the minimum system inertia.

Another critical indicator of frequency control is the frequency nadir. Chávez et al. (2014) proposed the overall generator power response in the event of a sudden loss of generation. Figure 8 depicts the relationship between the frequency nadir and drop power. It uses a simplified dynamic model that approximation underestimates the actual response and validates the assumption.

where f_0 is the nominal frequency and G_{sys} is the approximation-aggregated ramp rate limit of the system primary reserve. Re-arranging the integral limits leads to a lower limit equal to zero so that the integral of Eq. 5 between time 0 and t_{nadir} of the frequency nadir can be formulated by

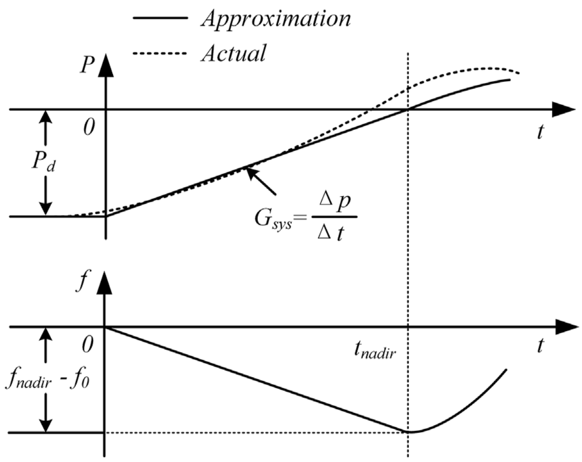

FIGURE 8
Relationship of the frequency nadir and drop power in primary control.

$$\int_0^{t_{nadir}} \frac{df(t)}{dt} dt = \frac{f_0}{2H_{sys}} \int_0^{t_{nadir}} P_d dt. \tag{6}$$

An approximation ramp rate G_{sys} of total governor responses is assumed (Chávez et al., 2014) to facilitate the definite integral calculation of power imbalance, as shown in Figure 8.

$$f_{nadir} - f_0 = -\frac{f_0}{2H_{sys}} \cdot \frac{P_d^2}{2G_{sys}}, \tag{7}$$

where t_{nadir} is the time frequency it takes to reach the nadir, and it can be represented by

$$t_{nadir} = \frac{P_d}{G_{sys}}. \tag{8}$$

In Liu et al. (2020), it establishes a frequency nadir prediction model (FNP) and predicts the time required to reach the maximum frequency deviation, following a major disturbance. The analytical FNP model has a simple structure to the polynomial fitting step response for each governor. The minimum-squared-error method for governors in the islanded model is used to solve the coefficient vector $P_i = [p_{r0}$, i, p_{r1}, i, $\ldots p_{rn}$, i,]. Here, α_i is the transfer coefficient per unit; the time of maximum frequency deviation can also be represented by

$$t_{nadir} = \frac{\left[-\frac{1}{2}A + \sqrt{\frac{1}{4}A^2 + \frac{16}{3}BH_{sys}}\right]}{\frac{4}{3}B}, \tag{9}$$

where

$$\begin{cases} A = \sum_{i=1}^{N_G} \alpha_i p_{r1}, i \\ B = \sum_{i=1}^{N_G} \alpha_i p_{r2}, i \end{cases} \tag{10}$$

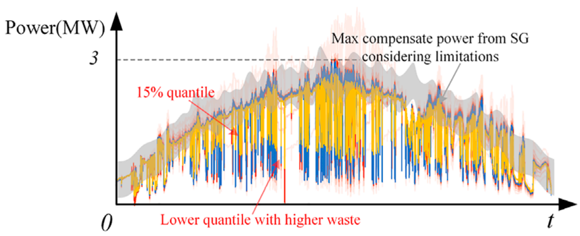

FIGURE 9
Single daytime forecasting results.

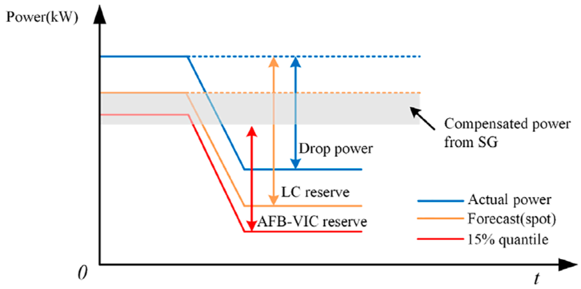

FIGURE 10
Reserved power control using forecasting results.

3.2 Forecasted reserve control

A lasso-based short-term forecasting model for a PV system is proposed in Zhao et al. (2019) and Wang et al. (2022). It constructs a penalty function that allows it to compress some regression coefficients to obtain a refined model. Zhang et al. (2020b) proposed a hybrid forecasting framework based on the LSTM model. The quantile regression architecture for deep learning is probabilistic forecasting.

In this work, the forecast model is trained on a publicly available dataset obtained on Oahu Island, Hawaii, installed by the National Renewable Energy Laboratory (NREL). The details of the dataset are recorded in Sengupta and Andreas (2014). The results of single-daytime forecasting are shown in Figure 9, with cloudy conditions, resulting in significant forecast errors. The blue line is the actual PV power. The orange line represents the determined forecast information. The red line represents the quantile results of the probabilistic forecast. A deeper red color indicates that the results are closer to 50%. The gray area depicts the ability of SGs to compensate for power using Eq. 5 and Eq. 7. If the PV power fluctuated between gray areas, the frequency deviations could adhere to the NEM limitations by only using SGs to regulate the frequency. When PV power fluctuates dramatically, the determined forecast has lower accuracy. For probabilistic forecasting, lower quantile results perform better in terms of accuracy at unstable states. However, in a stable irradiance state, it wastes power.

The proposed reserve strategy is to add the filter and determine quantile processing. The SG boundary, as shown in Figure 9, can cover a portion of the forecasting results. The SG boundary primarily coincides with 15% quantile results. As a result, the quantile can be calculated. The reserve strategy is illustrated in Figure 10. The blue line represents the actual power drop, while the yellow line represents the determined forecasted power. Forecasted results may not equal actual power at the start of the operation. Thus, even if the calculated forecasted drop power results are equal to the actual drop power, the LC reserve strategy wastes energy due to initial errors. The AFB-VIC was more concerned with the power shift. It has reduced the amount of energy wasted due to initial errors. Furthermore, Eq. 5 and Eq. 7 show that the constant inertia of SG results in a limited boundary of power change. This portion of the power can also be reduced to reduce the energy waste. The power drop can be handled by the sum of virtual inertia in the PV and constant inertia in the SG.

3.3 Inertia control strategy

Inertia has a relationship with RoCoF and the frequency nadir. Thus, the system inertia demand can be calculated by the normalized forecasting results. The system inertia demand, according to Eq. 5 and Eq. 7, is the sum of H_{rocof} and H_{nadir}. The system inertia distribution of SG, PV, and ESS is expressed by

$$H_{sys} = \sum_{i\epsilon\phi SG}^{N_G} H_i x_i + \sum_{i\epsilon\phi PV}^{N_G} H_j x_j + \sum_{i\epsilon\phi ESS}^{N_G} H_k x_k, \tag{11}$$

where ϕSG, ϕPV, and ϕESS are sets of SGs, PVs, and ESSs in the islanded micro-grid, and the SG has constant inertia. The requirement for minimum system inertia can be evaluated by the adaptive virtual inertia of the PV and ESS.

The SG maintains constant inertia. If the stable PV is working at the MPP, it cannot provide virtual inertia to the micro-grid. When the rapid power drops from the shaded PV, the SG may not be able to compensate for the total system inertia demand. The remaining virtual inertia must be distributed adaptively by reserve power at the stable PV and ESS. Figure 11 depicts the inertia demand when PV power is reduced in a single day. The actual power drop at the shaded PV station is depicted by the blue line. The orange line depicts the LC strategy. It reserves power at the shaded PV by determined forecasting. The red line represents the virtual inertia supplied by the remote stable PV *via* AFB-VIC. The gray portion represents the constant inertia provided by the SG. The remainder of the inertia demand needs to be compensated by the PV and ESS. As a result, SG inertia reduces the power demand in a remote stable PV. The PV reserve power can be used to charge the ESS when considering the ESS recovery process. As a result, the PV and ESS have distributed

```
Input: Given initial power drop $P_d$, reserved power $P_r$
Initialization;
for each time $t$ do
    Collect PV output power $P_{pv}$, determined forecast power $P_f$ ;
end
for $P_f \in availablePVpower$ do
    $P_d = P_{pv} - P_f$
end
if $P_d \geq 0$ then
    $P_r = P_d$
else
    $P_r = 0$
end
Update the LC reserve power $P_r$ ;
```

Algorithm 1. LC – pseudo code.

virtual inertia, and the parameters of H_{pv} are governed by the NEM guideline limitation.

Maximum power point tracking (MPPT) control, local curtailment (LC), determined region reserve (DRR), and AFB-VIC are the four PV power control strategies. The MPPT control is defined as the PV operating at the MPP at all times. It does not require any forecasting data. Based on forecast information, LC is the reserved power in the local PV station. It has a ramp limit to reserve power before the PV power drops. As a result, the reserved processing avoids frequency deviation. Algorithm 1—Local curtailment—Pseudo Code depicts the control strategy. The DRR is comparable to LC control. It uses the determined forecast result at PV1 but reserves power at a stable PV station.

Based on probabilistic forecast data, AFB-VIC is a method of reserving power at geographically separated, stable PV stations. It also has a ramp limit for power reserves. When the other PV station is shaded, the reserved power at the stable PV station can be released to compensate for the loss of power. The system inertia consists of SG, PV, and ESS. SG has constant inertia. The required virtual inertia is provided by the PV and ESS. The value of virtual inertia is thus adaptively changed for different forecasted PV power levels, according to Eq. 7. Within the limits of RoCoF and the frequency nadir, the SG can compensate for a constant power deficit. The PV and ESS must supply the remainder of the predicted power and inertia demand. As a result, the power reserved in the PV can be calculated using the Algorithm 2-AFB-VIC-pseudo code.

4 Simulation results

As shown in Figure 1, an islanded micro-grid with the SG, PV, ESS, and load has been modeled using MATLAB/Simulink. The actual power change in a single day (36000s, 7:30–19:30) is

```
Input: Given initial $H_{sg}, H_{pv}, H_{ess}, P_d, P_r$
Initialization;
for each time $t$ do
    Collect PV output power $P_{pv}$, determined forecast power $P_f$, determined probabilistic forecast $P_{pf}$ ;
end
Solve maximum compensate power $P_{sg}$ from SG using Eqs.(5)(7).;
for $P_{pf} - P_{sg} \in availablePVpower$ do
    $P_d = P_{pf} - P_{sg}$
end
if $P_d \geq 0$ then
    $P_r = P_d$
else
    $P_r = 0$
end
Solve minimum inertia $H_{pv}$ using Eqs.(7) for $H_{pv} > 0$ do
    Solve $P_r$ using Eqs.(5)(7)
end
Update the AFB-VIC reserve power $P_r$ and virtual inertia $H_{pv}$ ;
```

Algorithm 2. AFB-VIC – pseudo code.

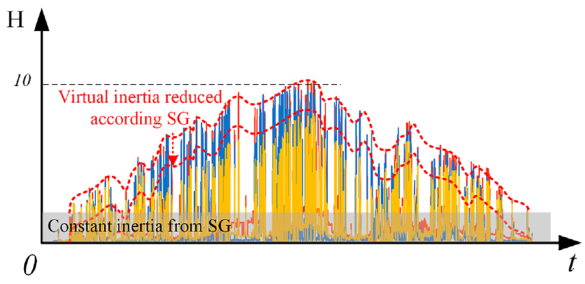

FIGURE 11
Inertia demand and distribution.

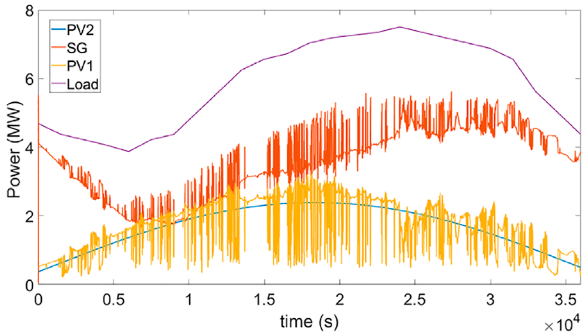

FIGURE 12
Basic output power and load demand in 36,000 s of a single daytime.

TABLE 1 Corresponding parameters of the tested system.

Parameter	Value
Constant inertia of SG H	1.7 s
Constant damping of SG D	1.2 p.u.
Virtual inertia of ESS H	1.0 s
Virtual damping of ESS D	1.0 p.u.
SG time constant T_d	0.6 s
Capacity of SG	6 MW
Capacity of shading PV	3.2 MW
Capacity of the stable PV	2.2 MW
Load	8 MW
Ramp rate limit Rs	40 W/s

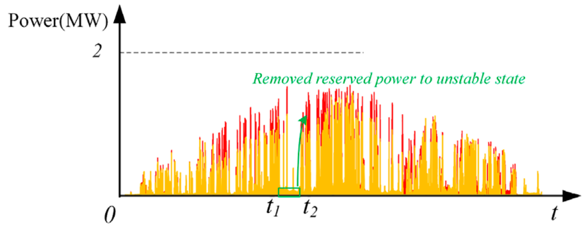

FIGURE 13
Reserved power of the determined forecast and AFB-VIC probabilistic forecast reserve strategy.

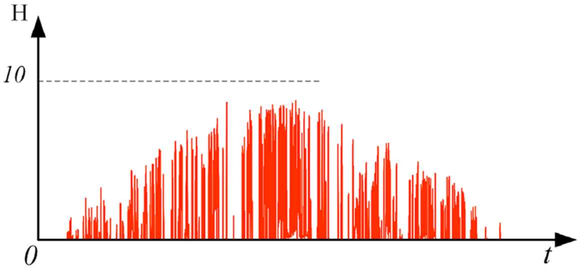

FIGURE 14
Value of virtual inertia in the PV using AFB-VIC.

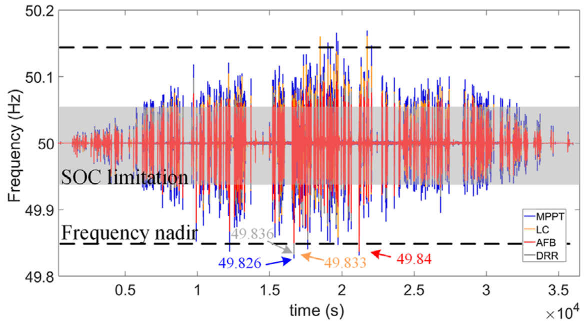

FIGURE 15
Micro-grid frequency response with different control strategies.

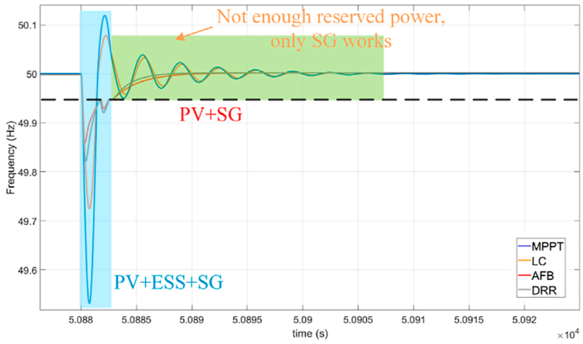

FIGURE 16
Close-up view of the frequency deviation.

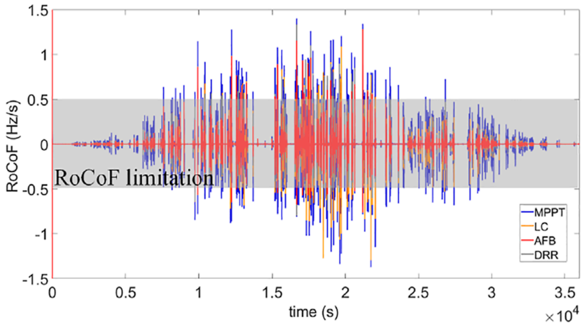

FIGURE 17
RoCoF response.

depicted in **Figure 12**. PVs, ESS, and SG supply load demand in this islanded micro-grid system. The AFB-VIC strategy employs two PVs to simulate the frequency variation. According to the forecasting results, one of the PV stations will be shaded. The other has consistent irradiance. **Table 1** shows the corresponding parameters of the tested system.

To validate the effectiveness of the proposed AFB-VIC strategy, the other three cases, including traditional MPPT, DRR, and LC strategies, are simulated and compared. Podder et al. (2019) used a traditional MPPT control strategy that employs a fixed-step-size perturb and observed the algorithm (P&O). Single-day forecasting results, including spot and probabilistic methods, are used for power reservation purposes. LC uses determined forecast results of PV1 and makes PV1 reserve power before shading and lets PV2 always work at its MPP. The DRR uses a determined forecast to reserve power at PV2 and then releases it to provide VIC, which performs PV1 work at the MPP. AFB-VIC reserves power in stable PV2 by probabilistic forecasting while allowing shaded PV1 to operate at

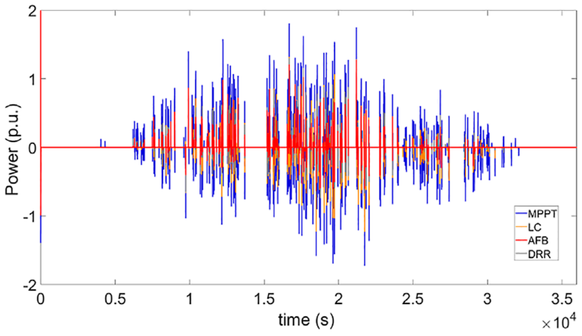

FIGURE 18
ESS power provided to the micro-grid.

the MPP. The ESS is configured to compensate power only when frequency deviations exceed ±0.05 Hz. It is designed with infinite capacity and no constraints to ignore the effect of the energy capacity that could show the different rated energy capacities controlled with four strategies.

4.1 Photovoltaic reserved power

Using the forecast information in **Figures 9**, **Figure 13** depicts the reserved power change for LC, DRR, and AFB-VIC. The orange zone denotes reserved power *via* LC and DRR control. The reserved power was shown in red using AFB-VIC. At a stable state, LC control has reserved power ranging from t_1 to t_2. AFB-VIC reduced the reserved power between t_1 and t_2. Furthermore, in an unstable state, it reserves more power. The LC **Algorithm 1** obtains the new working point to reserve power in shaded PV1. When shading arrives, ESS and the reserved power in PV1 should compensate for PV1 power loss. However, if the determined forecast is incorrect, the actual power drop will exceed the calculated forecast. It leads to PV1 becoming a burden in this islanded micro-grid system. More power is required from the SG and ESS to regulate the frequency. AFB-VIC uses PV2 to reserve power and employs probabilistic forecast results from PV1. If there is a forecast error in PV1, PV2 can continue to provide power indefinitely. It has the advantage of the structural parameter variety for AFB-VIC. A probabilistic forecast can accommodate a higher power change than a determined forecast. As a result, AFB-VIC can mitigate some of the effects of forecast errors in PV1. Compared to these two methods, AFB-VIC has a higher maximum reserve power than LC. Furthermore, as shown in **Figure 14**, AFB-VIC has provided adaptive virtual inertia in the PV to limit frequency deviation.

4.2 Frequency response

We simulated the single daytime frequency deviations of MPPT, LC, DRR, and AFB-VIC strategies in **Figure 15** using the irradiance results in **Figure 9**. In NEM, the frequency nadir is represented by the black dashed line. The frequency limit is 49.85 Hz. The MPPT control strategy is represented by the blue line. It has a frequency nadir of 49.826 Hz. Moreover, there are four ways to exceed the frequency nadir limitation. The orange line represents the frequency response of the LC control strategy. The frequency nadir falls below the limitation once during a single daytime simulation, reaching 49.833 Hz, and it has three chances to shoot over the frequency limitation. The gray line depicts the DRR results. The frequency nadir is 49.536 Hz, and it has three points above the frequency nadir. The ESS and SG cannot compensate for the power and inertia caused by the determined forecast error. The red line represents the AFB-VIC strategy. There is only one instance of the over-frequency nadir during the single daytime simulation. It has the lowest nadir frequency of 49.84 Hz. The SG provides the majority of the inertia. AFB-VIC has lower frequency deviations and times of the over-frequency nadir when compared to these methods.

Figure 16 shows a close-up of the frequency response at 3.58 h. The black dashed line represents a SOC constraint. When the frequency falls below 49.95 Hz, the ESS is discharged. The PV, ESS, and SG all worked together to control the frequency in the first 3 s. Only the ESS and SG are used in the MPPT control strategy to compensate for power and provide inertia. As a result, the frequency nadir is lower, and the recovery time is longer. Due to the MPPT and LC not having any reserve power after

TABLE 2 Results of the MAPE and RMSE.

		AFB-VIC	LC	DRR	MPPT
MAPE	Frequency	**0.08**	0.10	0.09	0.11
	RoCoF	**0.18**	0.24	0.21	0.30
RMSE	Frequency	**5.25**	5.67	5.49	6.40
	RoCoF	**18.31**	19.21	18.97	24.06
Times over limitation	Frequency	**1**	3	3	9
	RoCoF	**28**	52	45	137
Charge and discharge times		**120**	183	156	287
ESS capacity (p.u.)		**1.7**	2.4	1.9	3.7

The bold values means the minimum results is the best performance in frequency response.

the first 3 s, the frequency regulation has only relied on the SG after that. The DRR can provide VIC using reserved power, but it has a lower reserve capacity than AFB, so it takes longer to reach 50 Hz. In comparison to these methods, AFB-VIC limits frequency deviation to a narrower range and reduces more subtle oscillations. Furthermore, AFB-VIC only uses 10 s to restore the frequency.

Accordingly, the RoCoF limitation is another condition in the micro-grid of NEM. **Figure 17** shows the RoCoF response of these methods. The RoCoF change is mainly concentrated because irradiance rapidly changes. The blue line shows the RoCoF change region of the MPPT. It is −1.3 ˜1.4 Hz/s. With the power being reserved in PV1 using LC, the PV power drop is reduced. Therefore, the RoCoF change region is −1.2 ˜1.3 Hz/s of local curtailment. Because the DRR reserve power in stable PV2 uses determined forecasting results, it provides power and virtual inertia when irradiance changes in PV1, and the RoCoF deviation region is −1.0 ˜1.3 Hz/s. The AFB-VIC using probabilistic forecasting results has reduced the RoCoF change region to −0.6 ˜1.2 Hz/s. For the RoCoF, AFB-VIC has reduced 21.7%, 28%, and 33%, compared to DRR, LC, and the MPPT strategies, respectively. Moreover, the times over the RoCoF limitation using MPPT, LC, DRR, and the AFB-VIC strategy are 137, 52, 45, and 28, respectively.

The mean absolute percentage error (MAPE) and root mean squared error (RMSE) are considered. The MAPE and RMSE are standard criteria to evaluate the accuracy of frequency or RoCoF.

$$MAPE = \frac{100\%}{n}\sum_{i=1}^{n}\left|\frac{\hat{y}_i - y_i}{y_i}\right|, \tag{12}$$

$$RMSE = \sqrt{\frac{1}{n}\sum_{i=1}^{n}(\hat{y}_i - y_i)^2}. \tag{13}$$

$\hat{y}_i$ denotes the frequency or RoCoF value, while y_i denotes the reference value of frequency and RoCoF. Although the maximum range of deviations and times over frequency or the RoCoF limitation can offer a comparison of the control strategies, the accuracy of deviations is still an essential result of the model.

4.3 Energy storage system

The ESS is programmed to operate at 50% SOC and has an infinite power capacity. It clearly shows the maximum ESS power used for frequency regulation. The charge and discharge power capacity of these methods is depicted in **Figure 18**. As shown in **Table 2**, the times of charge and discharge of MPPT, local curtailment, DRR, and AFB-VIC are 287, 183, 156, and 120, respectively. Thus, the AFB-VIC has the potential to reduce costs by extending the life cycle. The MPPT control has a maximum ESS capacity of 3.7 p.u. in the 36000 s daytime simulation due to PV being continuously operated at the MPP. The local curtailment reduces the ESS power capacity to 2.4 p.u. The DRR requires 1. p.u. of the ESS capacity. The AFB-VIC strategy has a minimum power capacity of the ESS. It only requires 1.7 p.u.

5 Conclusion

The AFB-VIC method is proposed in this study to improve the system stability caused by the irradiance drop. It simulates a daytime of continuous operations. With the high penetration of the PV and the geographical distance between the PVs, we proposed a power reserve strategy based on probabilistic forecasting results to reduce the reserved power with stable irradiance and increase the power reserve with unstable irradiance. Using the stable PV station generates VIC. The adaptive virtual inertia and power reserve are controlled by the NEM RoCoF and frequency nadir limitation. The proposed AFB-VIC offers advantages in the following areas:

The RoCoF and frequency nadir can both be restricted. The virtual inertia is changed adaptively based on the forecasted PV power drop. It continuously provides virtual inertia, even with an initial forecast error in shaded PV stations. Furthermore, it shortens the time required for frequency regulation.

The AFB-VIC proposed a method for calculating and filtering quantile regression from probabilistic forecasting results. It reduces the power waste in a stable state and increases reserve power in a large range of areas. It improves the reserved power efficiency in the frequency nadir and RoCoF limitation.

The ESS power capacity has been reduced due to the proposed AFB-VIC. Furthermore, it extends ESS aging by reducing charge and discharge times.

Data availability statement

The original contributions presented in the study are included in the article/Supplementary Material; further inquiries can be directed to the corresponding author.

Author contributions

All the authors listed have made a substantial, direct, and intellectual contribution to the work and approved it for publication.

Funding

This work was supported by the Xi'an Jiaotong-Liverpool University, Research Development Fund of XJTLU (RDF-17-01-28); and the AI University Research Centre (AI-URC) through the XJTLU Key Programme Special Fund (KSF-P-02).

Conflict of interest

The authors declare that the research was conducted in the absence of any commercial or financial relationships that could be construed as a potential conflict of interest.

Publisher's note

References

Askarian, I., Eren, S., Pahlevani, M., and Knight, A. M. (2018). Digital real-time harmonic estimator for power converters in future micro-grids. *IEEE Trans. Smart Grid* 9 (6), 6398–6407. doi:10.1109/tsg.2017.2711016

Belhachat, F., and Larbes, C. (2019). Comprehensive review on global maximum power point tracking techniques for pv systems subjected to partial shading conditions. *Sol. Energy* 183, 476–500. doi:10.1016/j.solener.2019.03.045

Chang, J., Du, Y., Lim, E. G., Wen, H., Li, X., and Jiang, L. (2021). Coordinated frequency regulation using solar forecasting based virtual inertia control for islanded microgrids. *IEEE Trans. Sustain. Energy* 12 (4), 2393–2403. doi:10.1109/tste.2021.3095928

Chávez, H., Baldick, R., and Sharma, S. (2014). Governor rate-constrained opf for primary frequency control adequacy. *IEEE Trans. Power Syst.* 29 (3), 1473–1480. doi:10.1109/tpwrs.2014.2298838

Chen, X., Du, Y., Wen, H., Jiang, L., and Xiao, W. (2019). Forecasting-based power ramp-rate control strategies for utility-scale pv systems. *IEEE Trans. Ind. Electron.* 66 (3), 1862–1871. doi:10.1109/tie.2018.2840490

Crăciun, B.-I., Kerekes, T., Séra, D., and Teodorescu, R. (2014). Frequency support functions in large pv power plants with active power reserves. *IEEE J. Emerg. Sel. Top. Power Electron.* 2 (4), 849–858. doi:10.1109/jestpe.2014.2344176

da Luz, C. M. A., Vicente, E. M., and Tofoli, F. L. (2020). Experimental evaluation of global maximum power point techniques under partial shading conditions. *Sol. Energy* 196, 49–73. doi:10.1016/j.solener.2019.11.099

Dreidy, M., Mokhlis, H., and Mekhilef, S. (2017). Inertia response and frequency control techniques for renewable energy sources: A review. *Renew. Sustain. Energy Rev.* 69, 144–155. doi:10.1016/j.rser.2016.11.170

Gu, H., Yan, R., and Saha, T. K. (2018). Minimum synchronous inertia requirement of renewable power systems. *IEEE Trans. Power Syst.* 33 (2), 1533–1543. doi:10.1109/tpwrs.2017.2720621

Hammad, E., Farraj, A., and Kundur, D. (2019). On effective virtual inertia of storage-based distributed control for transient stability. *IEEE Trans. Smart Grid* 10 (1), 327–336. doi:10.1109/tsg.2017.2738633

Han, Y., Wang, N., Ma, M., Zhou, H., Dai, S., and Zhu, H. (2019). A pv power interval forecasting based on seasonal model and nonparametric estimation algorithm. *Sol. Energy* 184, 515–526. doi:10.1016/j.solener.2019.04.025

Hoke, A., and Maksimović, D., "Active power control of photovoltaic power systems," in 2013 1st IEEE Conference on Technologies for Sustainability (SusTech), 01-02 August 2013, Portland, 2013, pp. 70–77.

Hua, T., Yan, X., and Fan, W., "Research on power point tracking algorithm considered spinning reserve capacity in gird-connected photovoltaic system based on vsg control strategy," in 2017 IEEE 3rd International Future Energy Electronics Conference and ECCE Asia (IFEEC 2017 - ECCE Asia), 03-07 June 2017, Kaohsiung, Taiwan, 2017, pp. 2059–2063.

Li, X., Wen, H., Zhu, Y., Jiang, L., Hu, Y., and Xiao, W. (2019). A novel sensorless photovoltaic power reserve control with simple real-time mpp estimation. *IEEE Trans. Power Electron.* 34 (8), 7521–7531. doi:10.1109/tpel.2018.2880461

Liu, J., Yushi, M., Ise, T., Yoshizawa, J., and Watanabe, K., "Parallel operation of a synchronous generator and a virtual synchronous generator under unbalanced loading condition in microgrids," in 2016 IEEE 8th International Power Electronics and Motion Control Conference (IPEMC-ECCE Asia), 22-26 May 2016, Hefei, China, 2016, pp. 3741–3748.

Liu, L., Li, W., Ba, Y., Shen, J., Jin, C., and Wen, K. (2020). An analytical model for frequency nadir prediction following a major disturbance. *IEEE Trans. Power Syst.* 35 (4), 2527–2536. doi:10.1109/tpwrs.2019.2963706

Mahmud, K., Azam, S., Karim, A., Zobaed, S., Shanmugam, B., and Mathur, D. (2021). Machine learning based pv power generation forecasting in alice springs. *IEEE Access* 9 (46 117), 46117–46146 128. doi:10.1109/access.2021.3066494

Mararakanye, N., and Bekker, B. (2019). Renewable energy integration impacts within the context of generator type, penetration level and grid characteristics. *Renew. Sustain. Energy Rev.* 108, 441–451. doi:10.1016/j.rser.2019.03.045

Podder, A., Roy, N., and Pota, H. (2019). Mppt methods for solar pv systems: A critical review based on tracking nature. *IET Renew. Power Gener.* 13, 1615–1632. doi:10.1049/iet-rpg.2018.5946

Sengupta, M., and Andreas, A. (2014). *Oahu solar measurement grid (1-year archive): 1-second solar irradiance; oahu Hawaii(data).* Colorado: Nrel.

Tielens, P., and Van Hertem, D. (2016). The relevance of inertia in power systems. *Renew. Sustain. Energy Rev.* 55, 999–1009. doi:10.1016/j.rser.2015.11.016

Ulbig, A., Borsche, T. S., and Andersson, G. (2014). Impact of low rotational inertia on power system stability and operation. *IFAC Proc. Vol.* 47 (3), 7290–7297. 19th IFAC World Congress. doi:10.3182/20140824-6-za-1003.02615

Wang, F., Lu, X., Mei, S., Su, Y., Zhen, Z., Zou, Z., et al. (2022). A satellite image data based ultra-short-term solar pv power forecasting method considering cloud information from neighboring plant. *Energy* 238, 121946. doi:10.1016/j.energy.2021.121946

Wang, F., Xuan, Z., Zhen, Z., Li, Y., Li, K., Zhao, L., et al. (2020). A minutely solar irradiance forecasting method based on real-time sky image-irradiance mapping model. *Energy Convers. Manag.* 220, 113075. doi:10.1016/j.enconman.2020.113075

Woodhouse, M., Jones-Albertus, R., Feldman, D., Fu, R., Horowitz, K., Chung, D., et al. (2011). *On the path to sunshot - the role of advancements in solar photovoltaic efficiency, reliability, and costs.* Seattle: Semanticscholar.

Yan, X., Li, J., Wang, L., Zhao, S., Li, T., Lv, Z., et al. (2018). Adaptive-MPPT-based control of improved photovoltaic virtual synchronous generators. *Energies* 11 (7), 1834–1918. doi:10.3390/en11071834

Yang, Y., Blaabjerg, F., Wang, H., and Simões, M. G. (2016). Power control flexibilities for grid-connected multi-functional photovoltaic inverters. *IET Renew. Power Gener.* 10 (4), 504–513. doi:10.1049/iet-rpg.2015.0133

Zhang, C., Xu, Y., and Dong, Z. Y. (2020). Robustly coordinated operation of a multi-energy micro-grid in grid-connected and islanded modes under uncertainties. *IEEE Trans. Sustain. Energy* 11 (2), 640–651. doi:10.1109/tste.2019.2900082

Zhang, H., Wang, J., Sun, Z., Zurada, J. M., and Pal, N. R. (2020). Feature selection for neural networks using group lasso regularization. *IEEE Trans. Knowl. Data Eng.* 32 (4), 659–673. doi:10.1109/tkde.2019.2893266

Zhao, Y., Xu, K., Zhu, E., Liu, X., Zhu, X., and Yin, J. (2019). Triangle lasso for simultaneous clustering and optimization in graph datasets. *IEEE Trans. Knowl. Data Eng.* 31 (8), 1610–1623. doi:10.1109/tkde.2018.2865342

Frontiers in Energy Research

TYPE Original Research
PUBLISHED 09 January 2023
DOI 10.3389/fenrg.2022.1022905

EDITED BY
Fei Wang,
North China Electric Power University,
China

REVIEWED BY
Liansheng Huang,
Hefei Institutes of Physical Sciences
(CAS), China
Jiarong Li,
Tsinghua University, China

*CORRESPONDENCE
Jie Lou,
✉ loujie00@sdu.edu.cn

SPECIALTY SECTION
This article was submitted to Smart Grids,
a section of the journal
Frontiers in Energy Research

RECEIVED 19 August 2022
ACCEPTED 20 December 2022
PUBLISHED 09 January 2023

CITATION
Xu Q, Lou J, Ning D and Li P (2023),
Transient stability enhancement control
through VSC-HVDC system and fast
frequency response resources.
Front. Energy Res. 10:1022905.
doi: 10.3389/fenrg.2022.1022905

Transient stability enhancement control through VSC-HVDC system and fast frequency response resources

Qingshen Xu[1], Jie Lou[1]*, Dalei Ning[2] and Peihao Li[3]

[1]School of Electrical Engineering, Shandong University, Jinan, China, [2]State Grid Jinan Power Supply Company, Jinan, China, [3]State Grid Binzhou Power Supply Company, Jinan, China

In addition to the traditional long-distance and bulk power transmission application, the HVDC system can bring additional benefits to the system by providing ancillary service. The high-voltage direct-current transmission (HVDC) system can regulate its power flow in a very short time and can be used to provide emergency support to rescue the disturbed system from very bad conditions. However, because traditional generators cannot meet the great power demand of the HVDC system in a short time, the fast response of the HVDC system may cause severe power-unbalance events in the power supporting system. In this paper, a combination frequency response control (CFRC) is proposed for the fast frequency response (FFR) and HVDC system coordinating under the contingency. With the proposed combination frequency response control, the most use of the frequency response capacity of the HVDC system could be made. Meanwhile, the coordination between the HVDC system and fast frequency response could prevent the frequency of the power-source-provided system from dropping to an unacceptable level. The simulation study is conducted on a highly reduced power system model of the three North American interconnections. The simulation verification shows the effectiveness and feasibility of the proposed combination frequency response control and indicates that the frequency stability for both side systems of the HVDC system could be significantly improved with the proposed combination frequency response control. In the future, the communication delay between energy storage and HVDC will be considered in the strategy to further improve the accuracy of fast frequency response.

KEYWORDS

HVDC system, fast frequency response, combination frequency response control, frequency stability, frequency oscillation

1 Introduction

Over the past decade, high-voltage direct-current transmission (HVDC) systems have witnessed continuous increases around the world with the development of advancing power electronic technology (Sun et al., 2021a; Xiao et al., 2021; Sun et al., 2022a). In Asia, China, which has the greatest number of HVDC operating and planning systems, has continuously led the global HVDC system construction in recent years (Li et al., 2019). In the United States, HVDC transmission technology has been widely accepted as a good choice to achieve economic long-distance and bulk power transmission and to interconnect all three interconnections independently (Sun et al., 2019a).

With the advancement of voltage source converter (VSC) technology, the applications of the HVDC system have been greatly improved (Sun et al., 2017; Sun et al., 2019b). In addition to

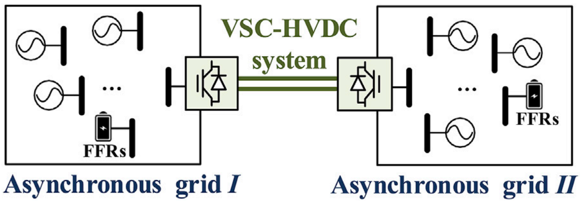

FIGURE 1
Configuration of the two-terminal VSC-HVDC system interconnecting two asynchronous grids.

the long distance and bulk power delivery, the HVDC system could provide a quick dynamic response to different types of system disturbances. Sharing the frequency response reserves *via* the HVDC system is a high-value product. Over the past decade, some projects and researchers have considered including HVDC systems in frequency control. MISO (2014) adopted the VSC-HVDC system to share the frequency response reserve that could bring 25% financial benefits to the system operator, which justifies the economy of the HVDC transmission system. In 2017, the Interconnection Seam Study project was cooperatively investigated by the Department of Energy (DOE) and research partners, including national laboratories and universities. In this project, sharing the frequency response reserve was one of the critical benefits that could bring a major contribution to the operating financial benefits of the HVDC system (NREL). The Pacific Northwest National Laboratory also studied the possibility of the frequency response serviced from multi-terminal HVDC networks in the American grid (Elizondo and Kirkham, 2016).

Different from the traditional synchronous generators in the electric power grid, the active power control of the HVDC system is decoupled from the frequency (Sun et al., 2020). Thus, the HVDC system could realize a quick frequency response to the disturbed system under the contingency. In practice, the power regulation of the HVDC system under an event can be up to hundreds of MW per second, which could significantly improve the frequency of nadir during the event (Belkin, 2012). However, the typical large fossil-fired thermal generator could only ramp 1% of its capacity in 1 min (Kirby). Due to the response rate deviation, the unrestricted power regulation rate of the HVDC system may cause huge frequency oscillations in the supporting system and even cause power outages. Therefore, improving the system frequency response performance through the HVDC system or guaranteeing the operating safety of the support-provided system is a clear dilemma in system frequency control.

Due to the great need for frequency regulation and the consequent economic advantage, numerous fast frequency response (FFR) resources represented by energy storage equipment, such as batteries and flywheels, have been recently installed into the system (Kim et al., 2017). The FFRs have very high cycle stability, high power density, and fast charging and discharging owing to low inner resistance (Zhao et al., 2015). Under the frequency event, the FFRs could provide a quick response to the system, which could digest part of the influence caused by the HVDC system frequency control.

The coordination operation of the HVDC system and energy storage has been recently investigated in some papers mainly focusing on renewable energy integration improvement (Junyent-Ferr et al., 2015; Xu et al., 2019; Sun et al., 2022b) and HVDC system operation enhancement (Yang et al., 2019; Sun et al., 2021b; Sun et al., 2021c; Judge and Green, 2019). Some papers have also discussed the effect of energy storage on HVDC system frequency control (Ray et al., 2009; Rakhshani et al., 2017; Pathak et al., 2017; Yang et al., 2019; Judge and Green, 2019). However, most of the research aims to use energy storage to assist the HVDC system frequency control for performance improvement. Considering energy storage as FFRs to coordinate the HVDC system frequency response for both sides of system operating safety has not received much attention.

In the past, the communication and real-time situational awareness of the devices in the system could not satisfy the fast frequency response requirement. Thanks to the advancement of the wide-area monitoring system, the device information interaction is fast enough and more reliable to enable the HVDC system and FFRs coordination control (You et al., 2016; Zhou et al., 2016). In this paper, a combination frequency response control (CFRC) strategy is developed for the FFRs and HVDC system coordinating under the contingency. The proposed combination control is based on the active power control of the HVDC system and FFRs, as well as real-time communication. With the proposed combination frequency response control, the most use of the frequency response capacity of the HVDC system could be made. Meanwhile, the coordination between the HVDC system and FFRs could also prevent the frequency of the power-source-provided system from dropping to an unacceptable level.

This paper is organized as follows: Section 2 introduces the studied system model. Section 3 introduces the motivation of this paper and the transient stability analysis of the system with FFRs and HVDC system integration. The operation principle and control strategy of the proposed combination frequency response control are described in Section 4. The simulation verifications are presented based on a highly reduced power system model of the three North American interconnections in Section 5. Finally, the results and conclusion are discussed in Section 6.

2 Model description

In this paper, a two-terminal VSC-HVDC system interconnecting two asynchronous grids is depicted in Figure 1. The traditional fossil-fired thermal generator is adopted, and the battery energy storage system (BESS) is used as FFR.

The half-bridge VSC is adopted as the converter of the HVDC system; the equivalent circuit of one VSC of the VSC-HVDC system connected to an asynchronous AC grid is depicted in Figure 2.

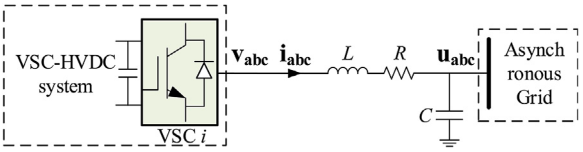

FIGURE 2
Diagram of a VSC in the VSC-HVDC system, where u_{abc} represents the AC voltage of the asynchronous grid, v_{abc} and i_{abc} are the output AC voltage and AC current of the VSC-HVDC system, and ***R*** and ***L*** denote the resistance and inductance of the interfacing reactor, respectively.

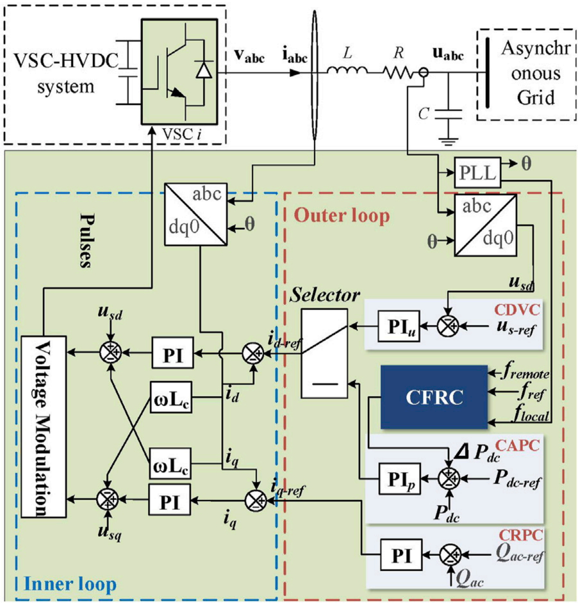

FIGURE 3
Basic control of the VSC-HVDC system (one terminal).

As shown in Figure 2, the VSC mathematical model can be rewritten according to Xiao et al. (2015):

$$\left.\begin{aligned} L\frac{\mathrm{d}i_\mathrm{a}}{\mathrm{d}t}+Ri_\mathrm{a}&=v_\mathrm{a}-u_\mathrm{a},\\ L\frac{\mathrm{d}i_\mathrm{b}}{\mathrm{d}t}+Ri_\mathrm{b}&=v_\mathrm{b}-u_\mathrm{b,}\\ L\frac{\mathrm{d}i_\mathrm{c}}{\mathrm{d}t}+Ri_\mathrm{c}&=v_\mathrm{c}-u_\mathrm{c}.\end{aligned}\right\} \tag{1}$$

For the inner current control loop of VSC, the synchronous *dq*-frame is adopted for the current controller implementation. The synchronous *dq*-axis voltage and current components are transformed with Park transformation from balanced static *abc*-axis voltages and currents. Thus, the VSC dynamic equations in the synchronous *dq*-frame could be expressed as

$$\left.\begin{aligned} L\frac{\mathrm{d}i_\mathrm{d}}{\mathrm{d}t}+Ri_\mathrm{d}&=v_\mathrm{d}-u_\mathrm{d}+\omega Li_\mathrm{q},\\ L\frac{\mathrm{d}i_\mathrm{q}}{\mathrm{d}t}+Ri_\mathrm{q}&=v_\mathrm{q}-u_\mathrm{q}-\omega Li_\mathrm{d},\end{aligned}\right\} \tag{2}$$

where ω represents the angular frequency of the AC grid. Based on Eq. 2, the inner current control loop of the VSC could be expressed as

$$\left.\begin{aligned} v_\mathrm{d\_ref}&=u_\mathrm{d}-\omega Li_\mathrm{q}+\left(k_\mathrm{p}+\frac{k_\mathrm{i}}{s}\right)\left(i_\mathrm{d\_ref}-i_\mathrm{d}\right),\\ v_\mathrm{q\_ref}&=u_\mathrm{q}+\omega Li_\mathrm{d}+\left(k_\mathrm{p}+\frac{k_\mathrm{i}}{s}\right)\left(i_\mathrm{q\_ref}-i_\mathrm{q}\right),\end{aligned}\right\} \tag{3}$$

where k_p and k_i are the proportional and integral gains.

The basic control of the VSC is shown in Figure 3, where CAPC is the constant active power control, CDVC is the constant DC voltage control, CRPC is the constant reactive power control, and CFRC is a combination frequency response control.

3 Problem description

3.1 Motivation

In addition to the long-distance and bulk power transmission, the advancement of the HVDC transmission technology brings more benefits to the power system, such as large-scale renewable integration and ancillary services. In some severe events, the HVDC could provide bulk power support to the disturbed system in a very short time, which could significantly suppress the influence of the disturbance and rescue the disturbed system from further deterioration or even outage. However, traditional generators cannot meet the great power demand of the HVDC system in a short time. The fast response of the HVDC system may cause severe power-unbalance events in the power supporting system. In order to avoid this issue, a compromise has to be made that limits the HVDC's fast response capability by setting operating constraints. However, with the increasing integration of large-scale renewable energy into the electric system, it is harder to meet the real-time power balance due to its random output. The fast controllability of the HVDC system should receive attention and needs a better coordination scheme for releasing its support capability to meet the growing demand for renewable energy output regulation.

The use of FFR motivates a prospective solution for the aforementioned problem such that the fast response capacity of the HVDC system could be best used. As shown in the following section, the participation of the local FFRs could prevent the power-sourced-provided grid from falling into unstable operating conditions, which enables the reaction of HVDC at a fast pace other than being limited. This paper does not claim by any means that the coordination control between the HVDC system and FFRs will bring more financially attractive benefits than single HVDC system control or FFRs response.

3.2 Transient stability analysis of the system with FFRs and HVDC system integration

This section shows that the use of FFR is beneficial to avoiding system instability when utilizing the fast controllability of the HVDC to support system frequency by using the extended equal-area criterion (EEAC) theory.

The EEAC theory is proposed by Professor Yusheng Xue as an effective method in the quantitative analysis of power system transient stability (Liao and Yun, 2004). The outstanding performances of EEAC have been demonstrated by online operation records in many energy management system (EMS) environments worldwide (Xu et al., 2017). If the power system is subject to a large disturbance (line break, short circuit, machine cut, load cut, *etc.*), the power system will be transiently stable under this large disturbance if the individual generating units can maintain synchronous operation and have acceptable voltage and frequency levels. The EEAC theory assumes that all generators in the system can be divided into two generator clusters under disturbance. Intuitively speaking, the generators being heavily disturbed are grouped and referred to as the critical cluster, whereas the rest are grouped as the remaining cluster.

When energy storage equipment and HVDC are connected to the power system, additional electromagnetic damping torque is generated on the generator side, which suppresses the oscillatory instability of the power angle. Analyzed in terms of the extended equal area method, FFR and HVDC deliver electromagnetic power to the power system, providing additional damping area and thus improving the transient stability of the system. Assuming that such two clusters have been found and the HVDC system and FFRs are included in the critical cluster, the whole system can be treated as a time-varying two-machine system. The equivalent inertia could be expressed as

$$\begin{cases} M_c\delta_c = P_{mc}(t) - P_{ec}(\delta(t)), \\ M_r\delta_r = P_{mr}(t) - P_{er}(\delta(t)), \end{cases} \tag{4}$$

where c represents the critical generator cluster and r represents the remaining cluster. M_c and M_r are the equivalent inertia of the critical generator cluster and the remaining cluster, respectively. P_{mc} and P_{mr} are the equivalent mechanical power of the critical generator cluster and the remaining cluster, respectively. P_{ec} and P_{er} are the equivalent electrical power of the critical generator cluster and the remaining cluster, respectively. δ_c and δ_r are the generator rotor angles.

With the standard simplifying assumptions, the motion of a system could be described as

$$M\ddot{\delta}_s = P_m - P_e \tag{5}$$

Here, M, P_m, and P_e can be described as

$$\begin{cases} M = \dfrac{M_c M_r}{M_{\text{total}}}, \\ M_{\text{total}} = \displaystyle\sum_{i=1}^{n} M_i, \\ P_m = \dfrac{M_c P_{mc} - M_r P_{mr}}{M_c + M_r}, \\ P_e = \dfrac{M_c P_{ec} - M_r P_{er}}{M_c + M_r}, \end{cases} \tag{6}$$

where M and M_{total} are equivalent inertia and total inertia of the system, respectively. P_m is the equivalent mechanical power and P_e is the equivalent electromagnetic power of the system.

As shown in Eq. 5, the stability problem of the system can be equivalent to the stability of the relative generator rotor angle:

$$\delta_s(t) = \delta_c(t) - \delta_r(t) \tag{7}$$

Equation 5 can be converted to

$$\ddot{\delta}_s = \left(\frac{P_{mc}}{M_c} - \frac{P_{mr}}{M_r}\right) - \left(\frac{P_{ec}}{M_c} - \frac{P_{er}}{M_r}\right) \tag{8}$$

When the HVDC system extracts the power from the supporting system to realize power support, P_{ec} is changed to

$$P_{ec}' = P_{ec} + (\Delta P_{\text{dc}} - \Delta P_{\text{ES}}) \tag{9}$$

where ΔP_{ES} is the injection power from FFRs to the power-sourced-provided system and ΔP_{dc} is the extracting power from the power-sourced-provided system to the HVDC system, which could be expressed as

$$\begin{cases} \Delta P_{\text{ES}} = R_{\text{ES}}(t), \\ \Delta P_{\text{dc}} = R_{\text{HVDC}}(t), \end{cases} \tag{10}$$

where R_{ES} and R_{HVDC} are the response rates of FFRs and the HVDC system.

The relative generator rotor angle could be expressed as

$$\ddot{\delta}_s' = \left(\frac{P_{mc}}{M_c} - \frac{P_{mr}}{M_r}\right) - \left(\frac{P_{ec}'}{M_c} - \frac{P_{er}}{M_r}\right) \tag{11}$$

where P_{ec}’ is the equivalent electrical power of the system after HVDC system support and δ_s’ is the relative generator rotor angle after HVDC system support.

The stability margin of the system’s first swing changes to

$$\eta' = \int_{\delta_0}^{\delta_{DSP}} (P_e' - P_m)\,d\delta \tag{12}$$

where δ_0 is the operating point of the equivalent generation before the HVDC system support, δ_{DSP} is the dynamic saddle point, η’ is the stability margin of the system’s first swing after HVDC system support, and P_e’ is the equivalent electromagnetic power of system after HVDC system support.

The stability margin deviation of the system’s first swing can be depicted as

$$\begin{aligned} \Delta\eta = \eta - \eta' &= \int_{\delta_0}^{\delta_{DSP}} (P_e - P_m)\,d\delta - \int_{\delta_0}^{\delta_{DSP}} (P_e' - P_m)\,d\delta, \\ &= \int_{\delta_0}^{\delta_{DSP}} (\Delta P_{\text{ES}} - \Delta P_{\text{dc}})\left(\frac{1}{M_c} + \frac{1}{M_r}\right)d\delta. \end{aligned} \tag{13}$$

Inserting Eqs 10, 13,

$$\Delta\eta = \eta - \eta' = \int_{\delta_0}^{\delta_{DSP}} (R_{\text{ES}}(t) - R_{\text{HVDC}}(t))\left(\frac{1}{M_c} + \frac{1}{M_r}\right)d\delta \tag{14}$$

As shown in Eq. 14, if $R_{\text{ES}}(t) - R_{\text{HVDC}}(t) > 0$, the stability margin deviation is large than 0 so that the system stability will not be affected by the frequency support of the HVDC system. If $R_{\text{ES}}(t) - R_{\text{HVDC}}(t) < 0$, the stability margin deviation is small than 0, so the system stability will be influenced by the HVDC system support. In order to demonstrate the impact of the HVDC system support and FFR coordination of the system transient stability, groups of frequency curves with different ratios k between $R_{\text{ES}}(t)$ and $R_{\text{HVDC}}(t)$ are depicted in Figure 4. The ratio k is defined as $k = R_{\text{ES}}(t)/R_{\text{HVDC}}(t)$.

Figure 4 shows that the response rate ratios between FFRs and the HVDC system significantly affect the transient stability of the power-sourced-provided grid. Figure 4 also shows that the faster response rate of FFRs could overcome the negative effect of the HVDC system on the supporting system stability during frequency support. Compared to traditional no FFR response, FFRs and the HVDC system coordination could support the system frequency without harming the system stability. Therefore, the coordination control of the HVDC system and FFRs is preferred during frequency support.

4 Combination frequency response control

Due to the increasing penetration of renewable energy and energy storage in the grid, the demand for real-time interactive source-load-storage response has increased significantly. Recently, FFR devices, represented by energy storage, have gradually started to be deployed as auxiliary services in the system. FFR can provide a fast power response to the measured or observed changes in system frequency, thus significantly mitigating power fluctuations due to the high proportion of renewable energy injected into the power system.

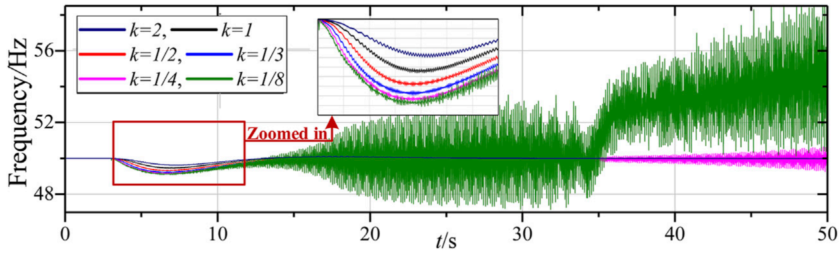

FIGURE 4
Frequency response curves with different ratios.

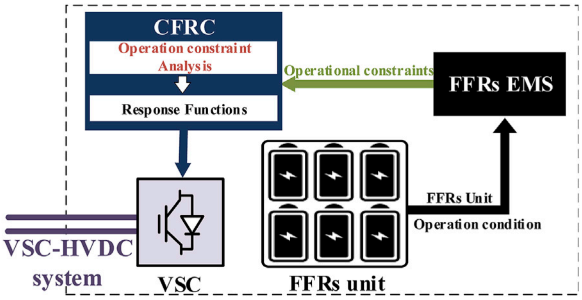

FIGURE 5
EMS structure of the system integrating the HVDC system and FFRs.

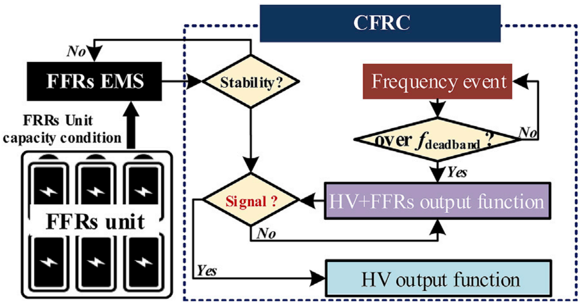

FIGURE 6
Basic control diagram of the CFRC.

In addition, voltage source converter-based high-voltage DC (VSC-HVDC) is a flexible DC transmission technology with fast power reversal capability. The active and reactive power can be controlled independently. It has many advantages, such as a black start and the ability to connect to weak AC networks, which can increase the flexibility of interconnected grids to support each other and regional standby complementarity. Owing to the voltage source converter-based characteristic, the FFRs could provide the same response rate output as the HVDC system. Thus, the frequency response control of the HVDC system should consider the capacity of the FFRs for the operating stability of the power-sourced-provided grid. This paper proposes a combination frequency response control (CFRC) strategy for FFRs and the HVDC system coordinating under the contingency. The detailed control strategy of the CFRC is introduced in the following sections.

4.1 General energy management system structure of the system integrating the HVDC system and FFRs

The realization coordination control of the HVDC system and FFRs needs a reliable real-time energy management system (EMS). Figure 5 shows the general EMS structure of the system integrating the HVDC system and FFRs to guarantee the operation of the proposed CFRC. As shown in Figure 5, the EMS is based on the wide-area monitoring system, and FFRs and the HVDC system information interaction could be achieved speedily and reliably. The PMU in the wide-area measurement system measures the frequency and phase angle quantities on the contact line associated with the FFR and then packages the data to send to the FFRs EMS. The EMS of the FFRs continuously monitors the operating condition of the FFRs, converts the FFRs' operation condition to the operating constraints, and then sends it to CFRC. After that, the operating constraints of the FFRs are sent to the CFRC for further analysis, and the response function of the HVDC system is determined if a frequency event occurs.

4.2 Combination frequency response control

The objective of the CFRC is to realize a reasonable HVDC frequency response control that makes the most of the fast response capacity of the HVDC system while guaranteeing the power-sourced-provided grid operating safety. Therefore, the CFRC is separated into two parts: one for HVDC emergency support control and the other for frequency stabilization identification control. The HVDC emergency support control is designed to quickly stabilize the system frequency and reduce system frequency variations after the occurrence of a disturbance. Then, the frequency stabilization identification ensures that the HVDC emergency support control is over. The CFRC is configured on one of the terminals of the VSC-HVDC system and works on constant active power control. The basic control diagram of the CFRC is depicted in Figure 6.

(1) HVDC emergency support control aims to reduce the amount of frequency change after an AC system incident. In conventional

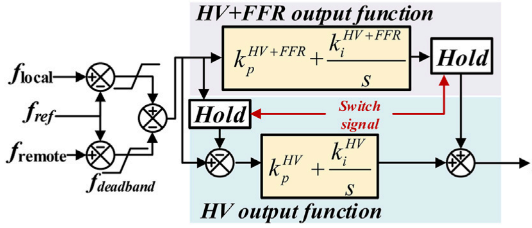

FIGURE 7
Flowchart of the HVDC emergency support control.

converter stations, HVDC frequency control mostly uses a fixed proportionality factor without considering the frequency regulation capability of the AC grid on the opposite side involved in frequency regulation. This leads to the possibility of large deviations in the frequency of the AC grid on the opposite side during the use of HVDC support power, affecting its own safe and stable operation. In order to overcome this problem, this paper adopts the amount of frequency deviation on both sides as the control quantity.

Figure 7 depicts the flowchart of the HVDC emergency support control. In Figure 7, f_{local} is the measured frequency of the PCC bus, f_{remote} is the measured frequency on the PCC bus of the other terminal of the VSC-HVDC system, f_{ref} is the nominal frequency, f_{deadband} is the dead-band of the CFRC activation, and k^{HV+FFR} and k^{HV} are the droop coefficients for the HVDC system frequency response under different operation conditions, respectively. The active-frequency regulation slopes k_p and k_i are determined by considering the online reserve capacity and inertia of the AC grid on both sides of the HVDC.

(2) The frequency stability identification control aims to determine the end moment of the HVDC emergency support control. Therefore, the current amount of power on the HVDC is automatically maintained after the system frequency has stabilized. The judgment criterion is shown as follows:

$$FFR_{op-\mathrm{cap}} \leq FFR_{\mathrm{cap}} - \lambda \tag{15}$$

where $FFR_{op\text{-}cap}$, FFR_{cap}, and λ are the operating capacities of the FFRs, the total capacity of FFRs, and the buffering coefficient for FFRs exiting, respectively.

As shown in Figure 6, the controller determines the frequency fluctuation condition of the system by monitoring the power of the AC system to which the DC station is connected. When the operating capacity is less than the capacity threshold, the controller sends a signal to keep the current amount of power on the HVDC stable. The frequency stability identification control ensures that the system is stable by identifying the system capacity before exiting the combined frequency response control.

(3) The CFRC process is described as follows: when a frequency event occurs at one connected grid and the frequency oscillation is over the dead band, the CFRC is activated to respond to the frequency oscillation. In order to suppress the influence of the HVDC system on the power-sourced-provided grid, FFRs in the power-sourced-provided grid are activated at the same time. FFRs provide support with the same response rate as the HVDC system. Meanwhile, its EMS continuously monitors the capacity condition of the FFR unit. When the capacity of the FFR unit reaches Eq. 15, FFRs exit the support process and send a signal to the CFRC. Once the CFRC receives the signal from FFRs, the CFRC will use the "hold" function to freeze the value of the current frequency change and the HV+FFR output function. Because the value of the current frequency change is frozen by the "hold" function, the HV output function is automatically activated and the CFRC will provide support to the disturbed grid with k^{HV} until the frequency at the disturbed grid is stable.

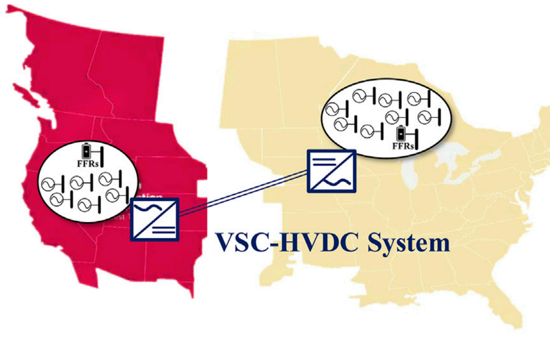

FIGURE 8
Configuration of the NAG system.

TABLE 1 Generation capacities of the highly NAG model.

EI		WECC	
Gen	Capacity (MW)	Gen	Capacity (MW)
G-EI1	102,410	G-WE1	11,350
G-EI2	104,593	G-WE2	12,875
G-EI3	115,006	G-WE3	10,713
G-EI4	116,854	G-WE4	11,682
G-EI5	107,176	G-WE5	11,858
G-EI6	50,809	G-WE6	3,467
G-EI7	3,603		
G-EI8	6,000		

With the proposed CFRC, the HVDC system could provide a fast enough response to the disturbed system to improve the frequency nadir and stabilize the frequency as soon as possible. Meanwhile, with the continuous monitoring of the capacity condition of the FFRs, the CFRC could adjust the response rate of the HVDC system to prevent the power-sourced-provided grid from falling into a bad operating condition.

5 Simulation verification

5.1 Model description

To verify the performance of the proposed CFRC, a highly reduced North American grid (NAG) model is adopted in PSCAD/EMTDC, as depicted in Figure 8. The highly reduced

TABLE 2 Converters' parameters in the VSC-HVDC system.

Converter station	Rated VSC power (MVA)	Nominal DC voltage (kV)	Nominal AC voltage (kV)
VSC1	4,000	±500	500
VSC2	4,000	±500	500

TABLE 3 Examples of the electrochemical energy storage suitable for fast response services.

Technology	Power range (MW)	Energy rating (MWh)	Response time	Discharge time
Flywheel (converter)	0.1–400	Up to 5	≤4 m	Up to 15 min
Lithium batteries	Up to 50 or more	Up to 20	Few to 40 m	Minutes to hours
Flow batteries	~3.50 possible	Up to 60	Few to 40 m	Seconds to hours
Advanced lead–acid batteries	Up to 40	Up to 40	Few to 40 m	Seconds to hours

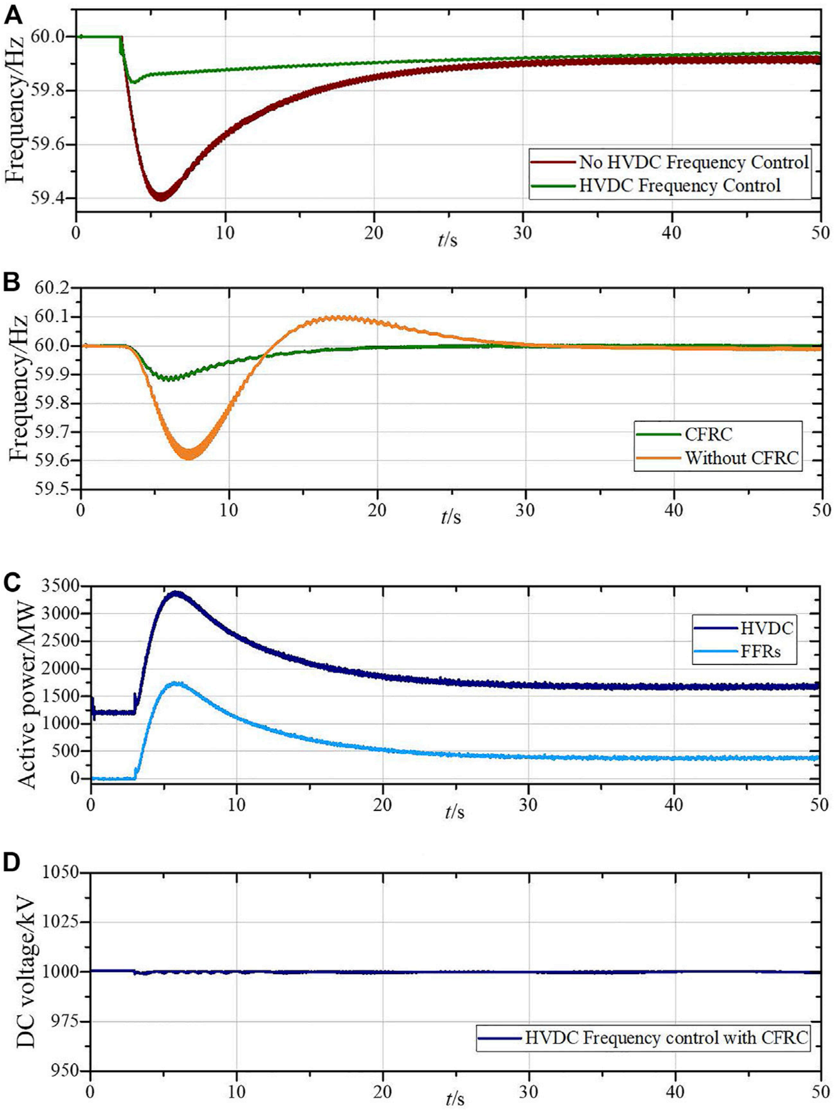

FIGURE 9
Simulation results of the VSC-HVDC system in frequency control. **(A)** Frequency of the EI with HVDC frequency control and without HVDC frequency control. **(B)** Frequency of the WECC with and without CFRC. **(C)** Power flow on the VSC-HVDC system and the output of FFRs. **(D)** DC voltage of the VSC-HVDC system during the HVDC frequency control with the CFRC.

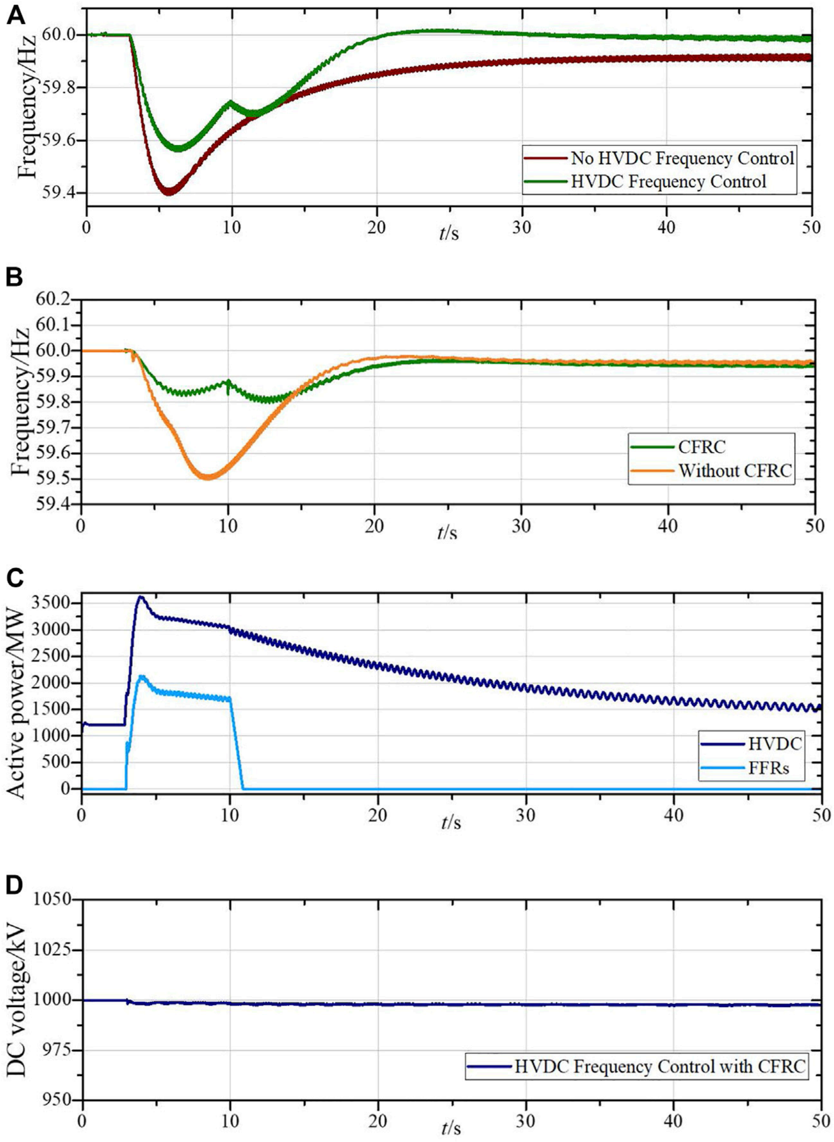

FIGURE 10
Simulation results of the VSC-HVDC system in frequency control. **(A)** Frequency of the EI with HVDC frequency control and without HVDC frequency control. **(B)** Frequency of the WECC with and without CFRC. **(C)** Power flow on the VSC-HVDC system and the output of FFRs. **(D)** DC voltage during the HVDC frequency control with the CFRC.

models are developed from an equivalent NAG model. The data of this NAG model have been openly published (CURENT, 1001; Geni). The equivalent NAG model has been validated by a full NAG model in power flow and frequency response perspective. Because the equivalent NAG model is too big for the PSCAD simulation, the EI and WECC systems are further reduced with the generation aggregation method, in which the EI system is represented by seven dynamic cluster generations and the WECC system is represented by six dynamic cluster generations. The data of these two systems are shown in Table 1. FFRs configured in the WECC and EI are assumed as VSC-based energy storage, and the capacity is assumed as 10 MWh/800 MW. A two-terminal VSC-HVDC system is embedded in highly reduced models, where the VSC1 is connected to WECC and the VSC2 is connected to EI. The VSC1 works at CAPC with CPFC, and the VSC2 works at CDVC. The frequency dead-band of the CPFC is set as .05 Hz, and the k^{HV+FFR} and $k_P{}^{HV}$ of the CPFC are set to 5 and 3, respectively. The parameters of the VSC-HVDC system are depicted in Table 2. The parameters of the electrochemical energy storage are depicted in Table 3 (Meng et al., 2020). The initial condition of the VSC-HVDC system is 1,200 MW, and the direction is from WECC to EI.

5.2 Case I: Trip one generator in EI (the response of FFRs does not exceed their capacity)

At t = 3 s, the generator G-EI7 (3,603 MW) is tripped in EI. Figure 9 shows the simulation results of the VSC-HVDC system using the CFRC to support the EI system.

As shown in Figure 9A, if the disturbed system only relies on its inner frequency response capacity, the frequency will drop to 59.6 Hz, which may activate the automatic under-frequency load shedding and lead to serious financial loss for the system operator and power customers. However, with the HVDC frequency control, the frequency nadir of the disturbed system can be significantly improved. It reduces the probability of serious events. However, owing to the fast response performance of the HVDC system, the frequency of the power-source-provided system will be affected.

As shown in Figure 9B, the frequency in the power-source-provided system drops to 59.6 Hz. It is not an acceptable operating frequency for the system's inner devices. With the proposed CFRC, the frequency drop in the power-source-provided system is suppressed, and the equipment in the power-source-provided system could operate well under this frequency until the contingency is clear.

Figure 9C shows the power flow change of the HVDC system and the power output change of FFRs. Figure 9D shows the DC voltage change of the HVDC system. As shown in Figures 9C, D, with the proposed CPFC, the FFRs could follow the HVDC system frequency response in real-time to mitigate the influence caused by the HVDC system frequency response to the power-source-provided system so that avoiding unacceptable frequency drops. The DC voltage during the CPFC working process is stable, which indicates that the CPFC will not influence the stability of the VSC-HVDC system's normal operation.

5.3 Case II: Trip one generator in EI (the response of FFRs exceeds their capacity)

At $t = 3$ s, the generator G-EI8 (6,000 MW) is tripped in EI. At $t = 10$ s, due to out-of-capacity, FFRs exit from the coordination control. Figure 10 shows the simulation results of the VSC-HVDC system using the CFRC to support the EI system.

As shown in Figure 10, after the generator trips in the EI, the HVDC system immediately responds to the frequency variation. With the CFPC, FFRs follow the HVDC system power flow change to suppress the frequency deviation in the power-source-provided system. At $t = 10$ s, FFRs exit from the support for out-of-capacity. As shown in Figure 10C, the output of FFRs drops to 0 MW with a constant ramping rate. According to the proposed CPFC, the output function of the HVDC system changes from the HV+FFR output function to the HV output function. As shown in Figure 10C, the response rate of the HVDC is decreased. During the function switch process, the frequency in the WECC (Figure 10B) and EI (Figure 10A) has acceptable oscillation. Figure 10D shows that the DC voltage is also stable during the CPFC working process. The simulation results indicate that the proposed CPFC could enhance the frequency response capacity of the HVDC system while avoiding unacceptable frequency variation of the power-source-provided system under the contingency.

6 Conclusion

The HVDC system could provide a quick dynamic response to various system disturbances. Providing ancillary services through the HVDC system is expected to be a high-value product for system operation. However, due to the response rate deviation between the traditional generators and the HVDC system, the unrestricted power regulation rate of the HVDC system may cause huge frequency oscillations in the supporting system and even cause power outages. Therefore, improving the system frequency response performance through the HVDC system or guaranteeing the operating safety of the support-provided system is a clear dilemma in system frequency control. In this paper, based on the coordination between the HVDC system and fast frequency response, a combination frequency response control is proposed to make the most use of the fast response capacity of the HVDC system and prevent the power-sourced-provided grid from falling into unstable operating conditions. The proposed combination frequency response control is demonstrated based on a highly reduced power system model of the three North American interconnections. The results from the simulation show that the proposed combination frequency response control is effective and performs well under different contingencies. With the proposed combination frequency response control, the frequency stability of the disturbed system could be significantly improved. Meanwhile, the frequency of the power-source-provided system will be kept within an acceptable level for the system's normal operation. In the future, the communication delay between energy storage and HVDC will be considered in the strategy to further improve the accuracy of fast frequency response.

Data availability statement

The original contributions presented in the study are included in the article. The data cannot be fully given because of NDA restrictions. Further inquiries can be directed to the corresponding author.

Author contributions

QX wrote a section of the manuscript. JL, DN, and PL contributed to data curation, analysis, and visualization. JL contributed to the manuscript revision. All authors approved the submitted version.

Conflict of interest

DN was employed by State Grid Jinan Power Supply Company. PL was employed by State Grid Binzhou Power Supply Company.

The remaining authors declare that the research was conducted in the absence of any commercial or financial relationships that could be construed as a potential conflict of interest.

Publisher's note

References

Belkin, P. (2012). *HVDC and power electronic systems for overhead line and insulated cable applications.* Paris, France: CIGRE San Francisco Colloquium.

Curent CURENT North American grid. Available: https://db.bettergrids.org/bettergrids/handle/1001/414.

Elizondo, M. A., and Kirkham, H. (2016). *Economics of high voltage dc networks*. USA: Pacific Northwest National Laboratory.

Geni Map. Map of United States of America electricity grid. Available at: https://www.geni.org/globalenergy/library/national_energy_grid/united-states-of-america/americannationalelectricitygrid.shtml.

Judge, P. D., and Green, T. C. (2019). Modular multilevel converter with partially rated integrated energy storage suitable for frequency support and ancillary service provision. *IEEE Trans. Power Del.* 34 (1), 208–219. doi:10.1109/tpwrd.2018.2874209

Junyent-Ferr, A., Pipelzadeh, Y., and Green, T. C. (2015). Blending HVDC-link energy storage and offshore wind turbine inertia for fast frequency response. *IEEE Trans. Sustain. Energy* 6 (3), 1059–1066. doi:10.1109/tste.2014.2360147

Kim, Y., Del-Rosario-Calaf, G., and Norford, L. K. (2017). Analysis and experimental implementation of grid frequency regulation using behind-the-meter batteries compensating for fast load demand variations. *IEEE Trans. Power Syst.* 32 (1), 484–498. doi:10.1109/tpwrs.2016.2561258

Kirby, B. A method and case study capability of a control area or balancing authority and implications for moderate or high wind penetration. Available: https://www.nrel.gov/docs/fy05osti/38153.pdf.

Li, J., Zuo, X., Zhao, Y., Lv, X., and Wang, J. (2019). Operation, analysis and experiments of DC transformers based on modular multilevel converters for HVDC applications. *CSEE J. Power Energy Syst.* 5 (1), 87–99. doi:10.17775/cseejpes.2017.00630

Liao, H., and Yun, T. (2004). Qualitative analysis of the CCEBC/EEAC method. *Sci. China Ser. E Technol. Sci.* 47.

Meng, L., Zafar, J., Khadem, S. K., Collinson, A., Murchie, K. C., Coffele, F., et al. (2020). Fast frequency response from energy storage systems—a review of grid standards, projects and technical issues. *IEEE Trans. Smart Grid* 11 (2), 1566–1581. doi:10.1109/TSG.2019.2940173

Miso (2014). *MISO transmission expansion planning (MTEP).* Carmel, Indiana, UAE: MISO Energy.

Nrel Interconnections seam study. Available: https://www.nrel.gov/analysis/seams.html.

Pathak, N., Verma, A., and Bhatti, T. S. "Utilizing HVDC links as a energy storing device in AGC operation of hydro-thermal-gas based interconnected power systems," in Proceedings of the 2017 International Conference on Technological Advancements in Power and Energy (TAP Energy), Kollam, India, December 2017.

Rakhshani, E., Mehrjerdi, H., Al-Emadi, N. A., and Rouzbehi, K. "On sizing the required energy of HVDC based inertia emulation for frequency control," in Proceedings of the 2017 IEEE Power & Energy Society General Meeting, Chicago, IL, USA, July 2017.

Ray, P. K., Mohanty, S. R., Kishor, N., and Mohanty, A. "Small-signal analysis of hybrid distributed generation system with HVDC-link and energy storage elements," in Proceedings of the 2009 Second International Conference on Emerging Trends in Engineering & Technology, Nagpur, India, December 2009.

Sun, J., Li, M., Zhang, Z., Xu, T., He, J., Wang, H., et al. (2017). Renewable energy transmission by HVDC across the continent: System challenges and opportunities. *CSEE J. Power Energy Syst.* 3 (4), 353–364. doi:10.17775/cseejpes.2017.01200

Sun, K., Li, K. J., Zhang, Z., Liang, Y., Liu, Z., and Lee, W. J. (2022). An integration scheme of renewable energies, hydrogen plant, and logistics center in the suburban power grid. *IEEE Trans. Ind. Appl.* 58 (2), 2771–2779. doi:10.1109/tia.2021.3111842

Sun, K., Li, K. J., Lee, W. J., Wang, Z. D., Bao, W., Liu, Z., et al. (2019). VSC-MTDC system integrating offshore wind farms based optimal distribution method for financial improvement on wind producers. *IEEE Trans. Ind. Appl.* 55 (3), 2232–2240. doi:10.1109/tia.2019.2897672

Sun, K., Qiu, W., Dong, Y., Zhang, C., Yin, H., and Liu, Y. (2022). WAMS-Based HVDC damping control for cyber attack defense. *IEEE Trans. Power Syst. Early Access*, 1. doi:10.1109/tpwrs.2022.3168078

Sun, K., Qiu, W., Yao, W., You, S., Yin, H., and Liu, Y. (2021). Frequency injection based HVDC attack-defense control via squeeze-excitation double CNN. *IEEE Trans. Power Syst.* 36 (6), 5305–5316. doi:10.1109/tpwrs.2021.3078770

Sun, K., Xiao, H., Pan, J., and Liu, Y. (2021). A station-hybrid HVDC system structure and control strategies for cross-seam power transmission. *IEEE Trans. Power Syst.* 36 (1), 379–388. doi:10.1109/tpwrs.2020.3002430

Sun, K., Xiao, H., Pan, J., and Liu, Y. (2021). VSC-HVDC interties for urban power grid enhancement. *IEEE Trans. Power Syst.* 36 (5), 4745–4753. doi:10.1109/tpwrs.2021.3067199

Sun, K., Xiao, H., Sundaresh, L., Pan, J., Li, K., and Liu, Y. (2019). Frequency response reserves sharing across asynchronous grids through MTDC system. *IET Gener. Transm. Distrib.* 13 (21), 4952–4959. doi:10.1049/iet-gtd.2019.1006

Sun, K., Xiao, H., You, S., Li, H., Pan, J., Li, K. J., et al. (2020). Frequency secure control strategy for power grid with large-scale wind farms through HVDC links. *Int. J. Electr. Power Energy Syst.* 117, 105706. doi:10.1016/j.ijepes.2019.105706

Xiao, H., Sun, K., Pan, J., Li, Y., and Liu, Y. (2021). Review of hybrid HVDC systems combining line communicated converter and voltage source converter. *Int. J. Electr. Power Energy Syst.* 129, 106713. doi:10.1016/j.ijepes.2020.106713

Xiao, H., Xu, Z., Tang, G., and Xue, Y. (2015). Complete mathematical model derivation for modular multilevel converter based on successive approximation approach. *IET Power Electron* 8 (12), 2396–2410. doi:10.1049/iet-pel.2014.0892

Xu, M., Wu, L., Liu, H., and Wang, X. (2019). Multi-objective optimal scheduling strategy for wind power, PV and pumped storage plant in VSC-HVDC grid. *J. Eng.* 2019 (16), 3017–3021. doi:10.1049/joe.2018.8435

Xu, X., Zhang, H., Li, C., Liu, Y., Li, W., and Terzija, V. (2017). Optimization of the event-driven emergency load-shedding considering transient security and stability constraints. *IEEE Trans. Power Syst.* 32 (4), 2581–2592. doi:10.1109/TPWRS.2016.2619364

Yang, B., Sang, B., Yang, Z., Li, M., Xiang, W., Lu, X., et al. (2019). Coordinated control strategy of a DC grid with energy storage system. *J. Eng.* 2019 (16), 1778–1782. doi:10.1049/joe.2018.8717

You, S., Guo, J., Kou, G., Liu, Y., and Liu, Y. (2016). Oscillation mode identification based on wide-area ambient measurements using multivariate empirical mode decomposition. *Electr. Power Syst. Res.* 134, 158–166. doi:10.1016/j.epsr.2016.01.012

Zhao, H., Wu, Q., Xu, H., and Rasmussen, C. N. (2015). Review of energy storage system for wind power integration support. *Appl. Energy* 137, 545–553. doi:10.1016/j.apenergy.2014.04.103

Zhou, D., Guo, J., Zhang, Y., Chai, J., Liu, H., Gui, X., et al. (2016). Distributed data analytics platform for wide-area synchrophasor measurement systems. *IEEE Trans. Smart Grid* 7 (5), 2397–2405. doi:10.1109/tsg.2016.2528895

Frontiers in
Energy Research

Advances and innovation in sustainable, reliable and affordable energy

Explores sustainable and environmental developments in energy. It focuses on technological advances supporting Sustainable Development Goal 7: access to affordable, reliable, sustainable and modern energy for all.

Discover the latest Research Topics

See more →

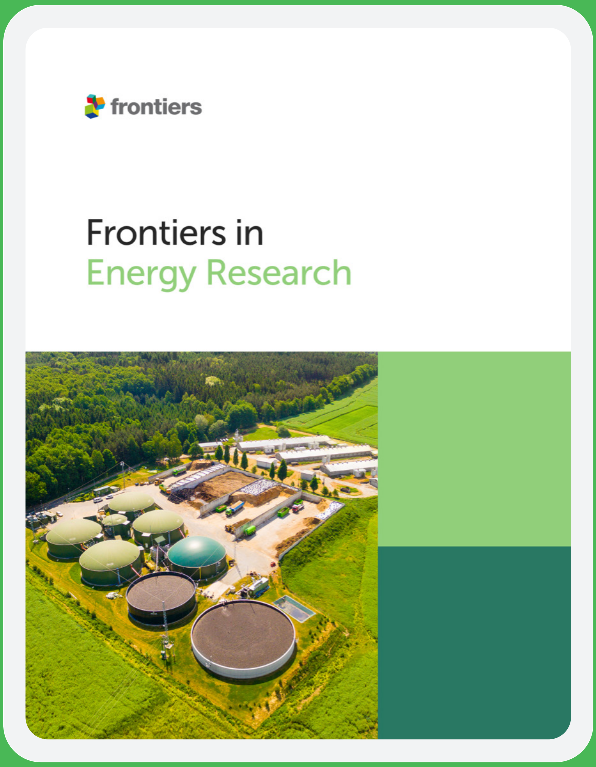
frontiers

Frontiers in
Energy Research

Frontiers

Avenue du Tribunal-Fédéral 34
1005 Lausanne, Switzerland
frontiersin.org

Contact us

+41 (0)21 510 17 00
frontiersin.org/about/contact